Development of an Auto-Calibrated Receiver in Planar Technology at Millimetre-Wave Frequencies

Memoria de la Tesis Doctoral realizada por

Ainara Rebollo Mugueta

Y dirigida por

Dr. Iñigo Ederra Urzainqui

Para optar al grado de

Doctora en Ingeniería de Telecomunicación

upna Universidad Pública de Navarra
Nafarroako Unibertsitate Publikoa

Universidad Pública de Navarra
Departamento de Ingeniería Eléctrica y Electrónica
Pamplona, Junio 2015

A mi familia,
A mis amig@s,
A Oskar.

Agradecimientos

Después de varios años en mi segunda casa, la Universidad Pública de Navarra, por fin ha llegado el momento de finalizar una etapa y comenzar una nueva. Una etapa nueva, llena de ilusiones, que no puede empezar sin ántes agradecer a todas aquellas personas que me han acompañado, ayudado, impulsado y soportado a lo largo de esta montaña rusa que es la investigación, con sus subidas y bajadas.

En primer lugar me gustaría dar las gracias a mi Director de Tesis, Iñigo, por abrirme las puertas del mundo de la investigación de par en par y permitirme desarrollar esta apasionante Tesis, por su incondicional apoyo y por su total disponibilidad a la hora de juntarnos un rato para resolver dudas y problemas. No ha sido fácil y tampoco nadie dijo que lo fuera pero siempre has estado ahí y has sido una fuente de energía e inspiración para mí. Muchas gracias!

En segundo lugar me gustaría agradecer a todos los miembros del Grupo de Antenas de la Universidad Pública de Navarra por acogerme, ayudarme, compartir conocimientos, darme la oportunidad de participar en cursos y Congresos y por dejarme disfrutar como una enana de sus laboratorios. Gracias a los Seniors del Grupo, Ramón, Jorge, Carlos, Juan Carlos y Miguel por vuestros ánimos, planteamientos y por exponer puntos de vista diferentes que mi cabezonería no me permitía ver. Gracias a todos los Junior, Itziar, Belén, Iñigo, Amagoia, Gonzalo, Inés, Etayo, Asier, Aitor e Irina y a las "nuevas" incorporaciones, Unai, Torres, Baha, Pacheco, Pablo, Jaime, Carlos y Jose, por esos coffe breaks, barbacoas, cenas, Congresos, cursos, pastas... en definitiva por todos esos grandes momentos que hemos compartido hablando de temas técnicos, fabricaciones, campos electromagnéticos, medidas, inquietudes, problemas, logros, frikadas... Gracias por lo que viene siendo un fiestón de telekos ;-)

Por último pero no menos importante, mi más profundo agradecimiento a mis padres, a mi hermana, al resto de mi familia y amig@s. Muchas veces me he esforzado por explicaros qué es lo que he hecho en esta Tesis sin conseguirlo. Pero, a pesar de no entenderlo, siempre habeís estado ahí para escucharme, apoyarme, confiar en mí, animarme y facilitarme el día a día.

Y gracias a ti Oskar, gracias por soportar mis cambios de humor, hacerme reir, ayudarme a desconectar, quererme y cuidarme. Sin ti no se si esto hubiera sido posible.

Abstract

This dissertation deals with the development of an auto-calibrated receiver at W-band for Passive Millimetre-Wave imaging applications. The proposed receiver has three main characteristics. Firstly, its differential configuration allows performing the internal calibration of the system. As opposed to total power receivers, this configuration reduces the effect of receiver instabilities. Secondly, it is entirely built in planar technology. As a consequence, a broadband planar antenna could be included in the same substrate resulting in a compact and light receiver. And finally, the W-band auto-calibrated receiver is based on a direct detection scheme which makes it simpler extending the number of receivers. Moreover, it uses commercially available low loss dielectric substrate and MMIC devices such as low noise amplifiers and detectors.

This dissertation tackles all the required steps for the development of the W-band auto-calibrated receivers. Firstly, the theoretical analysis of the differential configuration was done highlighting its main advantages. Once this configuration was analyzed, the design of its W-band planar components, i.e. a quadrature hybrid coupler, WR10 waveguide to microstrip transition based on an E-plane probe and Vivaldi antenna fed by a slotline to microstrip transition, and the selection of the MMIC devices, i.e. low noise amplifier, reference load and detector, were carried out. Then, the analysis of the real configuration of the receiver was accomplished, identifying the effect of each component on its performance.

After finishing the design, the proposed components were characterized. This process includes, as first step, the analysis of the dielectric constant and loss tangent of several substrates in order to determine their properties in the W-band. Afterwards, an inline WR10 waveguide to microstrip transition, required to characterize multiple planar devices at W-band frequencies with

waveguide based measurement equipment was designed, manufactured and validated. This was the basic block used to characterize the manufactured components. Once the performance of these components was verified, the packaging metal block was designed and manufactured. It includes an innovative solution, based on a pin surface, in order to avoid the propagation of undesired modes, which can penalize the performance of the planar receiver. The experimental results prove the suppression of these cavity modes. Finally, the complete W-band auto-calibrated receiver was assembled and characterized in terms of input reflection coefficient, dynamic range, RF-DC response, effective bandwidth and equivalent noise temperature.

This dissertation was carried out into the frame of the project "Desarrollo de Receptores en banda sub-milimétrica para aplicaciones de seguridad" which was focused on the development of a millimetre wave range imaging camera for security applications. This project, led by the company Alfa Imaging, was funded by the Spanish Ministry of Science and Innovation under contract IPT-2011-0960-390000.

Resumen

En esta Tesis se ha desarrollado un receptor autocalibrado en banda W para aplicaciones de captación de imágenes de manera pasiva en ondas milimétricas. El receptor propuesto en esta Tesis tiene tres características principales. La primera es que el receptor consta de una configuración diferencial que realiza internamente la calibración del sistema. Además, a diferencia de los receptores de potencia total, esta estructura es capaz de eliminar los problemas relacionados con las inestabilidades producidas por alguno de los componentes del receptor, como por ejemplo los amplificadores de bajo ruido. La segunda característica es que el receptor está completamente diseñado en tecnología plana. Por lo tanto, una antena plana de banda ancha tipo Vivaldi puede ser integrada con el resto de componentes obteniendo un receptor más compacto y ligero que aquellos que utilizan componentes en guía de onda. Finalmente, el receptor está basado en detección directa, lo cuál simplifica el extender el número de receptores. Adémas, el receptor propuesto en banda W utiliza un sustrato comercial de bajas pérdidas y dispositivos MMIC comerciales, como por ejemplo amplificadores de bajo ruido y detectores.

Esta Tesis aborda todos los pasos necesarios para el desarrollo de receptores autocalibrados en banda W. Primero, se lleva a cabo un análisis teórico de la configuración diferencial del receptor destacando sus principales ventajas. Una vez que el funcionamiento de la estructura balanceada del receptor ha sido analizado, se realiza el diseño de sus componentes microstrip y se explica la selección de sus dispositivos commerciales MMIC. Por un lado, los componentes microstrip que se diseñan son el híbrido en cuadratura, la transición de guía de onda WR10 a microstrip basada en una sonda de plano E y la antena Vivaldi alimentada por una transición de tecnología slotline a microstrip. Por otro lado, los dispositivos MMIC que se seleccionan son los amplificadores de bajo ruido, la carga de referencia y los detectores. Después,

se ha analizado por simulación el receptor tratando de identificar el efecto de cada uno de sus componentes reales en su funcionamiento.

Después de finalizar los diseños, los componentes propuestos son caracterizados. El primer paso de este proceso es el análisis de la constante dieléctrica y la tangente de pérdidas de varios sustratos para determinar sus propiedades en la banda W. A continuación, se diseña, fabrica y valida una transición en línea de guía de onda WR10 a microstrip necesaria para caracterizar los componentes planos del receptor con el equipamiento de medida basado en guía de onda en banda W. Éste es el bloque básico utilizado para caracterizar los componentes fabricados, por ejemplo, el híbrido en cuadratura, la antena Vivaldi y la carga de referencia. Una vez que sus funcionamientos han sido verificados, se ha llevado a cabo el diseño y fabricación del bloque metálico que contiene todos los componentes del receptor, incluyendo los circuitos DC necesarios para alimentar los amplificadores y adecuar las señales de salida. Éste bloque metálico incluye una solución innovadora, basada en una superficie de pines, para evitar la propagación de modos de cavidad que pudieran degradar el funcionamiento del receptor. Los resultados experimentales corroboran la supresión de estos modos de cavidad. Finalmente, el receptor autocalibrado en banda W ha sido fabricado, montado y caracterizado mediante la medida de su coeficiente de reflexión de entrada, su rango dinámico, su respuesta RF-DC, su ancho de banda equivalente y su temperatura equivalente de ruido.

Esta Tesis ha sido realizada dentro del marco del proyecto “Desarrollo de Receptores en banda submilimétrica para aplicaciones de seguridad” cuyo objetivo es el desarrollo de una cámara de imagen en ondas milimétricas para aplicaciones de seguridad. Este proyecto, liderado por la empresa española Alfa Imaging, fue financiado por el Ministerio Español de Ciencia e Innovación bajo el contrato IPT-2011-0960-390000.

Contents

Chapter 1

Introduction

1.1 Background: Passive Millimetre-Wave Imaging

Passive millimetre-wave (PMMW) imaging is a method of forming images by means of the passive detection of naturally occurring millimetre-wave radiation from a scene [1]. Its interest is based on two reasons: the availability of new sensor technology which allows PMMW imaging at video rates and the ability of forming images in a variety of low-visibility conditions, during the day or night, in clear weather or even through certain materials. These advantages are useful for a wide range of applications. Examples of these are military imaging missions (surveillance, precision targeting, navigation, aircraft landing, refuelling in clouds, search and rescue, metal detection in a cluttered enviroment, and harbor navigation in fog), civilian missions (commercial aircraft landing aid in fog, airport operation in fog, harbor surveillance, highway traffic monitoring in fog, and concealed weapons detection in airports and other locations), bio-medicine (pharmaceuticals, biopsies, imaging...) and materials research (spectroscopy, surface analysis, solid state reactions, inspection of foams, ceramics, plastics...). In addition, like visible and infrared (IR) sensors, the PMMW sensors do not emit any discernible and detrimental radiation, as opposed to radar and lidar.

Examples of passive imaging sensors are the human eye and the IR sensors. The human eye responds to the scattered light by seeing different colours because the spectral radiation of the objects when the sun is radiating, at about 6000 K, is concentrated in the visible range, see Fig. 1.1 b). However,

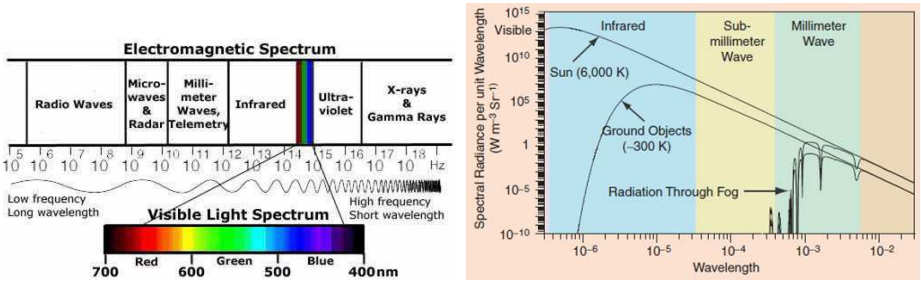

(a) (b)

Figure 1.1 – a) Frequency spectrum and b) the effect of fog on the blackbody radiation intensity of the sun (6000 K) and a ground object ($\sim$ 300 K) as a function of wavelength. Curves are shown both for objects without fog and with the effect of 1 km of fog.

IR sensors are required to make night vision feasible in absence of sunlight. The THz region, which includes millimetre, i.e. 30-300 GHz, and sub-millimetre wave ranges, i.e. 0.3-10 THz, as can be seen in Fig. 1.1 a), allows formation of images under low-visibility conditions, such as fog, rain, clouds or dust storms, both during the day and night, because the spectral radiation of the objects under these conditions is located in this frequency range.

The propagation of electromagnetic waves in the THz regime is affected by the attenuation produced by the continuum and resonant absorption of various atmospheric constituents such as water, oxygen, nitrogen, carbon dioxide or ozone. Whereas in the IR range the waves are strongly attenuated in the presence of fog, in the millimetre and sub-millimetre regimes they are mainly attenuated by the water vapor, as can be seen in Fig. 1.2. However, propagation windows exist in the millimetre wave range at 35, 94, 140 and 220 GHz, in which the attenuation is relatively modest in clear weather and fog [1], [2]. Moreover, it is merely affected by sun or artificial illumination. Therefore, millimetre waves are the best candidate for imaging in most low visibility conditions during the day or night. As a matter of fact, taking into account these frequency windows in which the attenuation is relatively small, many receivers have been developed for applications such as radar [3] - [6] and communication systems [7] - [9].

PMMW imaging is feasible in the millimetre wave range because the objects reflect and emit passive radiation just as they do in the IR and visible

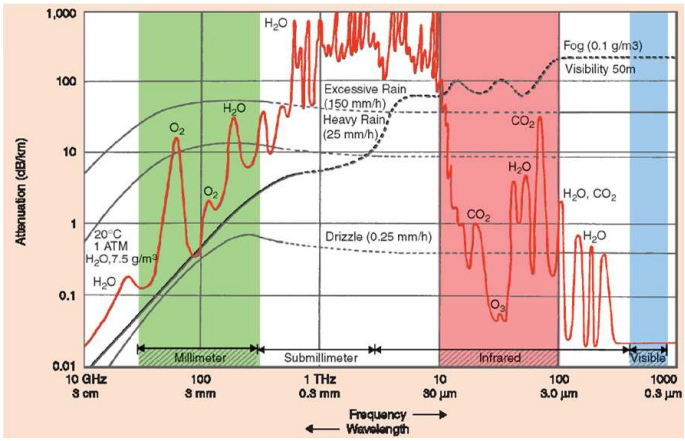

Figure 1.2 – The attenuation of millimetre waves by atmospheric gases, rain and fog [1].

regimes. This radiation is related to the emissivity of its physical temperature, the reflectivity of the illumination temperature and the transmission of the background temperature. Therefore, every object emits an specific radiation and it can be detected unequivocally in the millimetre wave regime [10] - [12]. Furthermore, the millimetre wave sensors are non-ionising and consequently harmless. They offer a good penetration depth ($\sim$ cm) which makes the detection of hidden objects feasible and also high sensitivity. The limitation of PMMW imaging is that its image resolution ($\sim$ mm) is worse than in the IR and visual ranges. Conversely, it can be improved by increasing the aperture size of the receiver optics or the operating frequency. Therefore, the selection of the propagation window is crucial and depends on the application requirements.

1.1.1 Applications

A wide range of applications have been reported taking advantage of the possibility of "seeing" under low-visibility conditions [13] or through certain materials such as paper, plastics, wood, leather, hair and even dry walls with little attenuation [14], [15]. These PMMW applications can be classified into three groups: applications focused on defence and security [16] - [31], astrophysics [32] - [35] and agriculture [10]- [11].

(a) (b)

Figure 1.3 – Examples of reconnaissance and surveillance applications of PMMW imaging: Detection of a) an aeroplane C-17 and b) roadways and buildings through clouds [1].

Within defence and security applications, which take advantage of the PMMW ability of seeing under low-visibility conditions, we can find poor weather navigation, aircraft landing and guidance, search and rescue, ground navigation, drug interdiction, beacon detection, oil-spill detection, monitoring volcano activity through smoke, control of vehicular traffic through smoke and smog inside the galleries, perimeter surveillance of harbours, docks and other designated areas and reconnaissance and surveillance by detecting ship wakes, low-radar cross-section boats, critical mobile and other targets. In Fig. 1.3, images taken by a PMMW imaging camera mounted on a Twin Otter [1], are superimposed on the corresponding visible-light images. Fig. 1.3 a) shows an aeroplane C-17 which is resolved from an altitude of 900 m. In this PMMW image, black colour shows colder objects such as metals. In this way, roadways and building have been imaged through a cloud bank, from an altitude of 580 m, see Fig. 1.3 b).

Other example of defence and security applications of PMMW imaging is related to the detection of hazardous objects hidden under clothes or certain materials. This includes weapons or guns [21] - [26], explosives [27] - [30] and chemical components [31]. For instance, Fig. 1.4 shows the detection of a gun using PMMW imaging at 94 GHz. Indeed, Fig. 1.4 a) [25] shows an outdoors PMMW image of a man carrying a gun in a bag whereas a man with a gun concealed under his clothing is indoors imaged in Fig. 1.4 b) [26]. As

(a)

Figure 1.4 – Example of defence and security applications of PMMW imaging related to the detection of a gun at 94 GHz: a) Outdoors PMMW image of a man carrying a gun in a bag [25] and b) indoors PMMW image of a man with a gun concealed under clothing [26].

can be seen, images acquired indoors present less contrast than those acquire outdoors.

In addition, a PMMW camera is useful in astrophysics applications. An example of that is the exploration of the Cosmic Microwave Background (CMB) carried out by the ESA's Planck mission [35], see Fig. 1.5. In this Figure, sky maps of the cosmic microwave background at the nine operating frequencies of the Planck mission, i.e. 30, 44, 70, 100, 143, 217, 353, 545 and 857 GHz, are shown. The combination of this collected data is crucial to achieve an optimal reconstruction of the foreground signals in order to subtract them and reveal the underlying Cosmic Microwave Background.

One example of PMMW applications related to agriculture includes the detection of the water content of farming fields [10]- [11] which can determine the necessity to be watered.

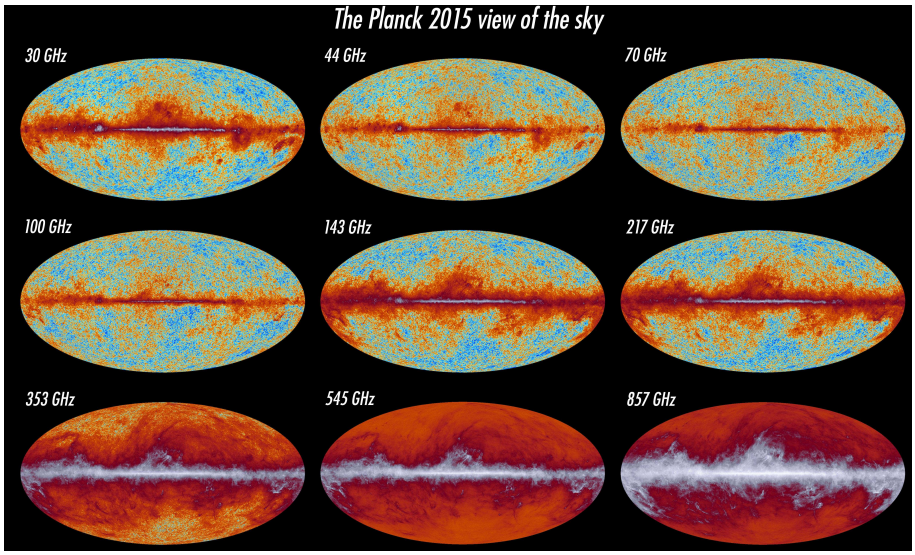

Figure 1.5 – All-sky maps of the cosmic microwave background at Planck mission nine different frequencies [35].

1.1.2 Commercial PMMW cameras

The commercial PMMW cameras, which have been developed mainly focused on defence and security applications, are described in Table 1.1. Note that most of them work at a frequency range centred at 94 GHz.

The receivers used in these PMMW cameras at W-band are based on direct detection mainly due to the availability of Monolithic Microwave Integrated Circuits (MMIC) devices such as low noise amplifiers and detectors and also low loss dielectric substrates which minimize the dielectric losses of the receivers. This last feature decreases the noise temperature of the system and, consequently, it improves the sensitivity or resolution of the receivers. Some research groups work in the development of low noise amplifiers with higher operating frequency such as Fraunhofer Institute for Applied Solid State Physics (IAF) which presented a low noise amplifier working up to 600 GHz [43]. However, low noise amplifiers are commercialised up to 160 GHz by OMMIC [44] and up to 140 GHz by Northrop Grumman [45]. For higher frequencies, heterodyne receivers must be implemented.

Table 1.1 – Commercial PMMW cameras.

Company	Product	Frequency (GHz)	Stand-off distance
Alfa Imaging [36]	A3S	$80-100$	$2-20$ m
Digital Barriers [37]	TS4	250	$3-10$ m
	TS5	250	$6-20$ m
Microsemi [38] (Brijot)	AllClear	$100-200$	$\sim$ cm
	Gen2	$80-100$	$\sim$ 1m
	MobileScan	$80-100$	$\sim$ 1m
Millivision [39]	X250	$80-100$	–
	S350	–	Portal area
	Walk-by-System 350	–	$\sim$ 7m
	Stand-off System 350	–	$3-4$ m
Rapidscan Systems [40]	Wave Scan 200	$80-100$	–
Trex Enterprises [41] (Sago Systems)	Sago ST-150	94	$\sim$ 5m
Qinetic [42]	SPO-7	–	14 m
	SPO-20	94	20 m
	SPO-30	90	$5-30$ m

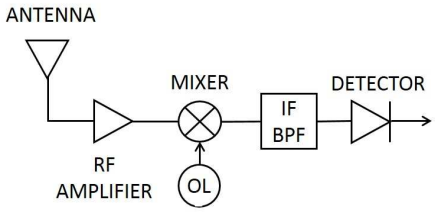

Figure 1.6 – Total power receiver.

1.1.3 Types of receivers

In this Section, different configurations of receivers are explained starting with the total power receiver. It is the simplest structure and the most commonly used. The main problem of this basic receiver structure is related to the gain and noise fluctuations of the amplifiers which strongly penalize its sensitivity. Therefore, other receiver configurations have been proposed in order to cope with this problem. The main configurations which remove the effect of receiver instabilities are Dicke receiver, differential receiver and correlation receiver.

In order to generalised this explanation, heterodyne receivers based on these configurations are shown. However, as mentioned, the use of a mixer and local oscillator are not required at those frequency ranges in which direct detection is feasible, such as W-band.

1.1.3.1 Total power receiver

The total power receiver is the simplest configuration, see Fig. 1.6, and it is considered as the basic receiver [46]. Many characteristics of more complex receiver configurations can be deduced from the corresponding total power receiver. The antenna couples the RF signal to the receiver and is amplified by a low noise amplifier. Next, the mixer down-converts this RF signal with a local oscillator (LO) producing an output signal at an intermediate frequency (IF). This IF signal is then amplified and finally, it is detected by a square law detector whose output DC voltage is directly proportional to the input noise power. In this receiver, it is assumed that the amplifier is linear with constant gain and its bandpass characteristic is rectangular.

Considering the effective noise temperature of the antenna radiation resistance as T_A in K, its noise power per unit bandwidth is given by kT_A,

where k is Boltzmann's constant, i.e. $1.38 \times 10^{-23} J/K$. Hence, the antenna noise power in watts is $N_A = kT_A B_{HF}$ in which B_{HF} stands for the high frequency bandwidth in Hz.

The receiver itself adds noise to the system owing to the thermal and shot noise in the receiver components and also due to losses in the transmission lines which connect the different components of the receiver. Usually, the high frequency gain, G_{HF}, is high enough and the system noise temperature of the receiver in the antenna port is defined by its first components. Therefore, it is important to use short transmission lines with low losses in order to obtain receivers with low noise temperatures. Anyway, the system noise power at the antenna terminal is:

$$N_{SN} = N_A + N_R = k(T_A + T_R)B_{HF} \tag{1.1}$$

and the system noise temperature referred to the antenna terminals is $T_{SN} = T_A + T_R$, where T_R is the receiver noise temperature. From now on, the receiver will be taken into account without the antenna in order to compare the proposed receiver in this dissertation with some commercial systems using the same standard horn antenna. Therefore, the receiver noise temperature will be considered as the system noise temperature, i.e. T_{SN}.

It is important to know that the input power of a receiver consists of broadband noise whose statistics features do not differ from the originated noise of the receiver itself or from the coupled noise through the antenna. Therefore, levels of input signals below the receiver noise temperature are concealed and they are undetectable. In passive systems it is essential to minimize the noise contribution of the receiver in order to be able to detect small differences in the total noise.

Considering the signal noise temperature or change in antenna temperature to be measured, i.e. ΔT, the output power of the RF amplifier is:

$$N_{HF} = G_{HF} k \left(T_{SN} + \Delta T\right) B_{HF} \tag{1.2}$$

N_{HF} is the input power of the detector taking into account direct detection. The DC output voltage of the detector, i.e. $V_D + \Delta V$, is directly proportional to the input power:

$$V_D + \Delta V = \beta G_{HF} k T_{SN} B_{HF} + \beta G_{HF} k \Delta T B_{HF} \tag{1.3}$$

In which β is the sensitivity of the detector. High amplification of ΔV is required to obtain a detectable output signal because $\Delta V \ll V_D$. In order to make this amplification easier, the voltage V_D is cancelled by a DC voltage $-V_D$ in the post-detection section of the receiver. Therefore, ΔV is the output signal voltage from the detector. Hence, the output signal power of the detector is:

$$W_{det} = G_{HF}^2 \beta^2 \left(k\Delta T B_{HF}\right)^2 = C \left(k\Delta T B_{HF}\right)^2 \tag{1.4}$$

Where C is a constant. In addition to ΔV, a noise voltage also exists at the detector output. The low frequency components of this voltage from DC to B_{HF} are due to different IF noise voltage components in the frequency range from $f_{IF} - B_{HF}/2$ to $f_{IF} + B_{HF}/2$ beating with each other in the detector. The resulting low frequency power spectrum is triangular shaped, because the number of IF noise voltage components giving a certain noise component at frequency f_{LF}, which varies from DC to B_{HF}, is proportional to $B_{HF} - f_{LF}$. Taking into account $\Delta T \ll T_{SN}$, the maximum low frequency power density close to zero frequency is [47]:

$$W_{LF_{max}} = 2C \left(kT_{SN}\right)^2 B_{HF} \tag{1.5}$$

In the post-detection section, the detector output voltage is filtered through a low pass filter amplifier in order to reduce fluctuations. This filter has an effective bandwidth B_{LF} much smaller than B_{HF}. If the low pass filter has a rectangular passband from zero to B_{LF} and a power gain G_{LF}, the fluctuating noise power output is:

$$W_{LF} = G_{LF} 2C \left(kT_{SN}\right)^2 B_{HF} B_{LF} \tag{1.6}$$

And the corresponding signal power due to the noise temperature ΔT is:

$$W = G_{LF} C \left(k\Delta T B_{HF}\right)^2 \tag{1.7}$$

The sensitivity or receiver resolution is the minimum variation of temperature that the receiver is capable of detecting and it is referred to ΔT_{min}. The sensitivity is defined as the signal noise temperature ΔT_{min} which produces a receiver DC output power, i.e. W, equal to the noise output power, i.e. W_{LF}:

$$\Delta T_{min} = T_{SN}\sqrt{\frac{2B_{LF}}{B_{HF}}} = \frac{T_{SN}}{\sqrt{B_{HF}\tau_{LF}}} \tag{1.8}$$

As mentioned, B_{LF} is the equivalent bandwidth of the low pass amplifier. In particular, an ideal integrator with an integration time $\tau_{LF} = 1/2B_{LF}$ can be used as a low pass filter.

As can be seen in Equation 1.8, the sensitivity of the receiver increases by increasing the pre-detection bandwidth, i.e. B_{HF}, and the equivalent integration time, i.e. τ_{LF}, and by decreasing the system noise temperature of the receiver, i.e. T_{SN}. On the one hand, B_{HF} is mainly limited by the bandwidth of the amplifiers, mixer and detectors. On the other hand, increasing the integration time beyond certain limits is undesired since it increases the scanning time of an image.

In order to obtain the previous equation of the sensitivity of the receiver, the gain of the amplifiers has been considered constant along the entire frequency band. However, this is not true in practice. As a matter of fact, gain variations can be produced by bias voltage variations and by ambient temperature fluctuations. Moreover, the sensitivity in this type of receivers is seriously penalised by gain fluctuations in the amplifiers, variations of the noise figure and of the bandwidth of the receiver. As a consequence, the receiver is not able to distinguish between the increase in signal power and the increase due to these factors. If the gain fluctuations are considered in the analysis of the sensitivity of the receiver, the following equation is obtained [46]:

$$\Delta T_{min} = T_{SN}\sqrt{\left(\frac{1}{B_{HF}\tau_{LF}}\right)^2 + \left(\frac{\Delta G}{G_0}\right)^2} \tag{1.9}$$

Where ΔG is the effective value of the RF gain fluctuations of the receiver and G_0 corresponds to the average RF gain of the receiver. As can be seen, output fluctuations due to gain variations are independent of the fluctuations resulting from the receiver noise. In practice, the term related to gain fluctuations is the main term of the sensitivity. Therefore, there are two main options in order to obtain high sensitivity, either the implementation of a gain stabilization method [48], [49] in total power receivers or the use of other receiver configuration which copes with the effect of receiver instabilities.

Taking into account receivers based on direct detection, several total power receivers have been proposed working at 35 [50]- [52] and 94 GHz [53]- [65].

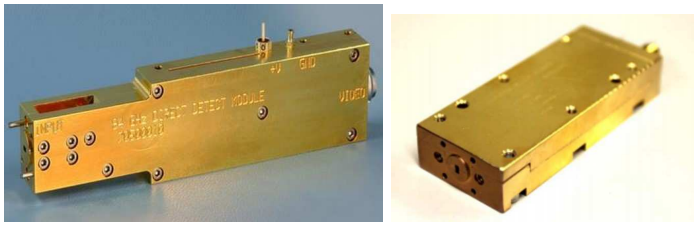

(a) (b)

Figure 1.7 – Photographs of the commercial total power receivers at W-band by a) Farran Technologies [64] and b) Anteral [65].

Some examples are shown in Table 1.2. The comparison between receivers in terms of sensitivity is difficult because in some articles the integration time is not specified. Moreover, the receiver instabilities are not taken into account in the calculation of these sensitivities. In spite of these, their sensitivities are at least below 1 K. Note that receivers require to detect temperature changes as small as 0.5 K to obtain a good image quality in low contrast environments, e.g. indoors [66].

With respect to the proposed total power receivers working at 94 GHz, some of them are those used in the PMMW cameras commercialised by Trex Enterprises [54], Millivision [55], Brijot [59], Alfa Imaging [61] and Qinetic [62]. Furthermore, the last two total power receivers shown in the Table [64], [65] are currently commercialised packaged in a metal module with WR10 waveguide input as can be seen in Fig. 1.7.

1.1.3.2 Dicke receiver

Dicke [67] introduced the use of the modulation principle in order to remove the effect of receiver instabilities. Fig. 1.8 shows the most basic structure of a Dicke receiver in which the main change is the introduction of a switch at the input port of the system. This switch commutes between the antenna and a reference load at a frequency rate high enough to ensure that the gain is constant in this period of time. Then, the effect of these gain fluctuations can be removed by using a multiplier or a phase detector which is synchronised with the switch and in opposite phase to the integrator.

The sensitivity of a Dicke receiver is given by [46]:

Table 1.2 – Published performances of several total power receivers based on direct detection.

Authors affiliation	Frequency (GHz)	Sensitivity	τ_{LF} (ms)
SRC "Iceberg" [50]	33-38	0.31 K	1
Qinetic [51]	35	0.28 K	-
Tohoku University [52]	30-40	1 K	-
TUBITAK-MRC [53]	90-100	0.67 K	1
Trex Enterprises [54]	75-93	2-3 K	-
Millivision [55]	80-100	0.36 K	1
Northrop Grumman [56]	84-94	2 K	-
Fujitsu [57]	84-99	1 K	-
HRL - Brijot [58] [59]	80-109	0.3-0.7 K	3.125
University of Toronto [60]	85-104	5 K	30
Alfa Imaging [61]	80-105	< 1	-
Qinetic [62]	82-106	0.66 K	0.2
Farran Technologies [63] [64]	80-110	4 K	0.001
Anteral [65]	80-100	0.7 K	1

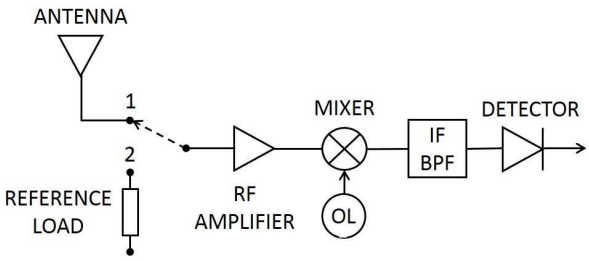

Figure 1.8 – Dicke receiver.

$$\Delta T_{min} = \sqrt{\frac{2\left(T_A + T_{SN}\right)^2 + 2\left(T_{ref} + T_{SN}\right)^2}{B_{HF}\tau_{LF}} + \left(\frac{\Delta G}{G_0}\right)^2 \left(T_A - Tref\right)^2} \tag{1.10}$$

In this expression, when the difference between T_{ref} and T_A is small enough, the effect of gain fluctuations is minimised. However, the sensitivity of the receiver is penalised. When $T_{ref} = T_A$, i.e. assuming a balanced receiver, these fluctuations are removed and the receiver sensitivity is only determined by its noise temperature:

$$\Delta T_{min} = 2\frac{T_{SN}}{\sqrt{B_{HF}\tau_{LF}}} \tag{1.11}$$

As can be seen, the sensitivity of a Dicke receiver is one half of the theoretical sensitivity of the total power receiver because the input signal is detected by the receiver only half of the time. In conclusion, the introduction of the switch in the input port of the system eliminates the effect of gain fluctuations at the expense of penalising the sensitivity of the receiver by a factor of 2. In addition, the switch usually limits the bandwidth of the system and increases its losses. Nowadays, to the best of our knowledge only three switches working along the entire W-band have been proposed [68]- [70]. However, the insertion losses added by these switches are between 1.4 dB [68] and 4 dB [70].

Dicke-type receivers have a long history in CMB observations and were successfully employed in the COBE-DMR instrument that first detected CMB anisotropies [71], [72]. These receivers are cooled and their sensitivities are around 20 mK. Moreover, Dicke receivers are mainly based on III-V

Table 1.3 – Published performances of several Dicke receivers based on direct detection.

Reference	Technology	Frequency (GHz)	Sensitivity	τ_{LF} (ms)
[73]	AlGaAd InGaAs HEMT	85-95	0.5	10
[74]	InP HEMT	80-110	0.4 K	3.125
[75]	0.18 μm SiGe BiCMOS	81-107	0.3-0.4 K	-
[76]	65 nm CMOS	80-98	1.1 K	30
[77]	0.13 μm SiGe BiCMOS	84-99	0.83 K	30
[78]	0.3 μm SiGe BiCMOS	100	<2 K	30
[79]	65 nm CMOS	183	2 K	30

technologies such as GaAs or InP HBTs/HEMTs [73], [74] which consist of two or three integrated circuits such as the switch, the low noise amplifier and the detector. However, the new advanced CMOS technology facilitates the development of Dicke receivers in a single-chip with small form factor [75]-[79].

Table 1.3 shows several published Dicke receivers based on direct detection. As can be seen, the majority of Dicke receivers work at 94 GHz. Moreover, CMOS based receivers can obtain as low sensitivities as receivers developed in GaAs and InP HEMT technology. Nowadays, to the best of our knowledge, the highest operating frequency of Dicke receivers based on direct detection is 183 GHz [79].

1.1.3.3 Differential receiver

Receivers based on a differential configuration carry on with the idea of performing a distinction between the RF signal and a signal produced by a known reference load in order to remove the effect of gain fluctuations, similarly to Dicke receivers. However, this type of receivers avoids the use of a switch in its input port achieving larger RF bandwidth and improving its sensitivity.

These receivers require two identical and matched receivers in which the gain and noise fluctuations of the amplifiers are completely correlated. The balanced structure of a differential receiver can be seen in Fig. 1.9. The input RF signals collected by its two antennas are equally divided by the input

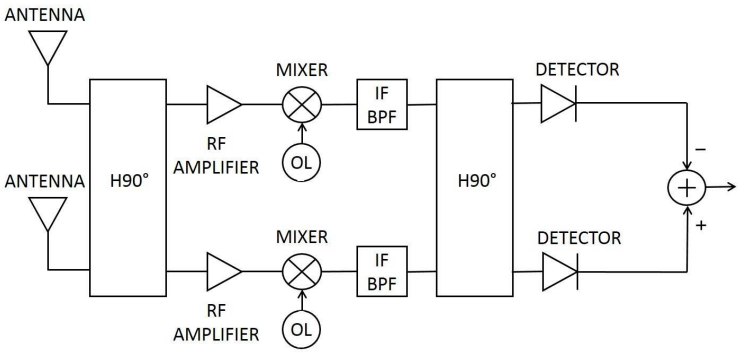

Figure 1.9 – Differential receiver.

quadrature hybrid coupler and distributed into the two amplifier chains. In this way, the two input signals suffer the same gain and noise fluctuations [80]. As a consequence, the effect of gain and noise fluctuations can be eliminated by implementing a subtracting operation between its two output voltages in its post-processing stage. Therefore, the output signal of the receiver is a voltage proportional to the difference between its two input signals.

As mentioned, the sensitivity is the minimum variation of temperature that the radiometer is capable of detecting and it is referred to ΔT_{min}. A passive radiometer based on a differential configuration has a sensitivity given by [46]:

$$\Delta T_{min} = \sqrt{2}\frac{T_{SN}}{\sqrt{B_{HF}\tau_{LF}}} \tag{1.12}$$

As can be seen, the removal of the effect of gain instabilities is also achieved in this type of receiver. Moreover, the sensitivity improves in a factor of $\sqrt{2}$ with respect to Dicke receivers, since the desired input signal is being continuously measured.

Pseudo-correlation receiver

Another type of differential receivers are pseudo-correlation receivers which allow continuous comparison and differentiation between two different observations. Different versions of pseudo-correlation receivers have been used for the second and third generation of space based radiometric instruments for

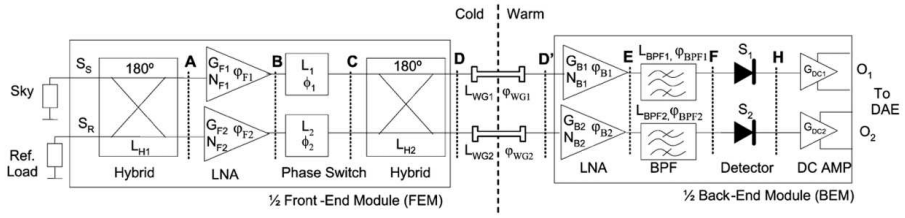

Figure 1.10 – Pseudo-correlation receiver used in the Low Frequency Instrument (LFI) on board the ESA Planck mission [84].

CMB anisotropy: NASA Wilkinson Microwave Anisotropy Probe (WMAP) [81]- [83] and the Low Frequency Instrument (LFI) on board the ESA Planck mission [84], [85].

The receivers of the WMAP instrument directly measure temperature differences between sky signals from two widely separated regions of the sky while the LFI receivers measure the difference between the sky and a stable internal cryogenic reference load cooled at about 4 K by the pre-cooling stage of the High Frequency instrument. The offset of approximately 3 K between the sky and reference load signals is compensated introducing a gain modulation factor which balances the output in the on-board data reduction phase.

The receivers used in the LFI on board the ESA Planck mission can be seen in Fig. 1.10. This Figure shows one of the two parallel receivers used in this satellite, one for each polarization of the radiation coupled through the antenna. It consists of an actively cooled front-end (20 K) and a 300 K back-end linked by waveguides. The two input signals, i.e. the sky signal and the signal from a stable reference load at approximately 4 K, are coupled to cryogenic low noise amplifiers via a 180° hybrid. One of the two signals is phase shifted between 0 and 180° at a frequency of 4096 Hz. The signals are then recombined by a second 180° hybrid, producing an output which is a sequence of signals alternating at twice the phase switch frequency. In the back-end of each receiver the RF signals are amplified, low-pass filtered and detected. Then, the sky and reference load signals are integrated, digitised and differenced after multiplication of the reference load signal by a gain modulation factor, i.e. r, which has the function to make the sky-load difference as close as possible to zero. A proper tuning of the parameter r ensures a very stable differential output with knee frequencies of the 1/f noise of the order of few mHz [85]. Indeed, the 1/f noise related to the 1/f gain

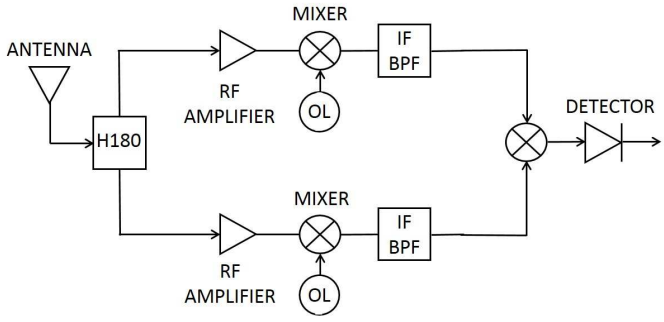

Figure 1.11 – Correlation receiver.

fluctuations in suppressed by applying the parameter r, leaving only the 1/f noise produced by fluctuations in amplifier noise temperature.

The receivers of the LFI on board the ESA Planck mission work at 30, 44 and 77 GHz.

1.1.3.4 Correlation receiver

The sensitivity of Dicke receivers assumes that it is a balanced structure, i.e. $T_A = T_{ref}$, in order to remove the receiver instabilities. Correlation receivers [86] ensure this feature without using a switch. They consist of two identical receivers connected to the same antenna, as can be seen in Fig. 1.11. The IF-output signals are multiplied. Therefore, the output signal of the correlation receiver is a signal proportional to the input noise coupled through the antenna, which is the same for both receivers. Note that the added noise power of each receiver is uncorrelated and no output DC voltage is produced.

The sensitivity of correlation receiver is:

$$\Delta T_{min} = \sqrt{2}\frac{T_{SN}}{\sqrt{B_{HF}\tau_{LF}}}\sqrt{1+\left(\frac{1/2T_A}{T_{SN}}\right)^2} \tag{1.13}$$

In which T_{SN} is the system noise temperature of the complete correlation receiver, i.e. $T_{SN} = \frac{1}{2}T_A + T_R$. The particularity of this system is that it is useful only when the noise temperature of the antenna, i.e. T_A, is small with respect to the noise temperature of each receiver, i.e. T_R. When this happens, the achievable sensitivity is identical to the sensitivity of a differential

receiver. On the other hand, when the noise temperature of the antenna is high enough in comparison to the noise temperature of the receiver, the sensitivity is identical to that of the total power receiver. Therefore, it is determined by the receiver instabilities.

The most common used correlation receiver contains two input antennas instead of one antenna and 180° coupler. It has been used in radio astronomy [87], [88] and satellite passive microwave remote sensing at L-band [89], [90] and at 22 GHz [91] for its ability to synthesize large antenna apertures using multiple small apertures. Due to the fact that the ideal correlation receiver responds only to coherent radiation, recently, it has been used in security sensing for close-range detection of human presence [92], [93]. These correlation receivers work at Ka-band using a LO frequency of 26 GHz and their sensitivities are 270 mK. In addition, they have also been applied in the measurement of the angular velocity of moving objects [94], [95]. Taking into account higher frequencies, a gas filter correlation receiver has been developed at infrared frequencies to detect different gases such as tropospheric carbon monoxide [96].

1.2 Motivation and Goal of this Work

Nowadays, large attention is being paid to the development of new commercial applications and systems using PMMW imaging. Both the Spanish and European Governments are funding several research projects focused on the development of passive receivers and imaging cameras at millimetre, sub-millimetre and THz frequencies. Indeed, this dissertation is framed within the IPT-2011-0960-390000 project funded by the Spanish Ministry of Science and Innovation within the INNPACTO program. Its main objective was the design and development of millimetre wave receivers for security applications. The project was lead by the company Alfa Imaging, which aimed at integrating them in their imaging cameras. In this project, besides conventional topologies, novel configurations of receivers have been explored. In particular, the auto-calibrated configuration explored in this thesis will help reducing the drifts encountered in the direct detection receivers used in Alfa Imaging cameras.

As mentioned, thanks to this project, this Thesis has been focused on the development of an auto-calibrated receiver at W-band to be used in a

Table 1.4 – Commercial total power receivers at W-band.

Company	Product	Frequency (GHz)	Sensitivity (K)
Farran Technologies [64]	PMMW-10-0001	$80-110$	4 ($\tau_{LF} = 1\ \mu s$)
Anteral [65]	TSW-90	$80-100$	0.7 ($\tau_{LF} = 1\ ms$)

PMMW camera. PMMW imaging in this frequency band has motivated the progress of a wide range of applications mainly focused on defence and security, such as those previously discussed. Moreover, direct detection at W-band is feasible due to the availability of MMIC devices such as low noise amplifiers and detectors. Therefore, a simple receiver in which the use of a mixer and a local oscillator is not required can be designed operating at this frequency band. Moreover, low loss dielectric substrates are also commercialised at W-band allowing the minimization of its dielectric losses, which improves the sensitivity of the receiver.

Apart from the advantages related to the operating frequency band, the selected configuration for the proposed receiver is based on a differential receiver which by performing an internal calibration by means of continuously measuring of a reference load is able to remove the effect of receiver instabilities improving the sensitivity in comparison with Dicke receivers.

Finally, the implementation of a receiver entirely built in planar technology will be carried out. This facilitates the integration of the MMIC devices. Moreover, the antenna and the receiver can be built on the same substrate which makes the development of an array of receivers easier. Besides, the resulting system has a relative small size and it is lighter than waveguide based receivers.

Currently, after the closure of MMIC Solutions [97], there are only two companies which commercialize receivers at W-band such as Farran Technology [64] and Anteral [65]. All of them are based on total power receivers, thereby, the calibration of the system has to be externally implemented. Therefore, the proposed auto-calibrated receiver presents the advantage of performing an internal calibration which facilitates the post-processing. These commercial total power receivers were shown in Fig. 1.7 and their main characteristics can be seen in Table 1.4.

The proposed W-band auto-calibrated receiver should feature a sensitivity of at least 0.7 K considering $\tau_{LF} = 1ms$ in order to be competitive with these commercial total power receivers. Moreover, this dissertation takes into account the fabrication, assembly and testing of the proposed W-band auto-calibrated receiver using the facilities provided by the THz Laboratory of Antenna Group of Public University of Navarra which is a national reference in this field.

1.3 Structure of the document

The current document is divided in the following sections:

Chapter 1

The present Chapter explains the background, goal and motivation of this work. The background of this Thesis gathers the importance of PMMW imaging, its applications and commercial systems.

Chapter 2

The second Chapter presents the theory behind the differential configuration of the proposed W-band auto-calibrated receiver and its advantages. Moreover, the design of the components which are part of the planar receiver is explained. Furthermore, the choice of the commercial MMIC devices such as the reference load, the low noise amplifiers and detectors is shown.

Chapter 3

This Chapter deals with the analysis of the performance of the W-band auto-calibrated receiver using the SW package Advance Design System (ADS) by Keysight Technologies. In this analysis, the simulated performance of the microstrip components, the selected commercial MMIC devices and the gold wire bondings required to connect the components have been taken into account. Specifically, the performance of the planar receiver has been analysed in terms of reflection coefficient, gain and also, noise temperature and noise figure determining the effect of each component on these parameters.

Chapter 4

Chapter 4 is focused on the fabrication and measurement of the planar components of the W-band auto-calibrated receiver. The characterization of these components is accomplished using waveguide based equipment. Therefore, the design, fabrication and validation of an inline WR10 waveguide to microstrip transition operating in the full W-band is firstly presented. In addition, the used low loss dielectric substrate in the receiver, i.e. 0.127 mm thick RO5880 substrate, and other low loss dielectric substrate, i.e. 0.1 mm thick COC polymer, have been characterized in order to retrieve their dielectric constants and loss tangents. These facilitate the comparison between experimental and simulation results of each planar component of the proposed receiver and validate their performances.

Chapter 5

This Chapter addresses the design of the packaging metal block of the W-band auto-calibrated receiver and the DC circuit which biases the low noise amplifiers and amplifies the output signals of the receiver. The packaging metal block includes the WR10 flange required to connect it with a standard horn antenna, this DC circuit and the cavity which contains the planar receiver. In particular, this cavity implements a periodic pin surface in order to avoid the propagation of undesired modes which can penalize the performance of the proposed receiver. Moreover, design guidelines for the pin surface are proposed in order to create a certain stop-band. Experimental results shown in this Chapter demonstrate the suppression of the unwanted modes and resonances.

Chapter 6

The assembly of the components in the packaging metal block and the bias process of the low noise amplifiers are explained and shown in this Chapter. Moreover, the measurement of the performance of the complete W-band auto-calibrated receiver is carried out: input reflection coefficient, dynamic range, RF-DC response, effective bandwidth and equivalent noise temperature are experimentally validated.

Chapter 7

Until this Chapter, the input port of the proposed W-band auto-calibrated receiver was a WR10 waveguide in order to connect it to a standard horn antenna or to the test equipment required for characterization. This facilitated the comparison between performances of this receiver and other commercial receivers. However, the Chapter 7 introduces the design, fabrication and measurement of a W-band Vivaldi antenna. This is an interesting alternative in order to reduce the size, weight and manufacturing complexity of an array of receivers. The challenge tackled in this design is the implementation of a broadband microstrip to slotline transition operating in the full W-band.

Chapter 8

This Chapter offers a brief summary of the results presented in this dissertation, together with some final conclusions and future work lines.

Chapter 2

Design of a W-band auto-calibrated receiver in planar technology

2.1 Introduction

The function of a passive radiometer is to receive the RF power radiated by the objects in a natural way. This emission normally consists of broadband noise whose statistical properties are similar to the noise produced in the receiver or from the background radiation coupled to the radiometer by the antenna. Therefore, the main requirements for a passive radiometer are high sensitivity and also high stability. These requirements can be improved by using a configuration different from the total power radiometer.

In this Chapter, the analysis of the architecture of the proposed W-band radiometer will be carried out highlighting its main advantages. Moreover, the explanation of the design of its microstrip components and also the choice of the commercial Monolithic Microwave Integrated Circuit (MMIC) devices will be explained. Although the use of a planar antenna would lead to a more compact solution, as it will be discussed in Chapter 7, this W-band auto-calibrated receiver will be connected to WR10 waveguide by means of a specific transition. Therefore, a WR10 waveguide to microstrip transition has been designed in order to connect the receiver to a standard horn antenna or to the test equipment required for characterization. In this way, this transition

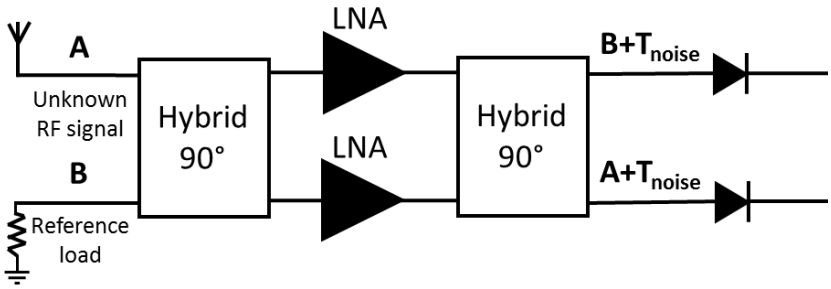

Figure 2.1 – Diagram of the proposed W-band auto-calibrated receiver.

will facilitate the comparison between the proposed receiver and a commercial W-band receiver based on a total power radiometer.

2.2 Receiver configuration and its advantages

The proposed W-band auto-calibrated radiometer can be shown in Fig. 2.1. This receiver consists of an antenna which collects the passive radiation of the objects, a reference load, two quadrature hybrid couplers, two low noise amplifier chains and one detector in each output of the radiometer.

The W-band receiver will be entirely designed in planar technology. This feature facilitates the integration of the MMIC components. The antenna and the quadrature hybrid couplers will be built on the same substrate which makes it easier the development of an array of receivers. Besides, the resulting system has a relative small size and it is lighter than waveguide based radiometers.

Moreover, a typical superheterodyne receiver with an output signal in an intermediate frequency is not needed at W-band. Direct detection at this frequency band is feasible taking advantage of the availability of commercial MMIC components such as Low Noise Amplifiers (LNA) and detector diodes.

Regarding the architecture of the receiver, it is based on a differential configuration in which the balanced structure of the receiver is achieved with two quadrature hybrid couplers. The input quadrature hybrid coupler distributes the unknown RF signal introduced by the antenna and the reference signal in two amplifier chains. Next, the output quadrature hybrid coupler combines these amplified signals and as a result two output signals are obtained. These output signals correspond to the amplified RF signal and

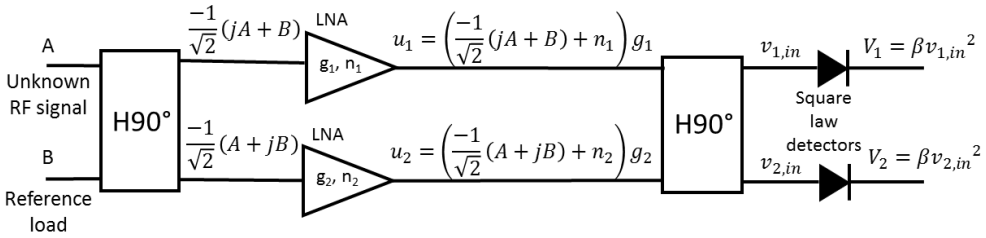

Figure 2.2 – Operation of the W-band auto-calibrated receiver based on a differential configuration in detail. The inputs and outputs of each device are shown.

the amplified reference signal. The use of a reference signal provides an auto-calibrated system whose main advantage is to reduce the effect of gain variations in the amplifiers. Gain variations are unavoidable and critical in the sensitivity of a total power radiometer. The detector can not distinguish an increase of signal power due to an increase in the received signal or an increase produced by gain fluctuations. Therefore, a differential configuration provides robustness to the system. It avoids gain fluctuations with lower penalty in the sensitivity than other receiver configurations which also cope with these instabilities such as Dicke radiometers. Next, the analysis of the receiver demonstrates how the effect of the gain fluctuations of the amplifiers is minimized.

Fig. 2.2 shows the differential configuration of the W-band auto-calibrated radiometer in more detail. The values of the input and output signals of each component are included in this Figure. A corresponds to the unknown RF signal introduced by the antenna and B corresponds to the reference signal. These signals are coupled through the input quadrature hybrid coupler. As a result, two combined signals, i.e $\frac{-1}{\sqrt{2}}(jA+B)$ and $\frac{-1}{\sqrt{2}}(A+jB)$, are distributed to the two amplifier chains. These signals are amplified in the same way as the noise produced by the amplifier itself, i.e. n_1 and n_2, as can be seen in Eq. 2.1 and 2.2 where u_1 and u_2 are the equivalent noise at the output of the amplifiers and, g_1 and g_2 are their gains.

$$u_1 = \left(\frac{-1}{\sqrt{2}}(jA+B)+n_1\right)g_1 \tag{2.1}$$

$$u_2 = \left(\frac{-1}{\sqrt{2}}(A + jB) + n_2\right) g_2 \tag{2.2}$$

Both u_1 and u_2 are combined in the output quadrature hybrid coupler obtaining the output signals $v_{1,in}$ and $v_{2,in}$ shown in Eq. 2.3 and 2.4.

$$v_{1,in} = \frac{-1}{\sqrt{2}}\left[\left(\frac{A - jB}{\sqrt{2}} + jn_1\right) g_1 + \left(\frac{-A - jB}{\sqrt{2}} + n_2\right) g_2\right] \tag{2.3}$$

$$v_{2,in} = \frac{-1}{\sqrt{2}}\left[\left(\frac{-jA - B}{\sqrt{2}} + n_1\right) g_1 + \left(\frac{-jA + B}{\sqrt{2}} + jn_2\right) g_2\right] \tag{2.4}$$

Applying the power addition in Equations 2.3 and 2.4, the resulting output signals $v_{1,in}$ and $v_{2,in}$ are as follows.

$$v_{1,in} = \sqrt{\left(\frac{B}{2}(g_1 + g_2)\right)^2 + \left(\frac{A}{2}(g_1 - g_2)\right)^2 + \left(\frac{1}{\sqrt{2}}(n_1 g_1 + n_2 g_2)\right)^2} \tag{2.5}$$

$$v_{2,in} = \sqrt{\left(\frac{A}{2}(g_1 + g_2)\right)^2 + \left(\frac{B}{2}(g_1 - g_2)\right)^2 + \left(\frac{1}{\sqrt{2}}(n_1 g_1 + n_2 g_2)\right)^2} \tag{2.6}$$

Each output signal has the contribution of the input signals, A and B and also the noise produced by the amplifiers. Note that the input signals can be separated with the differential configuration when the amplifiers are identical, i.e. $g = g_1 = g_2$ and $n = n_1 = n_2$. Then, the output signal in the first branch would correspond to the amplified reference signal, i.e. $v_{1,in} = \sqrt{(Bg)^2 + 2(ng)^2}$, and the unknown RF signal can be obtained in the second branch, i.e. $v_{2,in} = \sqrt{(Ag)^2 + 2(ng)^2}$. The contribution of the system noise in these two outputs is identical.

The detectors used in the configuration are square law devices. This implies that the output DC voltage of the detector is directly proportional to the output noise power of the pre-detection section of the receiver. Therefore, the DC outputs of the proposed W-band auto-calibrated receiver, i.e. V_1 and V_2, are shown in Eq. 2.7 and 2.8 where β stands for the sensitivity of the detector in V/mW.

$$\begin{aligned} V_1 &= \beta\left(\frac{B}{2}(g_1+g_2)\right)^2 \\ &+ \beta\left(\frac{A}{2}(g_1-g_2)\right)^2 \\ &+ \beta\left(\frac{1}{\sqrt{2}}(n_1g_1+n_2g_2)\right)^2 \end{aligned} \tag{2.7}$$

$$\begin{aligned} V_2 &= \beta\left(\frac{A}{2}(g_1+g_2)\right)^2 \\ &+ \beta\left(\frac{B}{2}(g_1-g_2)\right)^2 \\ &+ \beta\left(\frac{1}{\sqrt{2}}(n_1g_1+n_2g_2)\right)^2 \end{aligned} \tag{2.8}$$

The first two components of each output voltage, i.e. V_1 and V_2, contain the input signals multiplied by a gain component which is a combination of the gain of the amplifiers. If the amplifiers are identical in terms of gain, i.e. $g_1 = g_2$, the output voltages of the system are the amplified input signals separated in each output port of the receiver. The third term corresponds to the noise contribution of the amplifiers.

When a subtracting operation is implemented in the post-detection stage of the receiver, the effect of the gain fluctuations of the amplifiers can be removed by the differential configuration because their contribution in both input signals, i.e. A and B, are equal. The resulting subtracted output can be seen in Eq. 2.9.

$$V_2 - V_1 = \beta\left[A^2g_1g_2 - B^2g_1g_2\right] \tag{2.9}$$

In the case that the gains of the two amplifier chains are unbalanced, they have the same effect in both output signals of the receiver and can be also removed by the subtracting operation. In addition, the noise generated by the amplifiers has been also removed by the subtracting operation. The effect of gain imbalance in the output voltages of the differential receiver will be clearly explained in Section 3.2.

As mentioned in Chapter 1, two parameters mainly define the quality of a passive receiver and its ability of imaging, i.e. the Sensitivity (ΔT_{min}) and the System noise temperature (T_{SN}). The following expression for the sensitivity is obtained for a passive radiometer based on a differential configuration.

$$\Delta T_{min} = \sqrt{2}\frac{T_{SN}}{\sqrt{B_{HF}\tau_{LF}}} \tag{2.10}$$

A smaller ΔT_{min} corresponds to a higher sensitivity which is crucial in passive receivers. It depends on the system noise temperature T_{SN}, the high frequency operating bandwidth B_{HF} and the integration time τ_{LF}. Large operating bandwidth B_{HF} and low system noise temperature T_{SN} provide a receiver with high sensitivity.

2.3 Components of the W-band receiver

As mentioned in the previous Section, the receiver consists of two quadrature hybrid couplers which provide the balanced structure, two MMIC Low Noise Amplifiers distributed one in each amplifier chain, two MMIC Detector Diodes placed in the outputs of the system and a MMIC reference load. Below, the design of its microstrip components is carried out and the choice of the MMIC components at W-band is explained. Moreover, the design of a WR10 waveguide to microstrip transition is presented in order to allow the experimental comparison between the proposed receiver and a commercial W-band total power receiver using the same W-band standard horn antenna.

2.3.1 Substrate selection

The selection of a suitable substrate is essential to minimize the dielectric losses of the W-band auto-calibrated receiver because these losses increase the system noise temperature and penalize its sensitivity. The dielectric losses in the differential configuration of the receiver are produced by three microstrip components. These devices are the WR10 waveguide to microstrip transition needed to connect the standard horn antenna with the planar receiver, the two quadrature hybrid couplers and also the 50 Ω microstrip lines required to connect every component of the receiver by means of gold wire bonding.

Therefore, the substrate has to be low loss dielectric, i.e. low dielectric loss tangent ($tan\delta$), and also its thickness must be comparable to the thickness of

Name	ϵ_r	t (mm)	$\tan\delta$	Manufacturer
TLY	2.17-2.20 (10 GHz)	0.127	0.0009 (10 GHz)	TACONIC [98]
TLP	2.17-2.40 (10 GHz)	0.127	0.0009 (10 GHz)	TACONIC [98]
TacLamPLUS	2.10 (50 GHz)	0.100	0.0008 (50 GHz)	TACONIC [98]
DiClad880	2.17-2.20 (10 GHz)	0.127	0.0009 (10 GHz)	ARLON [99]
CuClad217LX	2.17-2.20 (10 GHz)	0.127	0.0009 (10 GHz)	ARLON [99]
NY9000	2.17-2.60 (10 GHz)	0.127	0.0009 (10 GHz)	NELCO [100]
RT/Duroid 5880	2.20 (10 GHz)	0.127	0.0009 (10 GHz)	ROGERS [101]
RO3003	$2.96 - 3.04$ (10 GHz)	0.127	0.001 (10 GHz)	ROGERS [101]

Table 2.1 – Available commercially substrates at W-band with low dielectric losses.

the commercial MMIC components at W-band. This last condition facilitates the bonding with gold wires, shortening the length of these connections and also minimising their losses. The thickness of commercial MMIC devices at W-band is mainly between 50 and 100 μm as can be seen in the following Subsections.

Nowadays, the standard thinnest substrates, which some manufacturers provide without increasing the fragility of the substrate sheet, are 100 and 127 μm. Table 2.1 shows the available commercial substrates with low dielectric losses, i.e. $tan\delta \leqslant 0.001$. The highlighted parameters in this Table are the dielectric constant, ϵ_r, the thickness, t, the dielectric loss tangent, $tan\delta$, and the manufacturer.

Any of the substrates shown in Table 2.1 is a good candidate for the W-band auto-calibrated receiver. The selected substrate has been RT/Duroid 5880 (RO5880) whose thickness is 127 μm because it is available in the Antenna Group at the Public University of Navarra.

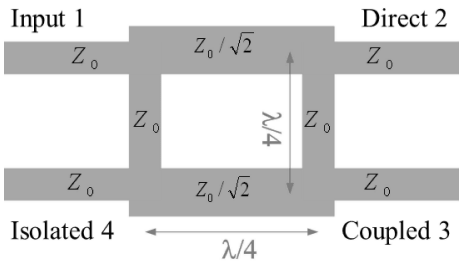

Figure 2.3 – Conventional design of a quadrature hybrid.

With respect to the dielectric loss tangent of the 127 μm thick RO5880, the manufacturer provides its measured value at 10 GHz. However, it is not demonstrated that this value is appropriate at higher frequencies such as W-band. As a matter of fact as will be shown in Section 4.2, the real loss tangent in the W-band is much higher, i.e. 0.01. Therefore, the considered dielectric loss tangent of RO5880 at W-band will be 0.01 instead of 0.0009. This value has been introduced in every design and it implies that the dielectric losses of the 50 Ω microstrip line at 92.5 GHz can be estimated as 0.1 dB/mm [102].

2.3.2 W-band quadrature hybrid coupler

The quadrature hybrid coupler is one of the key elements in many microwave circuits such as balanced amplifiers, balance mixers, phase shifters, power dividers, and beamforming networks for array antennas and for direction-finding antennas [103]. Usually, they are used to combine or divide signals with appropiate phase of ±90°. For our application, this element is crucial in the operation of the receiver. It equally divides the input and the reference signal and once they have been amplified it separates them, such that, in the ideal noise-less receiver, the outputs of the front-end receiver are the amplified input signal and the amplified reference signal. In this and many other applications, the coupler is required to be designed in planar microstrip technology for easy integration with other passive or active components of the front-end receiver such as MMIC devices.

The conventional design of the quadrature hybrid coupler, also called branch-line coupler, is based on single section quarter-wavelength transmission lines [102]. This structure can be seen in Fig. 2.3.

One of the drawbacks of the conventional design is the size because it utilizes $\lambda/4$ transmission lines. On the one hand, sizes of conventional couplers are too large for RF circuits at low microwave frequencies such as mobile frequencies and for radio frequency integrated circuits (RFIC). For example, when a coupler is integrated with a small size microstrip antenna [104], which is usually implemented over a low ϵ_r substrate. On the other hand, the sizes are also too large for MMIC applications, since increase the cost. Several techniques have been proposed in order to overcome the size problem of the branch-line coupler [105]- [108].

In our system, the application of a technique to reduce the size of the planar devices is not needed because the frequency operating band is high enough to obtain a relatively small wavelength. The main drawback for our interest is the narrowband performance of the branch-line coupler. However, in some applications this feature is interesting in order to develop systems which can operate at multiple frequency bands. Examples of these applications are mobile communications systems with cellular and personal communications system (PCS) bands, and wireless local area networks (WLAN) systems operating over 2.4 and 5 GHz bands. Several techniques have been implemented in order to achieve dual-band quadrature hybrid couplers [109]- [125] and even tri-band quadrature hybrid couplers [126].

A dual-band operation is not a requirement in the W-band front-end receiver. The requirement of the quadrature hybrid coupler must have a broadband response covering the full W-band. One solution to solve the problem of the narrowband operation of the branch-line coupler can be its design with two or more operating frequencies specified within the desired bandwidth. This results in a broadband response. However, if the frequency ratio between the highest and lowest frequency limits of the operating band, i.e. 110 and 75 GHz in the W-band, is less than 1.5 as in our case, i.e. $f_{High} = 1.47 f_{Low}$, very high and low characteristic impedances are needed for the quadrature hybrid coupler [114]- [125]. Thus, the widths of the required microstrip lines with high characteristic impedance in the design exceed the manufacturing limit. Moreover, when the frequency becomes higher, the required microstrip lines with low characteristic impedance create an undesirable aspect ratio between the width of these transmission lines and its distance of $\lambda/4$.

Different approaches have been investigated in order to increase the bandwidth of branch-line coupler based on the use of:

- Coupled lines. Examples of that are those proposed in [127]- [131]. They use microstrip-to-slot technology to achieve the increase of the bandwidth up to 4 : 1 and a very compact coupler. For instance, a multisection equal-ripple quadrature hybrid based on this technique is proposed in [130], see Fig. 2.4 a). This coupler is a simple structure with rectangular-shaped slot-coupled sections and its design overcomes the amplitude imbalance shown in [127]- [129] at the highest and lowest frequency limits of the operating frequency band which is excessive for some applications. Although this technique achieves broadband performance, the ports of the quadrature hybrid are on the top and the bottom layer of the substrate. In the W-band front-end receiver, this complicates the integration of the coupler with the MMIC devices and also its packaging. In [131], a microstrip ultrabroadband multisection quadrature hybrid based on the coupled lines is proposed. This design has all the hybrid ports in the same layer, however, the ground plane has complicated slot structures.

- Single-stub matching networks designed at the center frequency. These matching networks are applied to every port of a branch-line quadrature hybrid coupler [132] and [133]. An example of this structure is shown in Fig. 2.4 b) [132]. All the ports are in the same layer of the substrate.

- Consecutive multiple branches and lines with different impedances to form a multi-section coupler [134]- [136]. As an example of this technique, the structure proposed in [136] is shown in Fig. 2.4 c).

- Multi-branch coupler as the core structure and attach impedance matching line-stubs to all the ports, see Fig. 2.4 d) [137].

The last three techniques are suitable for the design of a W-band quadrature hybrid for the front-end receiver because of their relatively simple design, broadband performance and their single-layer structure. However, the design presented in [136] is the simplest one and some tables with the dimensions of a coupler depending of the bandwidth requirements are given. For this reason, this technique has been selected to design the W-band quadrature hybrid coupler.

This paper, [136], solves the main problem of multi-section couplers based on Butterworth and Chebyshev conventional designs. These designs

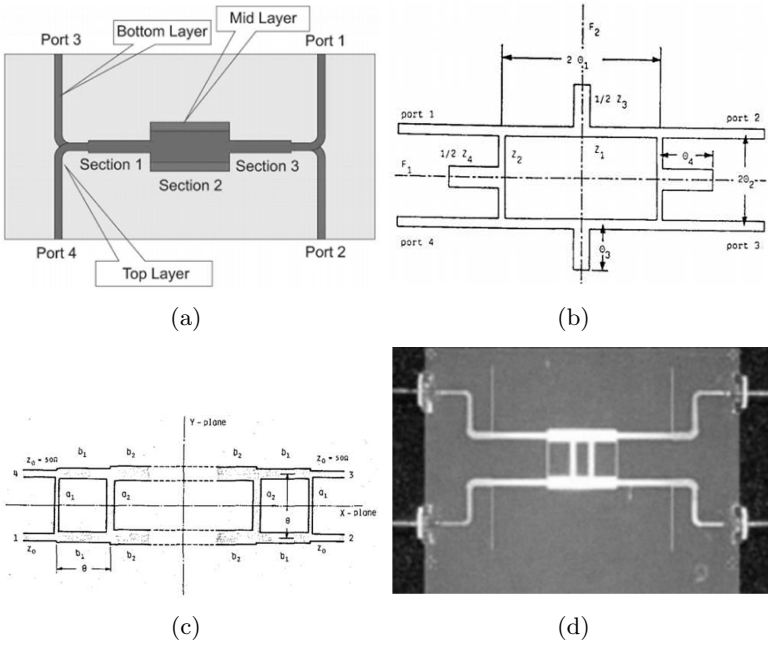

(a) (b)

(c) (d)

Figure 2.4 – Different techniques to increase the bandwidth of a quadrature hybrid coupler based on the use of a) coupled lines [130], b) single-stub matching networks designed at the center frequency [132], c) consecutive multiple branches and lines with different impedances [136] and d) multi-branch coupler as the core structure and attach line-stub structure to all the ports [137].

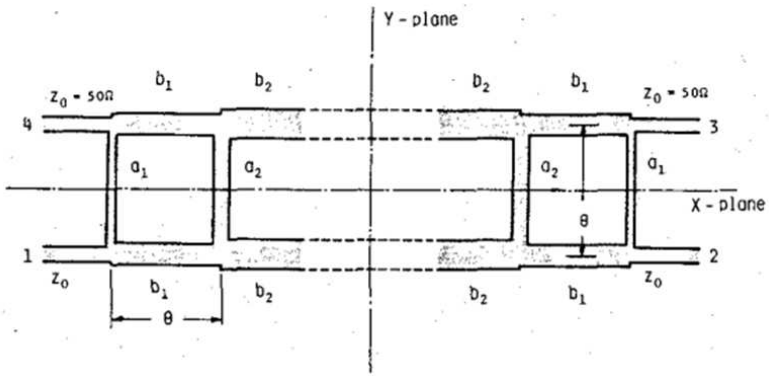

Figure 2.5 – A quadrature hybrid coupler with two-fold symmetry about the x and y planes proposed in [136].

generally require couplers with wide impedance ranges. Thus, very high impedances which exceed the manufacturing limit are needed to achieve more than four-branch couplers. This paper applies a computer-aided design using the general form of the Chebyshev function in order to obtain realizable ranges of impedances in microstrip technology. Moreover, this method takes into account the improvement of coupling characteristics such as the allowed amplitude imbalance and also the return and isolation losses along the entire operating band. The structure of the multisection quadrature hybrid coupler can be seen in Fig. 2.5 where its main parameters are defined.

It gives three tables in which several impedance solutions for two-, three- and four-section couplers are respectively shown. The addition of sections increases the operating bandwidth of the coupler. In each table, their solutions are compared with Butterworth and Chebyshev conventional designs.

For the design of a W-band quadrature hybrid coupler, the realizable impedance range is shown in Fig. 2.6. The selected substrate for the development of the W-band front-end receiver, i.e. 0.127 mm thick RO5880 substrate, has been taken into account for the calculation of these limits. On the one hand, the minimum realizable width with the intended manufacturing technique determines the highest characteristic impedance of a microstrip line. The manufacture of the planar circuit will be done by a laser milling machine, in particular, by a LPKF ProtoLaser 200. Thus, the minimum width of a microstrip line which this machine can mill is 0.05 mm. This implies that

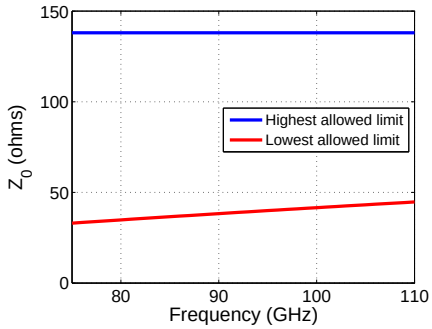

Figure 2.6 – Realizable impedance range of a microstrip line on 127 μm thick RO5880 depending on the frequency within the W-band.

the maximum allowed impedance of a microstrip line is 138 Ω. On the other hand, the lowest allowed limit of the microstrip line impedance is determined by the realizable width which keeps an acceptable ratio between the line width and the distance between branch-lines, i.e. less than $\lambda/4$. Therefore, the usable impedance range for a 0.127 mm thick RO5880 substrate in W-band is approximately 39 Ω-138 Ω considering the center frequency of the desired operating bandwidth, i.e. 92.5 GHz.

Paying attention to the tables given in [136], see Fig. 2.7, a four-branch coupler is required to cover the full W-band because both $BW_{R,I}$ and BW_C must be higher than 38 %. $BW_{R,I}$ and BW_C define the operating bandwidth. $BW_{R,I}$ corresponds to the frequency bandwidth (%) in which the return loss and isolation are better than 20 dB. BW_C corresponds to the frequency bandwidth (%) in which the coupling imbalance is better than -3.0 ± 0.43 dB. As can be seen in Fig. 2.7, only couplers 4-16 and 4-17 meet the bandwidth and the realizable impedance range requirements, i.e. 39 Ω-138 Ω, for the design of a W-band quadrature hybrid coupler. Therefore, the implemented coupler has been 4-16 because the performance is slightly better in terms of broader bandwidth. With respect to the distance between branch-lines, they initially correspond to quarter guided wavelength which depend on the impedance of the microstrip lines.

The schematic of the designed W-band quadrature hybrid coupler and the definition of its parameters are shown in Fig. 2.8. The initial dimension of parameter has been calculated based on the impedances shown in Fig. 2.7.

	D	b_1 [Ω]	b_2 [Ω]	a_1 [Ω]	a_2 [Ω]	$BW_{R,I}$ [%]	BW_C [%]	S_{min} [dB]	S_{max} [dB]	k_0 [dB]
4-1	—	39.97	30.33	263.85	52.82	43	32	∞	—	0
4-2	—	36.83	28.77	170.53	57.44	60	34	∞	22.14	0
4-3	16	44.34	39.40	152.95	90.96	63	44	36.02	20.51	0.28
4-4	20	44.14	39.15	162.39	85.32	60	40	36.23	22.73	0.19
4-5	24	45.03	41.99	157.52	91.12	58	38	29.03	23.02	0.14
4-6	16	39.40	30.66	*166.67	67.03	62	44	31.89	20.47	0.29
4-7	16	42.99	36.84	*156.25	83.91	63	44	47.30	20.45	0.28
4-8	16	47.16	44.76	*147.06	106.32	61	43	28.90	20.46	0.28
4-9	16	51.96	54.85	*138.89	136.09	57	43	23.47	20.39	0.26
4-10	16	57.37	67.39	*131.58	174.95	50	43	22.06	20.15	0.25
4-11	14	53.68	56.51	*142.86	*142.86	57	45	25.24	20.20	0.40
4-12	16	53.94	58.31	*142.86	*142.86	55	43	24.17	21.41	0.29
4-13	16	52.50	55.92	*138.89	*138.89	56	43	23.30	20.52	0.27
4-14	18	52.62	57.14	*138.89	*138.89	54	41	24.16	21.01	0.21
4-15	20	52.69	58.06	*138.89	*138.89	52	40	25.66	21.23	0.17
4-16	20	51.28	55.34	*135.14	*135.14	53	40	26.33	20.04	0.16
4-17	22	51.32	56.41	*135.14	*135.14	52	39	27.75	20.08	0.13

Figure 2.7 – Table of design characteristics of four-branch couplers [136].

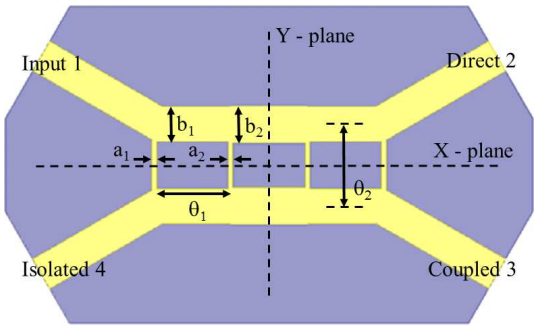

Figure 2.8 – Schematic of the designed W-band quadrature hybrid based on coupler 4-16 [136]. The parameters of the design are defined in this figure.

However, these dimensions have been optimized using the SW package Ansys HFSS. The values of each optimized parameter can be seen in Table 2.2.

Table 2.2 – Dimensions (mm) of the designed W-band quadrature hybrid coupler, see Fig. 2.8.

a_1	a_2	b_1	b_2	θ_1	θ_2
0.05	0.05	0.4	0.44	0.81	0.94

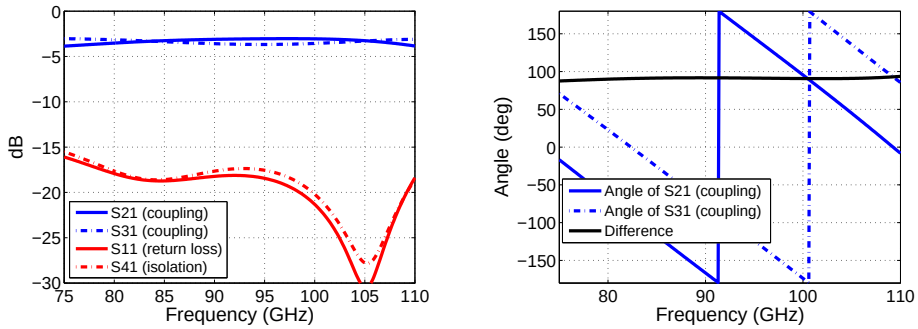

(a) (b)

Figure 2.9 – Simulated response of the designed W-band quadrature hybrid coupler in terms of a) S-parameters and b) phase of the coupling parameters and difference between them.

The electromagnetic performance of the designed W-band quadrature hybrid in terms of S-parameters and the phase difference between direct and coupled ports are shown in Fig. 2.9. Note that the considered dielectric loss tangent at W-band is 0.01, as mentioned in Section 2.3.1. The return loss and isolation are better than 15 dB along the entire W-band. With respect to the coupling, it ranges between 3.03 and 3.86 dB. The phase difference between direct and coupled outputs is $90° \pm 3°$. Therefore, the design complies with the requirements for a W-band quadrature hybrid coupler.

2.3.3 MMIC components

The MMIC devices which are part of the W-band auto-calibrated receiver based on a differential configuration are a reference load, Low Noise Amplifiers (LNA) and detector diodes. A suitable choice of these devices is crucial to minimize the system noise of the receiver and to improve its sensitivity. The complete datasheets of the selected MMIC devices are shown in Appendix A.

2.3.3.1 Reference load

Some solutions have been considered as a reference load in the W-band in order to allow the calibration of the system, such as 50 Ω thin film resistors and MMIC attenuators. Thin film resistors show high accuracy and stability.

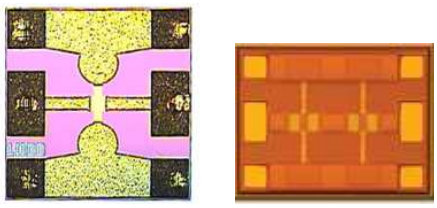

(a) (b)

Figure 2.10 – a) TGL4201 10 dB attenuator of TriQuint Semiconductor and b) HMC658 20 dB attenuator of Hittite.

However, their main drawback is the lack of availability of commercial thin film resistors that work above 20 GHz. Although commercial MMIC attenuators at W-band are also not available for the moment, this type of technology can work at higher frequencies such as 50 GHz. For this reason, a MMIC attenuator has been considered as the reference load of the W-band front-end receiver. The minimum attenuation needed is 10 dB in order to simulate a matched load in the isolated port of the input quadrature hybrid coupler of the auto-calibrated receiver.

Examples of commercial MMIC attenuators are TGL4201 of Triquint Semiconductor [138], see Fig. 2.10 a), and HMC658 of Hittite [139], see Fig. 2.10 b). They provide a fixed attenuation of 10 dB and 20 dB respectively. The dimensions of the chips are approximately the same, i.e. 0.50 x 0.50 x 0.1 mm and 0.42 x 0.45 x 0.1 mm. In both cases, the performance is ensured by the manufacturers up to 50 GHz. Although the datasheet of the Hittite's component, i.e. HMC658, is more detailed in terms of measurements and feasible assembly diagrams, the attenuation and also the input and output return losses of the TriQuint component, i.e. TGL4201, have been measured up to 110 GHz. These measurements can be seen in Fig. 2.11. Note that the green line corresponds to the selected attenuator, TGL4201-10. These results indicate that the TGL4201-10 attenuator of TriQuint Semiconductor can work well at W-band. It presents return losses above 15 dB and the attenuation is higher than 10 dB. Therefore, the selected MMIC attenuator for the W-band front-end receiver is the TGL4201-10 of TriQuint Semiconductor. However, it should be noted that the measurements have been carried out with probes from DC to 110 GHz and gold wires needed for assembly have not been considered.

The chip assembly of the TGL4201-10 device, as can be seen in Fig. 2.12,

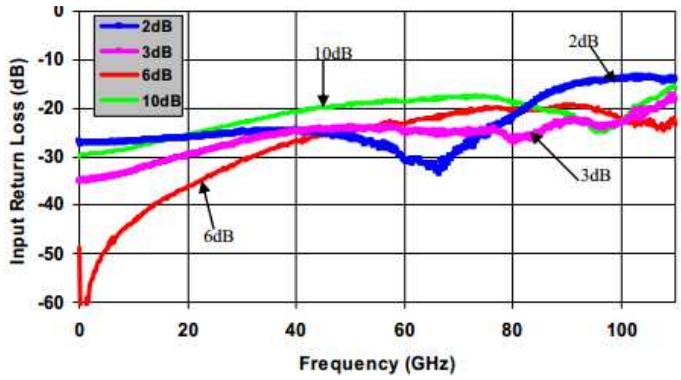

(a)

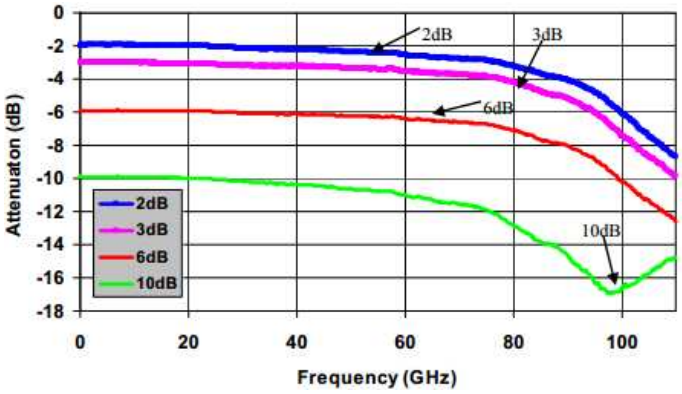

(b)

Figure 2.11 – Measurements of the TGL4201 MMIC attenuators of TriQuint Semiconductor given by the manufacturer; a) input return losses and b) attenuation. The measurement has been carried out with probes from DC to 110 GHz.

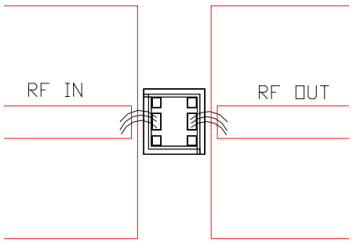

Figure 2.12 – Chip assembly diagram of the TGL4201-10 attenuator of TriQuint Semiconductor.

consists of input and output 50 Ω microstrip lines connected to the input and output ports of the attenuator by gold wires. Moreover, the ground contact is ensured by attaching the chip with silver epoxy to the ground plane. Therefore, the measurement of the MMIC attenuator at W-band taking into account gold wire bondings is needed in order to demonstrate that it is suitable as a W-band reference load. This measurement will be shown in Section 4.4.2.

2.3.3.2 W-band Low Noise Amplifier (LNA)

One of the main advantages of the proposed W-band front-end receiver is the possibility of direct detection and it is feasible thanks the availability of commercial MMIC Low Noise Amplifiers (LNA) and detectors at the operating frequency band, i.e. W-band. Some companies commercialise low noise amplifiers. Examples of these are Northrop Grumman Corporation (NGC) [140], United Monolithic Semiconductor (UMS) [141], HRL Laboratories [142] and OMMIC [143]. Their commercial MMIC LNAs at W-band can be seen in Table 2.3. The most important parameters are highlighted in this Table: the operating frequency band, the gain and the noise figure (NF).

Taking into account the sensitivity equation of a differential receiver configuration (Eq. 1.12), it can be improved as the operating bandwidth at RF increases and the noise temperature of the system decreases. Therefore, the low noise amplifier to be selected has to be broad bandwidth and have small contribution to the noise of the system, i.e. small noise figure. In this case, the operating bandwidth of the W-band front-end receiver covers the entire W-band. Thus, this is the minimum desired bandwidth. Other parameter to be considered is the gain.

Table 2.3 – Commercial MMIC Low Noise Amplifiers at W-band. The manufacturers are (1) NGP, (2) UMS, (3) HRL and (4) OMMIC.

Part	Description	Frequency (GHz)	Gain (dB)	NF (dB)
ALH283 (1)	InP HEMT	80 – 100	29	2.5
ALH495 (1)	InP HEMT	80 – 100	18	4.3
ALH497 (1)	InP HEMT	80 – 100	17	4.2
ALH503 (1)	InP HEMT	80 – 100	16	4.2
ALH504 (1)	InP HEMT	80 – 100	18	4.1
CHA1008 – 99F (2)	HEMT	80 – 105	16	5
LN4-110 (3)	InP	75 – 110	22	3.5
LN5-100 (3)	InP	70 – 100	24	3.5
CGY2190UH/C2 (4)	MHEMT	75 – 110	23	2.8

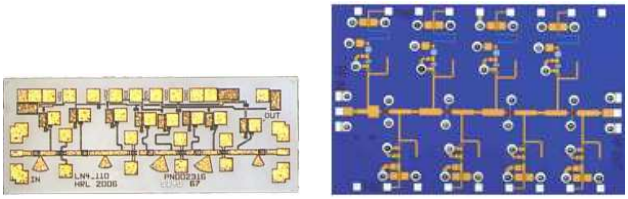

(a) (b)

Figure 2.13 – a) LN4-110 Low Noise Amplifier of HRL Laboratories and b) CGY2190UH/C2 Low Noise Amplifier of OMMIC.

According to this Table, both LN4-110 and CGY2190UH/C2, see Fig. 2.13, meet the bandwidth requirement being better the gain and the noise figure of the second device. However, the bias circuit in the second case has to be done from both the top and the bottom sides. This complicates the design of the two amplification branches of the front-end. The main problem is that the distance between these two branches has to be increased in order to have enough space for the bias circuit bonds. This also implies an increase in the length of the microstrip lines of the planar circuit which produces higher dielectric losses. For these reason, the selected MMIC Low Noise Amplifier is the LN4-110 of HRL Laboratories, whose bias can be done only from the top side.

The LN4-110 is a four stage MMIC amplifier that covers the entire

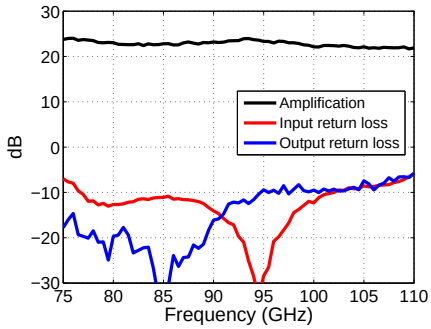

Figure 2.14 – S-parametes of the LN4-110 Low Noise Amplifier given by HRL Laboratories.

W-Band. The amplifier is fabricated using HRL's passivated H2 InP HEMT process. The LNA has a single drain supply and it is typically used with an independent gate bias for the first stage and a common gate bias for the remaining stages. The dimensions of the chip are 1 x 2.08 x 0.05 mm. Its typical gain and return loss performance are shown in Fig. 2.14.

Fig. 2.15 shows the assembly diagram of the LN4-110, it consists of input and output 50 Ω microstrip lines connected to the input and output ports of the amplifier by gold wires just like the MMIC attenuator. However, in this case the recommendation is to use ribbon wires instead of standard gold wires. Moreover, the ground contact is ensured by welding the component on the ground plane by silver epoxy. The bias circuit has to be connected from the top of the chip through a series of surface mount capacitors. The recommended values of these capacitors are specified in this Figure. In order to remove spurious oscillations of the amplifier which penalise its performance, it has to be place inside a 1.27 mm width channel.

2.3.3.3 W-band detector

The search of a MMIC detector that works along the entire W-band has been more difficult. In fact, only two companies have been found, i.e. HRL Laboratories [144] and Virginia Diodes Inc. (VDI) [145]. On the one hand, HRL Laboratories commercialises two different models of MMIC detector diodes at W-band, i.e. DD2 and V1A, see Fig. 2.16 a) and b) respectively. The

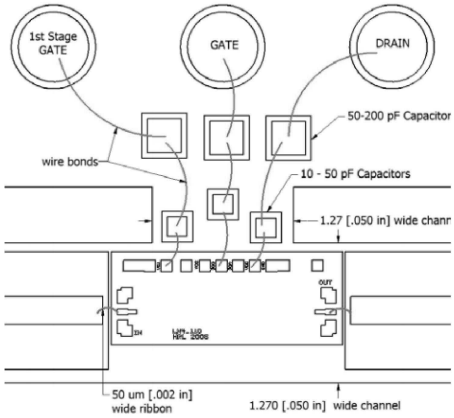

Figure 2.15 – Typical assembly diagram of the LN4-110 Low Noise Amplifier given by HRL Laboratories.

only two differences between these two components are the maximum input power and the dimensions. Although the size of the DD2 detector is smaller, it can not support input powers above -30 dBm. In the V1A detector, the maximum input power is -10 dBm. On the other hand, VDI commercialises the W band ZBD detector diode which is shown in Fig. 2.16 c). This diode is the smallest one. However, it is worse in terms of sensitivity and noise equivalent power (NEP). The sensitivity of HRL detectors is higher, 7 V/mW compared to 2 V/mW of the VDI diode. Moreover, The NEP of the VDI diode doubles the NEP of the HRL detectors. Therefore, for our application, HRL detectors are more suitable to be used in the W-band auto-calibrated receiver. The selected MMIC detector at W-band is the V1A whose dimensions are 0.74 x 1.475 x 0.05 mm.

The V1A is a tunnel diode W-band square law detector fabricated using InAs/GaAlSb growth. The zero bias diode produces a DC voltage proportional to the input power with high sensitivity. Linearity is excellent up to the -30 dBm input power level. Noise equivalent power is less than 1 $pW/Hz^{1/2}$. The detector is zero bias. Moreover, the assembly is the same as the attenuator.

The return loss and the typical sensitivity performance are shown in Fig. 2.17.

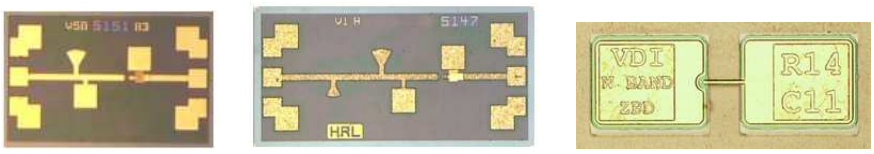

(a) (b) (c)

Figure 2.16 – a) DD2 Detector and b) V1A Detector, both of HRL Laboratories, and c) W band ZBD of Virginia Diodes Inc. (VDI).

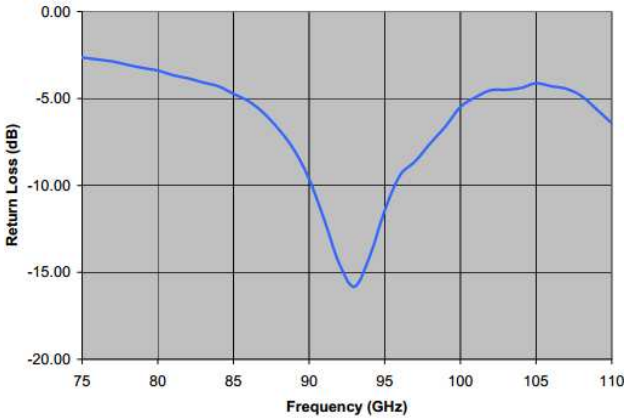

(a)

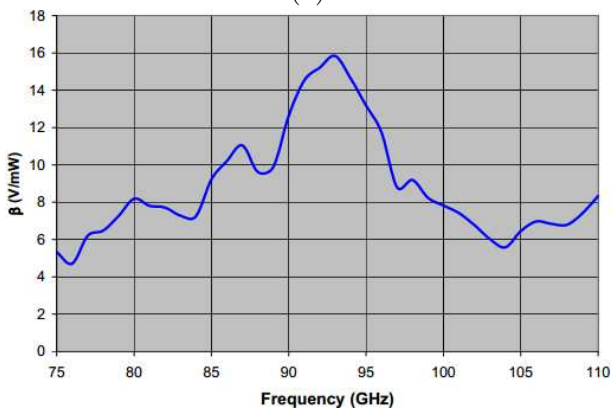

(b)

Figure 2.17 – a) Return loss and b) typical sensitivity performance of the V1A detector of HRL Laboratories.

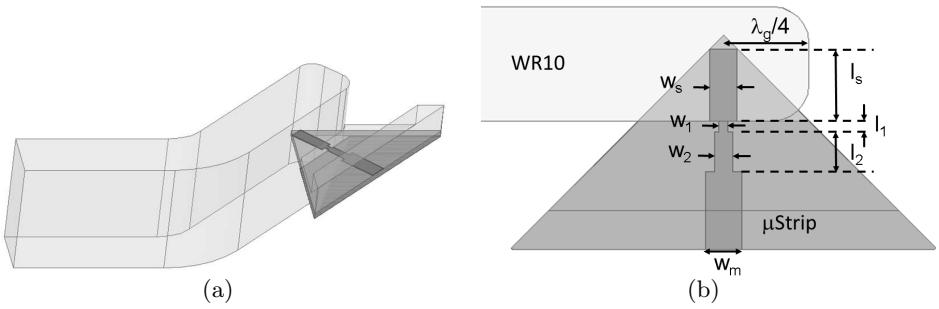

Figure 2.18 – The designed WR10 to microstrip transition for the W-band auto-calibrated receiver and its parameters.

2.3.4 WR10 waveguide to microstrip transition

A WR10 waveguide to microstrip transition has been also designed in order to connect the receiver to a standard horn antenna or to the test equipment required for characterization. This facilitates the comparison between the proposed receiver and a commercial W-band receiver based on a direct detection scheme. Therefore, the receiver under study will consist of the WR10 waveguide to microstrip transition shown in this Subsection and the balanced structure based on the differential configuration.

Several types of waveguide to microstrip transition have been previously proposed. These types can be classified depending on the field propagation direction in the waveguide and in the microstrip line. Section 4.3 explains in detail this classification. Therefore, this Subsection is only focused on the design of the selected transition.

The designed WR10 waveguide to microstrip transition for the receiver consists of a probe placed in the E-plane of the waveguide [146]- [148], see Fig. 2.18. This probe is an extension of the microstrip line which is introduced in the waveguide through a small aperture in the broad wall. The ground plane under the probe is removed.

The main advantages of this transition is that good return and insertion losses have been experimentally obtained at W-band in [147] and [148]. Besides, the microstrip circuit is welded in order to ensure the electrical connection between the metal block and its ground plane. This fact avoids misalignments between probe and waveguide.

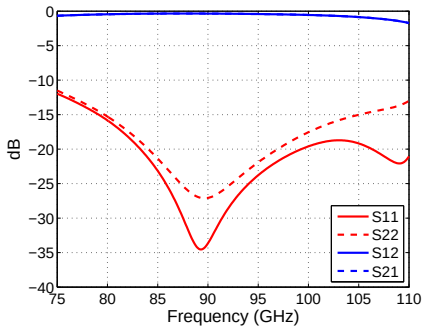

Figure 2.19 – S-parametes of the designed WR10 to microstrip transition.

The simplest design of this type of transition was chosen without considering modifications in the waveguide part as those proposed in [148]. This E-plane probe is placed at a distance of a quarter guided wavelength, $\lambda_g/4$, with respect to the waveguide short. Its bandwidth is improved by a multi-section matching transformer implemented in the microstrip line. The design parameters of the transition can be seen in Fig. 2.18 b) and their optimized dimensions are shown in Table 2.4. Note that the used substrate is the same as in the W-band quadrature hybrid coupler, i.e. 0.127 mm thick Rogers RT/Duroid 5880 whose considered dielectric loss tangent at W-band is 0.01. Due to the requirements of the substrate cutting method, the substrate has a triangular shape inside the waveguide. This makes the window in the waveguide wall larger than usual. However, it does not affect the transition performance.

Table 2.4 – Dimensions (mm) of the designed WR10 to microstrip transition based on the E-plane probe.

w_m	w_s	w_1	w_2	l_s	l_1	l_2
0.4	0.3	0.1	0.2	0.8	0.12	0.45

Fig. 2.19 shown the calculated S-parameters of the transition. As can be seen, the insertion losses are lower than 1.7 dB along the entire W-band. Moreover, the return losses are better than 11 dB. In the central part, i.e. 85-95 GHz, the insertion losses are lower than 0.8 dB and the return losses are better than 22 dB.

2.4 Conclusions

In this Chapter, the theoretical analysis of the differential configuration of the W-band auto-calibrated receiver has been carried out. With this analysis, the two main advantages of this configuration have been demonstrated. Firstly, its capability to separate the input and reference signals and to perform the internal calibration of the system. And secondly, the reduction of the effect of gain and noise fluctuations since their contribution in both the amplified signals are equal. Therefore, their effects are removed by including a subtracting operation in the post-detection stage of the receiver. Afterwards, taking into account the planar structure of the W-band auto-calibrated receiver, a low loss dielectric substrate required to minimize the dielectric losses has been selected in this Chapter. This is important because some receiver components such as the WR10 waveguide to microstrip transition and the two quadrature hybrid couplers are built on this substrate. Their dielectric losses increase the system noise temperature and penalize the sensitivity of the receiver. Moreover, the designs of these microstrip components and the selection of the suitable MMIC devices such as low noise amplifier, attenuator and detectors have been presented.

Chapter 3

Analysis of the W-band auto-calibrated receiver

3.1 Introduction

Once the W-band auto-calibrated receiver and its components have been explained, this Chapter will deal with the analysis of its performance. The proposed W-band auto-calibrated receiver built in planar technology is shown schematically in Fig. 3.1. Both the designed microstrip components and the commercial MMICs are included in the receiver. On the one hand, the designed components in microstrip technology are the WR10 waveguide to microstrip transition, which enables the connection of the planar receiver with waveguide based equipment, and the W-band quadrature hybrid couplers. On the other hand, the commercial MMICs are the W-band Low Noise Amplifiers LN4-110, the W-band Detector Diodes V1A and the 10 dB attenuator TGL4201-10. The RF connections between microstrip components and MMIC devices are carried out by gold wire bondings. Therefore, the total dimensions of the W-band auto-calibrated receiver is 7 mm wide, 32 mm long and 0.127 mm thick taking into account the length of the WR10 waveguide section.

The analysis of the planar receiver in terms of reflection coefficient, amplification and also, noise temperature and noise figure. It has been performed using the SW package Advanced Design System (ADS) by Keysight Technologies. This analysis has been carried out along the entire W-band excluding diode detectors.

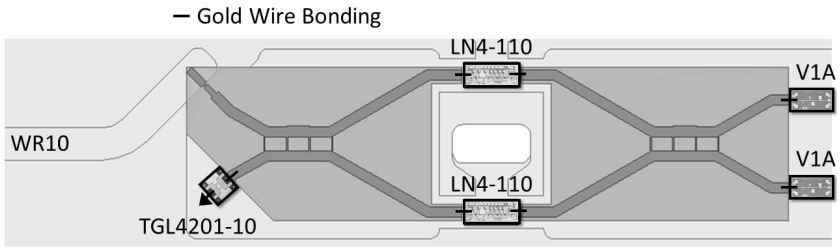

Figure 3.1 – Layout of the designed W-band auto-calibrated receiver.

In this Chapter, three analysis have been done in order to study the differential configuration of the receiver and the effect of each component on its performance. In the first analysis, the differential configuration with ideal components is considered to demonstrate its behaviour. Moreover, the effect of gain and noise imbalance of the amplifiers on its output signals is studied. Next, each real component of the receiver has been introduced to study its influence on the reflection coefficient, amplification and noise figure. Finally, gold wire bondings needed to connect 50 Ω microstrip lines with MMIC devices have been taken into account in the performance of the receiver.

3.2 W-band receiver with ideal components

The behaviour of the receiver considering ideal components is first studied. Some of the advantages of its differential configuration were already mentioned in Chapter 2. On the one hand, the configuration is able to separate input signals when the gain of the amplifier branches are identical. On the other hand, any gain or noise fluctuation in the amplifiers identically affects both output signals allowing to eliminate its effect. In this Section, ADS simulations have been carried out in order to demonstrate these statements. To this end, a receiver with ideal components has been introduced in ADS.

The receiver under study consists of two quadrature hybrid couplers and two amplifier branches, see Fig. 3.2. Ideal components for the quadrature hybrid couplers and low noise amplifiers have been selected. The S parameters of these components are depicted in Fig. 3.3 a) and b) respectively. In Fig. 3.3 a), S21 corresponds to the direct port whilst S31 corresponds to the coupled port of the coupler. The ideal quadrature hybrid coupler has a flat

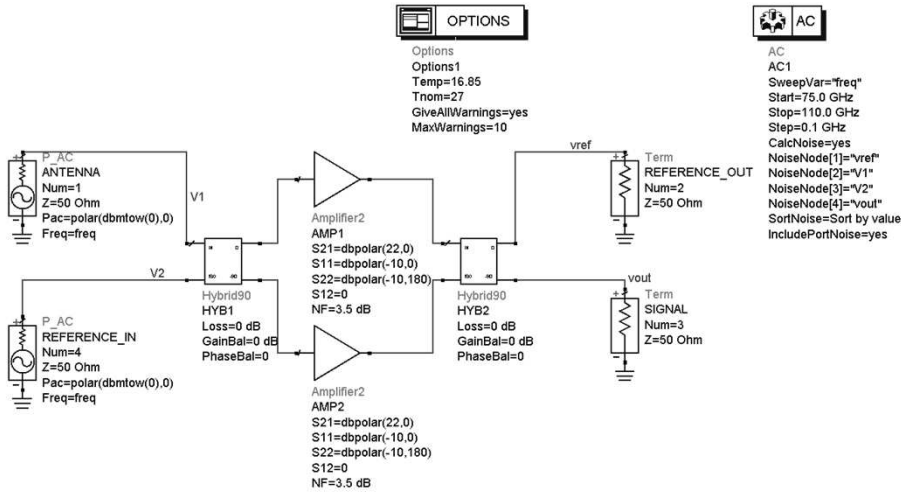

Figure 3.2 – ADS schematic of the ideal receiver.

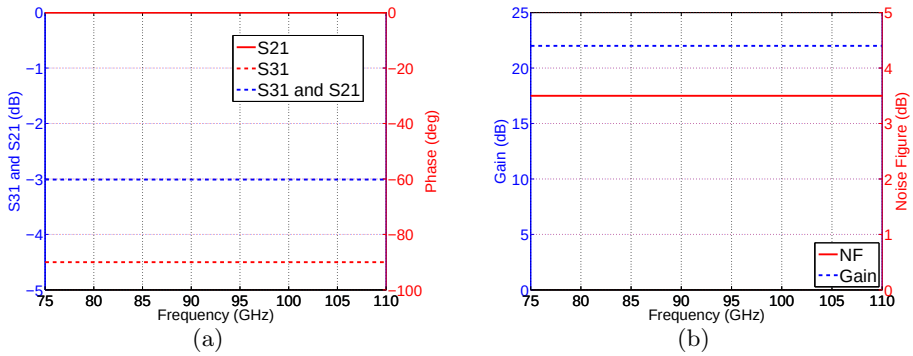

Figure 3.3 – a) S parameters and phase of the output ports of the ideal quadrature hybrid coupler and b) S parameters and noise figure of the ideal low noise amplifier.

response along the entire W-band keeping a 90° phase difference between its two outputs. Note that the defined parameters of the amplifier are the same as the nominal characteristics of the commercial LN4-110, i.e. gain= 22 dB and NF= 3.5 dB. Moreover, perfectly matched input and output ports are supposed.

It is important to remember that the expected output signals of the considered receiver in ADS simulation, i.e. $v_{1,in}$ for the first output and $v_{2,in}$ for the second output, are as follows:

$$v_{1,in} = \sqrt{\left(\frac{B}{2}(g_1+g_2)\right)^2 + \left(\frac{A}{2}(g_1-g_2)\right)^2 + \left(\frac{1}{\sqrt{2}}(n_1g_1+n_2g_2)\right)^2} \quad (3.1)$$

$$v_{2,in} = \sqrt{\left(\frac{A}{2}(g_1+g_2)\right)^2 + \left(\frac{B}{2}(g_1-g_2)\right)^2 + \left(\frac{1}{\sqrt{2}}(n_1g_1+n_2g_2)\right)^2} \quad (3.2)$$

An AC simulation has been performed in order to obtain the effect of the components on the output signals of the receiver. This facilitates the demonstration of the mentioned statements. If the reference and unknown input signals of the configuration, i.e. B and A, are noise defined as -69.8 and -65.6 dBm respectively and identical amplifiers are considered, the output signal in the first and second branches are -47.8 and -43.6 dBm, which correspond to the amplified reference signal and the amplified unknown signal. Therefore, both input signals have been separated by the differential configuration. With respect to the noise, the same contribution is obtained in each output, which corresponds to a noise figure of 3.5 dB. This value is identical to the noise figure of each amplifier, since these are the only elements that generate noise in the receiver.

When a difference between amplifier gains is introduced, i.e. $g_2 = g_1 + \Delta G$, the following equations define the output signals of the configuration:

$$\begin{aligned} v_{1,in}^2 &= \left(\frac{B}{2}(2g_1+\Delta G)\right)^2 \\ &+ \left(\frac{A}{2}\Delta G\right)^2 \\ &+ \left(\frac{1}{\sqrt{2}}(n_1g_1+n_2(g_1+\Delta G))\right)^2 \end{aligned} \quad (3.3)$$

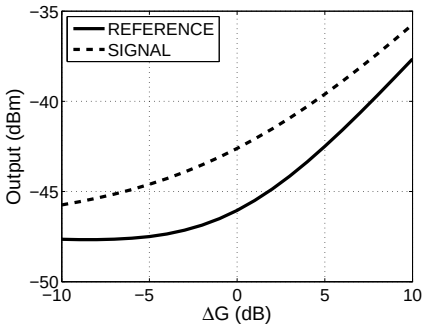

Figure 3.4 – Output (dBm) of the differential receiver depending on the gain imbalance, i.e. ΔG. The input reference noise is -69.8 dBm and the input signal noise is -65.6 dBm.

$$\begin{aligned} v_{2,in}^2 &= \left(\frac{A}{2}\left(2g_1+\Delta G\right)\right)^2 \\ &+ \left(\frac{B}{2}\Delta G\right)^2 \\ &+ \left(\frac{1}{\sqrt{2}}\left(n_1 g_1 + n_2\left(g_1+\Delta G\right)\right)\right)^2 \end{aligned} \tag{3.4}$$

As can be seen, part of the unknown signal, A, is coupled to the reference branch, i.e. $v_{1,in}$, and part of the reference signal, B, is coupled to the signal branch, i.e. $v_{2,in}$,. The smaller the gain imbalance between amplifiers, the smaller the undesired coupled signals in each output. For instance, when a reference and unknown input signals of -69.8 and -65.6 dBm, and also $\Delta G = -1$ dB are considered, i.e. $g_1 = 22$ and $g_2 = 21$ dB, the output signals are -46.9 and 43.5 dBm. In this case, the 4.2 dB difference between both signals is not kept due to the coupling. The effect of this coupling depending on the gain imbalance can be seen in Fig. 3.4.

However, the subtracting operation implemented after the diode detectors removes the effect of this coupling because the contribution of this gain imbalance is identical in both input signals. It can be seen in Eq. 3.5 where both input signals, i.e. A and B, are multiplied by the same gain factor.

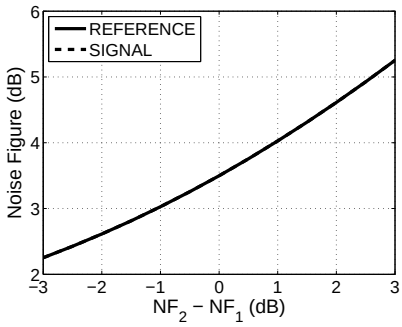

Figure 3.5 – Noise Figure of the differential receiver depending on the noise figure imbalance between amplifiers.

$$V_2 - V_1 = A^2 \beta g_1 \left(g_1 + \Delta G\right) - B^2 \beta g_1 \left(g_1 + \Delta G\right) \tag{3.5}$$

As can be seen in this Equation, the contribution of the noise generated by the amplifiers has been removed by the subtracting operation.

Regarding the imbalance of the noise figure of the receiver, if $NF_2 = NF_1 - 1$ dB and $NF_1 = 3.5$ dB, the obtained noise figure is 3 dB in each output. This value is a combination of NF_1 and NF_2 produced by the output quadrature hybrid coupler. Therefore, the imbalance in the noise figure of the amplifiers similarly affects both outputs as it is shown in Fig. 3.5. This Figure depicts the noise figure of the receiver in each output depending on the noise figure imbalance of the amplifiers. The noise figure in both outputs are the same.

The theoretical performance of the ideal receiver has been demonstrated by simulation in this Section. However, the designed microstrip and MMIC components are not ideal and it is needed to analyse their effect in the performance of the receiver.

3.3 W-band receiver with real components

In order to introduce the proposed receiver in ADS, the models of each designed microstrip component and commercial MMIC devices have to be defined. The models of the required real components are shown in Fig. 3.6

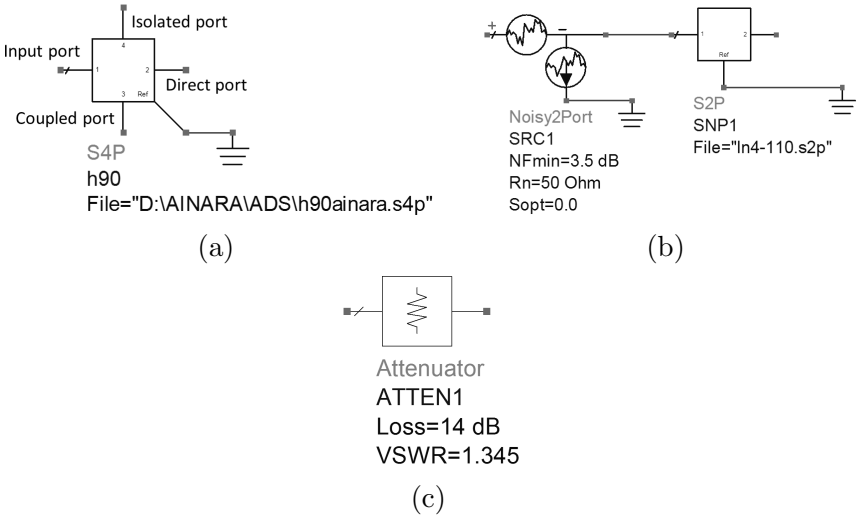

Figure 3.6 – ADS models for the a) designed W-band quadrature hybrid coupler, b) commercial LNA, i.e. LN4-110, and c) commercial attenuator, i.e. TGL4201-10.

and their electromagnetic behaviour can be seen in Fig. 3.7. These components are:

- The designed W-band quadrature hybrid coupler, see Fig. 3.6 a), which is defined by its S parameters obtained by HFSS, which were shown in Section 2.3.2.
- The commercial MMIC amplifier LN4-110, see Fig. 3.6 b). Its model includes two terms. On the one hand, a Noisy2Port element has been added in order to generate the noise figure of the amplifier. The used NF is that given by the manufacturer, i.e. 3.5 dB. On the other hand, the S parameters have been defined by the file given by the manufacturer.
- The MMIC attenuator TGL4201-10, see Fig. 3.6 c). Both attenuation and reflection coefficient have been obtained from the graphs shown in the component datasheet. Their worst values have been selected.

The effect of each component is discussed by simulation in terms of noise figure, noise temperature, amplification and reflection coefficient of

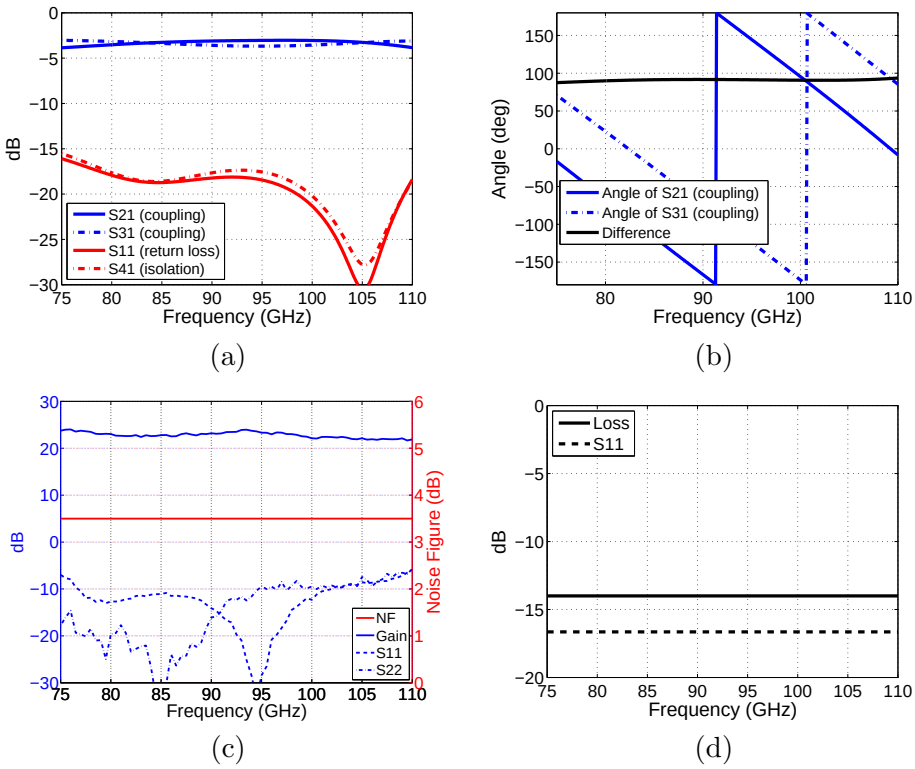

Figure 3.7 – a) S-parameters and b) phase of the coupling parameters of the designed W-band quadrature hybrid coupler and difference between them. c) S parameters and noise figure of the commercial low noise amplifier and d) S parameters of the commercial attenuator.

the receiver. Moreover, the substrate losses and the transition between WR10 waveguide to microstrip line are studied because these components are also part of the real implementation of the receiver. These analysis have been carried out by means of S parameter simulation in ADS. This type of simulation allows the calculation of S parameters and noise within a specified frequency band.

3.3.1 MMIC attenuator

Firstly, the commercial MMIC attenuator is included in the isolated port of the input quadrature hybrid coupler. Ideal components for the rest of the devices are taken into account, as can be seen in Fig. 3.8.

The obtained noise figure in the signal branch, i.e. port number 3 in Fig. 3.8, is 3.5 dB, the same value as in the ideal receiver. This also corresponds to the noise of the amplifier because the contribution of the attenuator in this output is non-existent when identical amplifiers are considered in terms of gain and noise. However, the noise figure given by ADS in the reference branch, i.e. port number 2 in Fig. 3.8, is 34.5 dB. This value is too high and erroneous due to two reasons. On the one hand, the software considers the input port of the unknown signal, i.e. antenna port in Fig. 3.8, as the input noise port in the calculation. When identical amplifiers and ideal quadrature hybrid couplers are taken into account, the noise contribution of the antenna port is insignificant in this reference output. This increases the noise figure. On the other hand, the attenuator is considered as a noisy element within the receiver and it is the main noise source in this output. The input noise port of this output should be the attenuator itself. Therefore, from now on, the noise figure will be only analysed in the signal branch of the receiver.

3.3.2 Low noise amplifiers

Secondly, the commercial amplifiers are also included in the schematic of the receiver as can be seen in Fig. 3.9.

The noise contribution of the commercial amplifiers model is the same as in the ideal model, therefore, the obtained noise figure of the receiver in the signal branch is identical, i.e. 3.5 dB. However, the commercial amplifiers determine the reflection coefficient and the amplification of the receiver, which are shown in Fig. 3.10. Whereas the reflection coefficient of the receiver was kept constant

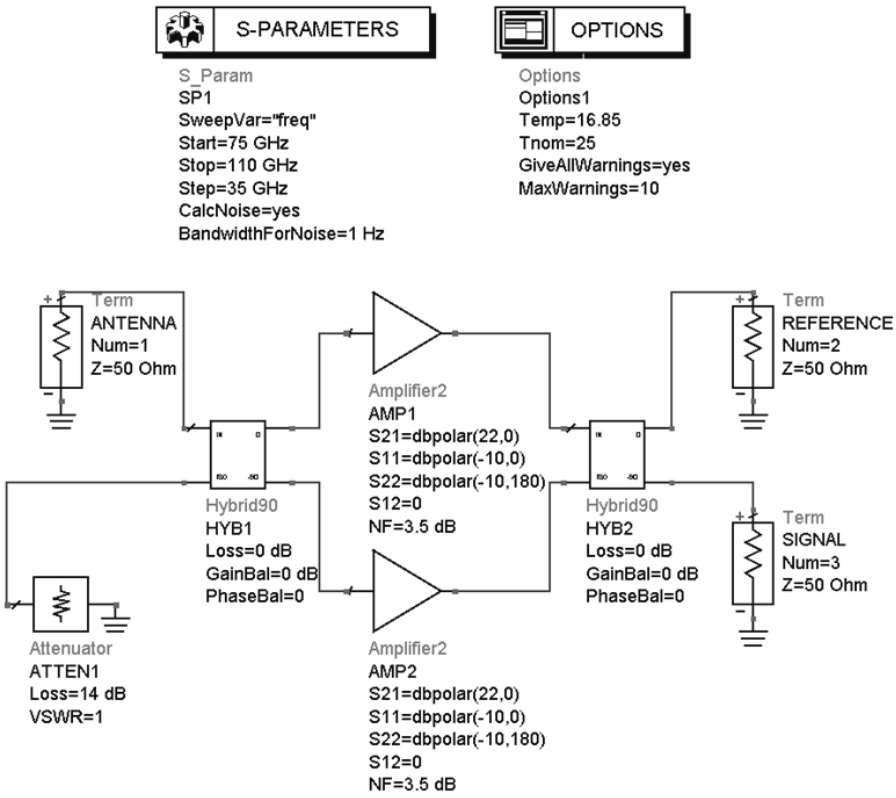

Figure 3.8 – ADS schematic of the ideal receiver with the commercial attenuator in the isolated port of the input quadrature hybrid coupler.

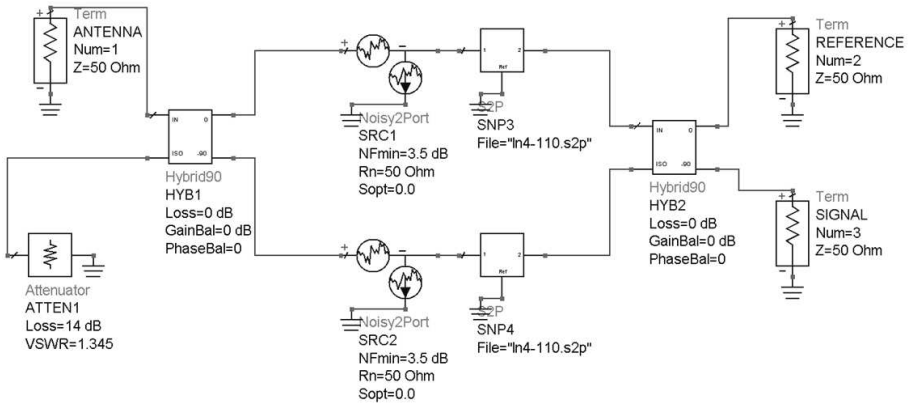

Figure 3.9 – ADS schematic of the ideal receiver with the commercial attenuator, which is placed in the isolated port of the input quadrature hybrid coupler, and commercial low noise amplifiers.

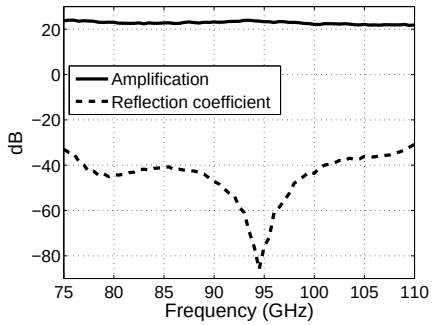

Figure 3.10 – Amplification and reflection coefficient of the receiver taking into account real models for the attenuator and the commercial amplifiers.

to −39 dB in the previous case, i.e. taking into account ideal amplifiers and couplers but the real attenuator, in this case, it is below −30 dB and it follows the same curve as the reflection coefficient of the amplifiers. With respect to the amplification of the receiver it is mainly defined by the amplifiers. For instance, its value at 92.5 GHz is 23.5 dB, see Fig. 3.10.

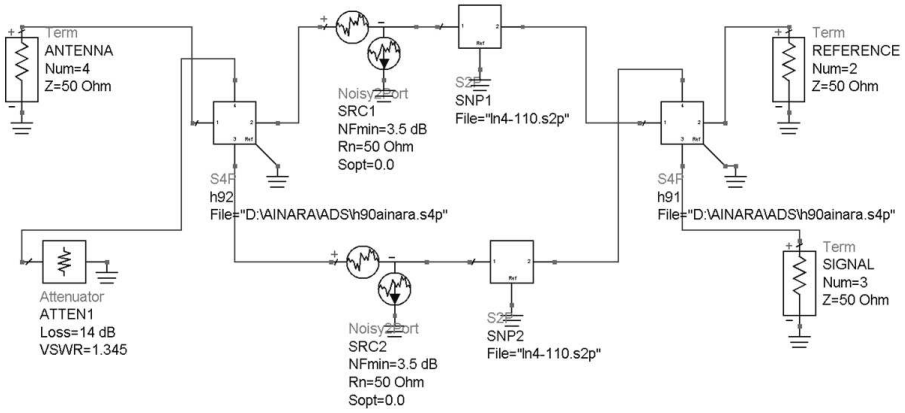

Figure 3.11 – ADS schematic of the receiver with the commercial attenuator, which is placed in the isolated port of the input quadrature hybrid coupler, the commercial amplifiers and the designed W-band quadrature hybrid couplers.

3.3.3 Quadrature hybrid couplers

The effect of adding the designed W-band quadrature hybrid couplers has been studying below. These couplers are not ideal. Their coupling range is between 3.03 and 3.86 dB. Moreover, the phase difference between direct and coupled ports is $90° \pm 3°$. In addition, the losses in the quadrature hybrid couplers generate noise. Therefore, the quadrature hybrid couplers are noisy elements in the receiver. The schematic of the proposed receiver taking into account real models for attenuator, low noise amplifiers and quadrature hybrid couplers are shown in Fig. 3.11.

The obtained noise figure of the receiver and its amplification and reflection coefficient can be seen in Fig. 3.12. The amplification of the receiver is penalized by the losses of the quadrature hybrid coupler. For example, the reduction is 2.08 dB at 92.5 GHz. Moreover, the reflection coefficient of the system increases because of the addition of these real components. With respect to the obtained noise figure of the receiver, it increases to at least 4.5 dB, being higher in the limits of the W-band due to the imbalance between the direct and coupled ports in the quadrature hybrid couplers. This effect is higher at the highest frequency limit of the W-band. This is produced by the noise introduced by the W-band quadrature hybrid coupler in its direct and coupled ports, see Fig. 3.13. This noise corresponds to the losses in the device

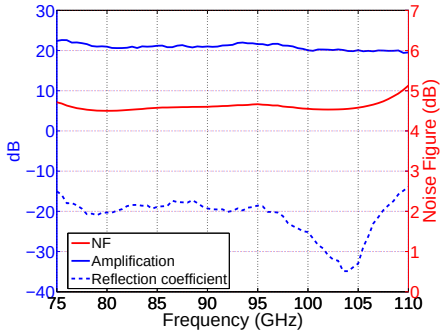

Figure 3.12 – S parameters and noise figure of the receiver taking into account real models of attenuator, commercial amplifiers and quadrature hybrid couplers.

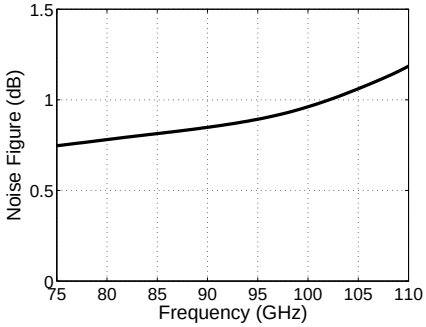

Figure 3.13 – Noise figure in direct and coupled ports of the designed W-band quadrature hybrid coupler.

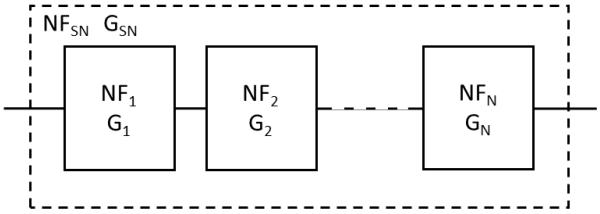

Figure 3.14 – Cascade of stages.

which increases with frequency.

If the proposed receiver is considered as a cascade of stages, see Fig. 3.14, the total noise figure, i.e. NF_{SN}, can be calculated using Friis equation, see Eq. 3.6, where NF_i and G_i correspond to noise figure and gain of the i-th component.

$$NF_{SN} = NF_1 + \frac{NF_2 - 1}{G_1} + \frac{NF_3 - 1}{G_1 G_2} + ... + \frac{NF_N - 1}{G_1 G_2 \cdots G_{N-1}} \tag{3.6}$$

Paying attention to this formula, the identification of components which contribute to the system noise figure is feasible. The components which mainly contribute to the noise of the system are the input quadrature hybrid coupler of the receiver and the amplifiers. The noise figure of the amplifiers is constant along the entire W-band, therefore, the noise system curve is affected by the input quadrature hybrid coupler. The output quadrature hybrid coupler hardly contributes to the noise system because it is behind the amplifiers whose gains are high enough.

3.3.4 Substrate losses

The 50 Ω microstrip lines have been lengthened in order to have enough space to place the required bonds to polarise the MMIC amplifiers and also to connect the rest of the planar components. These microstrip lines have dielectric losses due to the selected substrate, i.e. 0.127 mm thick RO5880. Therefore, they also contribute to the noise of the receiver.

The ADS model of a microstrip line is shown in Fig. 3.15 in which the properties of the dielectric substrate must be previously defined in the MSUB block. The main properties are the dielectric thickness, H, the dielectric

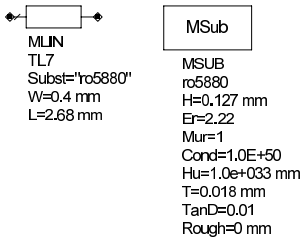

Figure 3.15 – ADS model for the definition of substrate losses.

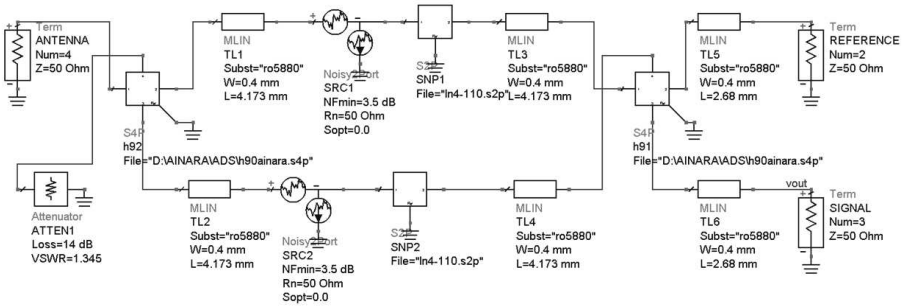

Figure 3.16 – ADS schematic of the real receiver taking into account substrate losses.

constant, E_r, the thickness of the copper clad, T, and the dielectric loss tangent, *TanD*. Note that the dielectric loss tangent of the substrate has been specified as 0.01. With respect to the microstrip line model, i.e. MLIN block in Fig. 3.15, the requirements are the width of the microstrip line which defines its impedance, W, and its length, L.

The required microstrip lines have been included in the schematic of the receiver, as can be seen in Fig. 3.16. These are placed before and after the amplifiers and, besides, before the outputs of the receiver in order to connect them with the diode detectors.

The dielectric losses of the microstrip lines penalise the amplification of the receiver whereas they have a negligible effect in the reflection coefficient, see Fig. 3.17. The reduction of the amplification produced by the substrate losses is 1.18 dB at 92.5 GHz. Therefore, the amplification of the receiver is 20.24 dB at this frequency. Regarding the noise figure of the system, it increases as expected. The average increase is approximately 0.5 dB. Moreover, the noise

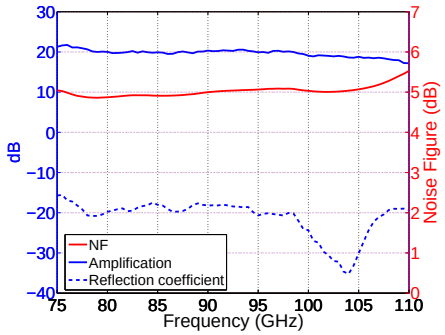

Figure 3.17 – S parameters and noise figure of the real receiver taking into account substrate losses.

figure curve is not as flat as in the previous analysis because the dielectric losses increases with frequency.

3.3.5 WR10 waveguide to microstrip transition

Finally, the model of the designed WR10 waveguide to microstrip transition is defined and included in the schematic. The model is based on its S parameters obtained by HFSS. The model and its performance are shown in Fig. 3.18. As can be seen, the insertion losses of the transition are around 0.8 dB in the central part of the frequency band. However, these losses increases when the frequency moves away from this central part. This increment is more pronounced at the highest limit of the W-band. Therefore, although the expected noise figure of this component is small, it is slightly higher at higher frequencies.

The schematic of the proposed receiver in which the designed WR10 waveguide to microstrip transition has been included are shown in Fig. 3.19. Now, the first noisy component of the proposed receiver is this transition.

The insertion losses of the transition mainly penalise the amplification of the receiver at the lowest and highest limits of W-band, see Fig. 3.20. The amplification of the receiver at 92.5 GHz is 19.9 dB. Furthermore, the noise figure of the system increases to at least 5.2 dB. As can be seen in this Figure, the noise figure increases with frequency and it is more pronounced at higher frequencies due to the noise contribution of this first element, i.e. the WR10

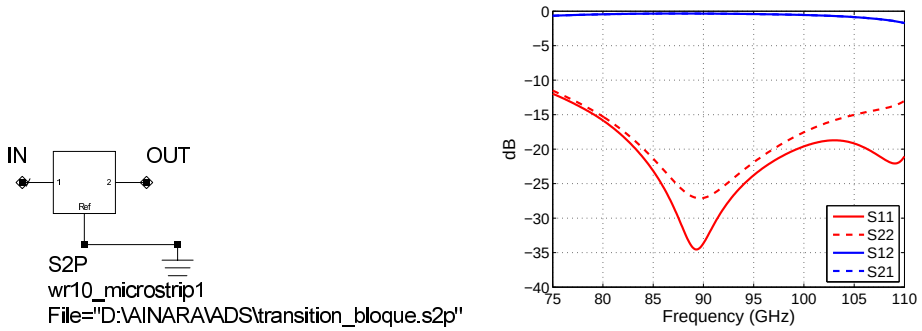

Figure 3.18 – a) ADS model for the designed WR10 to microstrip transition and b) its S parameters.

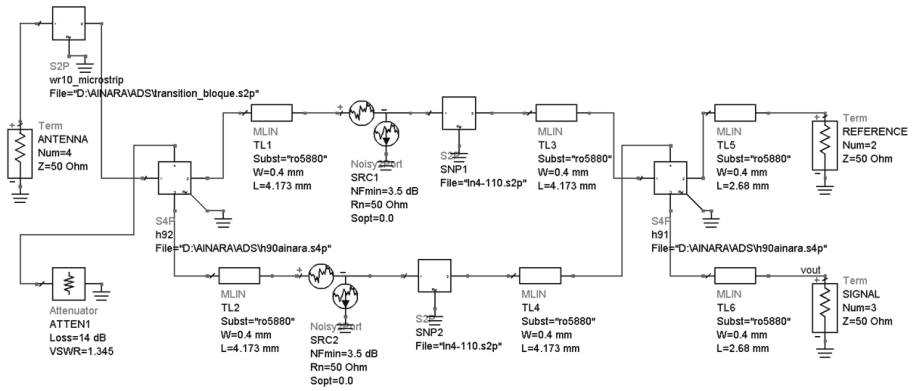

Figure 3.19 – ADS schematic of the real receiver taking into account substrate losses and WR10 waveguide to microstrip transition.

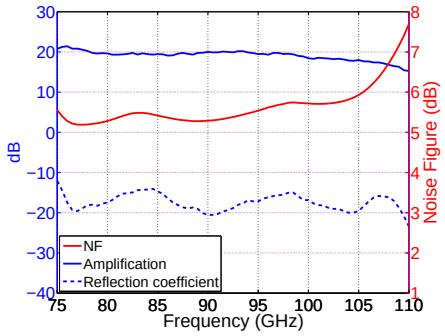

Figure 3.20 – S parameters and noise figure of the real receiver taking into account substrate losses and the WR10 waveguide to microstrip transition.

waveguide to microstrip transition. Regarding reflection coefficient, it has also been modified although it remains below −10 dB.

The noise temperature of the proposed W-band receiver with the designed microstrip components and commercial MMIC devices is shown in Fig. 3.21. It is below 1417.1 K along the entire W-band and specifically, 711.2 K at 92.5 GHz. The sensitivity of the receiver can be calculated using Equation 1.12 shown in Section 1.1.3 considering 1 KHz video bandwidth, which corresponds to an integration time of $\tau_{LF} = 1$ ms, an operation HF bandwidth of the receiver $B_{HF} = 35$ GHz (from 75 to 110 GHz) and the noise temperature obtained in this simulation. This calculation demonstrates that the expected sensitivity of the proposed receiver is better than 0.34 K along the entire W-band and it is 0.17 K at 92.5 GHz. These are good results if we compare them with other commercial W-band receiver as those formerly commercialised by Anteral [**?**] whose sensitivity is 0.7 K taking into account an operating frequency bandwidth from 80 to 100 GHz. If the full W-band is considered as its operating band, the sensitivity of this commercial system will be 0.53 K. This value is still higher than our expected sensitivity.

Although this simulation suggests that low noise temperature and therefore, good sensitivity can be achieved with the differential configuration of the proposed receiver, in practice the realization of ideal connections between elements is not possible. These connections require gold wire bondings at this high frequency. Therefore, it is important to calculate the contribution of gold wire bondings to the noise temperature of the system.

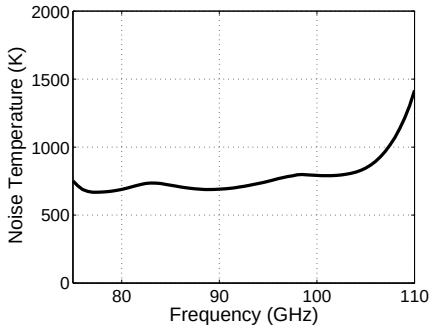

Figure 3.21 – Noise temperature of the real receiver taking into account substrate losses and WR10 waveguide to microstrip transition.

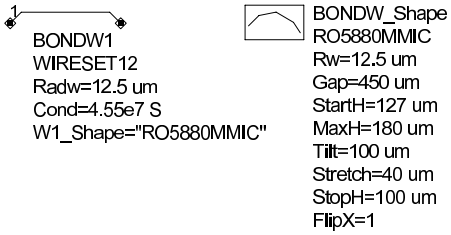

Figure 3.22 – ADS model for gold wire bonding.

3.4 Effect of the gold wire bondings

In order to study the effect of the wire bondings, a third analysis has been carried out. In this case, a model of the gold wire bondings has been defined, as shown in Fig. 3.22. There are some parameters to establish the shape of this type of connection. The most important parameters of the model are:

- The radius of the bondwire, i.e. $R_w = 12.5$ μm,
- The total distance the wire expands, i.e. Gap.
- Start height of the bondwire above the ground plane, i.e. StartH. It is defined by the thickness of the substrate.
- Maximum height of the bondwire above the ground plane, i.e. MaxH. It has been fixed to 180 μm.

- Stop height of the bondwire above the ground plane, i.e. StopH. The thickness of the MMIC component determines this value.

- The conductivity of the wire, i.e. Cond. In this case, a gold wire is recommended. Therefore, the conductivity is 45.5 MS.

The schematic of the receiver taking into account these gold wire bondings between components can be seen in Fig. 3.23. They are placed in the input and output ports for all MMIC devices. In this simulation the parameter under study is the effect of the bondwires length in the receiver performance in terms of input return losses and amplification of the system and also noise temperature and figure.

All bondwires which are part of the receiver are considered identical, i.e same shape and length, in order to simplify the analysis. The considered values for bondwires lengths, i.e. the variable gap in the bondwires model, are 0.15, 0.20, 0.25 and 0.30 mm. These values are achievable in practice with the available equipment.

The noise temperature and noise figure of the receiver with different lengths of bondwires are depicted in Fig. 3.24 a) and b) respectively. These results are compared to the receiver with ideal connections between microstrip and MMIC components, i.e. the black line in the Figure. As can be seen, the length of the bondwires is critical in the performance of the receiver because a standing wave is created due to reflections in the wire junctions. Moreover, lengths above 0.20 mm drastically increase both noise temperature and noise figure in specific frequency ranges within the W-band. This implies a loss of sensitivity in the receiver. For instance, the simulated noise temperature of the W-band auto-calibrated receiver considering 0.20 mm long gold wire bondings is less than 2800 K along the entire W-band. It almost doubles the noise temperature obtained in the receiver with ideal connections. Therefore, this provides a sensitivity of 0.67 K, which is comparable to those 0.7 K of some W-band receivers formerly commercialised by Anteral [**?**].

Therefore, the length of the bondwires has to be carefully considered in the assembly and connection between the components of the receiver to obtain high sensitivity. Furthermore, these bondwires also deteriorate the input return losses and the amplification of the radiometer as can be seen in Fig. 3.25 b). This behaviour can be explained by means of a study of the bondwire itself.

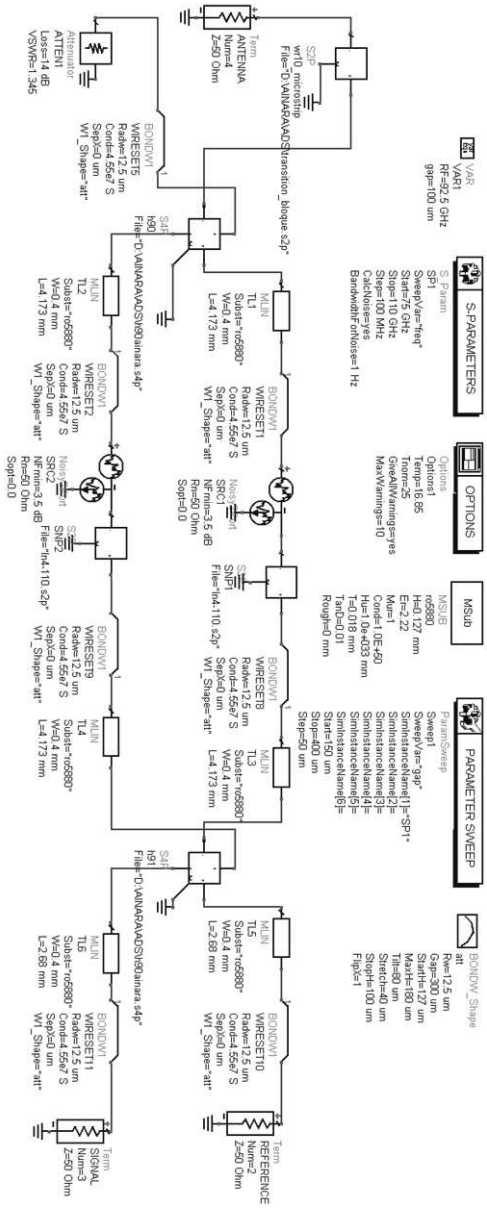

Figure 3.23 – ADS schematic of the W-band auto-calibrated receiver based on a differential configuration taking into account gold wire bondings connecting elements.

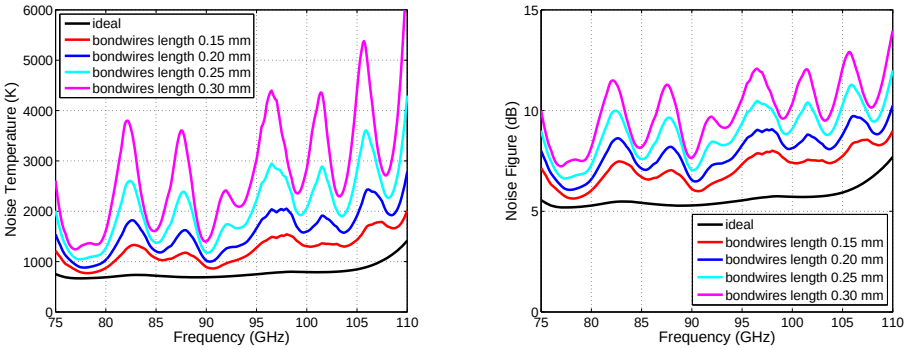

(a) (b)

Figure 3.24 – a) Simulated noise temperature and b) noise figure of the proposed W-band auto-calibrated radiometer considering different bondwire lengths compared to the receiver with ideal connections.

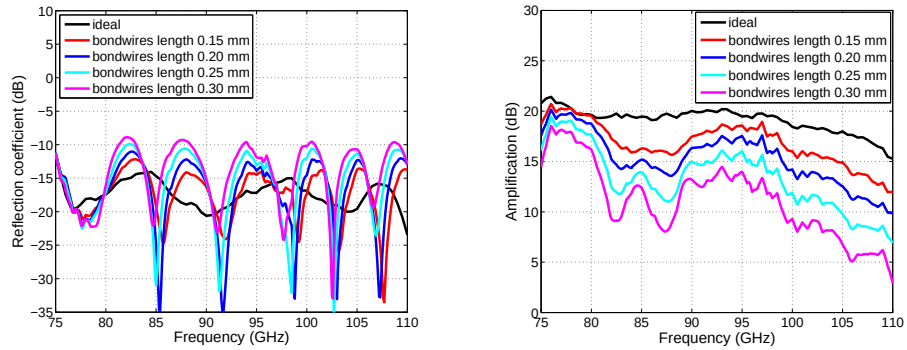

(a) (b)

Figure 3.25 – a) Reflection coefficient and b) amplification of the proposed W-band auto-calibrated radiometer taking into account the differential configuration with and without gold wire bondings.

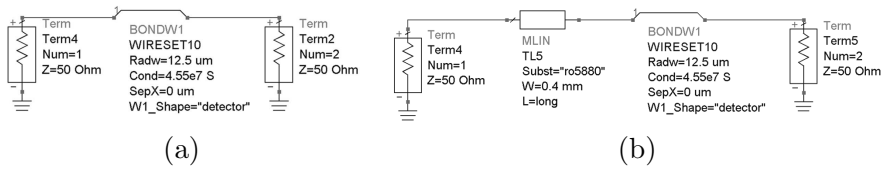

(a) (b)

Figure 3.26 – Schematic of a) a bondwire connected to two matched ports and b) a 50 Ω microstrip line and a bondwire connected to two matched ports.

Different lengths of a bondwire connected to two matched ports have been taken into account in a ADS simulation, see the schematic shown in Fig. 3.26 a). The longer the bondwire, the worse its reflection and transmission coefficient as can be seen in Fig. 3.27. The matching of the bondwire is penalised when a length over 0.15 mm is considered. Therefore, it creates an undesired reflection.

Following the analysis, a microstrip line before the bondwire is included in the schematic, see Fig. 3.26 b). The considered microstrip line is not perfectly matched because its characteristic impedance is not exactly 50 Ω. For this reason, a standing wave is created due to reflections in the wire junction depending on the length of the microstrip line. This effect can be seen in Fig. 3.28. A 0.25 mm long bondwire and different lengths of a 50 Ω microstrip line, from 2 to 8 mm, have been taken into account in the simulation. As expected, more reflections are created when the length of the microstrip line increases.

Therefore, this study indicates that the reflection coefficient of the receiver is mainly produced by its components placed before the first bondwires, i.e. the bondwires at the input port of the amplifiers. These components are the WR10 waveguide to microstrip transition, the attenuator and the input quadrature hybrid coupler. If we analyse these first devices taking into account ideal connections, see Fig. 3.29 a), its obtained reflection coefficient agrees well with the reflection coefficient of the total receiver without bondwires. This comparison can be seen in Fig. 3.30 a). This demonstrates that the rest of the components have a negligible effect in this parameter. Thereby, the analysis of the bondwires can be carried out for this part of the receiver.

Two 50 Ω microstrip lines and bondwires connected to the output ports of the input quadrature hybrid coupler have been included, see the schematic shown in Fig. 3.29 b). The considered 50 Ω microstrip lines and bondwires

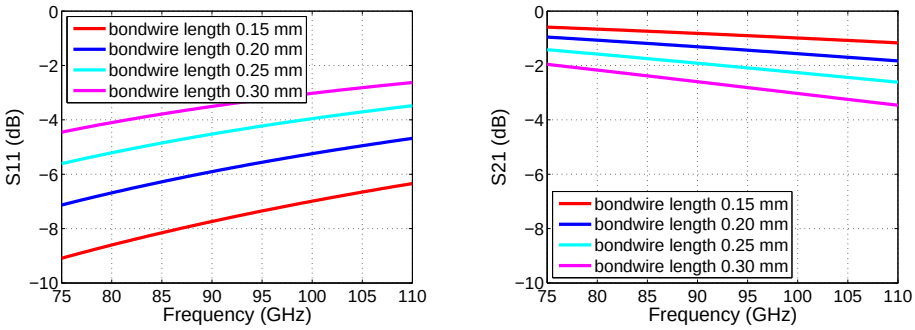

(a) (b)

Figure 3.27 – a) Simulated reflection and b) transmission coefficient of a bondwire connected to two matched ports. Different bondwire lengths have been considered.

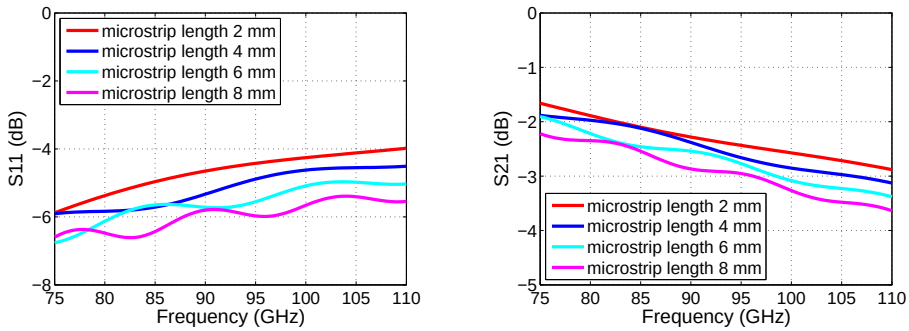

(a) (b)

Figure 3.28 – a) Simulated reflection and b) transmission coefficient of a microstrip line and a bondwire connected to two matched ports. A 0.25 mm long bondwire and different lengths of a 50 Ω microstrip line, from 2 to 8 mm, have been taken into account in the simulation.

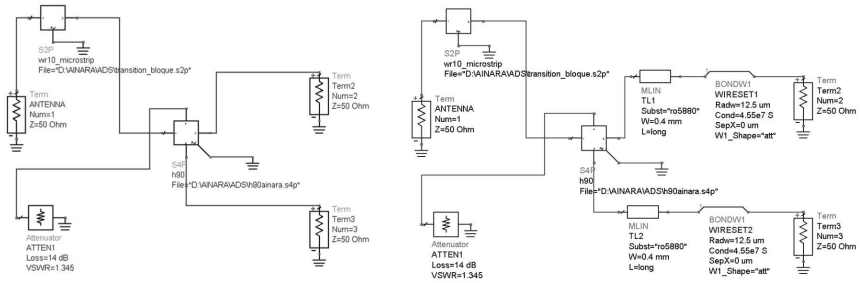

(a) (b)

Figure 3.29 – Schematic of the first components of the receiver considered in the following simulations of the reflection coefficient. a) With ideal connections and b) considering 4.173 mm long microstrip line and 0.25 mm long bondwires at the output ports of the input quadrature hybrid coupler of the receiver.

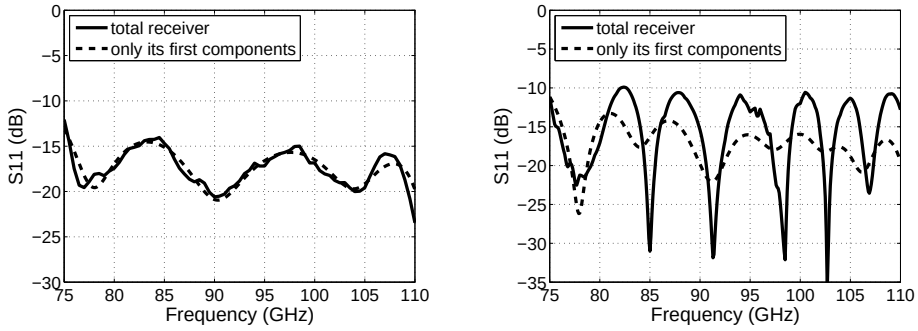

(a) (b)

Figure 3.30 – Comparison between the reflection coefficient of the total receiver and the reflection coefficient of the first components of the receiver, i.e. from input ports of the receiver to output ports of the input quadrature hybrid coupler. a) Considering ideal connections and b) taking into account 4.173 mm long microstrip lines and 0.25 mm long bondwires at the output ports of the input quadrature hybrid coupler of the receiver.

lengths are 4.173 mm and 0.25 mm respectively. The selected length corresponds to the length of these microstrip lines in the real implementation of the receiver. The comparison between reflection coefficients of this configuration and the total receiver is depicted in Fig. 3.30 b). As it is shown, the resonances of these two simulated parameters perfectly agree. Therefore, it is demonstrated that these bondwires produce reflections which create standing waves and the ripples shown in the receiver S11. This standing wave has a period which depends on the electrical length of the components placed before the bondwires.

In conclusion, the study of the effect of the bondwires demonstrates that the reflection coefficient of the total receiver is mainly affected by the standing wave created by the bondwires placed in the output ports of the input quadrature hybrid coupler. This is because the matching of the bondwires is penalised as their lengths increase. Therefore, these two bondwires should be as short as possible in practical realization of the receiver in order to obtain high sensitivity. However, their lengths will mainly depend on the distance between the microstrip lines and the low noise amplifiers.

3.5 Conclusions

This Chapter has reported the analysis of the receiver performance using the SW package Advanced Design System (ADS) by Keysight Technologies. This analysis has been carried out along the entire W-band. Firstly, the advantages of the receiver configuration, i.e. the reduction of the gain and noise imbalance effect of the amplifiers and the internal calibration of the system, have been demonstrated by means of an AC simulation taken into account ideal components. Next, the effect of each microstrip component and MMIC device has been discussed by simulation in terms of its impact on the noise figure, noise temperature, gain and reflection coefficient. Indeed, as Friis equation shows, the components which mainly contribute to the noise of the receiver are its first components, i.e. the WR10 waveguide to microstrip transition and the first quadrature hybrid and its input and output lines. It is therefore important to minimize these losses by using a low loss tangent substrate. The most critical part of the receiver has been demonstrated that it is the length of the gold wire bondings since standing waves are created due to reflections in the wire junctions. Specifically, lengths above 0.20 mm

drastically increase the receiver noise temperature, which imply a loss of sensitivity. Furthermore, these bondwires also deteriorate the input return losses and the gain of the receiver. In conclusion, the length of the bondwires have to be carefully considered in the assembly of the components of the W-band auto-calibrated receiver to obtain high sensitivity.

Chapter 4

Characterization of the planar components of the W-band receiver

4.1 Introduction

This Chapter presents the fabrication and measurement of the planar components of the W-band auto-calibrated receiver. These components are microstrip devices and MMIC components at W-band. Microstrip devices are built in 0.127 mm thick RO5880 substrate. Therefore, first of all, the characterization of this substrate at this frequency range, i.e. W-band, has been indispensable in order to validate these microstrip devices. This facilitates the comparison between simulated and experimental results of these components. Once the substrate has been characterized, the measurement of the planar devices can be carried out. However, the available measurement equipment is based on waveguide technology, which consists of two VDI W-band VNA extenders connected to the Agilent PNA-X E3861C Microwave Network Analyser. Therefore, the design of a WR10 waveguide to microstrip transition suitable to characterize planar components has been required. This transition is presented and validated in this Chapter. Next, the characterization of the planar devices of the W-band auto-calibrated receiver, such as the quadrature hybrid coupler and the commercial MMIC attenuator, are carried out using the proposed WR10 waveguide to microstrip transition.

Moreover, the experimental results of the commercial MMIC low noise amplifier, which are measured at W-band by the manufacturer before the delivery, are shown.

4.2 Characterization of dielectric substrates

Until now, the dielectric loss tangent of 0.127 mm thick RO5880 substrate considered for the design of the microstrip components of the W-band auto-calibrated receiver has been fixed to 0.01. As mentioned in Chapter 2, this value is higher than that given by the manufacturer, which is measured at 10 GHz. This Section discusses the measurements carried out in order to determine this value in W-band.

Both the dielectric constant and loss tangent of this and other potentially low loss substrate in this frequency band have been retrieved following the procedure described in [149] starting from their transmittance. In order to measure the transmission coefficient of the substrates under study, two different set-ups have been implemented.

First of all, the problem and its required assumptions are described. Secondly, the problem has been simplified taking into account thin samples because the thickness of our interest are smaller than the working wavelength. Next, the set-ups and the measurement results of two different substrates are explained and shown.

4.2.1 Complex transmission coefficient

The general schematic of the set-up considered to measure the transmission of dielectric substrates can be seen in Fig. 4.1. It consists of a sample of thickness d, which is referred as medium 2 in the Figure, placed between two media, i.e. 1 and 3. The incident beam is supposed to be a plane wave which goes through the sample from medium 1 to 3 at a normal incidence. Note that in our case, both media 1 and 3 are air.

In order to retrieve the material properties, the normalised transmission coefficient of dielectric substrates has to be obtain. This implies the measurement of the transmission coefficient without the sample, i.e. the reference, and with the substrate sample. Moreover, the retrieval of the dielectric constant and loss tangent of these samples from the transmission is feasible taking into account the following assumptions:

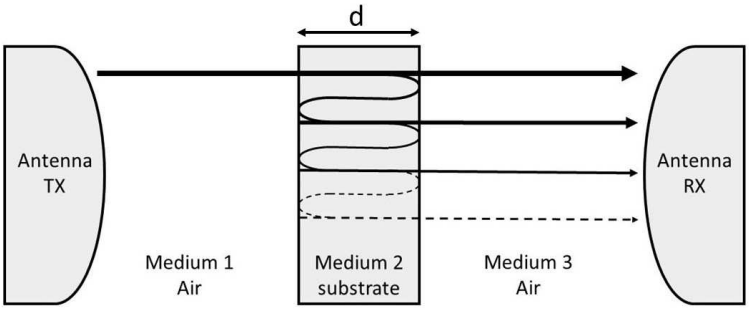

Figure 4.1 – Schematic of the set-up considered to measure the transmission of dielectric substrates.

- The sample is an homogeneous slab with parallel and flat faces.
- Both the sample and medium 1 and 3 are magnetically isotropic without surface charges.
- The electromagnetic response of the three media is linear.
- The polarization of the incident beam is linear and parallel to the surface of the sample.

With these assumptions, the following expression for the spectral component at angular frequency ω of the electric field of the plane wave transmitted through the sample is obtained as:

$$S_{sample}(\omega) = \eta(\omega)T_{12}(\omega)P_2(\omega,d)T_{23}(\omega)FP(\omega)E(\omega) \tag{4.1}$$

where E(ω) is the electric field of the plane wave emitted by the transmitting antenna, $T_{ab}(\omega) = \dfrac{2\widetilde{n}_a}{\widetilde{n}_a + \widetilde{n}_b}$ corresponds to the transmission coefficient from medium a to b, and $P_2(\omega,d) = exp\left[-j\dfrac{\widetilde{n}_2\omega d}{c}\right]$ is the propagation coefficient in the sample over a distance d. In these expressions, $\widetilde{n}_a = n_a - j\kappa_a$ stands for the complex refractive index of medium a which depends on the angular frequency ω. The reflection, transmission and propagation coefficients in medium 1 and 3 are included in the term $\eta(\omega)$. The backward and forward reflections in the sample, i.e. Fabry-Perot effect, are represented by FP(ω):

$$FP(\omega) = \sum_{k=0}^{+\infty} \left\{ R_{23}(\omega) P_2^2(\omega, d) R_{21}(\omega) \right\}^{\kappa} \tag{4.2}$$

in which $R_{23}(\omega) = \dfrac{\widetilde{n}_2 - \widetilde{n}_3}{\widetilde{n}_2 + \widetilde{n}_3}$ and $R_{21}(\omega) = \dfrac{\widetilde{n}_2 - \widetilde{n}_1}{\widetilde{n}_2 + \widetilde{n}_1}$ correspond to the reflection coefficient at the 2 - 3 and 2 - 1 interfaces respectively.

The spectral component of the electric field of the plane wave transmitted without the sample, i.e. the reference, is given by:

$$S_{reference}(\omega) = \eta(\omega) P_{air}(\omega, d) E(\omega) \tag{4.3}$$

Therefore, the complex transmission coefficient $T(\omega)$ of the sample can be obtained by dividing $S_{sample}(\omega)$ by $S_{reference}(\omega)$.

$$\begin{aligned} T(\omega) &= \frac{S_{sample}(\omega)}{S_{reference}(\omega)} \\ &= \frac{T_{12}(\omega) P_2(\omega, d) T_{23}(\omega) FP(\omega)}{P_{air}(\omega, d)} \\ &= \frac{4\widetilde{n}_2}{(\widetilde{n}_2 + 1)^2} exp\left[-j(\widetilde{n}_2 - 1)\frac{\omega d}{c} \right] FP(\omega) \end{aligned} \tag{4.4}$$

with $FP(\omega) = \dfrac{1}{1 - \left(\dfrac{\widetilde{n}_2 - 1}{\widetilde{n}_2 + 1} \right)^2 exp\left[-2j\widetilde{n}_2 \dfrac{\omega d}{c} \right]}$. As can be seen, the complex transmission coefficient depends on the complex refractive index of the sample, i.e. $\widetilde{n}_2 = n_2 - j\kappa_2$ and on the sample thickness, d.

4.2.2 Characterizing thin samples

The consideration of the Fabry-Perot effects in the complex transmission coefficient is indispensable when thin samples are taken into account due to multiple reflections in the substrate are superposed. The thickness of these thin samples is comparable with the working wavelength.

The retrieval procedure consists of numerically adjusting the theoretical solution to the experimental data. This is done for each frequency. The starting point of the numerical solution comes from the very low reflection assumption, so that:

$$n_2 \cong 1 - \frac{arg\left(T_{measured}(\omega)\right)}{\omega d/c} \tag{4.5}$$

$$\kappa_2 \cong \frac{ln \mid T_{measured}(\omega) \mid}{\omega d/c} \tag{4.6}$$

The starting value of n_2 has been obtained from the phase of the complex transmission assuming no Fabry Perot effect. On the other hand, κ_2 is mainly dependent on the attenuation of the complex transmission coefficient. To obtain the Equation 4.6, κ_2 has been considered small enough to measured a transmission signal, which is our case. The substrates we want to characterize are low loss dielectrics.

For materials with high absorption, the measurement of the reflection coefficient is more suitable. Other retrieval methods extract the material properties from both the reflection and transmission coefficients of a planar substrate sample. An example of these methods are those based on the Nicolson-Ross-Weir (NRW) technique [150]- [153]. However, these methods can not be considered here due to two main problems caused by the measurement of the reflection coefficient. First, the difficulty of determining the reference plane of the reflection coefficient which has to correspond to the surface of the substrate sample. The other problem is caused by the low level of reflection coefficient measured in low loss dielectrics. In particular, the added noise in the reflection coefficient produced by the network analyser makes the extraction of the material properties almost impossible.

Following the retrieval method from the transmittance, the dielectric constant and the loss tangent of a non-magnetic and low loss substrate are related to its complex refractive index by means of $\widetilde{n}^2 = \widetilde{\epsilon}_r$, in which $\widetilde{\epsilon}_r = \epsilon_1 - j\epsilon_2$ corresponds to the complex relative permittivity of the substrate. Its real part is the dielectric constant and it is related to the store energy within the sample. It can be calculated as $\epsilon_1 = n_2^2 - \kappa_2^2$. The imaginary part of the relative permittivity is related to the dissipation of the energy in the sample and it can be calculated as $\epsilon_2 = 2n\kappa$. Therefore, the dielectric loss tangent of the substrate is $tan\delta = \dfrac{\epsilon_2}{\epsilon_1} = \dfrac{2n\kappa}{n_2^2 - \kappa_2^2}$.

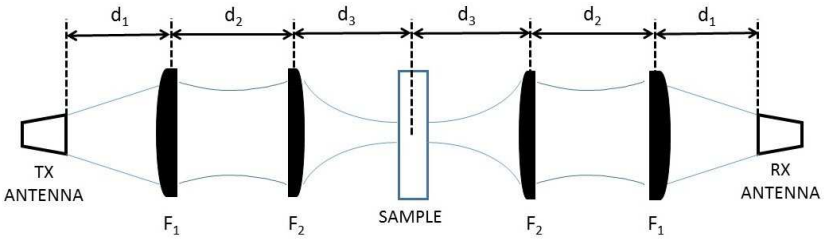

(a)

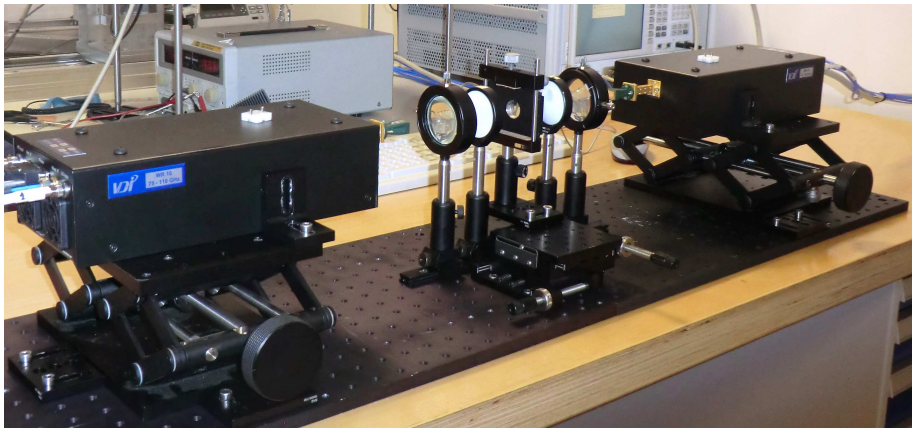

(b)

Figure 4.2 – a) Schematic and b) photograph of the quasioptical set-up based on lenses used to measure the transmission coefficient of substrate samples.

4.2.3 Measurement set-ups

In order to measure the transmission coefficient of thin substrate samples at W-band, two different set-ups have been implemented. Both measurement set-ups are far field configurations based on a quasioptical system. In the first one, the radiation beam is focused on the sample by lenses [154], [155]. On the other hand, the focusing method in the second set-up consists of a mirror system in which a plane wave impinges on the sample at normal incidence. In both systems the W-band signal is transmitted and received by two horn antennas, which are connected to two W-band VDI VNA extenders of the Agilent PNA-X E3861C Microwave Network Analyser.

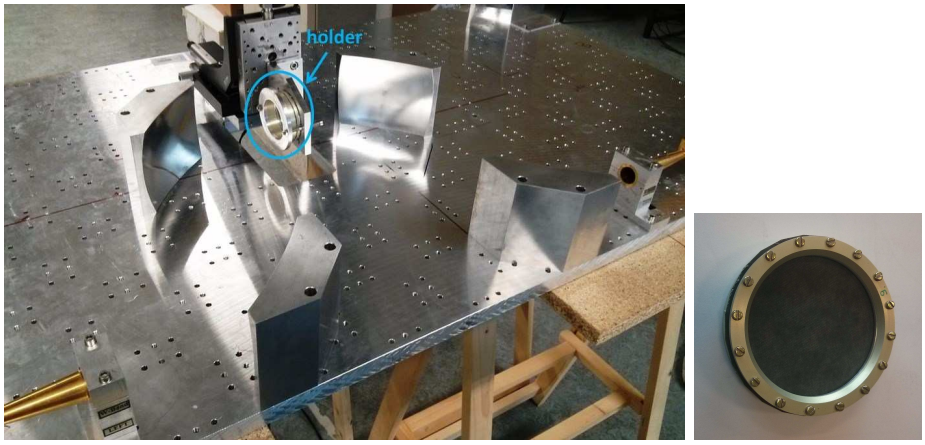

(a) (b)

Figure 4.3 – a) Photograph of the considered mirror system in order to measure the transmission coefficient of a substrate sample. b) A 0.127 mm thick RO5880 substrate sample placed into the holder. It is required to measure the substrate in this set-up.

4.2.3.1 Set-up based on lenses

The schematic of the first considered set-up can be seen in Fig. 4.2 a). The lenses included in this system are two different pairs of plano-convex lenses [155]. The beam waist diameter of this set-up in the sample position is theoretically 7 mm at W-band.

A photograph of this set-up is shown in Figure 4.2 b). The alignment of the elements must be carefully ensured. Thus, optical holders have been used to assemble the system.

4.2.3.2 Set-up based on mirrors

The second considered set-up is a quasioptical bench based on mirrors, as shown in Fig. 4.3 a). The expansion of the Gaussian beam generated by a corrugated horn antenna is controlled by four ellipsoidal mirrors. As a result, a plane wave impinges on the sample at normal incidence. The distance between mirrors is 28 cm. The distance between the phase center of the antenna and the first mirror, and also, between the sample and mirrors is 14 cm. In this

case, the beam waist diameter in the sample position is approximately 35 mm. Therefore, in order to ensure the sample flatness, it has to be placed into a holder, which has a diameter of 65 mm, see Fig. 4.3 b). It is larger than the beam waist in order to minimize diffraction. The only moving part in this set-up is the piece which attaches the holder.

4.2.4 Experimental results

As mentioned before, the values of the dielectric constant and loss tangent of the 0.127 mm thick RO5880 substrate given by the manufacturer are not demonstrated to be accurate at higher frequencies. Therefore, the RO5880 substrate has been characterized in these two measurement set-ups. Moreover, another low loss dielectric has been measured. This substrate is the Cyclic Olefin Copolymer (COC) manufactured by Topas Advanced Polymers [156]. It has been recently used to design a Sub-Harmonic Mixer at millimeter wave frequencies in [157] taking advantage of its low dissipation factor. Moreover, it is interesting because its dielectric constant, which is similar to that of RO5880 substrate, and loss tangent have been measured in the mentioned article using the Teraview Spectra 3000 TDS system [158]. These measured parameters are constant from 400 GHz to 1 THz, and their values are 2.34 and 0.002 respectively. At lower frequencies, the Teraview Spectra 3000 does not have enough dynamic range to accurately characterize the material. However, these results can help us to validate our characterization method at W-band.

Therefore, different thicknesses of both substrates, i.e. RO5880 and COC, have been characterized with the quasioptical set-ups.

4.2.4.1 Set-up based on lenses

With the first set-up, which consists of lenses, two different thicknesses of RO5880 and COC have been characterized: 0.127 and 0.797 mm for RO5880 substrate and 0.100 and 0.152 mm for COC substrate. The magnitude and phase of the measured transmittance of different thickness of RO5880 and COC substrates can be seen in Fig. 4.4. Some measurements have been done for each material and thickness in different days. However, the two measured transmittances which differ most are shown in the Figure for each thickness of dielectric substrate. As can be seen, the differences are larger in magnitude than in phase. Although the thicknesses of these substrates are different, we can roughly compare the results for the 0.100 mm thick COC substrate to

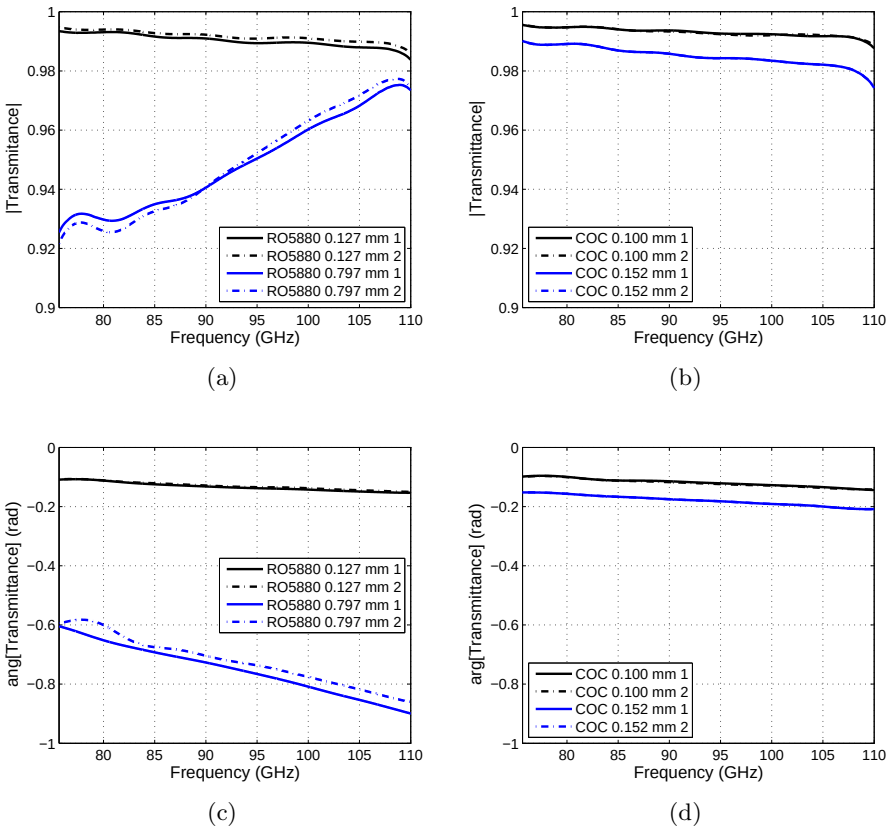

Figure 4.4 – a) and b) Magnitude of the measured transmittances of different thickness of RO5880 and COC substrates respectively. c) and d) Phase of the measured transmittances of different thickness of RO5880 and COC substrates respectively. The measurements have been obtained using the quasioptical set-up based on lenses.

the 0.127 mm thick RO5880 substrate. As can be seen, this COC substrate has higher transmittance than the RO5880 substrate. Therefore, given the fact that both have similar permittivity, the expected dielectric loss tangent of COC is smaller.

These results have been processed with the extraction method explained in previous Subsections. Fig. 4.5 shows the resulting dielectric constant and

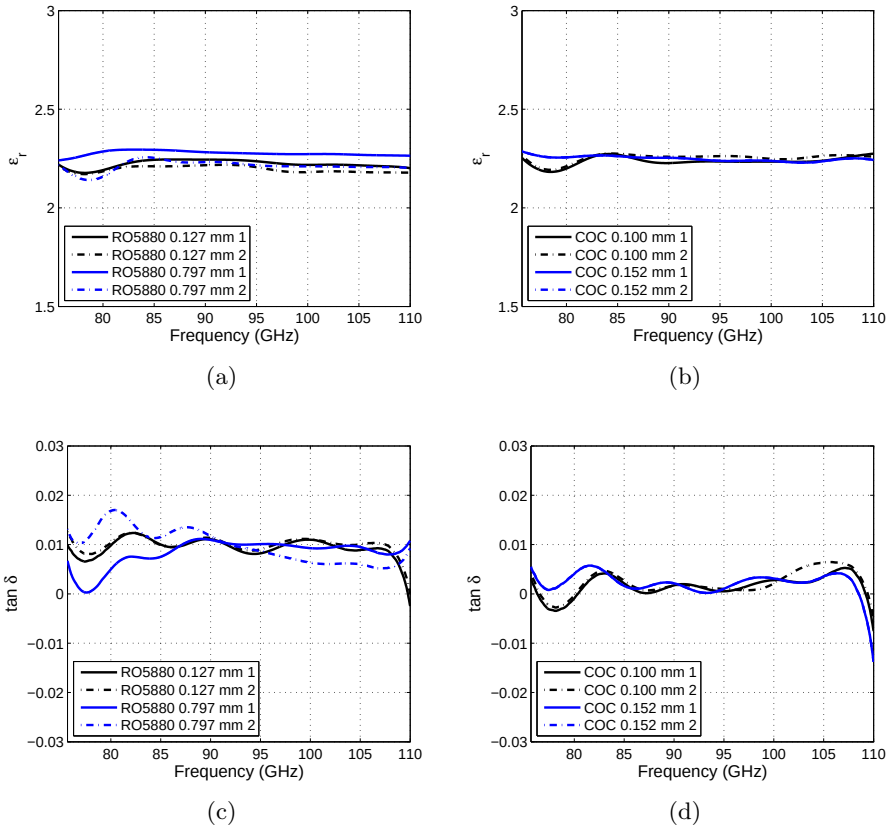

Figure 4.5 – a) and b) Retrieved dielectric constant of different thickness of RO5880 and COC substrates respectively. c) and d) Retrieved dielectric loss tangent of different thickness of RO5880 and COC substrates respectively. The measurements have been obtained using the quasioptical set-up based on lenses.

loss tangent of the different thickness RO5880 and COC substrates. As can be seen, the retrieved dielectric properties from the two measurements of each thickness, i.e. the two most differ measured transmittances, have been depicted in this Figure. The calculated dielectric constant of RO5880 and COC substrates at W-band are approximately 2.22 and 2.25 respectively. Moreover, the results show that the loss tangent of the COC substrate is smaller than that of the RO5880 substrate, as expected. Their values are approximately 0.002 for COC substrate and 0.01 for RO5880 substrate at the central part of the W-band. Note that some values in the limits of the W-band are negative because they are affected by the time gating applied in the measurements. This time gating effect can be also seen in the measured transmittances shown in Fig. 4.4. These retrieved values are identical for different thicknesses of the same substrate. In addition, the obtained loss tangent of the COC substrate agrees well with the measured value given in [157]. Therefore, the retrieval method and also the measurement set-up have been validated.

4.2.4.2 Set-up based on mirrors

With the second set-up, different thicknesses of RO5880 have been characterized. COC substrate can not be measured due to its cracking when it is placed into the holder. The substrate needs to be drilled in order to tighten the screws which fit the two pieces of the holder. The considered thicknesses of COC substrates are thin and fragile and when drilled cracks.

As in the set-up based on lenses, some measurements have been done for each substrate thickness in different days. Fig. 4.6 shows an example of the measured transmittance of three different thicknesses of RO5880. Note that the measurements in the limits of the W-band are affected by the applied time gating. In addition, the measurement results present an standing wave in the module of the transmittance. This standing wave has the same period in the measured transmittances of different thicknesses of RO5880 substrate. This implies that it is produced by the measurement set-up. In particular, it is generated by a reflection between the closest mirror of the sample and the holder. Since the reference is measured without the holder, when it is manually placed, a misalignment can create a reflection because the holder is wide enough to affect the transmission beam.

The extracted dielectric constant and loss tangent for these measured transmittances are shown in Fig. 4.7 a) and b). As can be seen, the retrieved

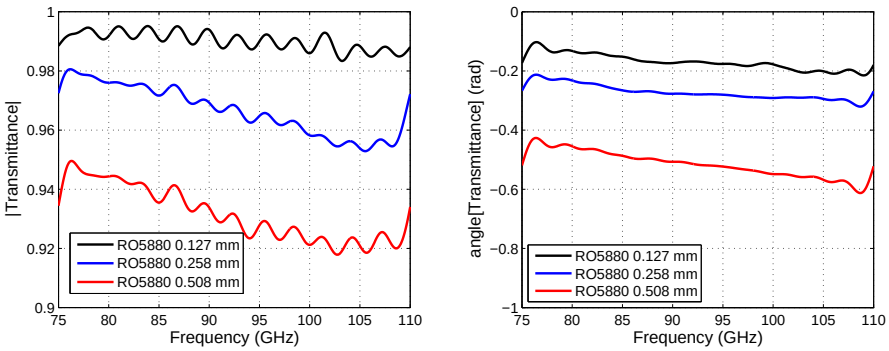

(a) (b)

Figure 4.6 – a) Magnitude and b) phase of the measured transmittance of different thicknesses of RO5880 substrate. The measurement has been obtained using the quasioptical set-up based on mirrors.

dielectric loss tangents fluctuate greatly due to problems in the measurement. Indeed, the dielectric loss tangent depends mainly on the magnitude of the measured transmission in which the standing wave appears. Therefore, this standing wave also appears in the calculated dielectric loss tangents and it makes the estimation of its value impossible. Conversely, the retrieved dielectric constants of different thicknesses of RO5880 are in good agreement.

The position of the holder was improved in a second measurement in order to minimize its reflections and to ensure a normal incidence of the transmitted plane wave. The retrieved dielectric constant and loss tangent of different thicknesses of RO5880 are shown in Fig. 4.7 c) and d). As in the previous measurements, the values in the limits of the W-band are affected by the applied time gating. The dielectric constants are around 2.22, which is the same value obtained with the set-up based on lenses. With respect to the loss tangents, see Fig. 4.7 d), their values are around 0.01. However, the standing wave is also created in these measurements. Moreover, when the thickness of the RO5880 substrate decreases, the retrieved values fluctuate more. The reason is that this substrate is more flexible as the thickness decreases, and when it is placed into the holder, it is bent and the impinging of the plane wave at a normal incidence is not ensured.

In conclusion, this set-up and its holder have to be improved in order to

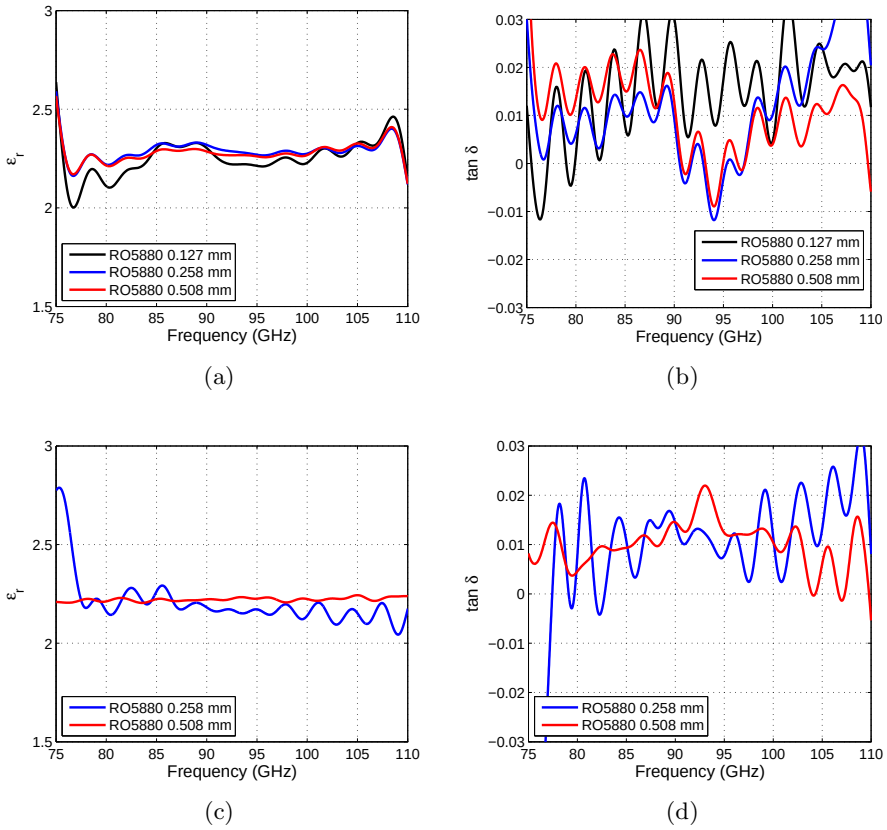

Figure 4.7 – Retrieved dielectric constant and loss tangent of different thicknesses of RO5880 substrate. The calculation has been done from the measured transmittance using the quasioptical set-up based on mirrors. a) and b) correspond to a first measurement and c) and d) correspond to a second measurement improving the position of the holder.

obtain accurate transmittance measurements. Some diffraction effects have to be removed and the placement of thin flexible substrates into the holder have to be improved. For these reasons, the first set-up based on lenses is more appropriate for these measurements. Moreover, the viability of the first set-up has been demonstrated by the calculation of the dielectric constant and loss tangent of the COC substrate. Their obtained values are close to those measured at 400 GHz in [157]. The beam waist of the set-up based on lenses is smaller and it facilitates the alignment, the incidence of the plane wave on the substrate sample and it minimizes the diffraction problems. The real values of the dielectric constant and also the considered loss tangent of RO5880 substrate in our designs have been experimentally validated at W-band. These values are 2.2 and 0.01 respectively.

4.3 Full W-band WR10 – μStrip inline transition

The available measurement equipment to characterize the planar devices of the W-band auto-calibrated receiver is based on waveguide technology. This waveguide based equipment at W-band consists of two VDI W-band VNA extenders connected to the Agilent PNA-X E3861C Microwave Network Analyser. Therefore, first of all, the design of a suitable WR10 waveguide to microstrip transition is required. This transition is presented and validated in this Section.

The design of a broadband microstrip to waveguide transition with low losses is indispensable in order to characterize the planar components of the W-band auto-calibrated receiver with this waveguide based measurement equipment and also, to be able to combine integrated circuits with waveguide components such as horn antennas. Other requirements to take into account are reduced size, simple design, easy alignment and manufacture which facilitate the repeatability of the assembly.

Several configurations of microstrip to waveguide transitions have been previously proposed depending on the field propagation direction both in the microstrip and in the waveguide. The most popular type of microstrip to waveguide transition is that in which the field propagation direction of the microstrip is transverse in relation to the waveguide. Normally, this transition consists of a probe placed in the E-plane of the waveguide [146]- [148]. This probe is an extension of the microstrip which is introduced in the waveguide

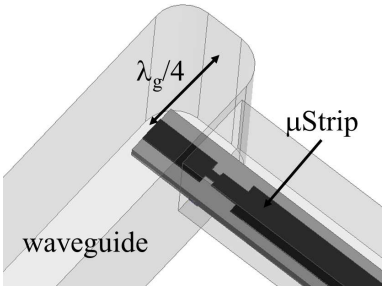

Figure 4.8 – Microstrip to waveguide transition based on a E-plane probe.

through a small aperture in the broad wall, see Fig. 4.8.

This E-plane probe is placed at a distance of a quarter guided wavelength, i.e. $\lambda_g/4$, with respect to the waveguide short. The bandwidth of this transition is improved by a multi-section matching transformer. In particular, some transitions of this type have been presented operating in the full W-band such as those proposed in [147] and [148] obtaining experimentally good return and insertion losses, whose values at 92.5 GHz are 1.15 dB and 0.6 dB respectively. However, the transition presented in [148] has a complicated design since the optimization of up to 15 parameters is required. Despite their good performance, these transitions have two main drawbacks. The first one is that the microstrip circuit requires to be welded to ensure the electrical connection between the waveguide and the microstrip, which complicates the repeatability. The second one is that the input port is usually perpendicular to the output port. This fact can make characterization of devices or antennas a cumbersome task, since additional bent sections must be added. This last problem is common to other type of transitions based on radiating elements such as quasi-Yagi antenna [159] and slotline antenna [160].

An alternative to couple the TE_{10} waveguide mode and the quasi-TEM microstrip mode is the use of an inline configuration in which the field propagation direction in the waveguide is the same as in the microstrip. Matching sections are used to optimize the transition both in the microstrip line and in the waveguide. For example, the stepped ridged waveguide [161], [162] uses a matching section in the waveguide part whereas in the radial-shaped probe [163] the matching section is made on the microstrip. Other possibilities are presented in [164] and [165] where matching sections in both media are considered. The first one obtains measured insertion loss of

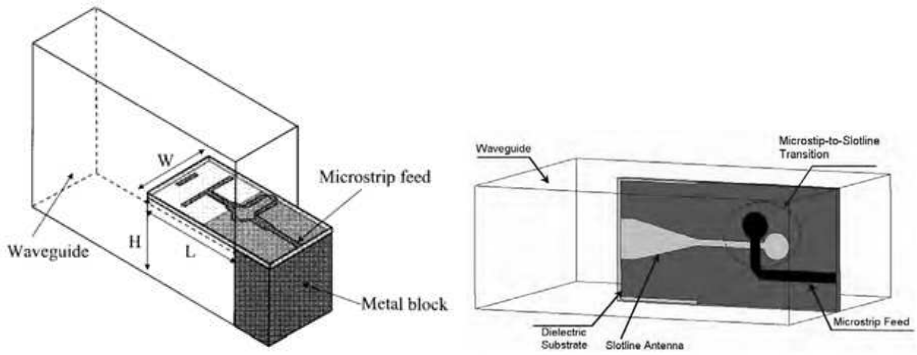

(a) (b)

Figure 4.9 – Microstrip to waveguide transitions based on radiating elements such as a) quasi-Yagi antenna and b) slotline antenna.

1.1 dB in a 2 GHz bandwidth around 9 GHz whereas the last one works in a 6 GHz bandwidth around 77 GHz obtaining an insertion loss of 1 dB at this frequency.

In this Section, an inline microstrip to waveguide transition operating in the full W-Band is presented and validated experimentally. This transition provides some improvements with respect to [164]. First, in terms of performance, its bandwidth has been broadened so that it covers the full W-band. Moreover, it features better return loss and lower insertion losses along the entire operating band. In addition, its manufacturing is simpler, since the bottom lid is flat, and does not require any additional machining, which can be cumbersome for W-band and even higher frequencies. Furthermore, a thick ground plane is not needed to ensure the placement of the microstrip circuit inside the waveguide transition. In conclusion, this proposed transition has better performance, easier manufacture, alignment and assembly than the low frequency version described in [164]. Also, note that the proposed transition, in contrast to other inline designs that feature full band performance [166], is a simpler design which does not use any soldering and that does not require a ridge waveguide section, which can be difficult to manufacture for W-band frequencies and above. These advantages avoid long assembly times and facilitate the repeatability. Therefore, the proposed inline transition is suitable for characterization of multiple devices built in planar

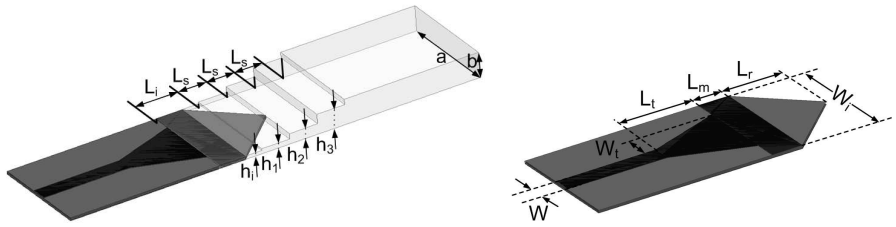

(a) (b)

Figure 4.10 – The proposed inline microstrip to waveguide transition covering the full W-band and its main parameters; a) Schematic of the complete transition. b) Schematic of the microstrip section.

technology with waveguide based measurement equipment as in our case.

4.3.1 Design of the WR10 microstrip to waveguide transition

The proposed microstrip to waveguide transition operating in the full W-band can be seen in Fig. 4.10. It couples progressively the quasi-TEM mode of the microstrip line with the TE_{10} mode of the rectangular waveguide by means of a broadband inline configuration.

The inline microstrip to waveguide transition consists of two parts:

- Transition from 50 Ω microstrip line to dielectric-filled rectangular waveguide, see Fig. 4.10 b). It is built in 0.127 mm thick Rogers RT/Duroid 5880 ($\epsilon_r = 2.2$ and $tan\delta = 0.01$ as experimentally measured at W-band). The height of the dielectric-filled rectangular waveguide corresponds with the thickness of the substrate and the width is 2.54 mm, the same as the standard WR10 rectangular waveguide. A linear microstrip taper of length L_t is used in order to achieve broadband and low loss impedance matching.

- Transition from dielectric-filled rectangular waveguide to standard WR10 rectangular waveguide. As can be seen in Fig. 4.10 a), the substrate is gradually removed between the dielectric-filled and the air-filled rectangular waveguide in order to reduce the return loss. Moreover, a multisection Chebychev waveguide transformer is used to match the 0.127 mm height rectangular waveguide with the 1.27 mm height

Table 4.1 – Dimensions (mm) of the proposed WR10 waveguide to microstrip transition.

a	b	W	W_i	W_t	h_i	h_1
2.54	1.27	0.40	2.54	0.60	0.16	0.25
h_2	h_3	L_i	L_t	L_s	L_m	L_r
0.52	1.00	1.15	1.70	0.75	0.70	1.40

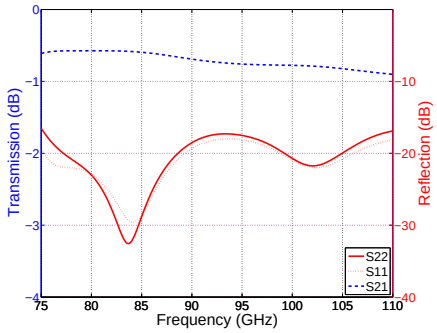

Figure 4.11 – Simulated S parameters of the proposed inline microstrip to waveguide transition over the W-Band.

standard WR10. Three $\lambda_g/4$ (quarter guided wavelength) sections are implemented to obtain return loss above 15 dB over the full W-band.

Table 4.1 shows the dimensions of the designed WR10 waveguide to microstrip transition. The definition of the different parameters are presented in Fig. 4.10. Note that only those parameters in grey are used in the optimization. The rest of them correspond to the input and output microstrip and rectangular waveguides.

The simulated performance of this microstrip to waveguide transition are shown in Fig. 4.11. The reflection coefficient is below −15 dB along the entire W-Band. With respect to the transmission, at the central frequency of the W-band, i.e. 92.5 GHz, the insertion loss is 0.73 dB being better than 0.9 dB in the whole frequency band.

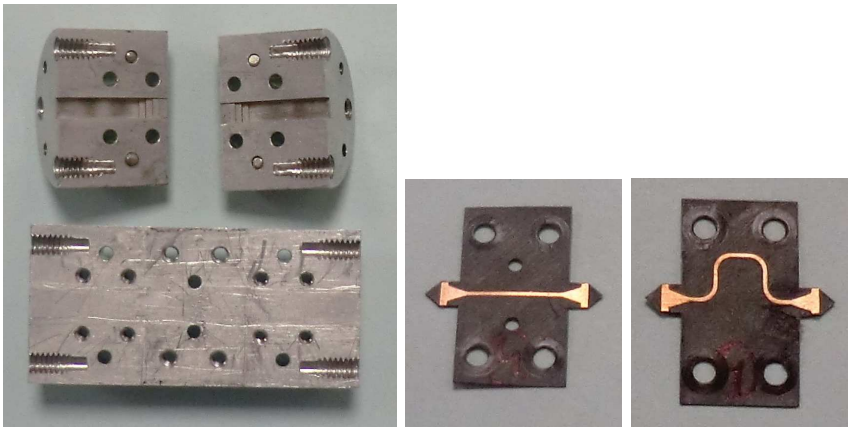

(a) (b) (c)

Figure 4.12 – Photographs of the manufactured inline microstrip to waveguide transition for a back-to-back measurement at W-band; a) waveguide block b) 8.6 mm long microstrip section c) 15 mm long microstrip section.

4.3.2 Manufacturing of the WR10 microstrip to waveguide transition

A back-to-back transition has been manufactured in order to characterize it with the available measurement equipment. Fig. 4.12 shows photographs of the manufactured prototype:

- The back-to-back aluminium waveguide transition was manufactured by a high-precision milling tool. This structure can be seen in Fig. 4.12 a). It contains two standard WR10 flanges in order to connect it with waveguide based measurement equipment. The block has been split at the lower edge of the waveguide along the H-plane in order to facilitate the assembly. The two parts of each waveguide transition are fitted by four M1.6 metal screws and their alignment is ensured by two dowel pins.

- The second part contains two microstrip transitions connected by a 50 Ω microstrip line built in 0.127 mm thick RO5880 substrate. Two different microstrip lengths, i.e. 8.6 mm and 15 mm (see Fig. 4.12 b) and c)), have been manufactured in order to validate the designed transition and also the dielectric losses of the substrate. These parts have been

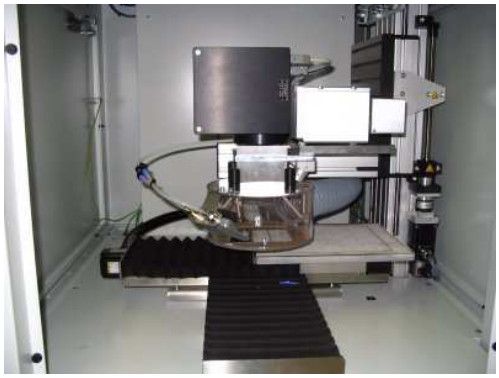

Figure 4.13 – Photograph of the working area of the LPKF Protolaser 200 machine.

manufactured by a LPKF ProtoLaser 200 micromachining system, see Fig. 4.13. This machine has a 50 μm resolution. Thus, no problem is presented in the manufacture of these circuits on a 0.127 mm thick RO5880 laminate with 17 μm thick copper cladding on both sides.

The alignment of the microstrip part with respect to the waveguide is ensured by the placement of four plastic screws and two dowel pins, see Fig. 4.17.

Manufacturing tolerances

Any manufacturing method includes a discrepancy between the dimensions of the design and the dimensions of the prototype. These tolerances can penalize the performance of the proposed transition. Therefore, it is important to analyse them. Thus, two manufacturing errors have been studied. On the one hand, the effect of air gaps between the dielectric and the side metal walls of the waveguide. On the other hand, the effect of air gaps between the metal of the microstrip and the top and bottom walls of the waveguide. This error causes the loss of the metal-to-metal contact in the transition.

Regarding the air gaps between the dielectric and the side walls of the waveguide, a manufacturing error in the cut of the microstrip substrate by the laser micromachining system has been considered. The tolerances in the side walls dimensions of the waveguide are much smaller because of the milling tool

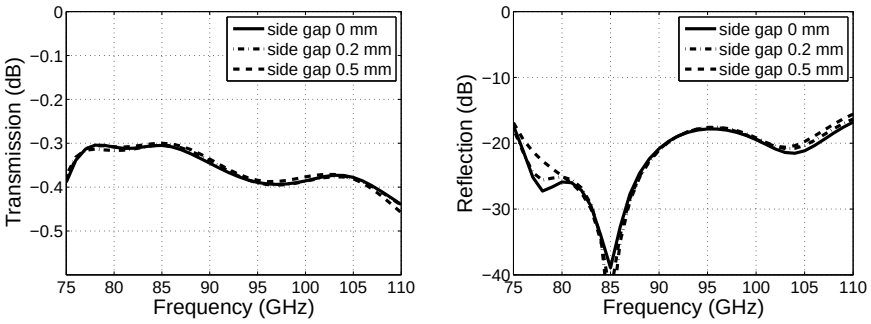

(a) (b)

Figure 4.14 – S-parameters of the proposed transition taking into account air gaps between the dielectric and the side walls of the waveguide due to the cutting error of the microstrip substrate; a) transmission and b) reflection coefficients.

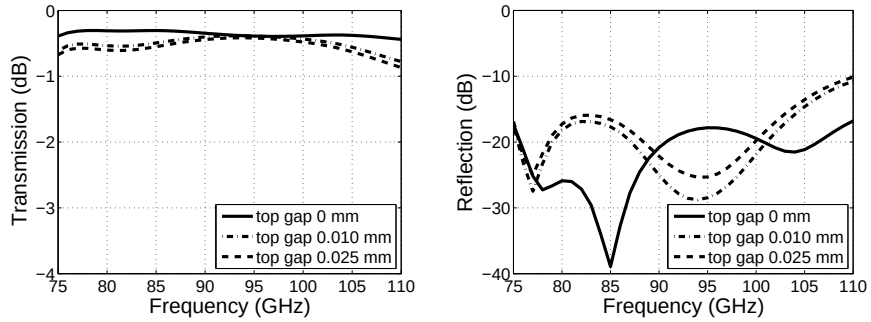

(a) (b)

Figure 4.15 – S-parameters of the proposed transition taking into account an air gap between the top metal of the microstrip and the top wall of the waveguide due to the manufacturing error of the waveguide block; a) transmission and b) reflection coefficients.

process. As can be seen in Fig. 4.14, the good performance of the transition is kept up to at least 0.5 mm side air gaps, significantly larger than the error of the cutting method of the microstrip circuit.

With respect to manufacturing tolerances in the aluminium waveguide block, an air gap between the top metal of the microstrip circuit and the top

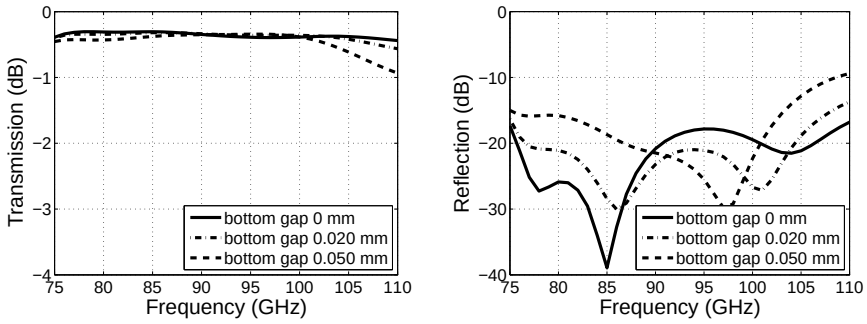

(a) (b)

Figure 4.16 – S-parameters of the proposed transition taking into account an air gap between the ground plane of the microstrip and the bottom wall of the waveguide; a) transmission and b) reflection coefficients.

wall of the waveguide can exist. It decreases the operating bandwidth of the transition and increases the insertion losses when this air gap is larger than 0.025 mm, see Fig. 4.15. However, the error provided by the high-precision micromachining of the waveguide part is smaller than 0.010 mm. Therefore, this tolerance might penalise the insertion losses but the transition continues working along the entire W-band.

Finally, Fig. 4.16 demonstrates that the existence of an air gap between the ground plane of the microstrip and the bottom wall of the waveguide has the same effect as air gaps in the top part. In this case, the operating bandwidth of the transition does not cover the full W-band when the air gap in the bottom part is larger than 0.05 mm.

In conclusion, the most critical error in the transition performance is the possibility of an air gap between the ground plane of the microstrip and the bottom wall of the waveguide. However, it requires air gaps larger than 0.05 mm which are very unlikely to happen if the parts of the transition are properly tightened during assembly.

4.3.3 Experimental results

Fig. 4.17 shows the S parameters measurement set-up of the manufactured back-to-back microstrip to waveguide inline transition. The manufactured block is connected to two VDI W-band VNA extenders.

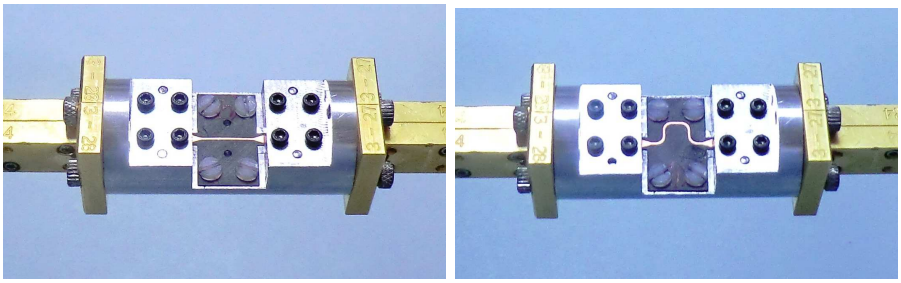

(a) (b)

Figure 4.17 – Photograph of the back-to-back inline transition prototype connected by a; a) 8.6 mm long and b) 15 mm long 50 Ω microstrip line.

The measured reflection coefficients of the 8.6 mm and 15 mm long 50 Ω microstrip sections are shown in Fig. 4.18 a) and b) respectively. Note that the reflection coefficient of each single transition is different since the manufacturing errors both in the microstrip section and in the metal block are different. However, the measured return losses are better than 15 dB in almost the entire W-band. Moreover, good agreement between simulations and measurements has been obtained.

The transmission coefficients depicted in Fig. 4.19 show that the experimental insertion losses of the manufactured microstrip circuits with two different lengths agree well with the simulations. In particular, the measured insertion losses of the 8.6 mm long 50 Ω microstrip line are 2.34 dB at 92.5 GHz and below 3 dB in the full W-band. Note that, theoretically, the dielectric losses of the 50 Ω microstrip line are 0.11 dB/mm [102] at 92.5 GHz because of the measured dielectric loss tangent of the RO5880 substrate at W-band, i.e. 0.01. Thus, the predicted dielectric loss at 92.5 GHz in this microstrip circuit is 0.88 dB. Therefore, the obtained insertion loss of a single transition can be estimated as 0.73 dB at 92.5 GHz and below 1.1 dB in the full W-band. These values are consistent with the simulations shown in Section 4.3.1.

In the 15 mm long microstrip circuit the agreement is also good, the losses in each transition can be determined taking into account the additional radiation losses produced by the 90^o bends. In conclusion, good agreement between the simulations and the experimental results has been obtained in the full W-Band for the proposed microstrip to waveguide inline transition.

Table 4.2 shows the state-of-the-art of microstrip to waveguide transitions

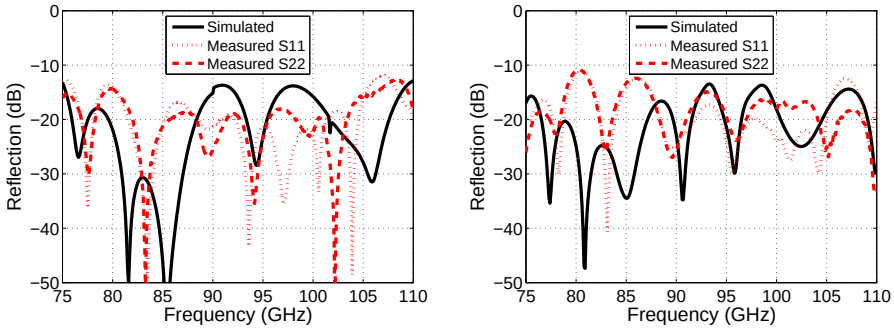

(a) (b)

Figure 4.18 – Comparison between simulated and measured reflection coefficients of the back-to-back inline transition connected by a) 8.6 mm and b) 15 mm long microstrip line.

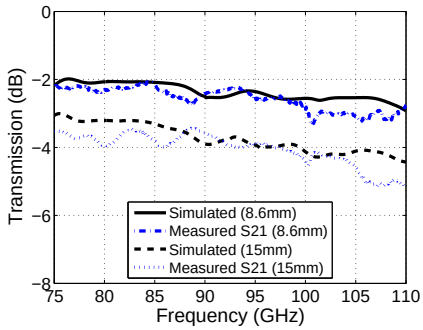

Figure 4.19 – Comparison between simulated and measured transmission coefficients of the back-to-back inline transition for the manufactured microstrip circuits with two different lengths.

Table 4.2 – Comparison between the proposed microstrip to waveguide transitions operating in the full W-band.

Reference	Insertion Losses		Dielectric Substrate (thickness)
	92.5 GHz	Full W-band	
[146]	1.15 dB	1.15 dB	Alumina (0.100 mm)
[148]	0.6 dB	1 dB	RO5880 (0.127 mm)
This work	0.73 dB	1.1 dB	RO5880 (0.127 mm)

operating in the full W-band. The proposed configuration shows similar performance than previous results. Therefore, this transition is suitable for characterization of multiple devices built in planar technology with waveguide based measurement equipment. In particular, this transition will be used in the measurement of some planar components which are part of the W-band auto-calibrated receiver such as the quadrature hybrid coupler and the MMIC attenuator.

4.4 Characterization of the planar devices of the W-band receiver

The designed WR10 waveguide to microstrip transition has been used to characterize the quadrature hybrid coupler and the MMIC attenuator of the W-band auto-calibrated receiver with the available waveguide based measurement equipment. Conversely, the commercial LN4-110 MMIC low noise amplifier has been measured by the manufacturer at W-band. These results are shown in this Section.

4.4.1 W-band quadrature hybrid coupler

Since the quadrature hybrid coupler is a 4-port device, four WR10 waveguide to microstrip transitions should be used in order to characterize it. Two of them will be connected to the VNA extenders and the other two to matched loads. A prototype to characterize the W-band quadrature hybrid coupler has been designed, as shown in Fig. 4.20. As can be seen, the microstrip lines have not been lengthened in order to minimize the dielectric losses. Conversely, given the small size of the hybrid, the waveguides of the transitions have

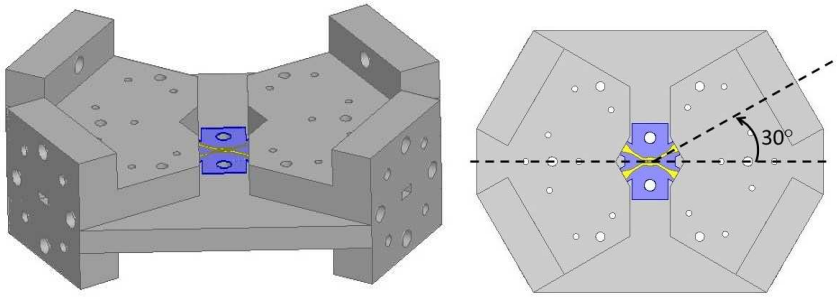

(a) (b)

Figure 4.20 – HFSS Schematics of the designed characterization block of the W-band quadrature hybrid coupler; a) lateral and b) top views.

been lengthened in order to accommodate the four WR10 flanges and the connections with two VNA extenders. Note that the transitions are placed at 30° with respect to a horizontal axis, see Fig. 4.20 b), in order to match to the microstrip ports of the quadrature hybrid coupler. Therefore, instead of following with the manufacturing of this specific prototype, the existing WR10 waveguide to microstrip transition has been used to characterize the W-band quadrature hybrid coupler.

To this aim, three microstrip circuits have been designed to characterize each port of the W-band quadrature hybrid coupler, see Fig. 4.21. With respect to the matching of the other two ports of each quadrature hybrid coupler, it is solved including Vivaldi antennas which are matched along the entire W-band, as will be shown in Chapter 7. Thus, the bottom layers of each circuit, see Fig. 4.21 b), d) and f), contain the ground plane of the microstrip circuit and the aperture of Vivaldi antennas. On the top layer of these circuits, see Fig. 4.21 a), c) and e), the microstrip section of the WR10 waveguide to microstrip transition has been included in each port we want to measure at W-band. The manufacturing of these circuits have been carried out by the LPKF ProtoLaser 200 machine.

For example, Fig. 4.22 shows two photographs of the microstrip circuit designed to measure the isolated port of the quadrature hybrid coupler. It is placed in the back-to-back WR10 waveguide to microstrip transition. Note that screws and dowel pins are required to ensure the alignment of the parts.

The comparison between the measurements of the direct, coupled and

(a) (b) (c) (d) (e) (f)

Figure 4.21 – Photographs of the microstrip circuits designed to measure each port of the W-band quadrature hybrid coupler using the manufactured back-to-back WR10 waveguide to microstrip transition; a) Top and b) bottom layer of the direct port measurement prototype, i.e. S21, c) top and d) bottom layer of the coupled port measurement prototype, i.e S31, and, e) top and f) bottom layer of the isolated port measurement prototype, i.e S41.

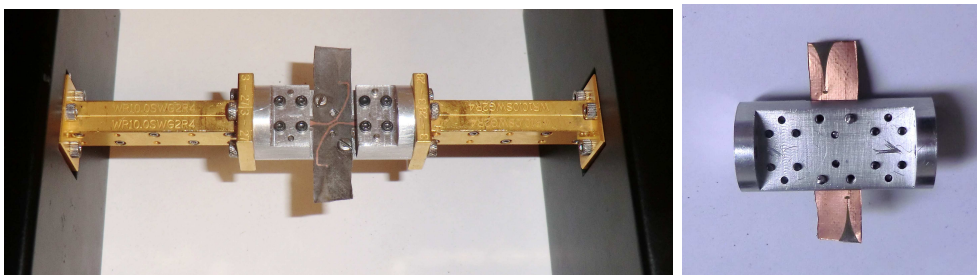

(a) (b)

Figure 4.22 – Photographs of the isolated port measurement of the W-band quadrature hybrid coupler using the back-to-back WR10 waveguide to microstrip transition; a) top and b) bottom view.

isolated ports of the W-band quadrature hybrid coupler and the simulated results of these prototypes are shown in Fig. 4.23. As can be seen in Figures b), d) and f), the reflection coefficients of these prototypes agree well with the simulations. Therefore, the WR10 waveguide to microstrip transition is appropriately working.

With respect to the transmission of each microstrip circuit, note that the simulated values are lower than those shown in Section 2.3.2 when the design of the quadrature hybrid coupler is explained. The reason for these additional losses is twofold. First, the addition of the insertion losses of the designed WR10 waveguide to microstrip transition, which are approximately 0.73 dB per single transition at 92.5 GHz. Therefore, 1.46 dB will be related to the back-to-back WR10 waveguide to microstrip transition. The second reason is the added dielectric losses due to the lengthening of the 50 Ω microstrip lines required to place each microstrip circuit in this back-to-back transition.

Taking into account the simulated transmission of the prototype designed to measure the direct port, see Fig. 4.23 a), its expected insertion losses at 92.5 GHz are 4.93 dB. At this frequency, the losses related with the back-to-back transition are 1.46 dB and the added dielectric losses are 0.37 dB because the 50 Ω microstrip lines have been lengthened 1.85 mm at each port. Therefore, 1.83 dB of losses have to be added to the S21 parameter of the W-band quadrature hybrid coupler which was shown in Section 2.3.2, i.e. 3.03 dB. These imply that the total expected insertion losses of the considered circuit to measure the direct port of the coupler are 4.83 dB, which is close to those 4.93 dB. As can be seen in Fig. 4.23 a) and c) the measurements agree well with the simulations obtaining at most 1 dB of difference between them. With respect to the measurement of the isolated port of the W-band quadrature hybrid coupler, it also shows a good agreement with the simulations, see Fig. 4.23 e). The transmission in the isolated port is lower than -12 dB, which is higher than those shown in Section 2.3.2 due to the influence of the WR10 waveguide to microstrip transition.

Another important parameter to validate the design of the W-band quadrature hybrid coupler is the phase difference between direct and coupled ports. The measured phase of these ports and also its difference are depicted in Fig. 4.24. The length of the 50 Ω microstrip lines in the circuits designed to measure the direct and the coupled ports are slightly different. They differ in 0.74 mm. Therefore, a phase correction of $e^{-j\frac{2\pi f\sqrt{\epsilon_{eff}}0.74}{c}}$ has been applied

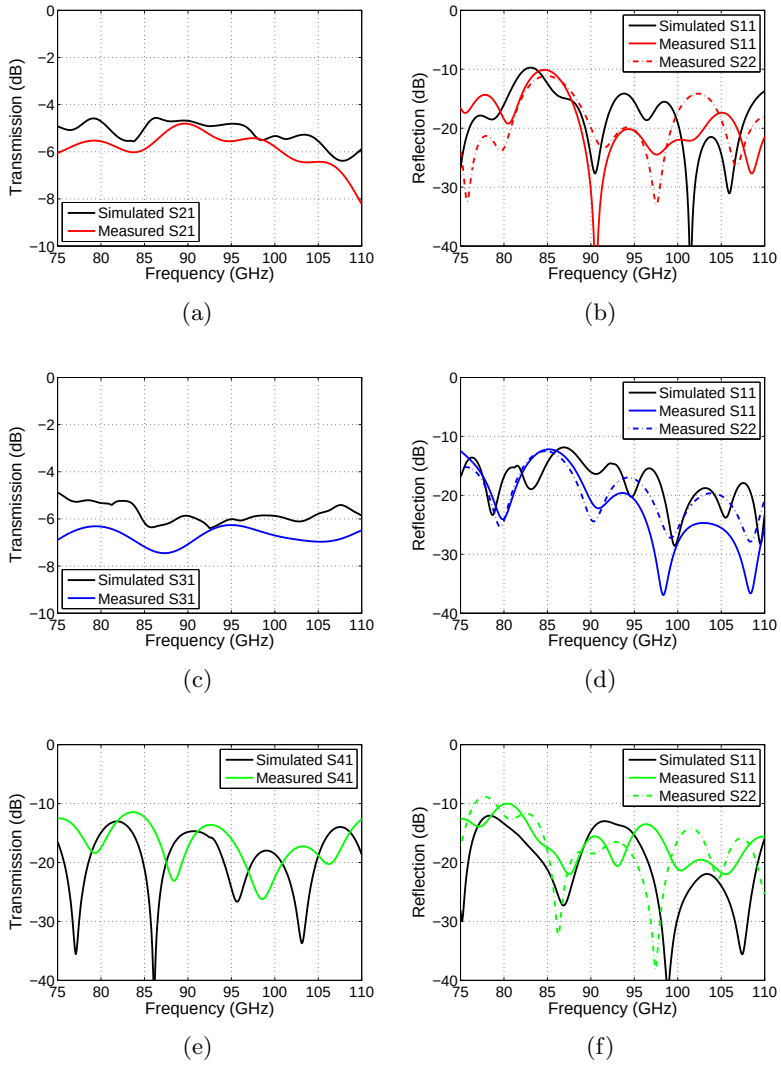

Figure 4.23 – Comparison between simulated and measured results of each microstrip circuit designed to measure the S-parameters of the W-band quadrature hybrid coupler; a) S21 and b) reflection coefficients, i.e. S11 and S22, of the direct port measurement prototype, c) S31 and d) reflection coefficients, i.e. S11 and S22, of the coupled port measurement prototype and, e) S41 and f) reflection coefficients, i.e. S11 and S22, of the isolated port measurement prototype.

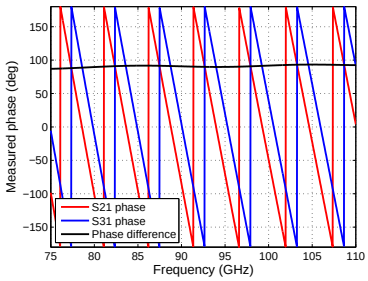

Figure 4.24 – Measured phase (deg) of the direct and coupled ports of the W-band quadrature hybrid coupler. The difference between them is also included.

to the measured phase of the coupled port. Note that ϵ_{eff} is the effective dielectric constant of a microstrip line [102]. As can be seen in the Figure, the measured phase difference between direct and coupled ports are almost constant around 90° along the entire W-band.

Therefore, the electromagnetic performance of the W-band quadrature hybrid coupler in terms of S-parameters and phase difference between direct and coupled ports have been experimentally validated.

4.4.2 W-band MMIC attenuator

The reference load of the W-band auto-calibrated receiver built in planar technology is the TGL4201 10 dB MMIC attenuator. The characterization of this component is simple. The set-up consists of the back-to-back WR10 waveguide to microstrip transition, which has been presented in Section 4.3, and 50 Ω microstrip lines that connect each port of the MMIC attenuator by gold wire bondings.

Fig. 4.25 shows a photograph of the MMIC attenuator assembly. It is based on the recommended chip assembly diagram given by the manufacturer, see Fig. 2.12 in Section 2.3.3.1. The considered microstrip circuit is identical to that manufactured to characterize the transition, see Fig. 4.12 b). This circuit has been welded to the bottom metal block of the transition for two reasons. The first one is to ensure its position. This is required because the gap in which the attenuator will be placed will be directly cut by a small cutter. The second reason is to completely fix the 50 Ω microstrip line which is printed in the circuit. When the gap is cut, these microstrip lines can not be lifted

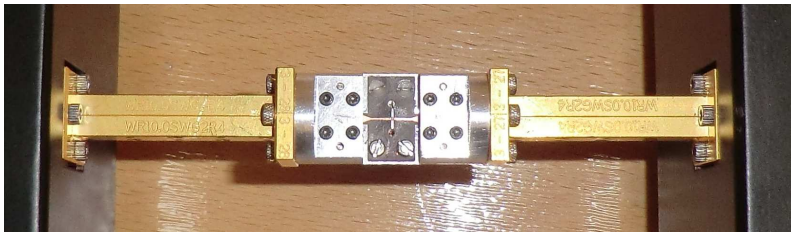

Figure 4.25 – Photograph of the TGL4201 10 dB MMIC attenuator assembled in the back-to-back WR10 waveguide to microstrip transition.

(a) (b) (c)

Figure 4.26 – Photographs of the a) TPT HB16D machine, b) vacuum pencil of the pick and place tool and c) a detail of the 25 μm wedge wire bonding tool.

because it will complicate the gold wire bonding.

The welding of the microstrip circuit and also of the attenuator in its gap is done with EPO-TEK-H20E silver loaded epoxy adhesive which is conductive at this high frequency. The selected curing temperature has been low, i.e. 100° C, in order to avoid cracking of the adhesive. Once the microstrip circuit is welded to the metal block of the transition, the gap is cut so that the distance between the bonds of the 50 Ω microstrip lines is as small as possible. This is important to shorten the length of the gold wire bondings. The shorter the gold wire bonding, the better the reflection coefficient, as analysed in Section 3.4. Next, the attenuator is placed by a vacuum pencil which picks and places the chip. It is also welded in its gap and the gold wire bondings can be done. Note that the ground contact between the attenuator and the metal block of the transition is ensured by the conductive epoxy adhesive. Both the

pick and place method and the gold wire bondings are carried out with the TPT HB16D machine, see Fig. 4.26 a).

The TPT HB16D machine is available in the Antenna Group at the Public University of Navarra. The HB16D is a bench top size wirebonder, easy to use. It provides a vacuum pencil with 203 μm diameter hole to pick and place MMIC devices with a placement accuracy of $\pm$25 μm, see Fig. 4.26 b). Moreover, gold wire bonding is feasible using the wedge tool. A detail of this 25 μm wedge wire bonding tool is shown in Fig. 4.26 c). Specifically, wedge to wedge bonding is the commonly method in semiconductor assembly. In our case, wedge wire bonding is selected instead of ball wire bonding because it requires narrower bonds to fix the junction. Moreover, wedge bonding offers a low, flat and short loop for maximum high-frequency electrical performance. Therefore, the reliable height of these bondings is smaller than those given by ball wire bonding. This last feature facilitates the packaging of MMIC components. For example, devices such as the LN4-110 amplifier has to be welded on a channel and the height of this channel is critical because undesired resonances can be excited. For this reason, it is important not to limit the smallest feasible height of the cavity inside the packaging. Normally, forward wedge bonding is preferred, i.e. the first bond is made to the chip and the second is made to the substrate. As a result, a wire tail is placed in the second bond. This forward method is the most suitable because the chip can be more susceptible to edge shorts between the wire and chip.

The assembly of the MMIC attenuator can be seen in Fig. 4.27. The attenuator is placed into a small gap. Moreover, its input and output ports are connected to 50 Ω microstrip lines by one, two or three gold wire bondings in order to analyse the effect of the number of wires in the performance of the attenuator. Although the wire bondings are too large, the distance between the microstrip line and the attenuator is less than 100 μm in each port. Therefore, the return and insertion losses included by these gold wires are expected to be suitable.

The measurement of the S-parameters of the attenuator connected by one, two or three bond wires has been carried out using the WR10 waveguide to microstrip transition and the waveguide based equipment. These results are shown in Fig. 4.28. Note that the comparison between measurements and the data given by the manufacturer is not suitable because the manufacturer data have been directly measured by RF microwave probes, i.e. without taking into account wire bondings. However, the expected performance of the attenuator

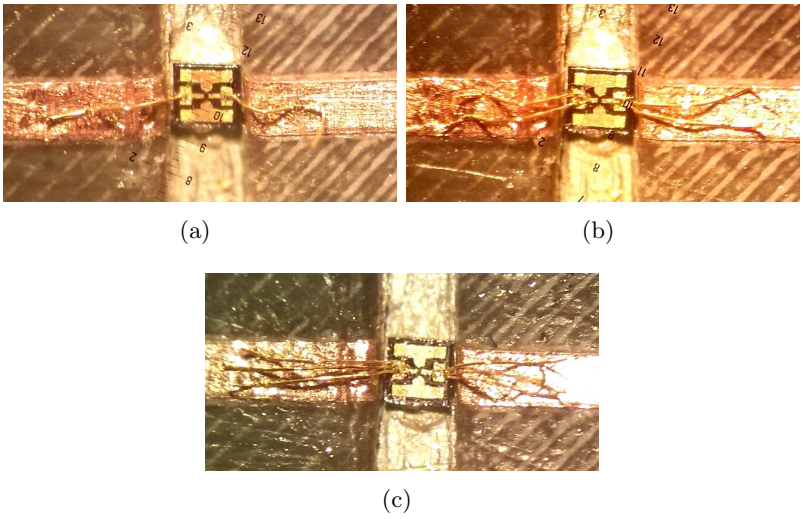

(a) (b)

(c)

Figure 4.27 – Photographs of the TGL4201 10 dB MMIC attenuator connected to 50 Ω microstrip lines by a) one, b) two or c) three gold wires.

are return and insertion losses above 10 dB in order to simulate a reference load in the isolated port of the input quadrature hybrid coupler of the W-band auto-calibrated receiver.

With respect to the measured return losses, they are above 6.5 dB, see Fig. 4.28 a) and b). However, they can be improved. The device is symmetrical but the results for the S22 are better due to the fact that the length of the gold wires are smaller. Regarding insertion losses shown in Fig. 4.28 c), they are above 15 dB along the entire W-band. The added insertion losses of the 8.6 mm long microstrip line placed in the WR10 waveguide to microstrip transition are less than 3 dB in the full W-band. Therefore, the insertion losses of the attenuator itself are at least 12 dB, which is a good result for our application.

Taking into account the measured results as a function of the number of gold wire bondings, the bonding of ports by only one wire is enough to obtain a suitable performance of the attenuator as a reference load. Moreover, the electromagnetic performance of the attenuator is almost identical when the bonding is done by one, two or three gold wires. However, the detachment of the bonding is more probable when only one wire is considered. Therefore, the bonding of ports with more than one wire is better in terms of hardness

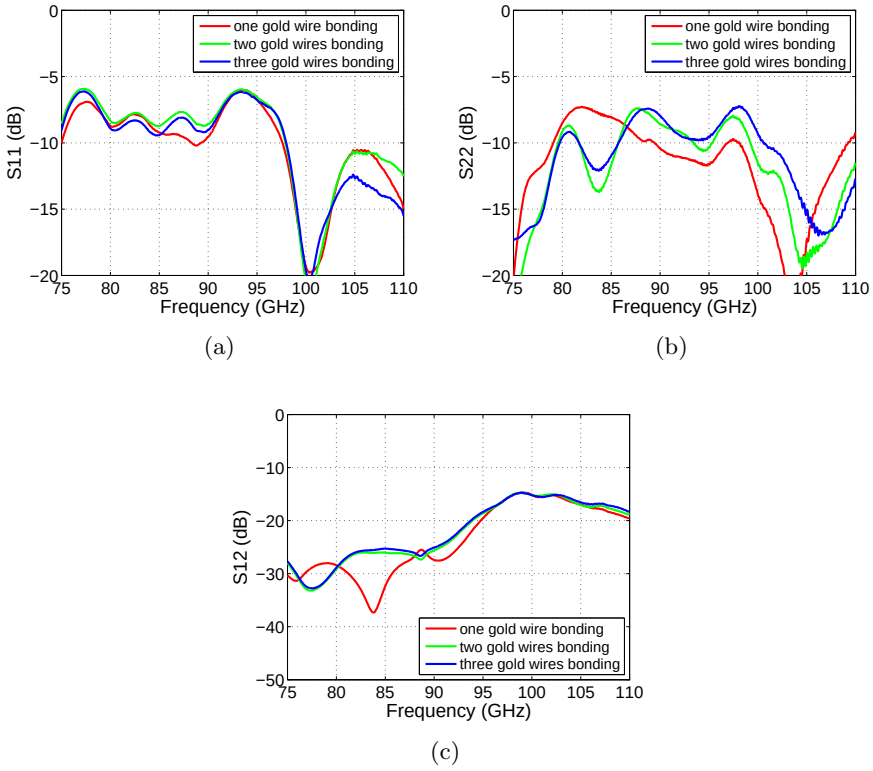

Figure 4.28 – Measurement results of the MMIC 10 dB attenuator with the W-band inline microstrip-to-waveguide transition which each port connected by one, two and three gold wires; a) S11, b) S22 and c) S12.

(a) (b)

Figure 4.29 – a) EPS150MMW Probe System, which is compatible with VDI VNA extenders, and b) a waveguide probe.

and durability of the junction.

The experimental results demonstrate that the use of the TGL4201 10 dB attenuator of TriQuint Semiconductor is appropriate in order to simulate a reference load of the W-band auto-calibrated receiver. The return losses are acceptable whilst the insertion losses are above 12 dB, as required.

4.4.3 W-band LNA

The characterization of the commercial LN4-110 low noise amplifier has been carried out by the manufacturer before delivery. An RF microwave probe station has been used to measure the return losses and the gain of each amplifier directly on wafer. This is the same technique used by TriQuint Semiconductor to measure the electromagnetic performance of the TGL4201 10 dB attenuator. One example of a microwave probe machine is shown in Fig. 4.29, i.e. EPS150MMW Probe System of Cascade Microtech [167]. The particularity of this machine is that it is compatible with the VDI extenders, thereby, the S-parameters of any two port device can be measured. Moreover, it is suitable to characterize this type of devices because one of the probe terminations consists of coplanar bonds, i.e. the same termination of these

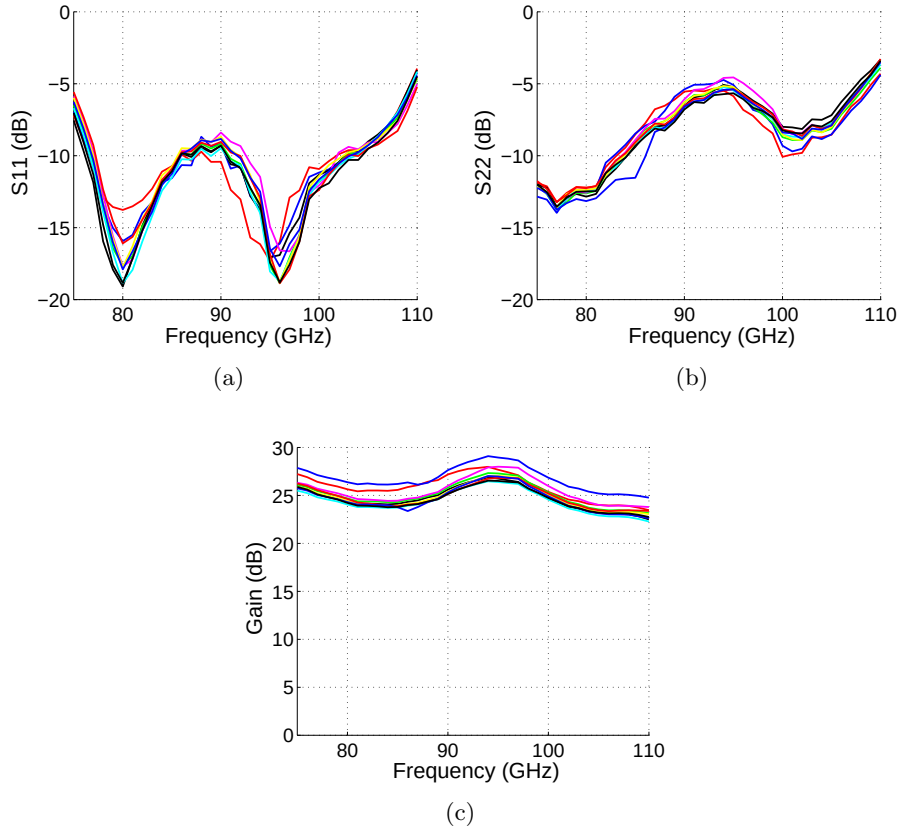

Figure 4.30 – On wafer measurement results of 10 different LN4-110 low noise amplifiers done by the manufacturer; a) S11, b) S22 and c) gain in the full W-band.

chips. Moreover, the manufacturer also gives information about the values of gate voltage and drain current, i.e. V_g and I_d respectively, required to optimized the performance of these characterized amplifiers. Whereas the values of drain current slightly differ from those recommended 35 mA, i.e. between 34.4 and 35.7 mA, the range of gate voltage in their optimized operation points is larger, i.e. from -80 to 80 mV.

The measured reflection coefficients of each port and also the gain of ten different amplifiers are depicted in Fig. 4.30. As can be seen, the matching

of the input port of the amplifiers, see Fig. 4.30 a), is better than that of their output ports, see Fig. 4.30 b). However, the matching of both ports get worse at the highest limit of the W-band. Regarding gain, their measured values in the full W-band are higher than the expected 22 dB, as it is shown in Fig. 4.30 c). Therefore, the experimentally obtained performance of the LN4-110 amplifiers imply that they work as well as expected.

Note that these devices require the design of a DC bias circuit. The design of this DC bias circuit will be explained in the next Chapter.

4.5 Conclusions

This Chapter has been presented the fabrication and characterization of the planar components of the W-band auto-calibrated receiver. The microstrip components are built on 0.127 mm thick RO5880 substrate. The dielectric constant and loss tangent of this substrate was measured by the manufacturer only at 10 GHz. Therefore, first of all, the characterization of this substrate in the W-band was indispensable in order to compare the simulation performance of these microstrip components with their experimental results. Two different set-ups have been taken into account to measure the transmission coefficient through a thin sample of these materials: one based on lenses and other one based on mirrors. The experimental results have confirmed that the set-up based on lenses is able to obtain better results thanks to its accurate alignment and narrower beam waist. In conclusion, the retrieved dielectric constant and loss tangent of 0.127 mm thick RO5880 substrate at W-band have been found to be 2.22 and 0.01 respectively. It is worth noticing that the losses are one order of magnitude higher than the value given by the manufacturer at 10 GHz. Then, in order to characterize the microstrip components of the receiver with waveguide based measurement equipment, the design, manufacture and validation of a novel inline WR10 waveguide to microstrip transition have been also shown in this Chapter. Next, the characterization of the quadrature hybrid coupler and the MMIC attenuator have been carried out with this transition. The experimental results have verified their expected performances.

Chapter 5

Packaging of the W-band auto-calibrated receiver built in planar technology

5.1 Introduction

Once the microstrip devices and the commercial MMIC components which are part of the receiver have been characterized and validated, the next step is to design the packaging of the proposed W-band auto-calibrated receiver. As shown in Chapter 3, its planar structure is as depicted in Fig. 5.1. A suitable packaging block has to be designed in order to protect this circuit without penalizing its performance. Moreover, other components are required to be included in the packaging such as the DC circuit to bias the amplifiers, the DC circuit to filter and amplify the output signals of the receiver and the WR10 flange. The flange is indispensable in order to connect the W-band auto-calibrated receiver with a standard horn antenna or with waveguide based measurement equipment.

This Chapter explains the design of the inner cavity of the packaging metal block in which the planar structure of the receiver will be contained. This cavity avoids the propagation of undesired modes which can penalize the performance of the receiver. The removal of these unwanted propagating modes has been experimentally validated. Next, the design of the DC circuits, which bias the LNAs and amplifies the output signals of the receiver has

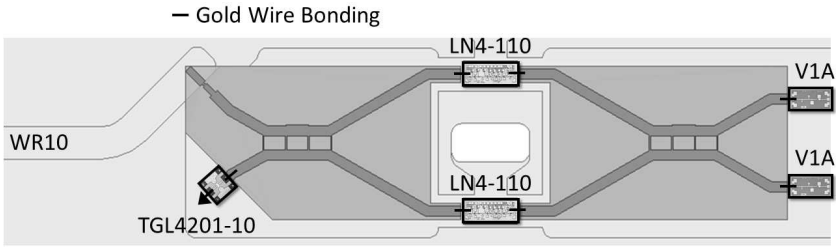

Figure 5.1 – Layout of the designed W-band auto-calibrated receiver.

been carried put. Finally, the design of the packaging metal block, which will contain the required elements of the receiver, is explained. This packaging metal block has to be suitable to allow an array implementation.

5.2 Design of the packaging cavity: removal of the unwanted resonances

As can be seen in Fig. 5.2, the assembly of the MMIC LN4-110 amplifier consists of two 50 Ω microstrip lines connected to its input and output ports by gold wire bondings. In addition, it requires to be placed inside a channel in order to avoid the propagation of undesired higher-order modes at W-band, a 1.27 mm width channel is recommended by the manufacturer. Moreover, the amplifier has to be fed by a DC circuit, which supplies voltages by means of a series of surface mount capacitors. These capacitors ground the RF signal in these connections. Therefore, enough space to place these required components has to be left on the top part of the LNA, where the bonds of its gates are, in order to short the length of the bond wires. For this reason and the fact that the proposed W-band receiver contains two amplifiers, the input and output 50 Ω microstrip lines of the amplifiers have been lengthened to separate the two amplifier chains of the receiver, see Fig. 5.1. Moreover, the ends of these microstrip lines have been put in a channel together with the amplifiers. In each amplifier branch the added length of the 50 Ω microstrip lines is 11.026 mm. These imply additional dielectric losses per branch of 1.1 dB. Their effect in the performance of the receiver was studied in Section 3.3.4.

Therefore, the dimensions of the planar structure of the proposed receiver are exactly 5.92 mm wide, 23.21 mm long and 0.161 mm thick. This is the

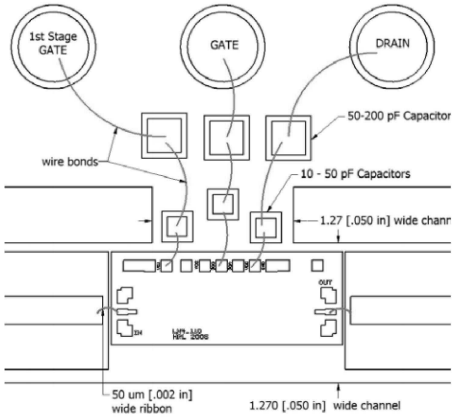

Figure 5.2 – Typical assembly diagram of the LN4-110 Low Noise Amplifier given by HRL Laboratories.

structure to package.

Packaging of millimetre wave microstrip circuits can be seriously affected by excitation of cavity modes and surface modes in the dielectric substrate. These may penalize the transmission of the quasi-TEM mode in the microstrip circuit [168] and degrade the circuit performance.

Traditionally, conventional microwave absorbers composed of materials with bulk resistive properties have been placed within the cavity of the packaged circuits in order to avoid the propagation of cavity modes [169]. However, the circuit performance may degrade because the undesired modes are not prevented but absorbed.

The aforementioned approach causes undesired losses which become more relevant as frequency increases. A more elegant solution to this problem can be found in the use of periodic structures in one of the ground plates of the packaging structure [170]- [175]. The used periodic textured surfaces implement an Artificial Magnetic Conductor (AMC) or a high-impedance boundary, which blocks parallel-plate mode propagation within a frequency band (stop-band) provided that the distance to the opposite Perfect Electric Conductor (PEC) plate is smaller than a quarter wavelength.

Besides the AMC behaviour, these 2D periodic structures act as an Electromagnetic Band Gap (EBG) which blocks the propagation of electromagnetic waves for all directions within a forbidden frequency band

[171]. Different kinds of EBG structures have been proposed for packaging microstrip circuits at microwave frequencies. Periodic structures such as Mushroom-Type EBG [172], Fakir's Bed of Nails [173] and Bed of Springs [174] are more suitable for relatively low frequencies, below 10 GHz, due to its easy manufacturing and low weight. As a matter of fact, when frequency increases, the bed of spring becomes too complex to be manufactured. Moreover, the drawback of the first two cases is to use a dielectric substrate since it adds losses and reduces the operating frequency bandwidth.

The difficulty of scaling to higher frequencies these periodic structures has led to other configurations being proposed. On the one hand, in [175], an EBG structure composed of holes with period half the guided wavelength, has been implemented in the upper metal plate of a shielded microstrip structure. This configuration allows the suppression of undesired cavity modes in a narrow stop-band centred at 76 GHz. On the other hand, the new gap-waveguide presented in [176] and experimentally validated around 15 GHz in [177] implements a periodic structure which consists of a lid of nails or a pin surface. Its main advantages are the omission of the dielectric substrate and its large bandwidth, up to an octave, demonstrated in [178]. Furthermore, this structure is easily scalable to higher frequencies. As shown in [179], manufacturing of this structure is feasible up to 340 GHz with Micro-ElectroMechanical System (MEMS) technology.

In this Section, the optimization of the pin surface for packaging of the auto-calibrated receiver covering the full W-band is presented. By means of a parametric study, a deep understanding of the behaviour of its modes and the influence of the different parameters on the performance, mainly on the bandwidth, is for the first time achieved. Moreover, in contrast to previous studies our design takes into account for the first time any direction of the propagating modes. This allows to determine accurately the stop-band of this periodic structure. So far, the pin structure has been used in packaging of microstrip circuits such as the feeding network of the eight ports of the eleven antenna in a broad frequency range from 5 GHz to 13.5 GHz [180]. Besides, when used together with microstrip circuits a significant improvement of their performance can be achieved. For example, critical microstrip passive devices such as filters have benefit from this technology [181]. In addition, the improvement of isolation between two high gain amplifier chains in Ku-band implementing this packaging alternative has been demonstrated in [182]. Moreover, the removal of resonances for the case of a single microstrip line

with two 90° bends around 15 GHz using the bed of nails has been shown in [183].

The performance of a square pin surface covering the full W-band has been optimized. This surface will be used for packaging of the proposed W-band auto-calibrated receiver built on 127 μm thick Rogers RT/Duroid 5880 substrate. The use of the pin surface will allow suppression of the unwanted modes and resonances. A stop-band covering the full W-band has been designed by means of a complete parametric study. In this analysis the Irreducible Brillouin zone of the dispersion diagram has been taken into account. Therefore, all propagating modes in any direction within the structure are completely studied. By contrast, in most articles only the transverse direction is studied. This causes that the limits of the stop-band are not determined accurately. Moreover, design guidelines of the pin surface are proposed in order to create a certain stop-band. Finally, the removal of the undesired modes is demonstrated both in simulation with Ansoft HFSS and experimentally by measurements of a prototype.

5.2.1 Pin surface: geometry and principle of operation

The geometry of a pin surface is shown in Fig. 5.3. The pin surface implemented in the upper metal of the package covers the microstrip circuit keeping an air gap between the end of the pin and the substrate. The pins are arranged in a square lattice configuration. The parameters that determine its performance are:

- The length of the pins, d.
- The period of the structure, p.
- The size of the square pin, s.
- The height of the air gap between the AMC surface and the opposite substrate, g.

In principle, if the period is small enough, the pins work as an AMC when its length, d, is approximately $\lambda/4$. Due to this length, the short circuit (PEC) is transformed into an open circuit (AMC).

When an AMC is introduced in the upper metal of two parallel metal plates separated by an air gap, it creates an ideal parallel plate cut-off, i.e

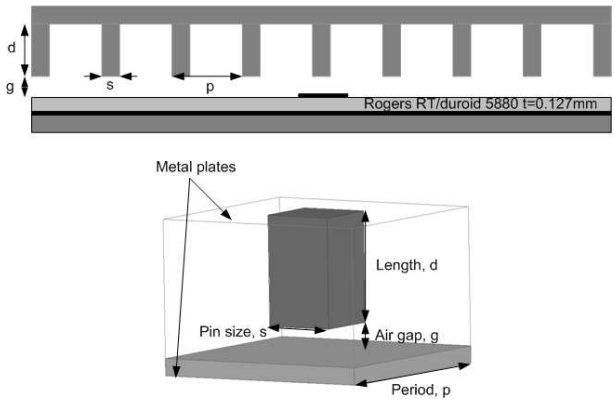

Figure 5.3 – Lateral view of a pin surface structure, the unit cell of a square lattice configuration of pins and its parameters.

a stop-band. The behaviour of this structure has one physical limit for the lower frequency and two physical limits for the upper frequency of the stop-band [178]. On the one hand, the lower limit is defined by the frequency at which the surface impedance changes from inductive to capacitive. At this point, the surface presents a high enough impedance to generate the cut-off of the propagation modes. On the other hand, the upper limit of the stop-band comes from both the impedance change from capacitive to inductive and, besides, the height of the air gap. Moreover, the distance between the plates must be smaller than half wavelength in order to create the parallel plate cut-off.

Therefore, when a pin surface is introduced, the stop-band is theoretically generated from the frequency at which the length of the pins is approximately $\lambda/4$ up to the frequency at which the spacing between parallel metal plates is $\lambda/2$ [177]. However, these limits are more flexible due to the capacitive effect of the air gap height.

Besides the AMC effect, the periodicity of the pin surface plays an important role in its behaviour. As in any periodic structure it will have a frequency range where no propagation is allowed. This will be the range of interest for our packaging application.

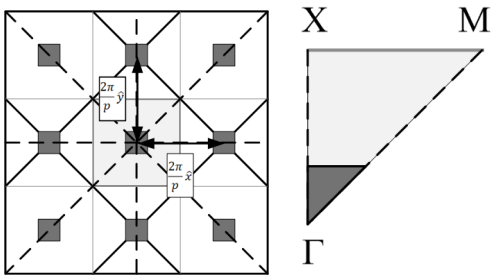

Figure 5.4 – (a) Schematic of the Brillouin zone in a square lattice configuration of pins (grey squares) and (b) Irreducible Brillouin zone.

5.2.2 Parametric Study of the Pin Surface

For the complete definition of the stop-band it is required to determine the propagating modes in any direction within the periodic structure. This study reduces to the edge of the *Irreductible Brillouin zone* where information about propagation in any direction in the $k-$space is taken into account [184]. For a square lattice, the *Irreductible Brillouin zone* is the triangular wedge in the upper right corner within the unit cell, as can be seen in Fig. 5.4. The rest of the Brillouin zone (central unit cell in Fig. 5.4 a)) consists of exact replicas of this wedge. The three points which determine the *Irreductible Brillouin zone*, Γ, X and M, correspond to $k_{\|} = 0$, $k_{\|} = \frac{\pi}{p}\hat{x}$ and $k_{\|} = \frac{\pi}{p}\hat{x} + \frac{\pi}{p}\hat{y}$, respectively.

In order to understand the behaviour of the pin structure and to determinate the limits of the stop-band, the dispersion diagrams of the pin surface have been calculated using Ansoft HFSS.

As mentioned above, the first step to study the cut-off properties of a lid of pins working as an AMC surface is to fix the pin length d equal to $\lambda_c/4$. In this case, λ_c is the wavelength of the central frequency of the W-band. This frequency is 92.5 GHz, therefore, the fixed length of the pins is 0.81 mm. The other parameters of the initial periodic structure have been fixed to $p = 1.6$ mm ($\lambda_c/2$), $s = 0.5$ mm and $g = 0.2$ mm.

The dispersion diagram of the first four propagation modes for this pin surface structure can be seen in Fig. 5.5. According to this figure, the stop-band of the periodic structure is determined by the gap between the two lowest order modes of the dispersion diagram. The highest frequency of the first order

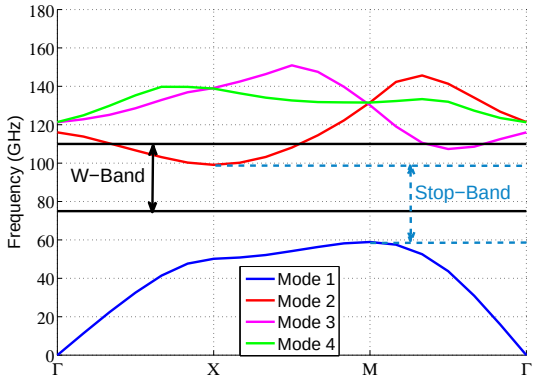

Figure 5.5 – Dispersion diagram of the pin surface covering a microstrip circuit over 127 μm thick Rogers RT/Duroid 5880 substrate. The length and the size of the pin, the period and the height of the air gap are 0.81 mm, 0.5 mm, 1.6 mm and 0.2 mm respectively.

mode defines the lower limit. Note that this highest frequency corresponds to the M point. This shows that the analysis covering the full Brillouin zone is required in order to determine the structure performance. On the other hand, the upper limit is defined by the lowest frequency of the second mode, which is in propagation within the W-band.

The normalized E-field magnitude of the first two propagating modes defined at those points of the dispersion diagram which limit its stop-band, i.e. the M point for mode 1 and the Γ and X points for mode 2, is shown in Fig. 5.6. This figure helps to understand the nature of each propagating mode inside the structure. As can be seen, the E-field of the first propagating mode is mainly localized in the air gap under the pin, but its field distribution in the vertical direction depends on the total height. Conversely, the second mode mainly propagates in the spacing between pins.

This study will highlight some peculiarities of the modal behaviour that are of great interest for the structure design. In particular, the effects of the period, the pin size and the height of the air gap will be linked to the mode structure. This analysis will allow to optimize the stop-band of the periodic structure to cover the full W-band. For this study only the points of the dispersion diagram which define the bandgap will be plotted.

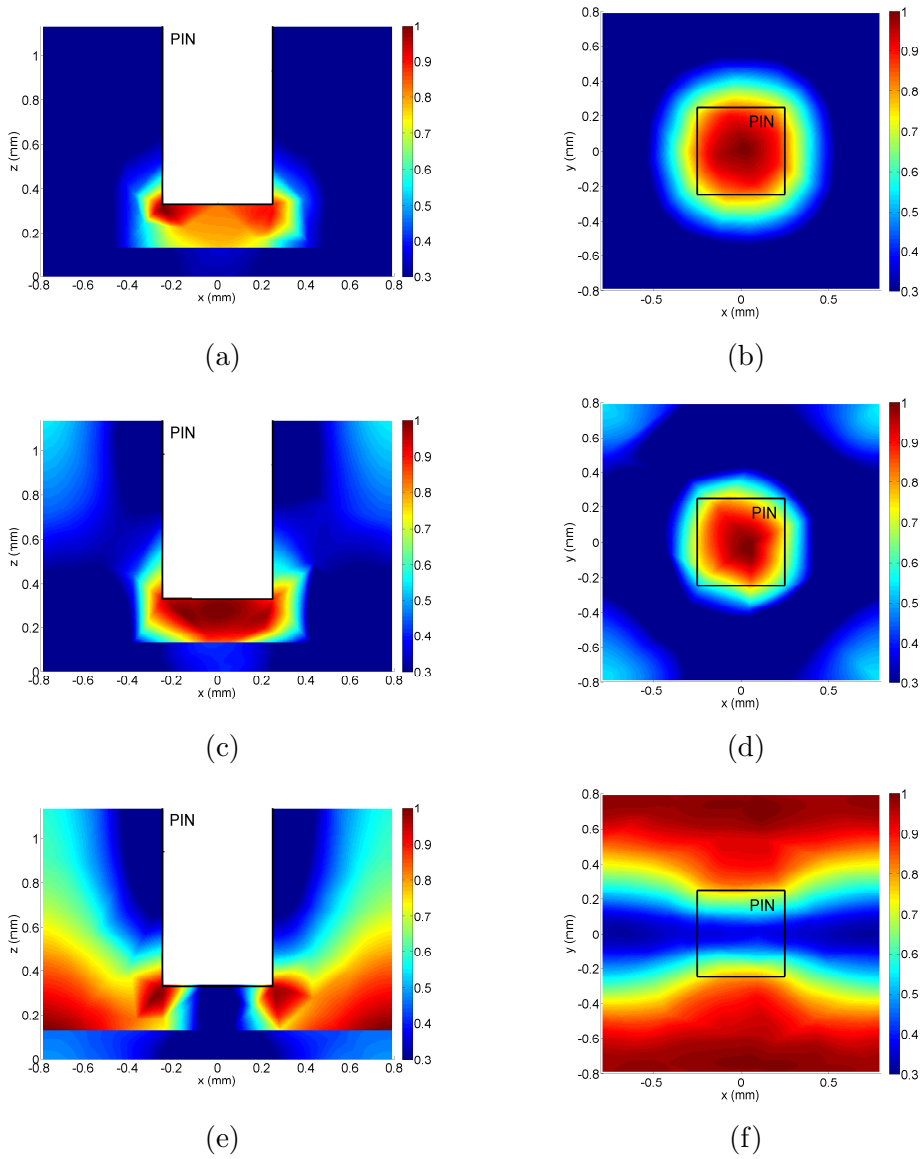

Figure 5.6 – Normalized E-field magnitude of the first two propagating modes defined in point of interest: a) First mode at the centre of the unit cell at point M, b) First mode on the substrate surface at point M, c) Second mode at the centre of the unit cell at point Γ, d) Second mode on the substrate surface at point Γ, e) Second mode at the centre of the unit cell at point X, f) Second mode on the substrate surface at point X. The black rectangle shows the dimensions of the pin.

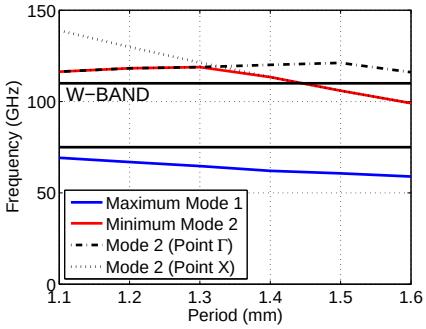

Figure 5.7 – Highest (second propagation mode) and lowest (first propagation mode) limits of the bandgap depending on the period. The length and the size of the pin, and the height of the air gap are 0.81 mm, 0.5 mm and 0.2 mm respectively.

5.2.2.1 Effect of the period

Since the bandgap of the initial pin surface is located at frequencies lower than the W-band, reducing its period would shift it towards higher frequencies. The dependence of the bandgap with the period is represented in Fig. 5.7, where the gap limits are given by the red and blue lines plotted in this figure. The lower limit of the gap behaves as expected in any periodic structure, i.e. its frequency decreases when the period increases. To obtain a lower frequency limit of the stop-band smaller than the lowest frequency of W-Band, i.e. 75 GHz, the period should be larger than 1 mm, which corresponds to a quarter wavelength at this frequency.

However, the upper limit of the gap behaves differently. As can be seen, depending on the period, the lowest frequency of the second order mode is determined by the point X or Γ. The behaviour of this higher limit of the bandgap has a maximum when the period is 1.3 mm, which corresponds to a distance between pins of $\lambda_c/4$. When the period is larger than this value, the upper frequency limit of the stop-band decreases following the behaviour of the mode for the X point due to the increase of the spacing between pins. Fig. 5.8 shows the normalized E-field magnitude of the second mode at the X point for different values of the period. As can be seen, the second mode propagates within the air region between pins. Therefore, when the period increases while keeping constant the size of the pin, the spacing between pins

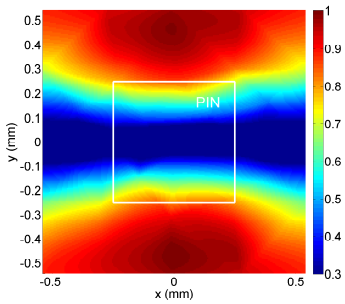

(a)

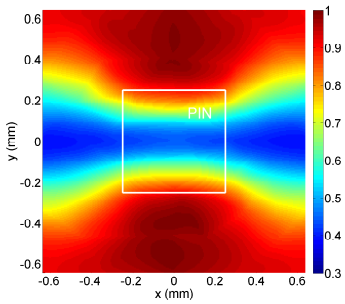

(b)

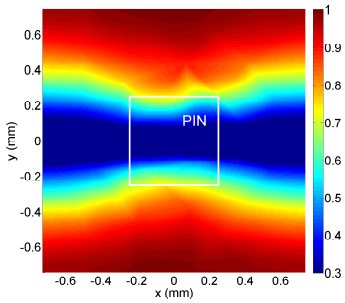

(c)

Figure 5.8 – Normalized E-field magnitude of the second order at the X point on the substrate surface for different values of the period: a) 1.1 mm, b) 1.3 mm and c) 1.5 mm. The white rectangle shows the dimensions of the pin.

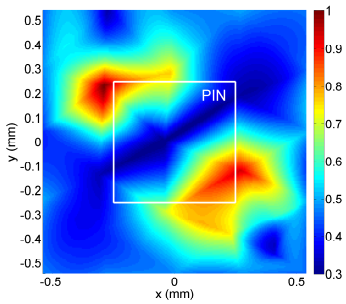

(a)

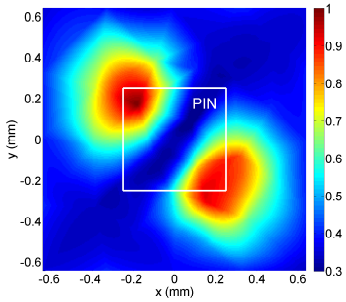

(b)

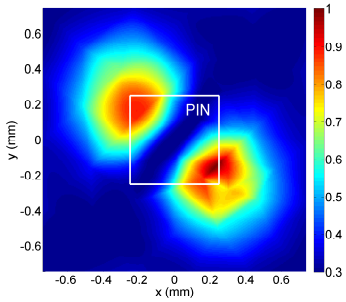

(c)

Figure 5.9 – Normalized E-field magnitude of the second mode at the Γ point on the substrate surface for different values of the period: a) 1.1 mm, b) 1.3 mm and c) 1.5 mm. The white rectangle shows the dimensions of the pin.

increases and the frequency at which this mode propagates decreases.

On the other hand, below this maximum, the mode at the Γ point defines the upper limit of the stop-band. At Γ, the mode frequency remains nearly constant. This can be explained by the field distribution of the mode, Fig. 5.9. In this figure it can be seen that the maximum of the E-field at point Γ is located on the edges of the pin for three different periods. As a consequence, its frequency is mainly determined by the pin size and it is not affected by the period. In this case, the optimum period in terms of largest bandwidth corresponds to the point where the frequency of the second mode at X equals the frequency of the mode at Γ. This will be the limit for the highest frequency of the gap. This optimum period corresponds to 1.3 mm.

5.2.2.2 Effect of the pin size

The study of the pin size has been carried out while keeping constant the period of the pin surface as 1.3 mm. Similarly, the pin size mainly affects the upper limit of the stop-band, as shown in Fig. 5.10. As previously mentioned, the upper limit can be given by the Γ or X point. The largest bandwidth is achieved when the size of the pin is 0.45 mm, which corresponds approximately to one third of the period. Below this value, the gap decreases because of the increase of the spacing between pins. The Γ point defines the upper limit of the stop-band when the pin size is larger than 0.45 mm, as happened with the period. In this case, increasing the size of the pin over this value means decreasing the pin spacing below $\lambda_c/4$. Nevertheless, the upper limit of the bandgap decreases more steeply than when period changes, since the pin size begins to be wider than the distance between pins. Therefore, coupling effects are stronger. To summarize the effect of the pin size on the pin surface performance, the propagation frequency of the second order mode at X point equals the maximum achievable frequency when the pin size is approximately 0.34 times the pin period, as shown in Fig. 5.10.

5.2.2.3 Effect of the air gap

Once the period and the pin size have been fixed to 1.3 mm and 0.45 mm respectively, the next step is to analyse the effect of the air gap height. According to Fig. 5.11, the larger the air gap, the narrower the stop-band due to the lower capacitive effects between the AMC surface and the metal plate. Consequently, a 0.2 mm air gap its enough to ensure the desired operation

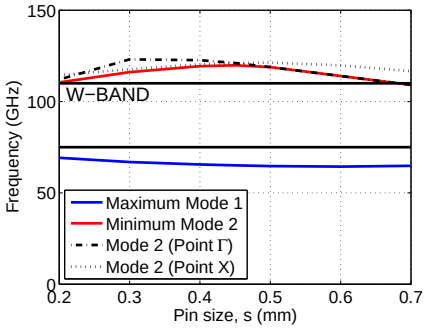

Figure 5.10 – Highest (second propagation mode) and lowest (first propagation mode) limits of the bandgap depending on the pin size. The length of the pin, the period and the height of the air gap are 0.81 mm, 1.3 mm and 0.2 mm respectively.

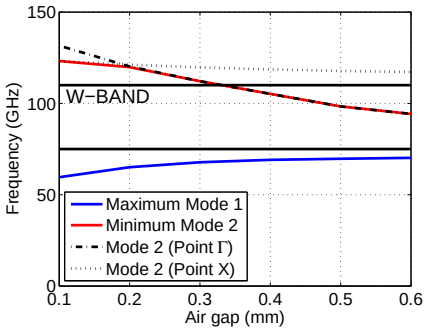

Figure 5.11 – Highest (second propagation mode) and lowest (first propagation mode) limits of the bandgap depending on the size of the air gap height. The length and the size of the pin, and the period are 0.81 mm, 0.45 mm, and 1.3 mm respectively.

bandwidth of the periodic structure, covering the full W-band. Moreover, this value is large enough to ensure that the pin surface does not affect the transmission of the quasi-TEM mode of the microstrip circuit.

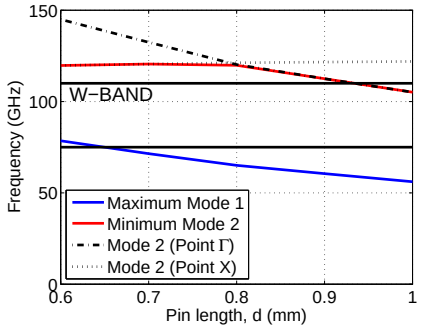

Figure 5.12 – Highest (second propagation mode) and lowest (first propagation mode) limits of the bandgap depending on the length of the pin. The period, the pin size and the air gap height are 1.3 mm, 0.45 mm and 0.2 mm respectively.

5.2.2.4 Effect of the pin length

The analysis of period, pin size and air gap height have been carried out assuming that the length of the pins should be $\lambda_c/4$ to work as an AMC. However, the analysis of the pin length has been considered in order to explain its contribution in the determination of the stop-band of the structure.

The variation in the length of the pin mainly alters the lowest frequency limit of the stop-band, see Fig. 5.12. The shorter the pin, the higher the lowest limit. This agrees with the fact that mode 1 is determined by the unit cell total dimensions. Moreover, the dependence of the highest frequency limit of the stop-band with respect to the distance between the parallel metal plates and the period can be also seen in Fig. 5.12. When the length of the pin increases over 0.81 mm, the highest frequency limit decreases since it is determined by mode 2 at Γ, which depends on the height of the cavity. Note that the structure has been optimized based on this length and this result is consistent with it. However, below this value, the highest limit of the stop-band is constant because it is limited by mode 2 at X, which depends on the period. As mentioned before, the highest achievable frequency of the stop-band is defined by mode 2 at Γ point. Therefore, as shown by the propagation frequency of the first mode and of the second mode at this point, plotted in Fig. 5.12, the pin length is the pin surface parameter that defines the centre frequency of the stop-band.

The dispersion diagram of the first four propagation modes for the

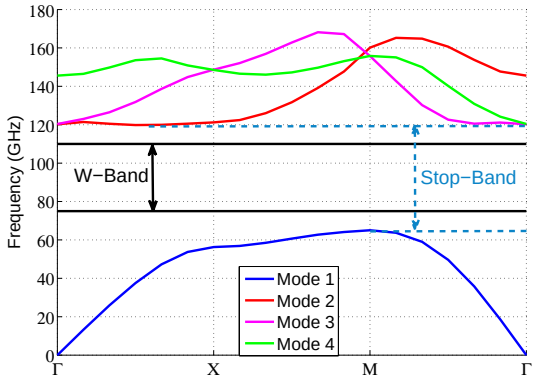

Figure 5.13 – Dispersion diagram of the optimum pin surface covering a microstrip circuit over 127 μm thick Rogers RT/Duroid 5880 substrate. The length and the size of the pin, and the height of the air are 1.3 mm, 0.45 mm and 0.2 mm respectively.

optimum pin surface structure, whose dimensions are $d = 0.81$ mm, $p = 1.3$ mm, $s = 0.45$ mm and $g = 0.2$ mm and its stop-band covering the full W-band have been plotted in Fig. 5.13. As it can be observed, the stop-band is larger than the W-band complying with the design goals.

5.2.2.5 Design guidelines

Taking into account the results above some design guidelines can be proposed for the pin structure in order to create a certain stop-band.

1. Fix the length of the pins at $\lambda_c/4$, where $\lambda_c/4$ corresponds to the central frequency of the stop-band.

2. The total height, i.e $d - t\sqrt{\epsilon_r} + g$ must be smaller than $\frac{\lambda_u}{2}$, where λ_u is the wavelength at the highest frequency of the stop-band. As a rule of thumb, the minimum value of the gap height is the thickness of the substrate to prevent affecting the transmission of the quasi-TEM mode of the microstrip line.

3. The period of the pin surface must be chosen inside the range $\lambda_u/2 < p < \lambda_l/4$, where λ_l is the wavelength of the required lowest frequency

limit of the stop-band. The limits of this range makes the maximum feasible frequency limit of the stop-band smaller than 2 times the lowest frequency limit.

4. Once the period is fixed, the pin size can be selected in the range from $0.3-0.38$ times the pin period in order to obtain the maximum achievable propagation frequency of the second mode at X point.

5.2.3 Structure Performance

The optimization of the pin surface has been realized in order to remove the resonances produced when packaging of the W-band auto-calibrated receiver. The demonstration that this periodic structure is able to suppress the propagation of unwanted modes has been done in simulation using Ansoft HFSS. First of all, the cavity which will contain the receiver has been designed. The considerations taken into account in this design have been:

- The two amplifier chains are placed into 0.127 mm width channels. Additional 1.27 mm width channels have been included in the middle of these amplifier channels in order to place the required series of surface mount capacitors, which feed the amplifiers. Therefore, the receiver cavity consists of two cavities connected by these channels. One quadrature hybrid coupler will be contained in each cavity.

- The pin surface is included in the upper metal plate of these cavities. Therefore, the side metal walls of these cavities have been separated in order to place an integer number of pin periods. For this reason, a gap exists between the substrate and the side metal walls of the cavities.

- With respect to the cavity which contains the input quadrature hybrid coupler, its side metal walls close to the transition are in contact with the substrate in order to facilitate its placement. This ensures an appropriate alignment of the WR10 waveguide to microstrip transition.

- Finally, more space are needed in the second cavity in order to place the detectors and also the bonds to the DC circuit which amplifies the output voltages of the receiver.

The dimensions of the cavity are shown in Fig. 5.14 a). Moreover, a detail of the microstrip part of the W-band auto-calibrated receiver placed into the

designed cavity, and its dimensions, can be seen in Fig. 5.14 b). Note that the empty spaces inside the channels in this Figure are for the placement of the LNAs. Moreover, the space between the second quadrature hybrid coupler and the side metal wall of the cavity is required in order to weld the detectors and connect them with the DC circuit. The placement of the MMIC components are shown in Fig. 5.14 c). In this Figure, the surface mount capacitors are included. Moreover, the holes needed to connect the feeding circuit to the amplifiers and the output voltages of the receiver to the post-processing circuit can be also seen.

In particular, only the microstrip structure of the receiver is taken into account in the simulation in order to demonstrate that the pin surface, which is implemented in the upper metal plate of the designed cavity, removes the propagation of undesired modes. This simplifies the problem because the MMIC components of the receiver are not included. Therefore, the two microstrip parts of the receiver have been connected by 50 Ω microstrip lines and the three ports of this structure have been defined as waveports in the simulation. In this way, two analysis have been carried out taking into account two packaging options; the first one uses a smooth surface in the upper metal plate of the cavity whereas in the second one the pin surface is inserted, see Fig. 5.15.

The comparison between transmission and reflection parameters of the microstrip part of the W-band auto-calibrated receiver inside this two packaging options are depicted in Fig. 5.16. Simulation results demonstrate that the resonances caused by the undesired modes within the cavity are removed when the pin surface is introduced in the upper metal plate of the cavity. The small losses observed in the transmission parameter in Fig. 5.16 a) are caused by both the dielectric substrate and the WR10 waveguide to microstrip transition.

5.2.4 Experimental Results

The experimental verification of the structure shown in Fig. 5.15 would be interesting to demonstrate the removal of the cavity resonances by using the pin surface in the upper metal plate of the packaging cavity. However, the microstrip part of the receiver configuration has three output ports which have to be perfectly matched and these matching loads were not available for this experiment. For this reason, an alternative circuit has been used in

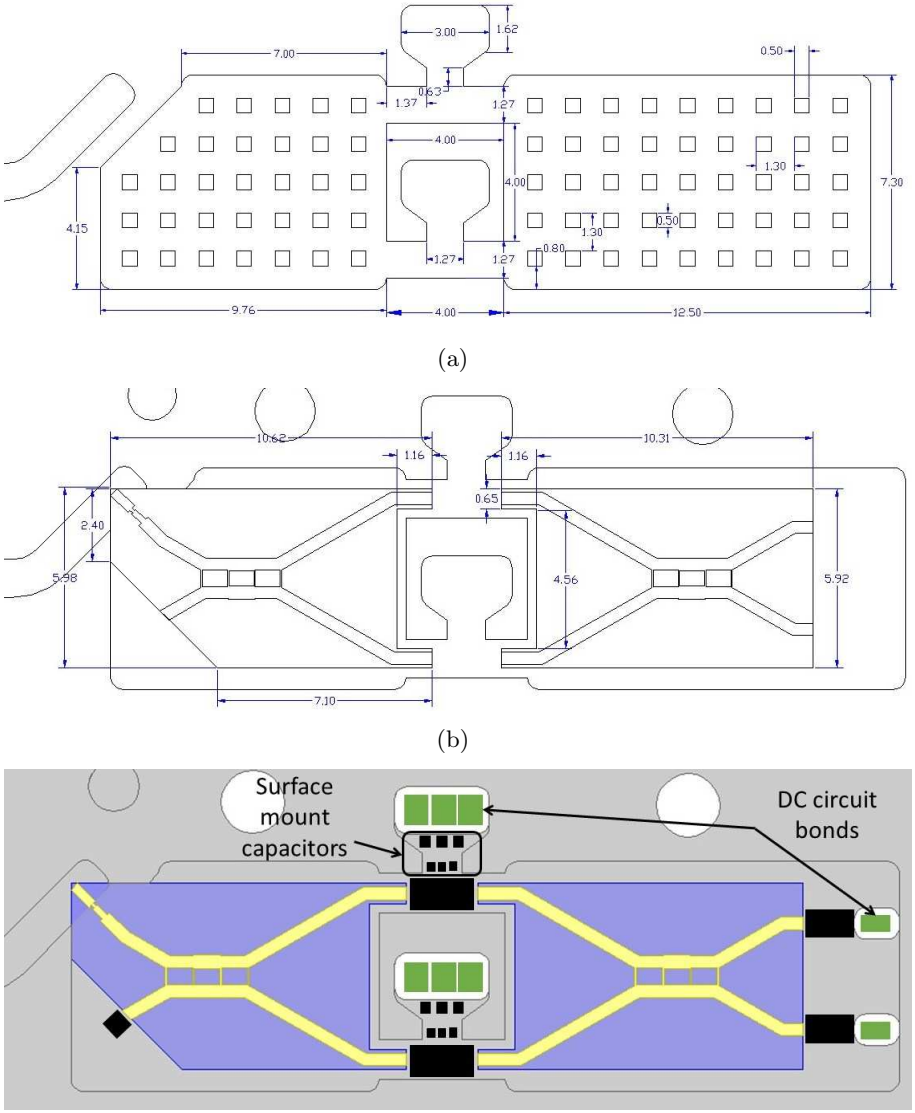

Figure 5.14 – Designed cavity which will contain the W-band auto-calibrated receiver; a) Top view of the cavity and its dimensions in mm, b) the detail of the placement of the microstrip part of the receiver into the cavity and its dimensions in mm and c) schematic of the W-band auto-calibrated receiver and its required components placed into the cavity.

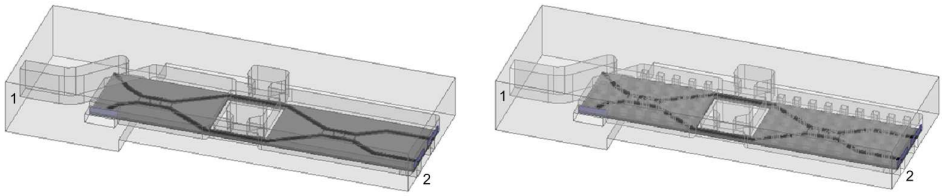

(a) (b)

Figure 5.15 – Schematic of the packaged W-band auto-calibrated receiver; a) smooth top metal plate. b) pin surface on the upper metal plate.

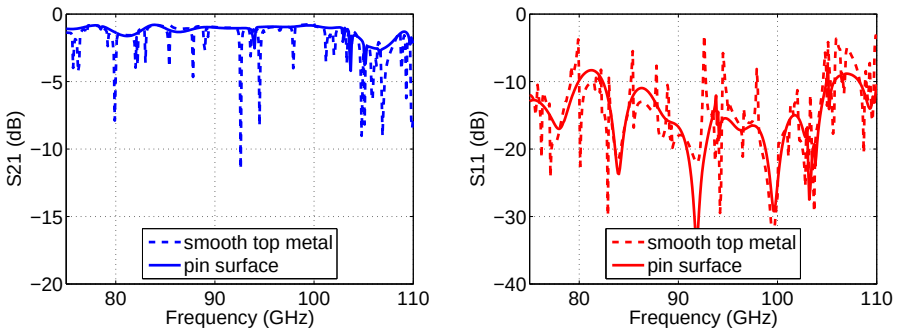

(a) (b)

Figure 5.16 – Comparison between the performance of the receiver when using a smooth surface metal package and a pin surface packaging; a) S21 and b) S11.

order to verify the pin surface behaviour. In order to excite the resonances a short microstrip line has been used, see Fig. 5.17. It consists of a transition from WR10 waveguide to microstrip and a 50 Ω microstrip line ended in open circuit. This open circuited line excites the resonances produced by the cavity. Thereby, the removal of these resonances with the pin surface can be checked by measuring the reflection at the waveguide input port.

A prototype of the packaging metal block for the W-band auto-calibrated receiver has been manufactured in aluminium using high precision milling. This packaging consists of two parts which are easily mounted through alignment pins and screws. The cutting plane of the packaging metal block in these two parts has been performed in accordance with the E-plane cut of the input waveguide to minimize losses. The bottom part has a cavity where the microstrip circuit is placed, see Fig. 5.17 a). Two different top parts have been manufactured in order to demonstrate the removal of the undesired resonances. The first one contains the smooth surface, whereas the second one implements the pin surface on its upper metal plate. Their photographs are shown in Fig. 5.17 c) and d). The short microstrip line was manually aligned and welded with silver epoxy adhesive to the bottom part as shown in Fig. 5.17 b).

Fig. 5.18 shows the comparison between the simulation and the measurement results of this packaged W-band microstrip line for the two packaging options. Some manufacturing errors in the microstrip circuit and also in its position have been detected and included in the simulation. In particular, the most relevant error is the 300 μm displacement of the microstrip circuit in the transition, caused by the manual assembly and by an error made in the substrate cutting. As can be seen, most of the resonances obtained with HFSS in the case of the smooth cavity appear in the measurements, see Fig. 5.18 a). Good agreement has been obtained in terms of the position of the resonances. In addition, the experiment confirms the removal of the resonances when the pin surface is used, see Fig. 5.18 b). However, there is a nearly constant difference in the reflection level of 1 dB, which can be ascribed to losses in the metal waveguide section. Apart from this difference, these results demonstrate experimentally that the pin surface removes the unwanted resonances.

Therefore, this designed cavity with a pin surface included in its upper metal plate will be used to package the W-band auto-calibrated receiver.

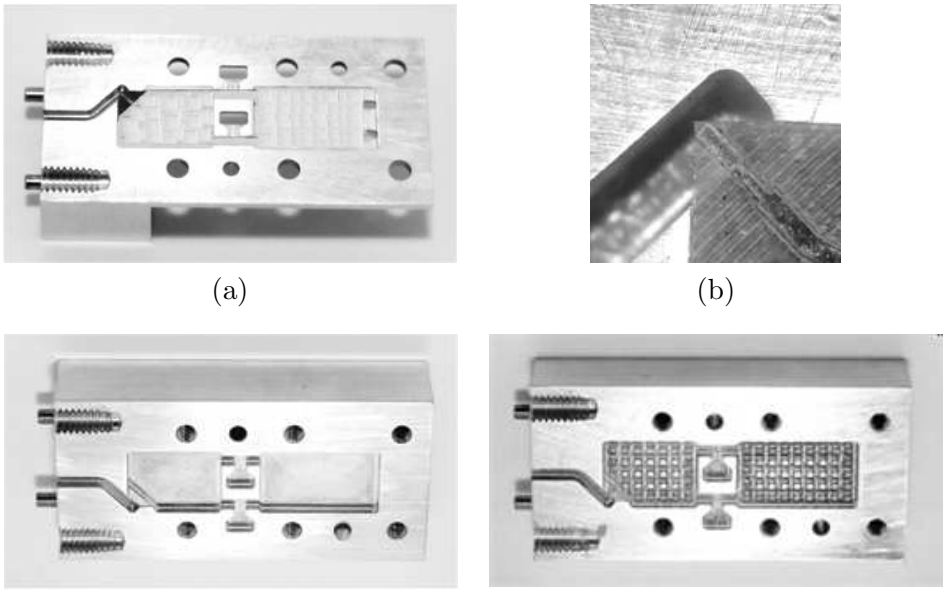

Figure 5.17 – Photographs of the manufactured packaged W-band microstrip receiver; a) bottom part with a microstrip line. b) detail of the transition from WR-10 to microstrip, c) top part with smooth metal surface and d) top part with pin surface.

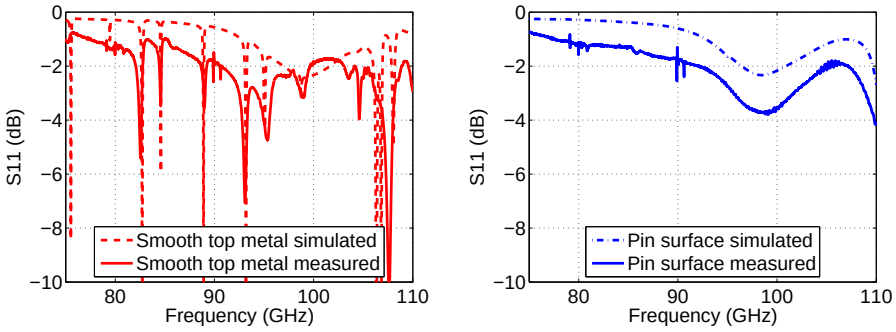

(a) (b)

Figure 5.18 – Comparison between simulated and measured results of the S11 parameter in the two packaging options: a) smooth metal and b) pin surface covers. Manufacturing errors in the microstrip circuit and in its position with respect to the input waveguide have been included.

5.3 Design of the DC circuit

Once the design of the cavity in which the planar structure of the W-band auto-calibrated receiver will be placed has been carried out, the whole packaging metal block can be designed. This metal block has to package the DC circuit and also it has to contain the WR10 flange required to connect the receiver with a standard horn antenna or waveguide based measurement equipment. Consequently, the DC circuit is the biggest component which has been packaged because of the size of the DC devices. Therefore, we start with the design of the DC circuit, which is explained in this Section.

The DC circuit of the W-band auto-calibrated receiver consists of two circuits. First, the DC bias circuit which polarizes and supplies the suitable current to the two amplifiers. The second part contains the filtering and the amplification of the output voltages of the receiver. The design of these circuits has been carried out using the software LTSpice of Linear Technology starting from a 5 V voltage, which is supplied by a single power source.

5.3.1 Bias circuit for the MMIC Low Noise Amplifiers

The LN4-110 has three bonds to bias: a single drain, an independent gate bias for the first stage and a common gate bias for the remaining stages. With

respect to the optimized point of their performance, the transient of the bias circuit has to comply with the following sequence:

- While the supplied drain voltage is 0 V, the voltages in both gates have to decrease at least up to −1 V. Note that the supplied current in every bond has to be zero. These gate voltages polarise the transistors of the amplifier.
- When the gate voltages are −1 V, the drain voltage is activated. The value of this voltage has to be fixed to 1.2 V, which creates the channel in the transistors of the amplifier.
- Once the channels are created, the current has to be supplied in the drain bond. It is carried out by increasing the gate voltages up to a value in which the supplied current in the drain is 35 mA. The drain voltage is kept to 1.2 V. In order to know these required gate voltages, the current in the drain bond has to be simultaneously measured. These voltages can differ from one amplifier to another.

The performance of this designed circuit is briefly explained right after. This circuit consists of two main blocks. First, the block which supplies the stable drain voltage, i.e. 1.2 V, and the second part is the block which provides the voltages to the gates. In addition, these two blocks are connected by a zener diode and a npn transistor in order to control their activations and consequently the creation of the required transient. Moreover, the possibility to adjust the voltages of the gates independently is performed by two potentiometers. These potentiometers are connected to a resistance net. And these nets are connected to two voltages: the stable voltage drain, i.e. 1.2 V, and a negative voltage high enough to allow the application of at least −1 V in the gates. The potentiometer based net of a gate voltage is shown in Fig. 5.19.

The stable drain voltage is supplied by the LT3020-1.2V low dropout linear regulator whose input voltage has to be also stable. This selected input voltage is 3.3 V, and it is obtained from the 5 V, supplied input voltage of the circuit. This is done by a LT1761-3.3V low noise micropower regulator. This part of the circuit can be seen in Fig. 5.20 a). Note that the IN and the $\overline{SHDN}$ contacts of the LT3020 component are connected. As later on will be shown, this connection will be changed when the whole circuit is designed.

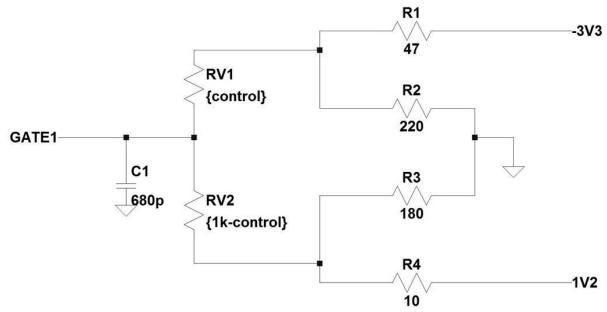

Figure 5.19 – LTSpice schematic of the output net of the gate voltage, which can be adjusted by the RV potentiometer.

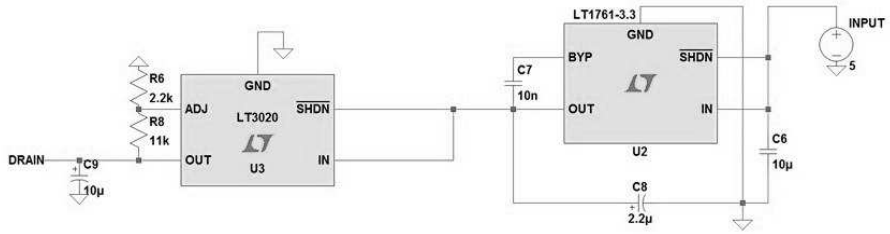

(a)

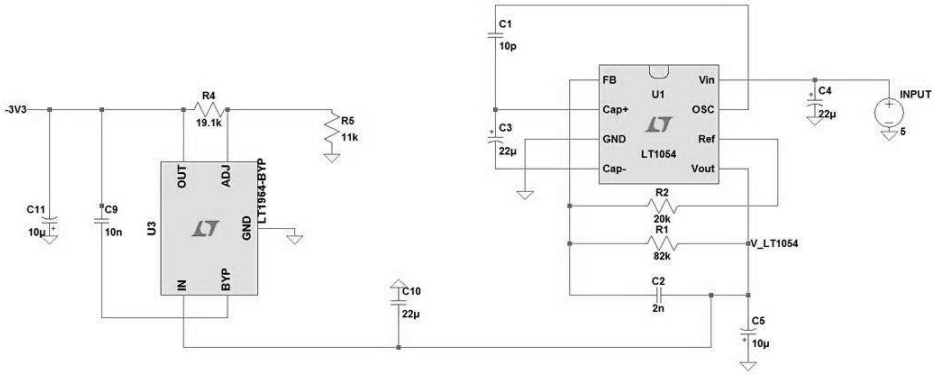

(b)

Figure 5.20 – The two blocks which are part of the DC bias circuit of the LN4-110 amplifiers; a) the block which supplies the drain voltage and b) the block which provides −3.3 V required to provide the negative gate voltages.

With respect to the gate voltages, starting from the 5 V supplied input voltage, a negative voltage high enough to supply at least −1 V on the gate bonds, i.e. the negative voltage connected to the potentiometer output net, is required. The selected negative voltage has been −3.3 V because this is also the rupture voltage of the zener diode, which controls the activation of the drain voltage. This part of the circuit is shown in Fig. 5.20 b). It consists of a LT1054 voltage converter and the LT1964 module which provides the desired −3.3 V by means of a voltage divider connected to its ADJ bond. Moreover, an 10 μF output capacitor has been used in order to obtain the required transient response.

Therefore, these two blocks are connected by a −3.3 V zener diode which controls a npn transistor. These components are placed between the output of the second block of the circuit, see Fig. 5.20 b), and the $\overline{SHDN}$ contact of the LT3020, which are part of the first block of the circuit, see Fig. 5.20 a). This can be seen in the LTSpice schematic of the complete bias circuit of one LN4-110 amplifier in Fig. 5.21. These components, in addition to the transient response of the output of the second block, delay the activation of the LT3020 block until the voltage in its $\overline{SHDN}$ contact is identical to the voltage in its input, i.e. 3.3 V. As can be seen in the Figure, two output potentiometers nets have been included in order to supply independently the required two gate voltages for one amplifier.

The designed bias circuit is capable of feeding at least two LN4-110 amplifiers, which is a requirement for the W-band auto-calibrated receiver. To this aim, the drain bond and also the potentiometers which provide the gate voltages have been duplicated in the final design of the bias circuit of the two amplifiers, which are part of the W-band auto-calibrated receiver. The gate potentiometers have been included to adjust these voltages independently for each amplifier.

Regarding the performance of this circuit, Fig. 5.22 a) shows its simulated output voltages. As can be seen, the required sequence for the drain and gate voltages is provided. Before the activation of the drain voltage, it is not exactly zero but it is within its acceptable range. This range is specified in the datasheet of the LN4-110 component. The maximum simulated drain voltage in this inactivated state is 0.3 V whereas its maximum acceptable value is 0.5 V. With respect to the gate voltages, they decrease up to −1 V and when the drain voltage is activated, they increase. These gate voltages can be controlled by the potentiometers in order to change their values

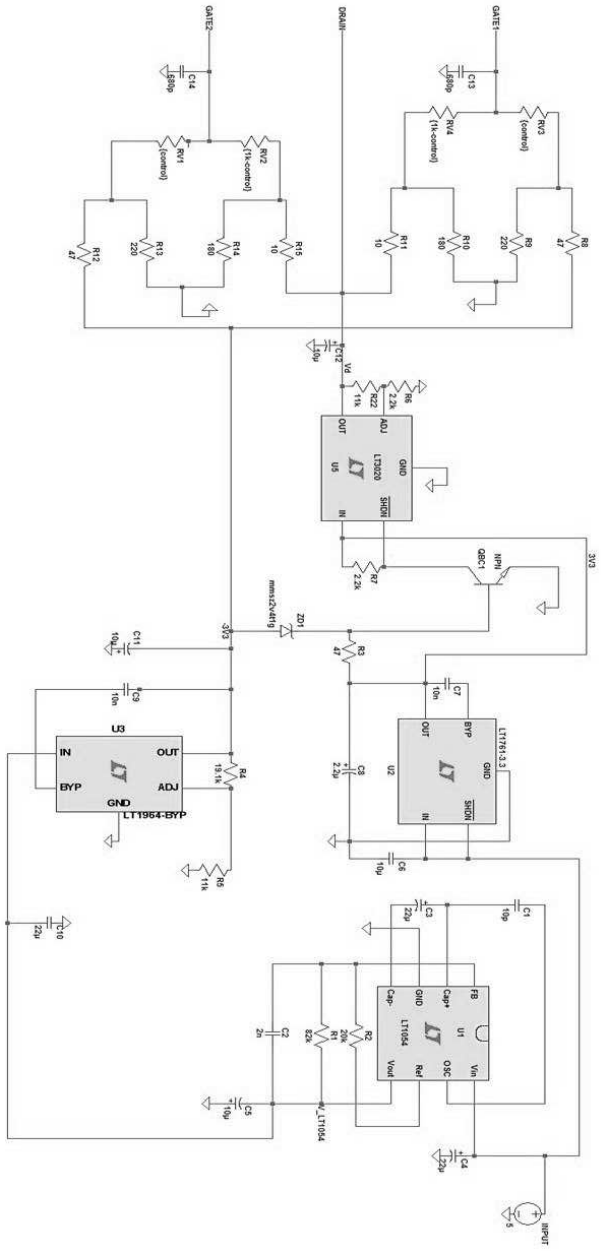

Figure 5.21 – LTSpice schematic of the DC bias circuit of one LN4-110 amplifier.

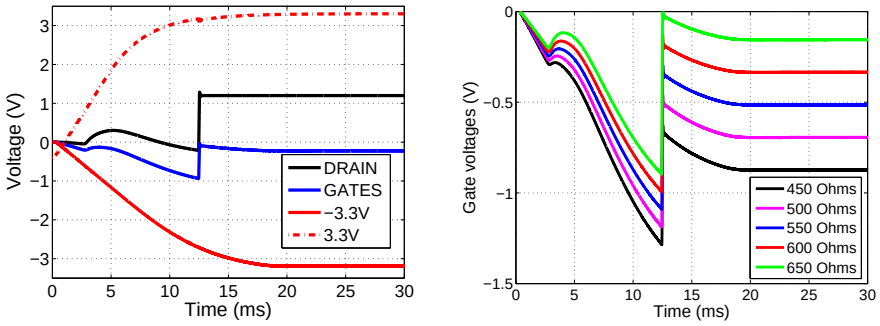

(a) (b)

Figure 5.22 – Simulated performance of the DC bias circuit of the LN4-110 amplifier; a) output voltages of the circuit and b) gate voltage as a function of the potentiometers resistance, i.e. RV1 and RV3 in the schematic shown in Fig. 5.21.

in the stationary state. These values can never reach 0.2 V according to the datasheet. On the other hand, the gate voltages as a function of the potentiometers resistances, i.e. RV1 and RV3 in the schematic shown in Fig. 5.21, are depicted in Fig. 5.22 b). As shown, the gate voltage is capable of decreasing around −1 V whereas its value in the stationary state is between −0.15 and −0.85 V, which is enough to supply the suitable current to the amplifier. In conclusion, the designed circuit works as expected.

5.3.2 Post-processing circuit of the output voltages of the receiver

The design of the post-processing circuit of the output voltages of the receiver is simpler than the design of the bias circuit of the amplifiers. The aim is to amplify the output signals of the detectors and filter them. A priori, the required amplification of this circuit is unknown. However, a quick estimation of this can be done roughly.

For instance, a target is supposed to be an object with a specific temperature, i.e. T_0, which according to Planck's radiation law [185] emits an electromagnetic power given by:

$$P = \frac{2h}{c^2} \int_{75GHz}^{110GHz} \frac{f^3}{e^{\frac{hf}{kT_0}} - 1} df \tag{5.1}$$

Where k is Boltzmann's constant, i.e. $1.38 \times 10^{-23}\ J/K$, and h is Planck's constant, i.e. $6.63 \times 10^{-34}\ Js$. If the temperature is $T_0 = 290\ K$, the power emitted would be 27.67 μW at W-band. The electromagnetic waves will be spread out when they travel through the air and suffer an attenuation, i.e. $\alpha = \frac{1}{4\pi d^2}$. Therefore, the input power to the receiver is defined by $P_{in} = \alpha P A_{eff}$ since $A_{eff} = \frac{G\lambda^2}{4\pi}$, i.e. the effective area of the antenna. The distance between the target and the antenna is assumed to be $d = 1$ m and the gain of a standard horn antenna at W-band is 20 dB. Taking this into account, the input power of the receiver at W-band is approximately 184 pW, i.e. -67.35 dBm. According to the ADS simulation shown in Section 3.4, the W-band auto-calibrated receiver has a maximum gain between the WR10 waveguide to microstrip transition and the detectors of 20 dB, considering ideal connections between components. Therefore, the input power of the detectors is -47.35 dBm. Assuming that the typical sensitivity of the detectors is $\beta = 7\ V/mW$, the output voltage of the receiver is 129 μV.

The measured voltage of the receiver when it is focused on a target with $T_0 = 290\ K$ is desired to be 0.1 V, therefore, the minimum required gain of the post-processing circuit is 777. However, this calculation has been carried out taking into account an ideal performance. If losses are included, the required amplification will be higher. Therefore, the post-processing gain has been designed to be externally controlled by one potentiometer per output voltage, i.e. the reference and the signal outputs.

Therefore, the post-processing circuit consists of an operational amplifier for each output voltage, whose gain is controlled by a potentiometer, and a subtracter, which performs the subtracting operation of the W-band auto-calibrated receiver. A low-pass filter is implemented in each output of the post-processing circuit, i.e. the reference, the signal and the difference between the signal and the reference. Note that the outputs of the whole receiver are these three voltages. The first two have been defined in order to test the performance of the receiver. The last one is the desired auto-calibrated output, i.e. the difference between the signal and the reference.

Fig. 5.23 shows the designed post-processing circuit. As can be seen,

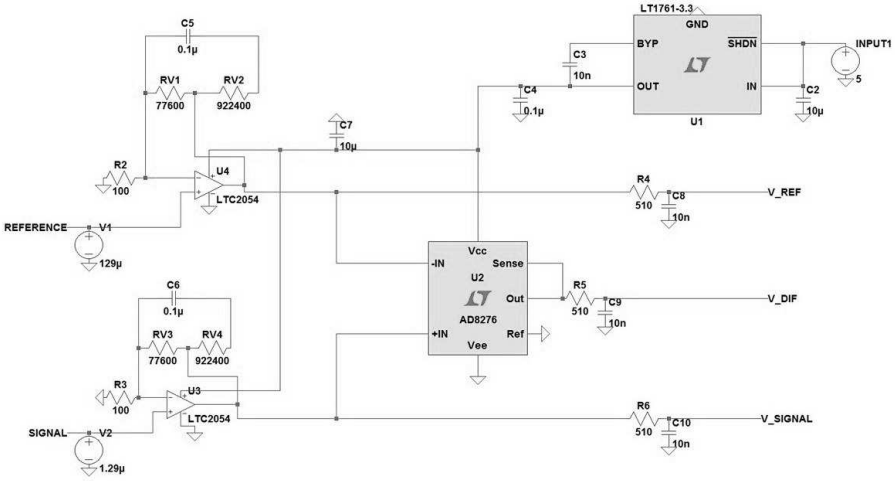

Figure 5.23 – LTSpice schematic of the post-processing circuit of the detectors outputs.

LTC2054 modules amplify the output voltages of the detectors and a AD8276 unity-gain difference amplifier performs the subtracting operation. These blocks require to be fed by 3.3 V, obtained from the LT1761 module since the input voltage of 5 V. The designed low-pass filters have a cutoff frequency of approximately 31 KHz.

If the output voltages of the detector in the reference and signal branches are defined as 129 μV and 1.29 μV respectively, the obtained post-processing circuit output voltages are those depicted in Fig. 5.24. Note that the depicted transitory is only related to the defined simulation. As can be seen, the output voltage in the reference and in the signal are 100.35 mV and 1.13 mV. Therefore, the LTC2054 is capable of detecting the input voltage defined in the signal branch. Due to the fact that the signal voltage is smaller than the reference voltage, the difference between signal and reference voltages is negative, i.e. -99.22 mV.

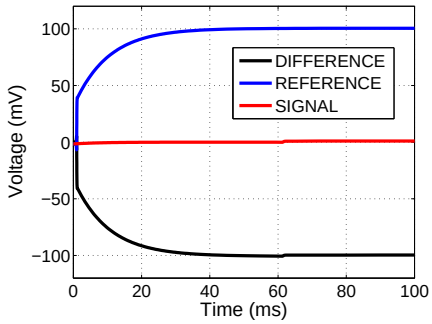

Figure 5.24 – Output voltages of the DC post-processing circuit of the W-band auto-calibrated receiver, which is shown in Fig. 5.23.

5.3.3 Complete DC circuit of the W-band auto-calibrated receiver

The two main blocks of the DC circuit of the receiver have been designed. Next, these two blocks have been arranged into the same PCB.

The PCB which contains these two circuits has to be also packaged. Therefore, its dimensions will depend on the packaging metal block. The main limitation is the width of the PCB, which is limited by the WR10 flange, i.e. 19.05 mm width, because it defines the minimum distance between two receivers on an array implementation, which has to be as small as possible. On the other hand, the length of the PCB is not limited. It depends only on the minimum space required by the whole circuit.

Taking into account the packaging cavity of the W-band auto-calibrated receiver, the bias of the amplifiers and also the bonds to the detector outputs have to be placed in the same layer of the PCB. Indeed, this layer will be in contact to the metal in which the receiver is placed on to. Thus, this bottom layer can not contain any of the components of the DC circuit. Therefore, all the devices are welded on the other side of the circuit, i.e the top layer.

In order to comply with the mentioned requirements, a four layer PCB has been designed using the CadSoft Eagle v6.0 PCB design software. This PCB is built in FR4 and its thickness is 1.55 mm. It consists of:

- A top layer, see Fig. 5.25 a). This layer contains all the components of the two blocks of the circuit. The PCB dimensions are specified in

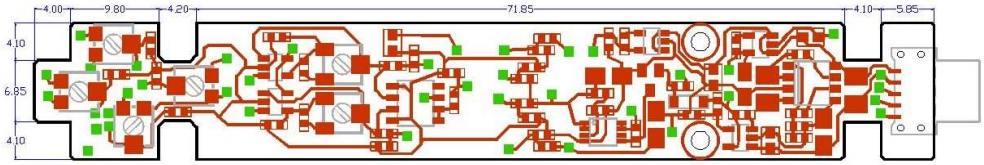

(a) Top layer

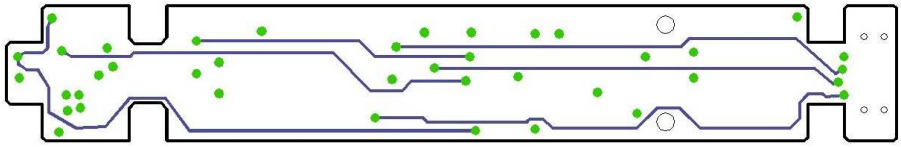

(b) Inner layer 1

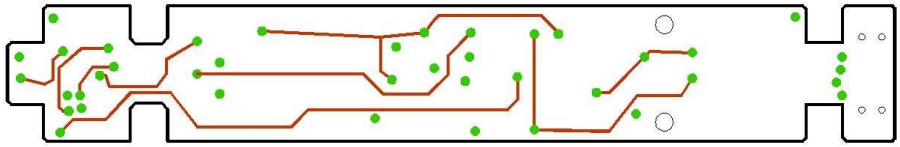

(c) Inner layer 2

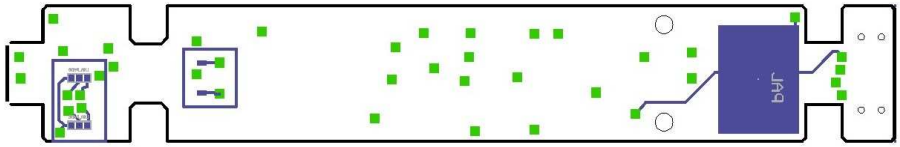

(d) Bottom layer

Figure 5.25 – Designed PCB of the DC circuit of the W-band auto-calibrated receiver and its dimensions in mm.

this Figure, i.e. 15.05 mm width and 99.8 mm length. As can be seen, the PCB is not a rectangle. The substrate has been removed in some parts of the PCB because some screws of the packaging will be placed there. Moreover, two screws, which are defined as two big circles in the middle of the PCB, will ensure the right placement of the circuit in the packaging. The other four small circles in the right part of the PCB are required to weld the connector.

- A bottom layer, see Fig. 5.25 d), which contains the pads of the amplifier bias and detectors which are placed inside the two blue rectangles at the left part of the PCB. The placement of these pads run exactly into the holes of the packaging cavity of the receiver, as shown in Fig. 5.14 c). Taking advantage of the fact that this layer is in contact to the metal block, a big ground pad, i.e. the blue filled rectangle in the Figure, has been placed in order to ensure the ground connection by welding.

- Two inner layers, see Fig. 5.25 b) and c), needed to do the remainder connections. The green squares and circles are the required vias.

The designed PCB has been manufactured by Eurocircuits [186] with a surface finish of chemical Ni/Au in order to facilitate the gold wire bondings between the detectors and the pads of the post-processing circuit and also between the surface mount capacitors and the pads of the bias circuit of the amplifiers. A photograph of the top layer of two manufactured PCBs are shown in Fig. 5.26. The surface finish of gold can be seen in the first one whereas in the second one, all the components have been welded, even the selected connector, i.e. SFM-105-02-L-DH-TR of Samtec [187].

The designed bias circuit of the amplifiers which is contained in the manufactured PCB has been characterized obtaining the desired performance. Fig. 5.27 shows the measured output voltages of the bias circuit of the amplifiers in the ON and OFF states, which have been measured for two reasons. First, to obtained the transitory state of the circuit and secondly, to check that the OFF state is inverse to the ON state, which is required to reset the MMIC amplifiers. As can be seen, both the drain and gates voltages have the desired transitory state. Moreover, the difference between the minimum voltages measured in the gates in these two states, i.e. -1.3 V in the ON state and -0.8 V in the OFF state, is caused by the potentiometers resistances. They are 500 Ω in the ON state whereas they are 650 Ω in the OFF state.

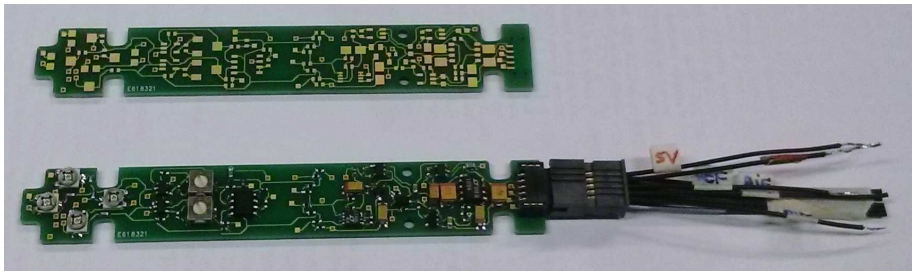

Figure 5.26 – Photograph of two manufactured PCBs, one of them with all the components welded.

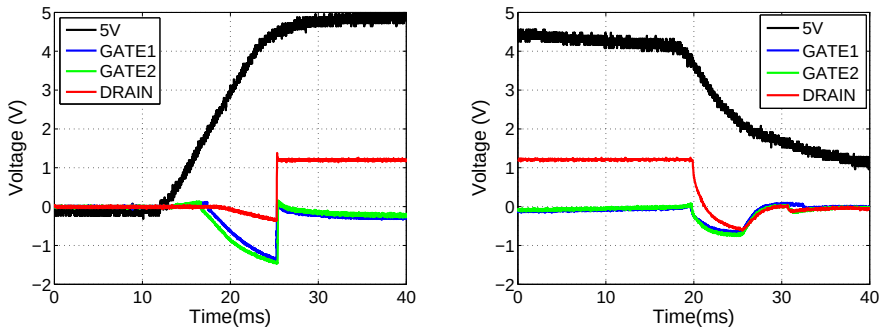

Figure 5.27 – Measured output voltages of the bias circuit of the low noise amplifiers included in the manufactured PCB of the W-band auto-calibrated receiver; a) ON and b) OFF stage.

These results are consistent with the simulated gate voltages as a function of the potentiometer resistance shown in Fig. 5.22 b). Therefore, the design, the manufacture and the assembly have been validated.

5.4 Design of the packaging metal block

At this point, the design of the metal block which packages all the components of the W-band auto-calibrated receiver can be carried out. These components are the inner cavity which contains the planar structure of the receiver and the designed DC circuit. Moreover, the WR10 flange has to be also included.

This flange determines the width of the packaging metal block and the DC circuit defines its length.

This metal packaging which consists of two main blocks can be seen in Fig. 5.28. The top block contains the planar structure of the receiver on one side, see Fig. 5.28 b), and packages the DC circuit on the other side, in green in Fig. 5.28 a). The designed DC circuit has vias in its bottom layer, i.e. the layer which will be in contact to the metal block, thereby the metal has been partially removed creating a gap between the PCB and the metal block. This can be seen in Fig. 5.28 a) in which a rectangular shape is shown under the DC circuit in the top block of the packaging. This is also done where the DC circuit has the feeding contacts of the amplifiers and the bonds of the detectors outputs. Moreover, a cover has been included to protect the DC circuit. The selected connector is also shown in the top block in Fig. 5.28 a) in which part of the metal has been removed in order to connect the back part of the connector. With respect to the bottom block of the packaging, it contains the top part of the cavity in which the pin surface is inserted.

These two parts have been split according to the E-plane of the WR10 waveguide in order to minimize the losses. As can be seen the WR10 waveguide has been bent in order to centre the WR10 flange included in the packaging. This minimizes its size. Moreover, twelve screws hold together these two blocks. Indeed, two of these screws fit the DC circuit to the top block to ensure its proper placing. However, the ground contact between the DC circuit and the metal block will be carried out by welding these parts with silver epoxy adhesive. On the other hand, the alignment of these two blocks of the packaging is done by four dowel pins as shown in the bottom block in Fig. 5.28 a).

With respect to the external shape of the packaging, four dowel pins for each side have been included to facilitate the assembly of several packaged W-band auto-calibrated receivers in an array configuration. It has been carried out in such a way that two different array configurations are feasible, as shown in Fig. 5.29. These array configurations are based on square and hexagonal implementations. As can be seen, in the external side of the bottom block of the packaging, two parts of metal have been removed because the four screws which fit the cover protrude from the block.

The dimensions of each metal block are shown in Appendix B. The total dimensions of the packaging metal block are 130.5 mm length and 19.05 mm width and height. All the dowel pins have a diameter of 1.6 mm and a length

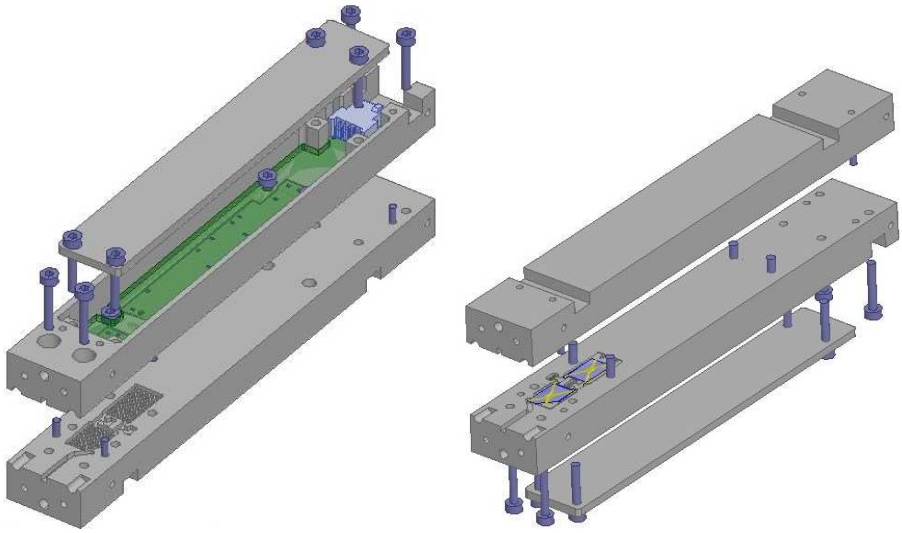

(a) Top view (b) Bottom view

Figure 5.28 – Designed packaging of the W-band auto-calibrated receiver; a) top and b) bottom view of the blocks which are part of the packaging. The DC circuit and the connector are included.

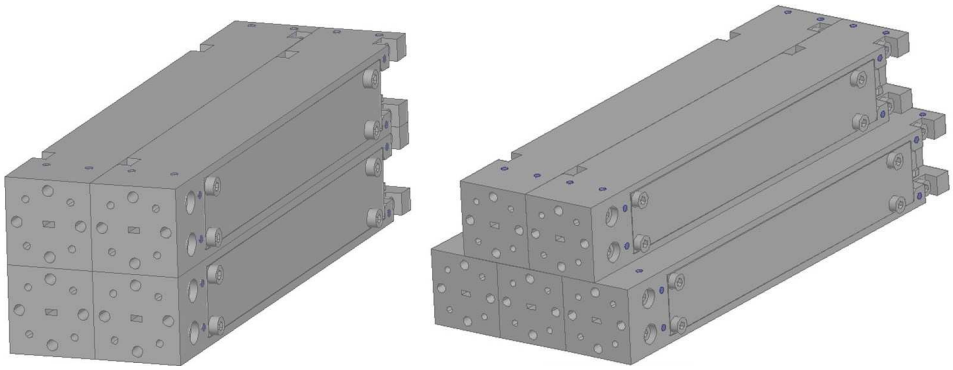

(a) (b)

Figure 5.29 – Feasible array configurations of W-band auto-calibrated receivers; a) square and b) hexagonal array.

of 8 mm and the screws are M2 with different lengths, i.e. eight screws of 12 mm and four of 6 mm. The shorter ones are those placed inside the cavity of the DC circuit. With respect to the flange is a standard WR10 flange whose width is 19.05 mm. It consists of the WR10 waveguide which has four 4-40 UNC-2B screws and four dowel pins. The dimensions of the cover are 100.63 mm length, 15.98 mm width and 2 mm thick.

5.5 Conclusions

In this Chapter, the design of the cavity which packages the planar structure of the W-band auto-calibrated receiver has been presented. This cavity uses an innovative solution in order to prevent resonances which degrade the receiver performance. The propagation of parallel-plate modes is blocked within a certain frequency band (stop-band) by means of a periodic structure placed in the top ground plate of this cavity. In particular, the selected periodic structure is based on a square pin surface. For the first time, a deep understanding of the behaviour of its modes and the influence of the different parameters on its performance have been shown in this Chapter. Besides, as a result of the acquired knowledge in the complete parametric study, the design guidelines of this pin surface have been defined in order to create a certain stop-band. Moreover, a prototype has been manufactured and assembled and the removal of the propagation of cavity modes has been demonstrated experimentally. At that point, the design of the last components of the W-band auto-calibrated receiver has been carried out, i.e. the DC circuit and the packaging aluminium block which will contain all the components. The DC circuit consists of two blocks: the circuit of the amplifiers and the DC output amplification circuit. Finally, the packaging metal block of the W-band auto-calibrated receiver has been designed considering the implementation of both square and pyramidal arrays of receivers.

Chapter 6

Assembly and characterization of the W-band auto-calibrated receiver

6.1 Introduction

This Chapter presents the assembly of the components which are part of the W-band auto-calibrated receiver, the realization of the connections with gold wire bonding, the bias process of the low noise amplifiers and the characterization of the W-band auto-calibrated receiver.

The components of the W-band receiver are the packaging metal block, the microstrip circuit which contains the WR10 waveguide to microstrip transition and the quadrature hybrid couplers, the DC circuit and the MMIC devices, i.e. the low noise amplifiers and the detectors. With respect to the DC circuit, its components have been welded and its performance has been validated in Chapter 5. Moreover, the MMIC devices are now available. Therefore, the only two components of the receiver required to be manufactured are the packaging metal block and the microstrip part. Their manufacturing and also the assembly of the components in the packaging metal block are presented in this Chapter. Moreover, the realization of the bondwire connections using the TPT HB16D bonder machine is commented.

Next, the bias process of the low noise amplifiers is explained. Once it is done, the measurement of the performance of the designed W-band auto-calibrated receiver is carried out in terms of input reflection coefficient, dynamic range, RF-DC response, effective bandwidth and equivalent noise temperature.

6.2 Manufacturing and assembly of the W-band auto-calibrated receiver

In this Section, the assembly of the components which are part of the W-band auto-calibrated receiver and the manufacturing of some components are presented. Indeed, the components which are needed to be manufactured are the packaging metal block and the microstrip part of the receiver.

Regarding the packaging aluminium block, it has been manufactured by UTILMET S.L. [188] using a high precision milling technique. The three parts of the packaging, which are the top and bottom blocks and the cover, are shown in Fig. 6.1. As can be seen in Fig. 6.1 a), the pin surface is included in the top layer of the inner cavity in which the planar receiver has to be contained. This pin surface is placed in the top block of the packaging. Moreover, the gaps milled inside the cavity in which the DC circuit has to be welded can be seen in the bottom block of the packaging, see Fig. 6.1 d). These gaps avoid the contact between some signal vias of the DC circuit and the metal block. The dimensions of the manufactured blocks have been validated.

With respect to the microstrip part of the W-band auto-calibrated receiver which contains the WR10 waveguide to microstrip transition and the input and output quadrature hybrid couplers, it is built on 0.127 mm thick RO5880 substrate. It has been manufactured with a LPKF ProtoLaser 200 micromachining system, see Fig. 6.2 a), and the outer cut has been carried out with a DAD320 dicing machine, see Fig. 6.2 b).

Once these components have been manufactured, the assembly of the components which are part of the W-band auto-calibrated receiver into the packaging aluminium block can be carried out. These components are the DC circuit, the microstrip part and the MMIC devices. All of them have been welded to the packaging using EPO-TEK-H20E silver loaded epoxy adhesive. This provides the same ground contact to all components. Once one component is positioned and aligned in the metal block, the block is

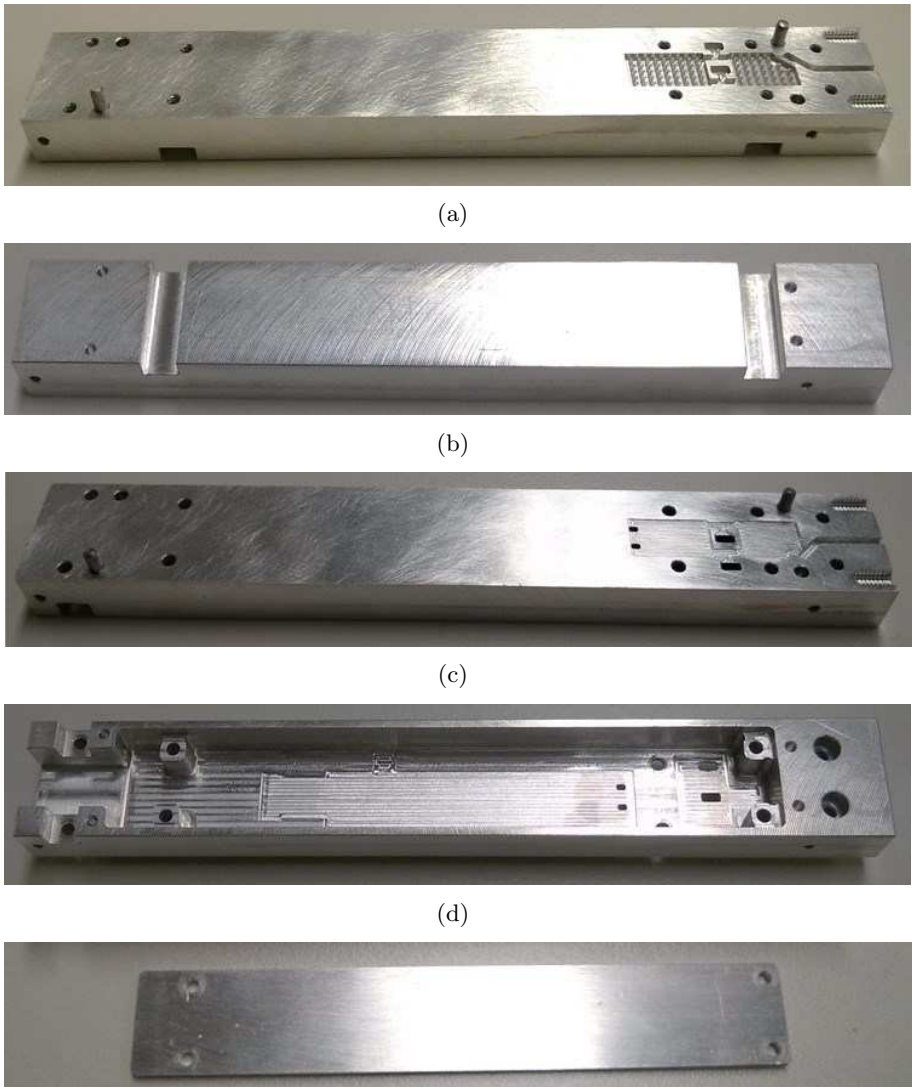

(a)

(b)

(c)

(d)

(e)

Figure 6.1 – Photographs of the manufactured aluminium packaging block: a) interior and b) exterior view of the top block of the packaging; c) interior and d) exterior view of the bottom block of the packaging and e) the cover.

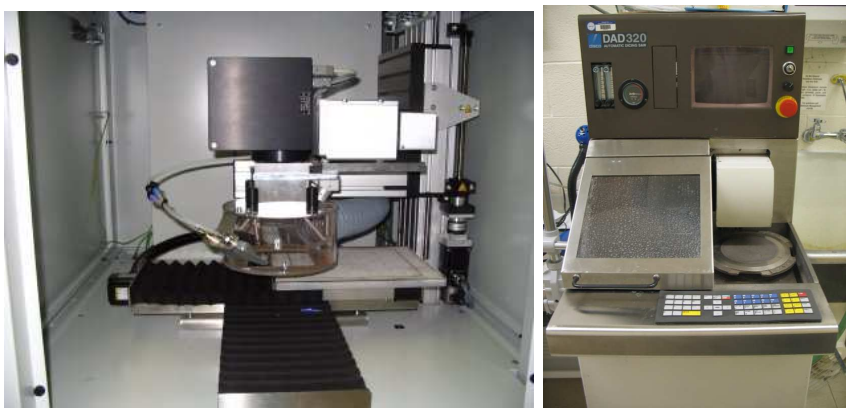

(a) (b)

Figure 6.2 – Photographs of the a) LPKF Protolaser 200 laser milling machine and b) DAD320 Automatic Dicing machine.

warmed up to 100° C during two hours in order to cure the epoxy. Therefore, the assembly of the components is carried out step by step, i.e. component to component, due to two reasons. The first one is that the DC circuit is on the opposite side of the planar receiver. In addition, this process avoids the unneeded overheating of the MMIC devices which could damage them.

Firstly, the DC circuit is welded using epoxy adhesive in its cavity, which is placed in the bottom block of the packaging. It has to be done taking into account two aspects. The first one is that the big ground pad of the DC circuit has to be in contact with the block to ensure the same ground contact. And the second aspect is that the bias pads of the amplifiers and the pads of the detectors have to be aligned in their holes in order to allow the realization of the required bondwires. The second component to be welded is the microstrip circuits. And finally, the MMIC devices can be positioned. The alignment of these last components is critical because the distance between the input and output microstrip lines has been fixed in order to shorten the required bondwires. Therefore, this alignment is carried out by means of the pick and place tool of the TPT HB16D bonder machine. Some photographs of these three assembly steps are shown in Fig. 6.3. The position of the pads of the DC circuit in their holes is shown in this Figure.

Once the components have been assembled, it is important to fit the gate

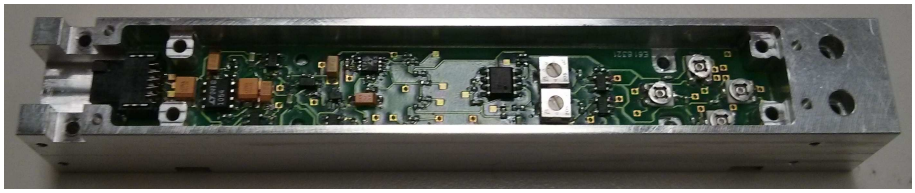

(a)

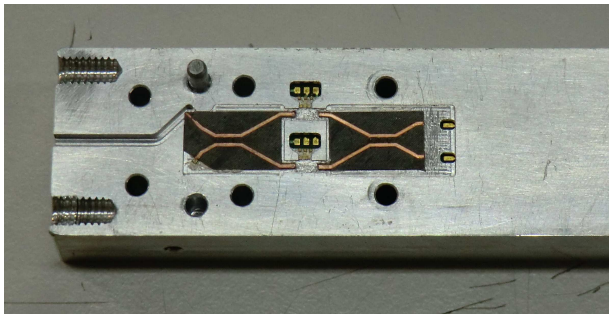

(b)

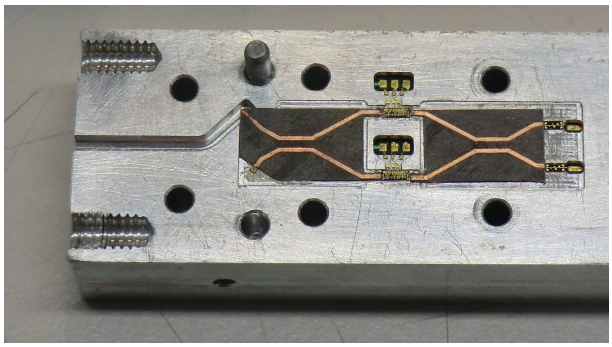

(c)

Figure 6.3 – Photographs of the assembly steps; the assembly of a) the DC circuit, b) the microstrip part of the receiver and c) the MMIC devices.

voltages provided by the DC circuit up to a value in which the amplifiers are in OFF states, i.e. -0.5 V, in order to protect them. Next, the required bondwires are done by the TPT HB16D bonder machine using its wedge tool and a 25 μm diameter gold wire. Fig. 6.4 shows photographs of the assembled components of the receiver. The gold wire bondings are shown in this Figure. As can be seen in Fig. 6.4 a) and b), two bondwires have been used to guarantee the connections in the bias pads of the amplifiers. In addition, the drain bias connections of the amplifiers are crossed due to a mistake in the placement of these pads in the DC circuit. The ground pads of the coplanar lines in the detectors and attenuator have been bonded to the metal block, see Fig. 6.4 c), d) and e). Finally, Fig. 6.4 f), g) and h) show the alignment of the transition and the input and output quadrature hybrid couplers of the microstrip part of the receiver. As can be seen, the last two components have been properly manufactured.

After the connections have been verified, the bias process of the LNAs can be done. The optimum operating point of these amplifiers is characterized by a drain current of 35 mA. Therefore, the bias process process consists of adjusting the gate voltages provided by the DC circuit up to values in which the drain current of the amplifier is that required. Consequently, the set-up shown in Fig. 6.5 a) is implemented to activate the amplifiers. This set-up facilitates the gate voltage adjusting while the drain current is being directly measured in the drain bias. This measurement is done by means of two tips which are placed in each capacitor of the drain bias, see Fig. 6.5 b), because the accuracy of the available multimeter is not enough to measure the current consumption of the DC circuit in the power supply source. Moreover, the potentiometers which control the gate voltages of the DC circuit have to be accessible in order to allow their adjustment, as it is shown in Fig. 6.5 c).

Before the bias process of each amplifier, it is verified that the current consumption of the DC circuit is identical to the current consumption of the DC circuit when the amplifiers are not connected, i.e. 0.23 A. This check implies that the amplifiers are in OFF state as expected. After that, the bias process is simple. Once the DC circuit is powered, the gate voltages of one amplifier have to be increased up to a values in which the drain current is 35 mA. Remember that the amplifiers have two gate voltages. Therefore, in order to simplify the process, these two voltages are simultaneously increased. When one amplifier is in its optimum operating point, i.e. its measured drain current is approximately 35 mA, the current consumption of the power supply

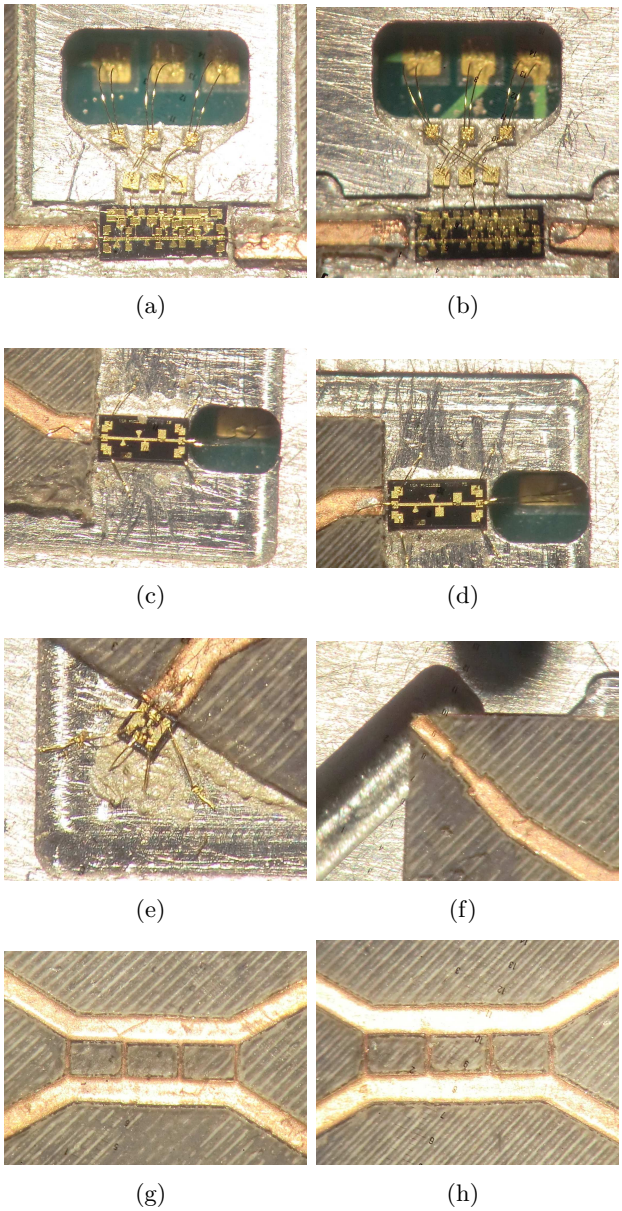

Figure 6.4 – Photographs of the assembled components of the W-band auto-calibrated receiver: a) and b) low noise amplifiers, c) and d) detectors, e) attenuator, f) WR10 waveguide to microstrip transition, g) and h) input and output W-band quadrature hybrid couplers.

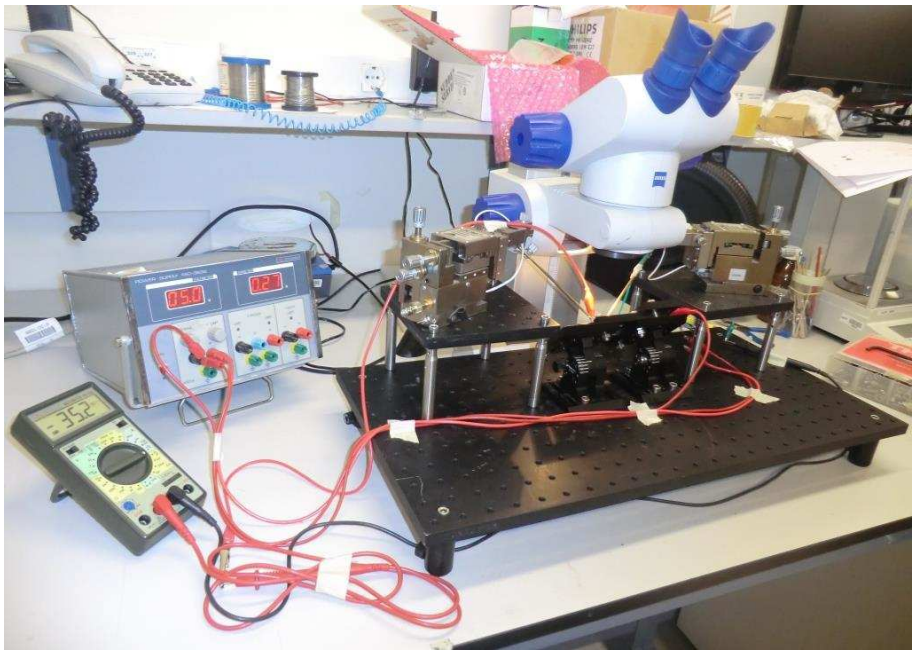

(a)

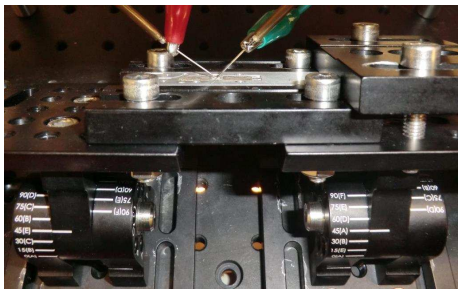

(b)

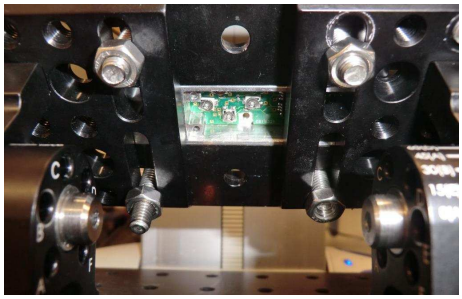

(c)

Figure 6.5 – Photographs of the amplifier gate voltages adjustment set-up.

source is 0.27 A, as can be seen in Fig. 6.5 a). This corresponds to the current consumption of the DC circuit itself in addition to the drain current consumption of one amplifier. Next, the other amplifier is connected to the tips and the process is repeated. In this implementation, the optimum gate voltages for the two amplifiers are −0.1 and 0.05 V respectively.

Once it is finished, the packaging metal block of the W-band auto-calibrated receiver is closed and ready for characterization with WR10 waveguide based equipment.

6.3 Characterization of the W-band auto-calibrated receiver prototype

The characterization of the W-band auto-calibrated receiver is carried out in terms of input reflection coefficient, dynamic range, RF-DC response, effective bandwidth and equivalent noise temperature.

This characterization is indispensable in order to calculate the sensitivity of the proposed receiver, i.e ΔT_{min}, see Eq. 1.12. It mainly depends on the effective bandwidth and the equivalent noise temperature of the receiver, i.e. B_{HF} and T_{SN} respectively. On the one hand, the RF-DC response is required to obtain the effective bandwidth as explained below. On the other hand, the measurement of the equivalent noise temperature is carried out using the Y-factor method which can be done taking into account the dynamic range of the receiver.

The measurement set-ups and the results are explained below.

6.3.1 Reflection coefficient

For the input reflection coefficient measurement, the W-band auto-calibrated receiver is powered at least half an hour before the connection to the equipment in order to stabilize its performance. The current consumption of the receiver is approximately 310 mA, which is the same consumption of the designed DC circuit itself when the amplifiers are activated, as shown in the previous Section.

A photograph of the set-up which carries out the reflection coefficient measurement of the receiver is shown in Fig. 6.6. One VDI W-band VNA extender of the Agilent PNA-X E3861C Microwave Network Analyser is used

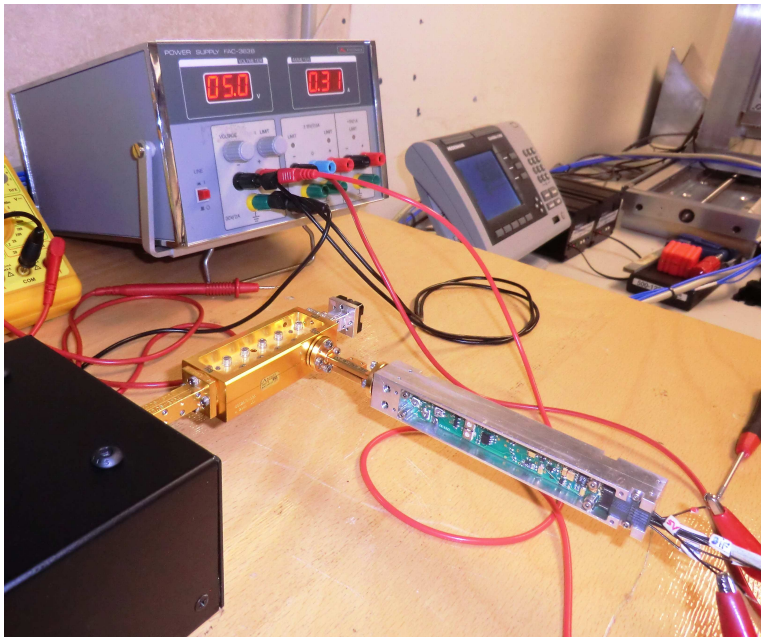

Figure 6.6 – Measurement set-up of the reflection coefficient of the W-band auto-calibrated receiver.

as a WR10 power source. The output power of this equipment needs to be attenuated because it is approximately 8 dBm and the maximum input power of the LN4-110 amplifiers is −20 dBm. Therefore, 25 dB of attenuation is applied to avoid the saturation of the LNAs by means of a 5 dB attenuator connected to the coupled port of a 20 dB directional coupler. This attenuation is enough because the losses produced by the input quadrature hybrid coupler and the WR10 waveguide to microstrip transition are higher than 3 dB. Moreover, the application of higher attenuation decreases the dynamic range of the measurement equipment. As can be seen in this Figure, a W-band load is connected to the direct port of the directional coupler and the receiver is connected to the output port of the 5 dB attenuator. Moreover, the equipment has been calibrated in this port in order to measure the input reflection coefficient of the receiver directly.

Fig. 6.7 shows a comparison between simulated and measured reflection coefficients of the W-band auto-calibrated receiver. The length of the

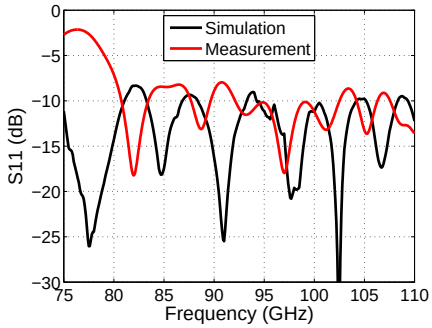

Figure 6.7 – Comparison between simulated and measured reflection coefficient of the W-band auto-calibrated receiver.

bondwires used in the connections between components in the receiver has been measured and introduced in the simulation results. Good agreement has been obtained between simulation and measurement. The major discrepancies are below 80 GHz due to fabrication errors in the microstrip part of the receiver and, consequently, the misalignment of the E-plane probe of the WR10 waveguide to microstrip transition.

The reflection coefficient measurement of the W-band auto-calibrated receiver has been also carried out with the LNAs in OFF state in order to show its effect. This can be seen clearly in Fig. 6.8. Whereas the reflection coefficients are similar when the amplifiers are in ON and OFF states, see Fig. 6.8 a), the effect of the amplifiers is more detectable in the inverse FFT of the measured reflection coefficient, see Fig. 6.8 b). The mismatching between components of the receiver can be detected clearly taking into account the reflection peaks in this Figure. These peaks are located at approximately 45, 95, 135, 166, 214 and 273 ps which correspond to the bend of the WR10 waveguide, the WR10 waveguide to microstrip transition, the input quadrature hybrid coupler, the attenuator, the amplifiers and the output quadrature hybrid coupler respectively. As can be seen, the reflection peaks change around 310 ps. This reflection is produced at a distance of 23 mm with respect to the WR10 waveguide to microstrip transition of the receiver, which corresponds to the location of the W-band detectors. Their input signal when the amplifiers are in ON state is higher; therefore, the reflected signal is also higher due to the mismatching of these components. This demonstrates that the amplifiers

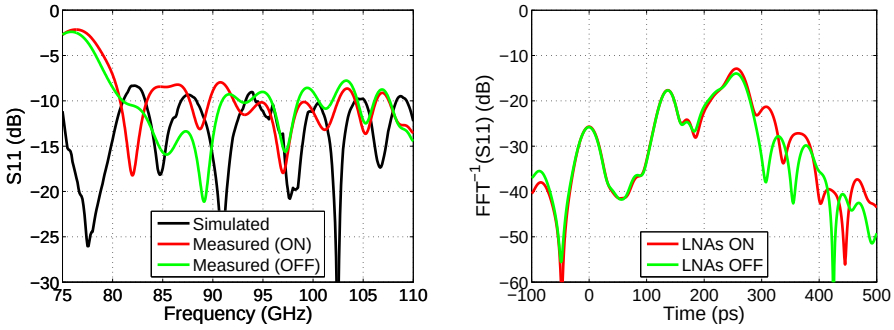

(a) (b)

Figure 6.8 – a) Comparison between simulated and measured reflection coefficients and b) the inverse FFT of the measured reflection coefficients when the two amplifiers of the W-band auto-calibrated receiver are in ON and OFF state.

are amplifying the W-band signal.

6.3.2 P_{in}-V_{out} response: Dynamic range

The dynamic range of the W-band auto-calibrated receiver is characterized by the measurement of the output detected voltage as a function of the input supplied power, i.e. the P_{in}-V_{out} response. The required input power swept for this measurement is from -70 to -15 dBm for each frequency. The lowest limit corresponds approximately to the emitted power of an object with $T = 77$ K. This power level is expected to be undetectable by the W-band auto-calibrated receiver because of its gain and the noise power level of the detectors themselves. However, it is interesting in order to obtain the performance of the receiver. On the other hand, -15 dBm is the maximum input power supported by the amplifiers, taking into account the losses of the WR10 waveguide to microstrip transition and of the input quadrature hybrid coupler.

A picture of the set-up for this measurement is shown in Fig. 6.9. In the W-band auto-calibrated receiver, three output DC voltages have to be simultaneously measured. They correspond to the auto-calibrated output, i.e. the difference between signal and reference, the signal and the reference.

Therefore, the set-up consists of two parts; the first one is the equipment which supplies the RF signal and the second part measures the output DC voltages of the receiver.

With respect to the available RF signal equipment, it consists of an ELVA G4-143e Millimeter Wave Generator in which output port an Elva IF-08 S-0405/05 isolator is connected in order to protect this equipment. It provides a maximum output power of 15 dBm from 90 GHz to 140 GHz which can be controlled by decreasing its percentage. However, this output power is higher than the desired range of input powers of the receiver. Therefore, a W-band 20 dB directional coupler and a 5 and 10 dB W-band attenuators connected to its coupled port have been used before the receiver to ensure that the amplifiers are not saturated. Moreover, a WR8 to WR10 waveguide transition is required to connect the output of the RF equipment with these W-band components. These components and the W-band auto-calibrated receiver can be seen in Fig. 6.9 b). An Erickson PM5 Submillimeter Power Meter has been connected to the direct port of the coupler in order to measure the power simultaneously. Consequently, the supplied input power of the receiver is calculated taking into account the measured performance of the attenuators and the directional coupler at W-band. Fig. 6.10 shows the maximum power which is supplied by the equipment in the input port of the receiver for each frequency. This power is below -20 dBm (the maximum input power of the amplifiers) along the entire considered frequency band. The maximum power measured by the power meter and the total attenuation of the set-up are also included in this Figure.

Regarding the DC output part of the set-up, it consists of three multimeters which measure the output voltages of the receiver. Both the equipment and the W-band auto-calibrated receiver have been switched on at least half an hour before the measurement to stabilize their performances, as well as in the reflection coefficient measurement. The potentiometers which control the amplification of the output DC voltages of the receiver have been adjusted so that the DC circuit is not saturated for the maximum available input power of the receiver, i.e. -21.22 dBm at 90 GHz.

The measured signal voltage (dBmV) as a function of the input power of the receiver, i.e. P_{in} (dBm), for each frequency in the range from 90 to 110 GHz, is shown in Fig. 6.11. Note that the sweep of P_{in} for each frequency is not linear because the equipment does not allow it. As can be seen, the measured P_{in}-V_{out} response of the W-band auto-calibrated receiver is higher

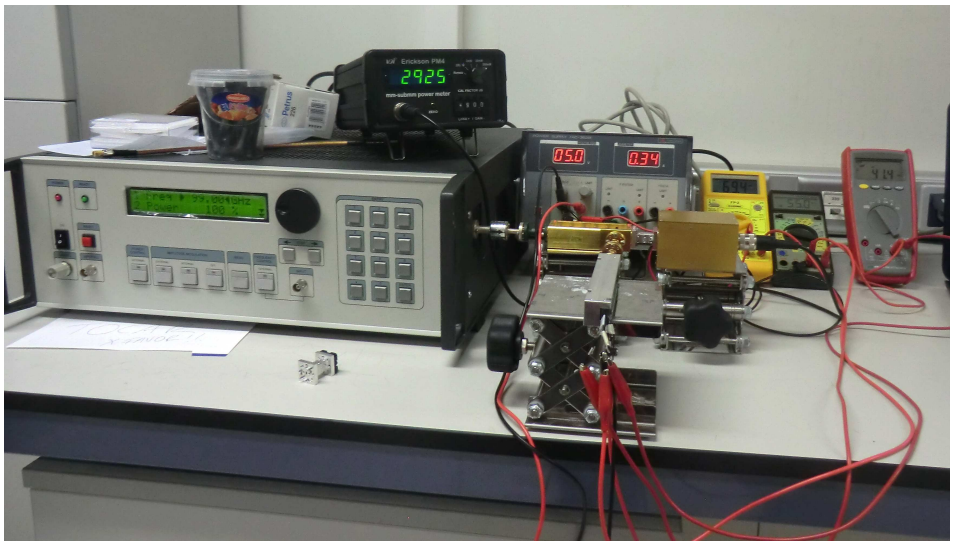

(a)

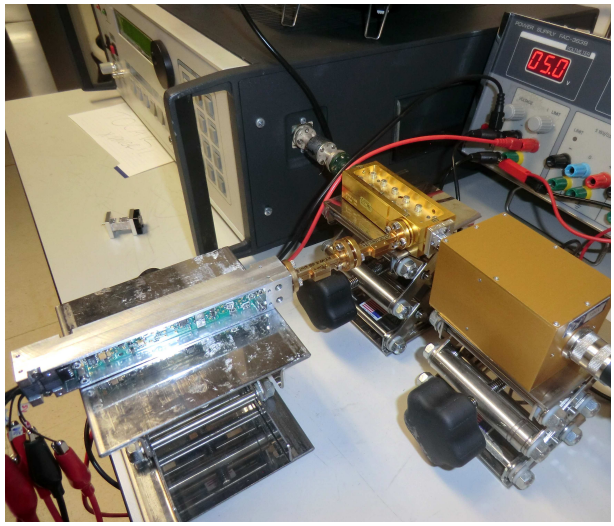

(b)

Figure 6.9 – Set-up considered to measure the dynamic range of the W-band auto-calibrated receiver.

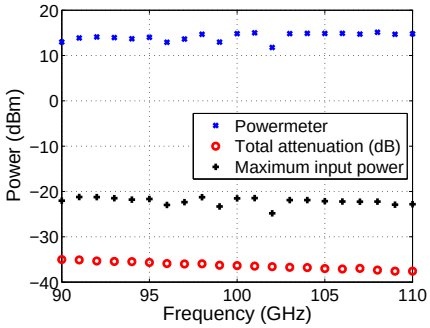

Figure 6.10 – Maximum input power supplied by the measurement set-up in the input port of the W-band auto-calibrated receiver. The maximum power measured by the power meter and the total attenuation of the system are also included.

in those frequencies at which the sensitivity and the impedance matching of the commercial detectors are higher, i.e. from 90 to 96 GHz, see Fig. 6.12. However, the measured minimum detectable power for each frequency, i.e. the lowest limit of the dynamic range, is higher than expected. The receiver is not capable of detecting signal powers below −40 dBm, as can be seen in Fig. 6.13. Remember that the emitted power of an object with $T_0 = 290\ K$ at W-band at a distance of 1 and 0.5 m are −67.35 and −61.30 dBm respectively.

This lack of sensitivity is produced by the limited gain of the receiver taking into account the noise equivalent power of the detectors. The noise equivalent power of the commercial V1A HRL detectors given by the manufacturer is less than 1 $pW/\sqrt{Hz}$ which corresponds to a maximum noise power lower than −37.33 dBm. Therefore, signal powers below this value are undetectable for the detectors. Taking into account the simulated RF gain of the receiver considering the lengths of its bondwires and also this noise power, the minimum detectable power can be calculated for each frequency, as it is shown in Fig. 6.13. As can be seen in this Figure, the results demonstrates that the expected gain is at least 10 dB lower at the best frequency, i.e. 93 GHz, and up to 23 dB in the worst frequency, i.e. 97 GHz. These gain reductions are really high and penalize the dynamic range of the receiver. They can be produced mainly by the fact that the amplifiers are not well activated. Another source of discrepancy can be the added dielectric losses in the microstrip part of the receiver, i.e. the WR10 waveguide to microstrip transition and the two

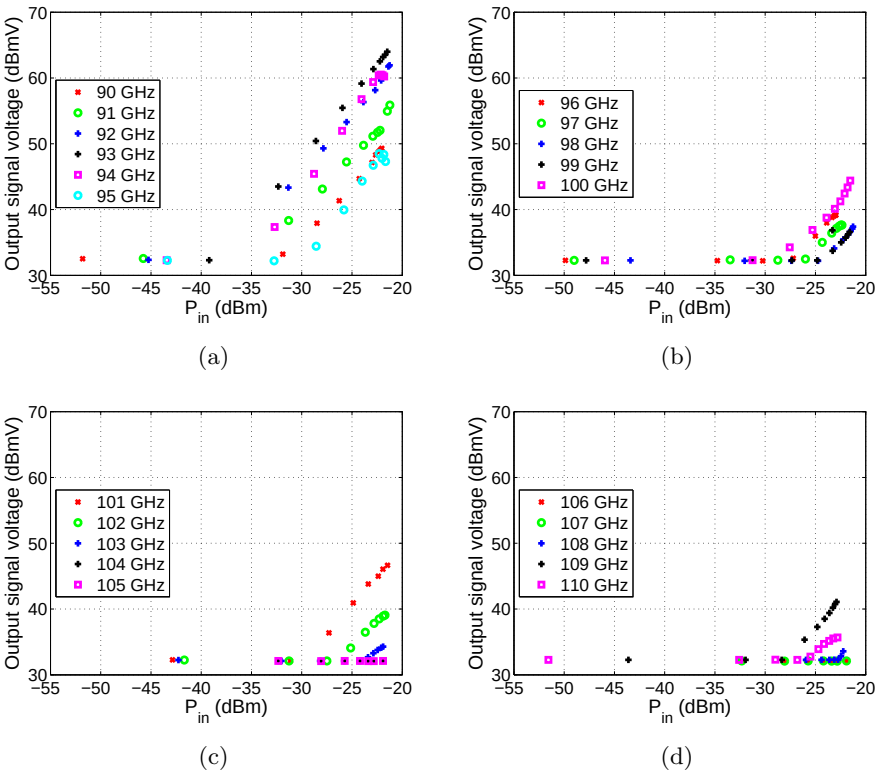

Figure 6.11 – Measured P_{in}-V_{out} response of the W-band auto-calibrated receiver in the signal output port from 90 to 110 GHz.

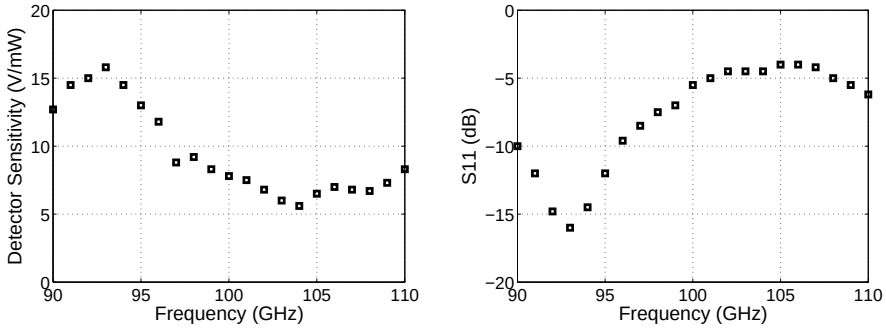

(a) (b)

Figure 6.12 – a) Sensitivity (V/mW) and b) reflection coefficient of the V1A HRL detectors at the considered frequency band for the measurement of the P_{in}-V_{out} response of the W-band auto-calibrated receiver. Nominal data provided by HRL Laboratories.

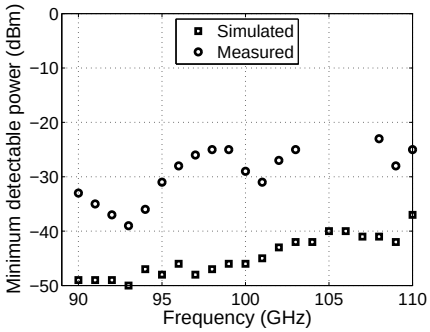

Figure 6.13 – Comparison between the measured minimum detectable power and the calculated minimum detectable power of the receiver taking into account the simulated gain and the detector noise equivalent power.

quadrature hybrid couplers. These facts will be discussed in Section 6.4.

In addition, the expected minimum detectable power of the W-band auto-calibrated receiver is not enough to detect an object with $T_0 = 290\ K$ because it is higher than the emitted power of this target. Therefore, the added losses produced by the length of the bondwires and the microstrip part of the receiver have to be improved. The possibility of using other low loss substrate such as

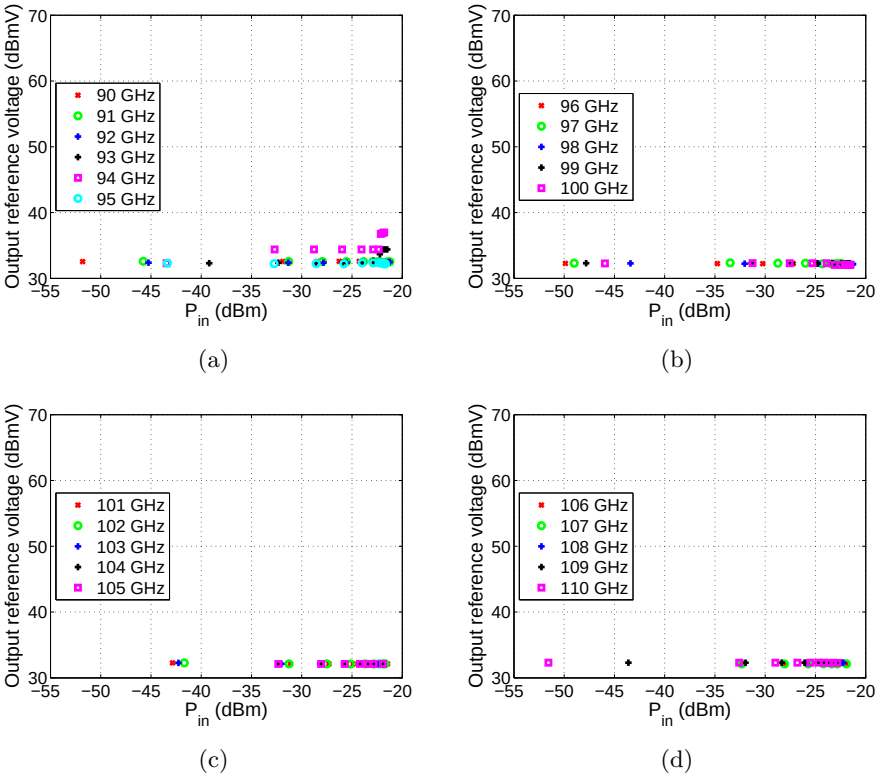

Figure 6.14 – Measured P_{in}-V_{out} response of the W-band auto-calibrated receiver in the reference output port from 90 to 110 GHz.

COC substrate could be an option. This would decrease the dielectric losses in at least 7 dB in the WR10 waveguide to microstrip transition and the two quadrature hybrid couplers.

With respect to the measurement of the P_{in}-V_{out} response of the W-band auto-calibrated receiver in the reference output port, it is depicted in Fig. 6.14 from 90 to 110 GHz. The reference output of the receiver performs the calibration of the system. Therefore, it has to be constant along the entire W-band. As can be seen in this Figure, the measured reference output voltage of the receiver is approximately 32 dBmV for each frequency and input applied power. Only the frequency 94 GHz is an exception, because apparently part of the input power is coupled to this port. However, this power coupling seems

to be an error in the measurements because it is almost constant as the input applied power increases. The measured output reference voltage is identical to the measured output signal voltage when the receiver is in OFF state or receiving an undetectable input power, see Fig. 6.11. Therefore, the results in the output reference port demonstrate that the balanced structure of the receiver is working properly and it is able to separate its two input signals.

6.3.3 RF-DC response and Effective Bandwidth

The measurement of the RF-DC response is required to obtain the effective bandwidth of the W-band auto-calibrated receiver. For this measurement, a constant input power has to be applied along the entire W-band. An input power between -67 and -61 dBm is interesting to obtain the performance of the receiver since this is the expected input power when working in a passive imaging system. However, this input power range is undetectable for the receiver as it has been demonstrated in the measurement of the P_{in}-V_{out} response. Therefore, taking into account that the sensitivity of the receiver is not enough, the RF-DC response can be measured by applying a constant input power which is inside the dynamic range of the receiver. However, the dynamic range is quite different in each measured frequency. Indeed, the receiver does not work in all of the measured frequencies, i.e. from 104 to 107 GHz. These non operating frequencies can be seen clearly if the RF-DC response of the receiver in the output signal and reference ports is depicted for each frequency taking into account a constant input power of -28 dBm, see Fig. 6.15.

Although the applied input signal is not realistic in a passive system, these results have been used to calculate the effective bandwidth of the receiver. If the input applied power is constant along the entire W-band, the effective bandwidth can be calculated as:

$$B = \frac{\left(\int_{f_1}^{f_2} \left(V_{out}(f) - V_{outoff}\right) df\right)^2}{\int_{f_1}^{f_2} \left(V_{out}(f) - V_{outoff}\right)^2 df} \tag{6.1}$$

Where $V_{out}(f)$ is the DC output voltage for each frequency and V_{outoff} is the DC output voltage when the power source is in OFF state. However, the measurements have been carried out in a certain number of frequencies because

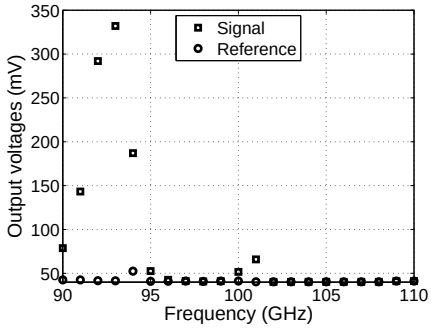

Figure 6.15 – Measured RF-DC response of the W-band auto-calibrated receiver for a constant input power of −28 dBm from 90 to 110 GHz.

the sweep has been step by step instead of a continuous ramp. Therefore, this expression can be written as:

$$B = \Delta f \cdot \left(\frac{N}{N+1}\right) \frac{\left(\sum_{i=1}^{N} V_{out}(i) - V_{outoff}\right)^2}{\sum_{i=1}^{N} \left(V_{out}(i) - V_{outoff}\right)^2} \tag{6.2}$$

Where N is the number of frequency points taken into account in the measurement and Δf is the frequency step. Taking into account that the input power is constant, the effective bandwidth does not depend on its value.

The resulting effective bandwidth of the W-band auto-calibrated receiver is 4.103 GHz instead of the expected 13.71 GHz. This expected value has been calculated taking into account the simulated gain of the receiver considering the lengths of its bondwires and the detector sensitivity provided by HRL Laboratories in the frequency range from 90 to 110 GHz. The resulting effective bandwidth, i.e. 4.103 GHz, is lower than that expected because it is affected by the mismatching between components of the receiver and also by the fact that the receiver gain is not constant along the W-band.

6.3.4 Equivalent Noise temperature

The equivalent noise temperature of a receiver is calculated using the Y-factor method [189], [190]. This method is based on the relation between the receiver outputs when two known noise temperatures are used as sources in its input port:

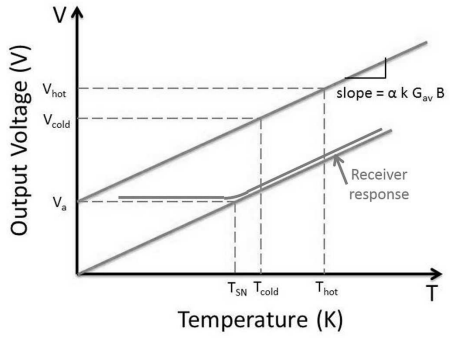

Figure 6.16 – Output voltage as a function of input temperature; linearity of the receiver.

$$Y = \frac{V_{hot}}{V_{cold}} \tag{6.3}$$

The noise output voltages, V_{hot} and V_{cold}, are the amplified input noise in addition to the noise added by the receiver itself. These two outputs have to be measured using input powers which are within the dynamic range of the receiver as can be seen in Fig. 6.16. For instance, when a cold source lower than the equivalent noise temperature of the receiver, i.e. T_{SN}, is considered, the obtained Y-factor is erroneous because it is lower than expected. In this Figure, V_a corresponds to the noise added by the receiver itself and it is proportional to the equivalent noise temperature of the receiver. If the receiver is ideal and no noise is added, V_a is 0. The slope of the curve is $\alpha k G_{av} B$ in which α is the sensitivity of the detector, B is the equivalent noise bandwidth, G_{av} corresponds to the gain of the receiver and k is the Boltzmann's constant.

As it is shown, V_{hot} and V_{cold} are proportional to the noise temperature of the hot and cold sources, i.e. T_{hot} and T_{cold} respectively.

In order to measure V_{hot} and V_{cold}, an absorbing material at ambient temperature is used as a hot source and the cold source is the same absorbing material soaked in liquid nitrogen at its boiling temperature (77 K). For the measurement, this two known noise temperatures are placed covering the receiver antenna. Note that they produce a noise temperature with a planar spectral power density. Therefore, the equivalent noise temperature of the receiver can be calculated as it is shown in Eq. 6.4.

$$T_{SN} = \frac{T_{hot} - YT_{cold}}{Y - 1} \tag{6.4}$$

Unfortunately, the measurement of the equivalent noise temperature of the W-band auto-calibrated receiver using Y-factor method is not feasible because its sensitivity is not enough to detect the emitted power of these known noise sources. Other W-band noise sources could be used to generate noise within the dynamic range of the receiver in order to measure the Y-factor and, consequently, its equivalent noise temperature [191]. However, these are not available within our group.

6.4 Discussion of the results and future improvements

The measurement of the dynamic range of the W-band auto-calibrated receiver demonstrates two aspects. The first one is the performance of the balanced structure and its capability of separate the input signals, i.e. the input signal and the reference. Conversely, it has been shown that the receiver does not have enough sensitivity to be used in a passive imaging system. This last statement is produced by the reduction of its gain which is affected by the following factors:

- Losses added by the length of the bondwires, specially those which connect the low noise amplifiers with the 50 Ω microstrip lines built in 0.127 mm thick RO5880 substrate.
- Impedance mismatching between components which produce ripple in the total gain of the receiver and, consequently, the reduction of its effective bandwidth.
- Losses due to the misalignment of the E-plane probe in the WR10 waveguide to microstrip transition. A mismatching in the lower part of the operating frequency band has been detected in the reflection coefficient measurement.
- Additional losses in the quadrature hybrid coupler due to the used substrate.

- Although the amplifiers are working as it has been demonstrated in the reflection coefficient measurement, the measurement of the dynamic range of the receiver and the calculation of the receiver's total gain show that the loss of receiver's gain is so high that it is produced by the fact that the gain of the amplifiers are not as large as expected, i.e. approximately 22 dB.

The losses added by the length of the bondwires can be improved in the assembly of the receiver's components improving the use of the TPT HB16D bonder machine and placing the components closer. Moreover, this also improves the mismatching between components and consequently, the effective bandwidth of the receiver since it reduces the ripples in the total gain of the receiver. The large the effective bandwidth, the better the sensitivity of the receiver, i.e. ΔT_{min}, which is its figure of merit.

With respect to the losses in the WR10 waveguide to microstrip transition and the quadrature hybrid couplers, it could be improved up to 7 dB if other low loss substrate such as COC polymer is considered. However, the realization of the gold wire bondings will be a challenge. So far, an improvement of the outer cut in the microstrip part of the receiver ensures the correct alignment of the transition and, consequently, better matching at least in the lower part of the W-band.

Regarding the gain of the amplifiers, it is clear that the obtained amplification is not as expected. Therefore, the last available low noise amplifier has been assembled in the receiver in order to check the drain current at which it is working in its optimum operating point. For this aim, the set-up shown in Fig. 6.17 has been implemented. It consists of a W-band power source, i.e. a VDI Wband VNA extender of the Agilent PNA-X E3861C Microwave Network Analyser, connected to a 20 dB directional coupler and a W-band attenuator which ensures the supply of a suitable input power which does not saturate the amplifier. This input power is measured by a power meter in the direct port of the directional coupler. The current consumption of the DC circuit and the output voltage of the receiver are controlled by two multimeters.

The current consumption of the DC circuit before bias process of the amplifier is 270 mA. Therefore, the drain current consumption of the amplifier is the consumption shown in the multimeter minus this value. In order to obtain the optimum performance of this amplifier, the two gate voltages are

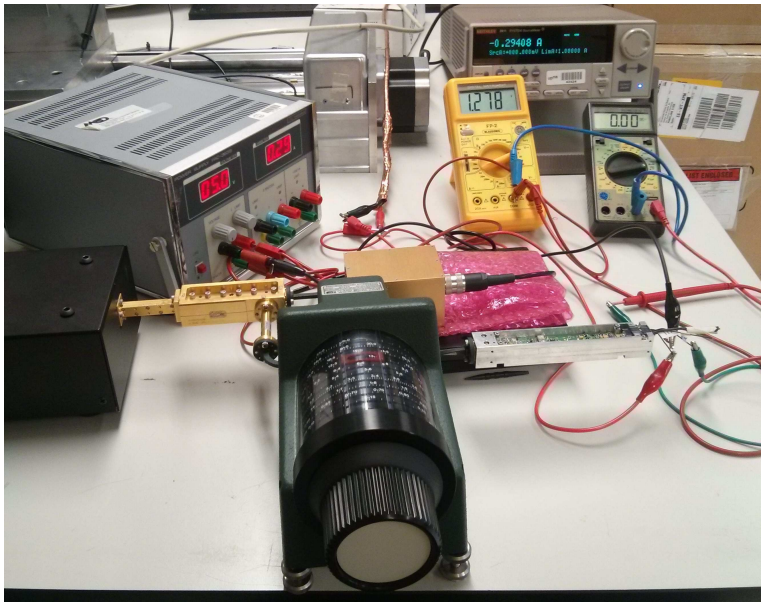

Figure 6.17 – Set-up for the measurement of the output voltage as a function of the drain current consumption of one low noise amplifier assembled in the W-band auto-calibrated receiver.

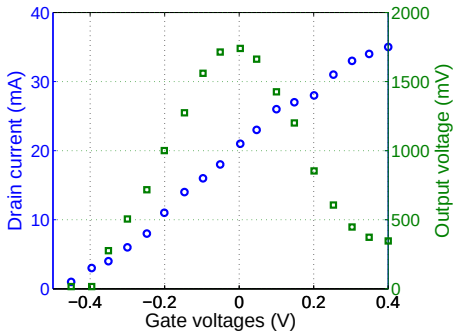

Figure 6.18 – Drain current consumption of the amplifier and output voltage of the receiver as a function of the gate voltages at 93 GHz.

increased simultaneously whereas the drain current and the output voltage are measured. The measurement has been carried out only at that frequency in which a better performance has been obtained in previous measurements, i.e. 93 GHz.

The results of this measurement can be seen in Fig. 6.18. The maximum output voltage of the receiver is obtained when the two gate voltages of this amplifier are approximately 0 V. At this value, the drain current of the amplifier is 20 mA which is quite different to those expected 35 mA, i.e. the value given by the manufacturer. The optimum 35 mA drain current measured by the manufacturer was obtained when the LNA was connected to W-band coplanar probes in the input and output ports. Therefore, the characteristic impedances of these ports are exactly 50 Ω. Conversely, these impedances are not ensure in the W-band auto-calibrated receiver and, it is postulated that these additional reflections produce modification of the optimum drain current.

The same set-up has been used to measure the P_{in}-V_{out} response of the receiver with only one amplifier working with two different drain currents at 93 GHz in order to compare its performance. These values are the drain current at which a maximum amplification has been obtained, i.e. 20 mA, and those given by the manufacturer, i.e. 35 mA. The input power of the receiver is controlled by the W-band attenuator. The results are shown in Fig. 6.19. Note that the reference output has not been measured because the

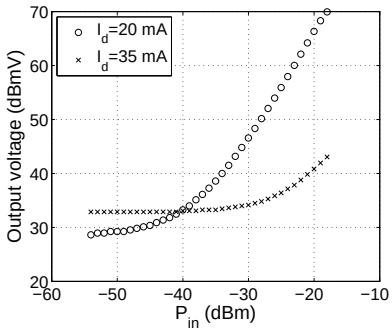

Figure 6.19 – P_{in}-V_{out} response of the receiver with only one amplifier working with two different drain current consumptions at 93 GHz.

balanced structure of the receiver with one amplifier does not exist.

As can be seen, the differences between the performance of the receiver with one amplifier working at two different drain currents are very large. The receiver detects up to −30 dBm with a drain current of 35 mA instead of −40 dBm, i.e. when the drain current is 20 mA. This implies at least an improvement of 10 dB in the gain of the amplifier. Moreover, it demonstrates that in previous measurements the loss in the total gain of the W-band auto-calibrated receiver can be at least 16 dB. This calculation has been done taking into account that the receiver with only one amplifier obtains at its output a quarter of the input signal. Moreover, we are supposing that the performance of the previous assembled amplifiers are identical to this one. It may not be entirely true. However, the main problem which strongly penalises the performance of the W-band auto-calibrated receiver has been found. If the gate voltages of the two amplifiers which are part of the W-band auto-calibrated receiver are readjusted in order to obtain its optimum drain current consumption, the odds are that the receiver works at least close to its behaviour obtained in simulation.

6.5 Conclusions

This Chapter has presented the fabrication and assembly of both the packaging metal block and the microstrip part of the receiver. Once it has been done,

the gold wire bondings and the biasing of the amplifiers have been carried out. This bias has been adjusted to 35 mA drain current, as the manufacturer recommended. Finally, the complete W-band auto-calibrated receiver has been characterized in terms of input reflection coefficient, dynamic range, RF-DC response and effective bandwidth. Moreover, the measurement of the dynamic range of the W-band auto-calibrated receiver in its output reference signal has verified that the balanced structure of the receiver works as expected and it is able to perform the internal calibration of the system. Although the measurement of its input reflection coefficient has confirmed that the amplifiers are amplifying, the dynamic range of the receiver has showed that the receiver gain is not as high as expected. Indeed, the reduction of receiver gain is between 10 and 23 dB. As explained in this Chapter, some problems have contributed to this reduction of receiver gain. Firstly, the added dielectric losses in the microstrip part of the receiver increase the receiver noise and reduce its sensitivity. The use of a lower loss substrate such as COC polymer could be an improvement. Indeed, simulations show that the receiver dielectric losses would decrease in at least 7 dB if COC polymer is used and the gold wire bondings are shortened. However, the reduction of the receiver gain has been found to be mainly produced by the fact that the amplifiers are not working at their optimum operating point as it has been demonstrated experimentally. Certainly, better results would be obtained if other bias point is used. An increase of at least 16 dB in the receiver gain at 93 GHz has been confirmed by analysing the differences between the dynamic range of the receiver taking into account two drain currents, i.e. the optimum experimental value (20 mA) and the value recommended by the manufacturer (35 mA). This implies that the performance of the amplifiers of the W-band auto-calibrated receiver are not optimum in the measurements. Therefore, readjusting the drain current of the amplifiers would be required in order to accomplish the expected performance of the receiver. However, the W-band auto-calibrated receiver can not be characterized taking into account the commented improvements because no MMIC amplifiers are now available.

Chapter 7

Design and characterization of a W-band Vivaldi antenna

7.1 Introduction

Most passive millimetre and submillimetre imaging cameras work with horn antennas connected to the receivers. These antennas allow achieving broadband systems and a very good control of the radiation pattern, which can be matched to the requirements of the optimum systems. However, the resulting multiple-beam systems can be heavy, bulky and more complicated to assemble. An interesting alternative in order to reduce the size and weight of these imaging cameras is the use of planar antennas with broadband performance. The integration of the W-band auto-calibrated receiver and the planar antenna on the same substrate provides a compact easy to manufacture the receiver. Moreover, this facilitates the implementation of a multiple pixel imaging system.

In particular, the selected planar antenna is a Vivaldi antenna which produces an end-fire radiation with symmetrical beam patterns whose peak directivity can be higher than 10 dBi. This type of antennas has broadband performance able to cover the entire W-band. Therefore, the challenge is the design of a broadband microstrip to slotline transition.

In this Chapter, the design process of the W-band Vivaldi antenna and their simulated performance are shown. And finally, these simulations have been experimentally validated with waveguide based equipment using the

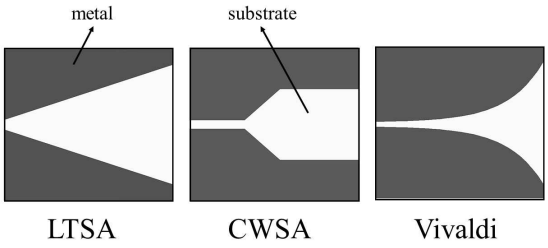

Figure 7.1 – Examples of Tapered Slot Antennas.

WR10 waveguide to microstrip transition presented in Section 4.3.

7.2 Planar Antennas

As mentioned, planar antennas are easy to integrate on the same substrate of the receiver and also, a large number of them can be easily implemented. Moreover, their manufacture using photo-lithographic techniques reduces the cost of a multiple-beam system [192].

The family of planar antennas can be classified in two groups depending on their direction of radiation with respect to the plane of the antenna: broadside and end-fire antennas. In the first group, the direction of radiation is perpendicular to the plane of the antenna, i.e. to the substrate the antenna is printed onto. Examples of this type are the microstrip patch, dipole and bowtie antenna. Conversely, end-fire antennas radiate along the plane of the antenna [193]. This category includes quasi-yagi antennas [194] and Tapered Slot Antennas (TSA). Examples of this last group depending on the aperture profile are the Linearly Tapered Slot Antenna (LTSA), the (partially) Constant Width Slot Antenna (CWSA) and the Vivaldi antenna, see Fig. 7.1.

The use of TSAs is interesting in those applications that require Directivities over 10 dBi, beamwidths between 12° and 60° [195] and large operating bandwidth. Therefore, these antennas are widely used in satellite communication systems, remote sensors, automotive radars [196], UWB systems [197], high capacity point-to-point radiolinks [198], radio telescopes for radio-astronomy and millimetre and/or submillimetre imaging cameras [199].

On the other side, the main advantages of Tapered Slot Antennas according to [195], [197] and [200] are:

- They are more appropriate than dipoles, slots or microstrip patch antennas in order to illuminate directly reflectors and lenses given their narrower beamwidths and higher directivities.
- In spite of their planar geometry, TSAs can produce symmetrical beam patterns.
- They have large bandwidth.
- The distance between elements within an array can be very small.
- They have low sensitivity to manufacturing errors at millimetre-wave frequency.

At millimetre wave frequencies, specifically in the W-band, several Tapered Slot Antennas have been designed and measured [201]- [204]. However, only in [202] and [204] the designed LTSAs covered the full W-band. In order to obtain this large bandwidth, the substrate had to be modified. The reason for these modifications, which are motivated by the influence of the substrate, will be explained in Section 7.3.1.

Within the TSAs, the Vivaldi antenna has been considered as the best option to be use in our multiple-beam system. This is because this antenna is smaller, has lower cross polarisation [205] and produces symmetrical beam patterns and lower sidelobes than LTSA or CWSA. For these reasons, this antenna has been designed for the W-band auto-calibrated receiver built in planar technology. Nevertheless, its behaviour has been compared with a LTSA.

7.3 Vivaldi antenna design

The aim of this Section is to design a Vivaldi antenna whose directivity is higher than 10 dBi, its E- and H-plane beamwidths are narrower than 60° and its sidelobe level is below −12.5 dB along the full W-band. These requirements come from the need to integrate the receivers in an imaging system. For this purpose, a study of the radiation performance of the exponential aperture with respect to its main parameters such as the aperture size and rate has

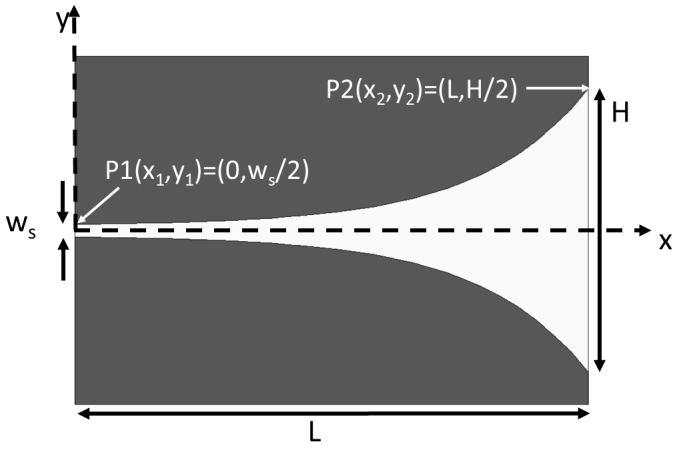

Figure 7.2 – Exponential aperture of the Vivaldi antenna.

been carried out. Moreover, the design of a suitable transition has been made in order to provide broadband matching covering the full W-band. Finally, the simulated results and the dimensions of the optimal W-band Vivaldi antenna are shown in order to demonstrate that the design complies with the requirements.

7.3.1 Vivaldi antenna aperture

The Vivaldi antenna was first proposed by Gibson in 1979 [206]. This antenna belongs to the class of frequency independent radiators [193], [207] due to its structure. It consists of a metal plate with a slotline whose width varies progressively in an exponentially way. In this way, for a given wavelength, only a fraction of the exponential slotline is efficiently radiating. Therefore, if the wavelength is scaled by a factor of n, then the radiation will occur in a section scaled by n.

The exponential tapering of the Vivaldi antenna is determined by the following equations, where the two initial points, P1(x_1,y_1) and P2(x_2,y_2) are defined in Fig. 7.2.

$$y = C_1 e^{-Rx} + C_2 \tag{7.1}$$

$$C_1 = \frac{y_2 - y_1}{e^{-Rx_2} - e^{-Rx_1}} = \frac{1}{2}\frac{H - w_s}{e^{-RL} - 1} \tag{7.2}$$

$$C_2 = \frac{y_1 e^{-Rx_2} - y_2 e^{-Rx_1}}{e^{-Rx_2} - e^{-Rx_1}} = \frac{1}{2}\frac{w_s e^{-RL} - H}{e^{-RL} - 1} \tag{7.3}$$

In these equations, L and H stand for the length and width at the end of the aperture, respectively. In addition, w_s corresponds to the initial width of the aperture, the slotline. And finally, R is the aperture rate of the exponential profile, which determines the gain, the beamwidths and the bandwidth of the Vivaldi antenna aperture. In particular, if the aperture rate of the exponential profile is equal to 0, the aperture profile will be linear, resulting in a Linear Tapered Slot Antenna (LTSA).

7.3.2 Substrate selection

Despite its frequency independent behaviour, the main limitation of the TSA comes from its sensitivity to the thickness and dielectric constant of the substrate. Yngvensson et al. [193] established experimentally an accepted range for good operation of these antennas based on the effective thickness, i.e. t_{eff}. It represents the electrical thickness of the supporting substrate and it is defined as

$$t_{eff} = t(\sqrt{\epsilon_r} - 1) \tag{7.4}$$

where t and ϵ_r stand for the thickness and the dielectric constant of the substrate, respectively. The accepted range is $0.005 < t_{eff}/\lambda_0 < 0.03$, where λ_0 is the free space wavelength at the operating frequency.

This range comes from two reasons. On the one hand, for substrate thickness above the upper bound, i.e. $t_{eff}/\lambda_0 \geqslant 0.03$, unwanted substrate modes can propagate and degrade the performance of the TSA. On the other hand, antennas on thinner substrates can increase the beamwidth of the main radiation lobe resulting in lower directivities.

Taking into account millimetre wave applications, the substrate has to be rather thin in order to comply with the range proposed by Yngvensson, specially when a substrate with high dielectric constant is considered, see Fig. 7.3. Due to the fact that thin antennas can be fragile and they are not practical in large arrays, several solutions have been proposed to extend

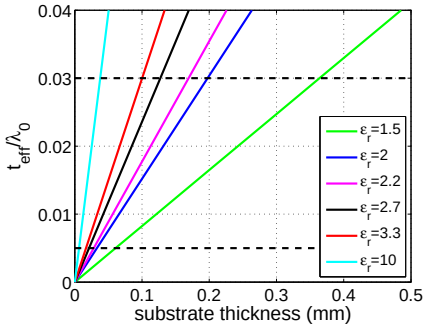

Figure 7.3 – Accepted thickness range for different substrates at 110 GHz, the highest frequency limit of the W-band.

the upper limit of this gap in order to obtain lower effective permittivity of the supporting substrate. This leads to an increase of the allowable substrate thickness. These proposed solutions consist of a partial removal of the substrate [201], [208], incorporating a photonic bandgap structure into the substrate [209], [203], considering a rectangular-grooved substrate [202], or using an air cavity backing substrate [210].

However, if we consider a substrate with low permittivity, e.g. 2.2, these solutions are not necessary at least in the W-band because of the availability of commercial thin substrates. Moreover, dielectrics with low permittivity usually improve the efficiency of the antenna and also its bandwidth. However, their main drawback is that the slotline impedance will be higher and it complicates the design of the antenna feeding system. This fact will be further explained in Section 7.3.4.

As mentioned in Section 2.3.1, nowadays, the standard thinnest substrates, which some manufacturers provide without increasing the fragility of the antenna, are 100 μm and 127 μm. These commercial thicknesses allow the consideration of dielectric constants below 3.3 and 2.7 respectively in order to comply with the upper limit of the effective thickness covering the full W-band, i.e $t_{eff}/\lambda_0 < 0.03$, see Fig. 7.3. Note that in this Figure, the highest frequency of the W-band has been considered because it defines the thinnest feasible substrate thickness to obtain a good operation of the antenna in the full W-band.

Table 7.1 shows the available commercial substrates which satisfy this

Name	ϵ_r	t (mm)	$\tan\delta$	Manufacturer
TLY	2.17-2.20 (10 GHz)	0.127	0.0009 (10 GHz)	TACONIC [98]
TLP	2.17-2.40 (10 GHz)	0.127	0.0009 (10 GHz)	TACONIC [98]
TacLamPLUS	2.10 (50 GHz)	0.100	0.0008 (50 GHz)	TACONIC [98]
DiClad880	2.17-2.20 (10 GHz)	0.127	0.0009 (10 GHz)	ARLON [99]
CuClad217LX	2.17-2.20 (10 GHz)	0.127	0.0009 (10 GHz)	ARLON [99]
NY9000	2.17-2.60 (10 GHz)	0.127	0.0009 (10 GHz)	NELCO [100]
RT/Duroid 5880	2.20 (10 GHz)	0.127	0.0009 (10 GHz)	ROGERS [101]

Table 7.1 – Available commercially substrates that comply with the upper limit of the effective thickness range at W-band.

condition. As the antenna will be integrated on the same substrate of the planar receiver thereby, only the substrates with lower losses, i.e. $\tan\delta < 0.001$, of each manufacturer have been taken into account. Note that this Table is similar to Table 2.1 shown Section 2.3.1. However, the substrate RO3003 has been removed because it does not meet the effective thickness requirement.

Any of the substrates shown in Table 7.1 is a good candidate for the antenna. Therefore, the selected option has been Rogers RT/Duroid 5880 (RO5880) whose thickness is 127 μm, which is the same substrate used in the design of the receiver. Moreover, the dielectric loss tangent of this substrate has been set to 0.01 as experimentally demonstrated in Section 4.2.

7.3.3 Optimization of the aperture

Once the supporting substrate has been chosen, the design of the W-band Vivaldi antenna can be carried out. For this purpose, three important antenna parameters have been studied as a function of the dimensional parameters of

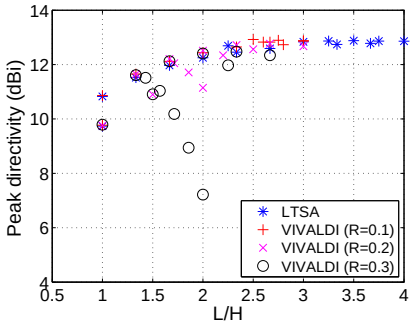

Figure 7.4 – Peak directivity for different Vivaldi antennas of different sizes at the central frequency of the band, i.e. 92.5 GHz.

the exponential aperture, i.e R, L and H. These three parameters under study are the peak directivity, the Half Power Beanwidth (HPBW) and the Sidelobe Level (SLL).

HPBW and SLL have been measured in the E- and H-plane of the radiation pattern of the antenna. Taking into account Fig. 7.2, the E-plane corresponds to the XY plane and the H-plane corresponds to the XZ plane.

Regarding the dimensions of the exponential aperture, a general consideration has been proposed in [193] as a starting point of the Vivaldi antenna design: the length L and the width H of the aperture ending have to be larger than λ_0 and $\lambda_0/2$, respectively, in order to produce efficient radiation. However, a preliminary study of the maximum affordable directivity of the aperture depending on its dimensions has been carried out in order to obtain a starting point for the length and the width of the aperture. In this study, the length and the width of the aperture have been swept from $1\lambda_0$ to $7\lambda_0$ and from $1\lambda_0$ to $3.5\lambda_0$ respectively taking into account aperture rates from 0 (LTSA) to 0.3. Note that λ_0 corresponds to the free space wavelength at the center frequency of the W-band, i.e. 92.5 GHz.

With respect to the peak directivity at 92.5 GHz of each considered pair of size and aperture rate of the antenna, Fig. 7.4, Vivaldi antennas can produce the same directivity of a LTSA with smaller size. For any aperture rate, directivity improvements are small from $L \geqslant 2H$. Therefore, the analysis of the Vivaldi antenna has been carried out keeping constant the relation $L = 2H$.

Other important parameter of the exponential aperture is the width of

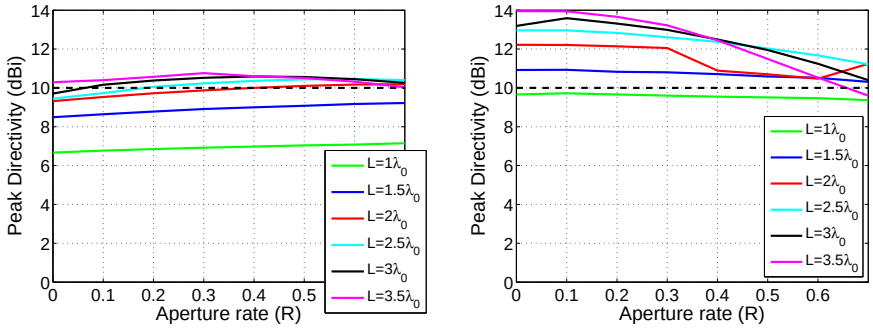

(a) 75 GHz (b) 110 GHz

Figure 7.5 – Peak directivity of Vivaldi antennas of different sizes as a function of the exponential aperture rate at a) 75 GHz and b) 110 GHz. The dashed line corresponds to the minimum required directivity, i.e. 10 dBi.

the initial slotline, w_s. The narrowest manufactured width by the laboratory equipment, LPKF ProtoLaser 200, has been selected in order to obtain the smallest feasible impedance. Having a low impedance in the slotline facilitates the design of the antenna feeding. This value is $w_s = 0.05$ mm, which corresponds to a characteristic impedance $Z_{0s} = 129\ \Omega$ at 92.5 GHz [211].

The performed analysis taking into account the three figures of merit, i.e. peak directivity, HPBW and SLL, determines the behaviour of the radiation of the antenna depending on the aperture rate for each antenna size. In this study several parameters have been fixed: the initial slotline, i.e. $w_s = 0.05$ mm and the ratio $L = 2H$. The considered ranges of the aperture rate and the length of the antenna have been from $R = 0$ to $R = 0.7$ and from $1\lambda_0$ to $3.5\lambda_0$ respectively.

7.3.3.1 Peak directivity

First of all, the peak directivity of the antenna aperture at the frequency limits of the W-band is shown in Fig. 7.5. Note that $R = 0$ is also added in these plots in order to compare the behaviour of an exponential aperture with respect to a linear taper.

Some conclusions can be drawn based on this Figure:

- For a required directivity, a Vivaldi antenna ($R > 0$) shorter than a

LTSA ($R = 0$) can be always found. For example, at 75 GHz, in order to obtain 10 dBi of directivity, the needed LTSA has approximately a length between $3\lambda_0$ and $3.5\lambda_0$, however, this directivity can be achieved with a Vivaldi antenna whose length is $2\lambda_0$ and its aperture rate is 0.4.

- For any given Vivaldi antenna length, there is an optimum aperture rate which maximises the directivity.

- A Vivaldi antenna larger than $2\lambda_0$ is required in order to satisfy the directivity requirement along the entire W-band.

One remarkable point is the fact that at the highest frequency, see Fig. 7.5 b), the directivity of the Vivaldi aperture for every antenna size decreases as the aperture rate increases because of the increase of the sidelobes level as will be explained later on.

7.3.3.2 Half Power Beamwidth (HPBW)

Fig. 7.6 shows the Half Power Beamwidth of the E- and H-plane of the radiation pattern for each antenna size depending on the aperture rate at the lowest and highest frequency of the W-band respectively, i.e. 75 GHz and 110 GHz. As expected, given the larger directivity, the beamwidth in both antenna planes is narrower at the highest frequency. As can be seen in these Figures, the H-plane is more sensitive to changes in the antenna size and it is always broader than the E-plane beamwidth. Moreover, the beamwidth in both planes becomes narrower as the antenna length increases for every aperture rate. The main advantage of the Vivaldi antenna with respect to the LTSA is that the radiation pattern is more symmetrical, which is important for being used as a pixel in a multiple-beam system.

In order to comply with the HPBW requirement, i.e. HPBW$< 60°$, the two feasible smaller Vivaldi antenna lengths are $L = 2.5\lambda_0$ and $L = 3\lambda_0$ whose aperture rates have to be $R \geqslant 0.7$ and $R \geqslant 0.3$ respectively.

In general, the beamwidth of the main lobe provided by the LTSA ($R = 0$) is broader than the beamwidth of a Vivaldi antenna in both planes. Moreover, LTSAs larger than $3.5\lambda_0$ have to be considered in order to comply with the required HPBW.

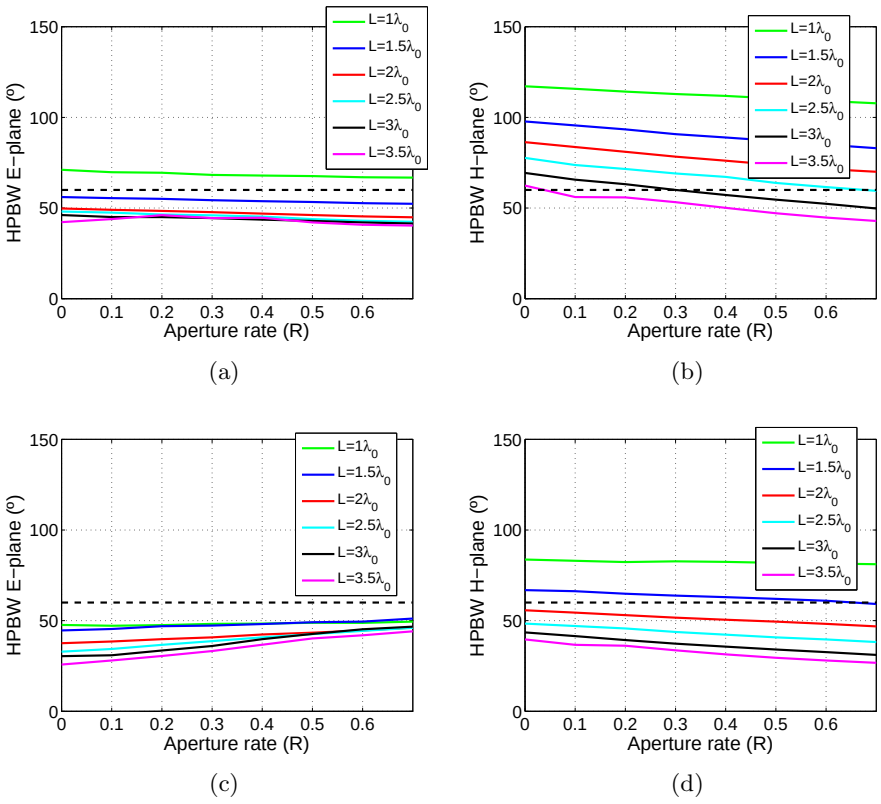

Figure 7.6 – Half Power Beamwidth of the radiation pattern of Vivaldi antennas of different sizes as a function of the exponential aperture rate for the a) E-plane and b) H-plane at 75 GHz, and also for the c) E-plane and d) H-plane at 110 GHz. The dashed line corresponds to the maximum required HPBW, i.e. 60°.

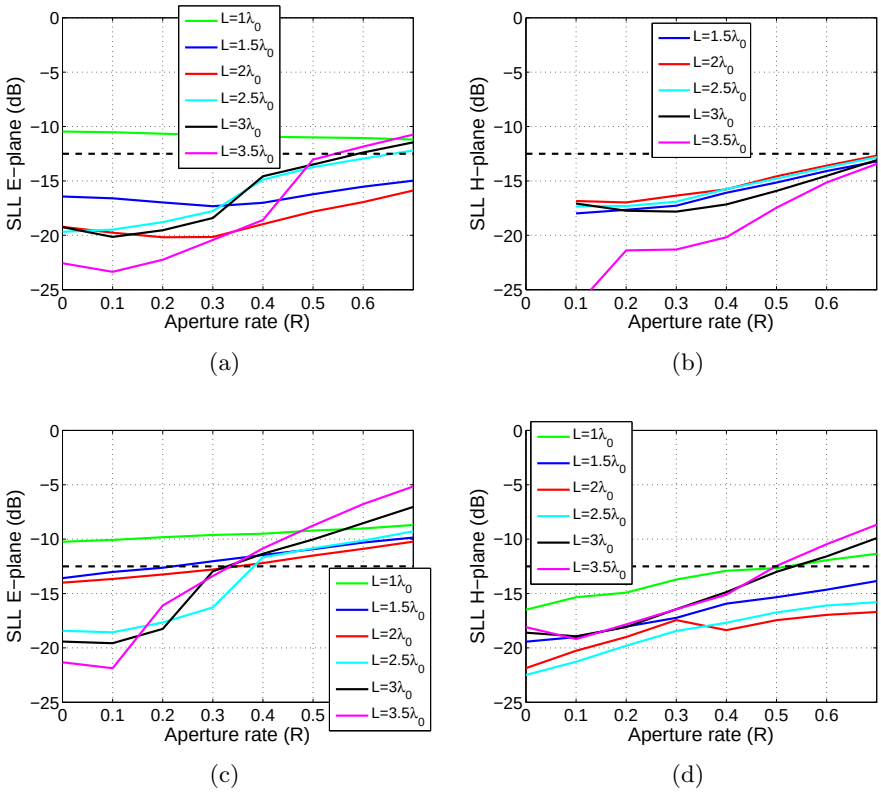

Figure 7.7 – Sidelobe Level (SLL) of the radiation pattern for Vivaldi antennas of different sizes as a function of the exponential aperture rate for a) E-plane and b) H-plane at 75 GHz and also, for c) E-plane and d) H-plane at 110 GHz. The dashed line corresponds to the maximum required SLL, i.e. −12.5 dB.

$D > 10$ dBi	$HPBW < 60°$	$SLL < -12.5$ dB
$L = 2\lambda_0$	–	$L = 2\lambda_0$ and $R \leqslant 0.3$
$L = 2.5\lambda_0$	$L = 2.5\lambda_0$ and $R \geqslant 0.7$	$L = 2.5\lambda_0$ and $R < 0.4$
$L = 3\lambda_0$	$L = 3\lambda_0$ and $R \geqslant 0.3$	$L = 3\lambda_0$ and $R \leqslant 0.3$
$L = 3.5\lambda_0$ and $R < 0.7$	$L = 3.5\lambda_0$ and $R > 0.1$	$L = 3.5\lambda_0$ and $R \leqslant 0.3$

Table 7.2 – A summary of the Vivaldi antenna aperture size and aperture rate that comply with each design requirement.

7.3.3.3 SideLobe Level (SLL)

Finally, the analysis of the behaviour of the sidelobe level of the radiation pattern of the exponential aperture with respect to changes in the antenna size and the aperture rate has been carried out. The sidelobe level of the E- and H-plane radiation pattern of the antenna at the lowest and highest frequency of the W-band, i.e. 75 GHz and 110 GHz, can be seen in Fig. 7.7. At the highest frequency, the sidelobe level increases whereas the HPBW is narrower. Following the comparison between Vivaldi antenna and LTSAs, the beamwidth of the main lobe of the radiation pattern of a LTSA is broader, thereby, the sidelobe levels of both planes are the lowest.

As we said before, the directivity of the Vivaldi antenna at higher frequency decreases as the aperture rate increases because of the increase of the sidelobe level. This effect can be seen more clearly in these Figures. For example, a $2\lambda_0$ long Vivaldi antenna undergoes a significant decrease of its directivity at 110 GHz when the aperture rate is higher than 0.3. Paying attention to the red line in Fig. 7.7 c), the SLL of the E-plane exceeds the value of -12.5 dB when this antenna size has higher aperture rate than 0.3.

Evaluating this parameter in both radiation planes, the antenna sizes which comply with the requirement ($SLL < -12.5$ dB) are $L = 2\lambda_0$ with $R \leqslant 0.3$, $L = 2.5\lambda_0$ with $R < 0.4$, $L = 3\lambda_0$ with $R \leqslant 0.3$ and $L = 3.5\lambda_0$ with $R \leqslant 0.3$.

A summary of the Vivaldi aperture size and aperture rate that comply with each requirement can be found in Table 7.2. Therefore, the smallest size of a Vivaldi antenna aperture which meets the design requirements is $L = 3\lambda_0$, $H = 1.5\lambda_0$ with $R = 0.3$.

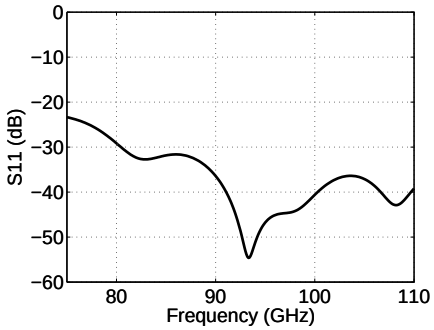

Figure 7.8 – Simulated reflection coefficient for the Vivaldi antenna whose dimensions are $L = 3\lambda_0$, $H = 1.5\lambda_0$ and $R = 0.3$.

7.3.4 Antenna feeding system

A Vivaldi antenna aperture with these dimensions has broadband matching covering the full W-band as can be seen in Fig. 7.8. However, the main drawback of using Vivaldi antennas comes from the fact that the design of a suitable feeding system is essential to maximise the operating bandwidth. This is because, according to [212], the feeding system determines the upper limit of the bandwidth of the antenna whereas the aperture size determines the lowest frequency limit.

The more usual feeding techniques for Vivaldi antennas are a coaxial cable soldered at the end of the slotline [207] or coupling the signal to the slotline through a microstrip circuit [198]. Although this first feeding technique provides larger operating bandwidth, the design of a wideband balun is not an easy task. For example, the use of a double-Y balun [207] produces an ideally infinite matching bandwidth but its main drawbacks are the number of air bridges across the coplanar line required to suppress its odd mode of propagation and also, their critical positions. Moreover, this kind of feeding is suitable when the characteristic impedance of the slotline is approximately 75 Ω. Good results have been obtained with this transition at frequencies around 4 GHz [207]. However, the impedance in the 0.05 mm width slotline is 129 Ω. Therefore, in terms of matching an impedance above 75 Ω the best option is to design a microstrip to slotline transition whose challenge is to obtain a broadband matching. Moreover, the microstrip to slotline transition is suitable for higher frequency, for example at 60 GHz [213]. In addition, this

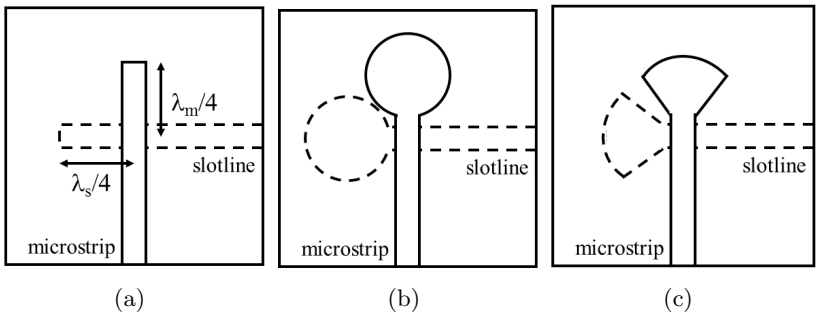

Figure 7.9 – Microstrip to slotline transitions proposed by a) Knorr [214], b) Schüppert [215] and c) Zinieris [216]. Solid lines corresponds to the microstrip line and dashed lines corresponds to the slotline.

transition facilitates the integration of the antenna and the planar receiver built in microstrip technology on the same substrate. And finally, it is a compact and easy to manufacture solution with low losses.

The simplest microstrip to slotline transition is a wideband transition proposed by Knorr [214]. The slotline, which is etched on one side of the substrate, is crossed at a right angle by a microstrip line on the opposite side. The slotline extends a quarter wavelength beyond the microstrip and the microstrip line extends a quarter wavelength beyond the slotline as can be seen in Fig. 7.9 a). Due to this quarter-wave transformation the microstrip open circuit stub appears as a short circuit while the slotline short circuit appears as an open circuit at the crossing reference plane. After that, some modifications in the stubs has been proposed in order to improve the bandwidth of this transition. For example, Schüppert [215] proposed the introduction of circular stubs, see Fig. 7.9 b). Moreover, [216] used radial stubs instead of circular or straight ones both in the microstrip and in the slotline ending, see Fig. 7.9 c). This solution exhibits broader bandwidth than straight and circular ones and alleviates the problem of overlapping the microstrip and slotline tunning stubs. Such overlapping generally disturbs the effectiveness of the microstrip ground plane. This last transition has been successfully implemented as a feeding system in a Vivaldi antenna obtaining a bandwidth from 2.5 GHz to 10.6 GHz in [217].

Although transitions using these techniques have broadband characteristics, their insertion loss typically increases gradually as frequency increases. And

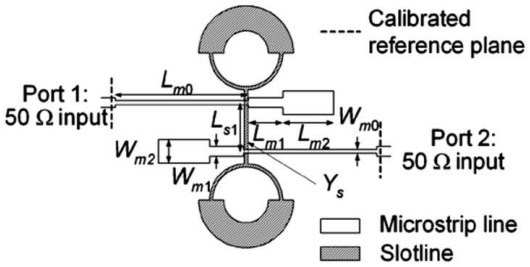

Figure 7.10 – Microstrip to slotline transitions proposed in [218].

this insertion loss is partly caused by the change in the slotline characteristic impedance with frequency and the slotline radiation loss. The microstrip to slotline transitions designed in all of these articles are wideband because the implementation of narrow slots, which result in lower slotline impedances from 50 Ω to 80 Ω, has been feasible. However, when higher slotline impedances are considered, the introduction of some impedance matching technique is required.

Recently, in order to reduce radiation losses in the microstrip to slotline transition, the use of a slotline stepped impedance circular ring termination has been reported in [218], see Fig. 7.10. This technique is useful to reduce the insertion losses in the transition and it is capable of matching to 50 Ω the slotline characteristic impedance of 91 Ω. However, it also increases the design complexity of the transition.

A simpler design, which reduces also the insertion losses up to 1 dB at 10 GHz, was proposed in [219]. This transition is an improved version of [216] that consists of a microstrip Chebyshev multisection matching transformer and a right-angle crossing of a microstrip radial stub and a slot radial stub. The radiation loss is decreased by employing a extremely large angle slot radial stub, see Fig. 7.11. The slotline characteristic impedance in this case is 108 Ω; therefore, it is a suitable microstrip to slotline transition for the Vivaldi antenna due to its simple design, broadband performance and capability of matching higher slotline characteristic impedance.

The geometry of the designed microstrip to slotline transition as the feeding system of the W-band Vivaldi antenna is shown in Fig. 7.12. The slotline and the slot radial stub are in the ground plane of the antenna. The microstrip line and the microstrip Chebyshev multisection matching transformer are at

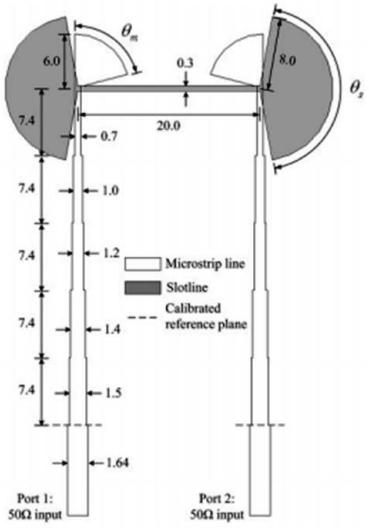

Figure 7.11 – Microstrip to slotline transitions proposed in [219].

the opposite side of the substrate in the microstrip line.

The transition is built on the same substrate of the exponential aperture, i.e. 127 μm thick Rogers RT/Duroid 5880. Thereby, the width of the 50 Ω microstrip line is $w_m = 0.4$ mm. With the slotline width $w_s = 0.05$ mm, its impedance is $Z_{0s} = 129$ Ω at 92.5 GHz. In order to match this Z_{0s} to 50 Ω, a three-section Chebyshev transformer (ripple level $\Gamma = 0.05$) with section impedances of 104, 81 and 62 Ω is required [102]. Therefore, the width of each microstrip Chebyshev section corresponds to $w_1 = 0.11$ mm, $w_2 = 0.2$ mm and $w_3 = 0.32$ mm. The dimensions of the radial stubs are $r_m = \lambda_m/4 = 0.55$ mm and $r_s = \lambda_s/4 = 0.58$ mm, where λ_m and λ_s are the guided wavelengths of the microstrip line and the slotline at the center frequency, respectively.

After a parametric study of the transition using the commercial full-wave electromagnetic simulator Ansys HFSS, the optimum design parameters were set as follows: $l_{cheb} = 0.6$ mm, $\theta_s = 160°$ and $\theta_m = 75°$. Moreover, a 90° bend in the 50 Ω microstrip line has been optimized in order to facilitate the integration of the antenna with the receiver, to allow the implementation of a future array and not to penalise the reflection and transmission coefficients of the transition.

The simulated S-parameters of the optimal microstrip to slotline transition

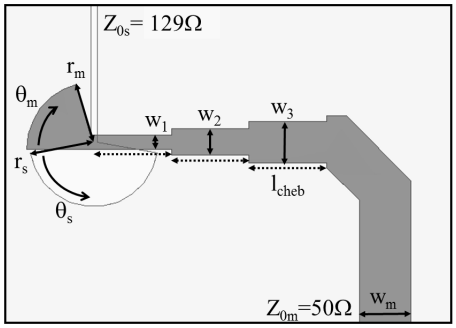

Figure 7.12 – Geometry of the designed microstrip to slotline transition of the W-band Vivaldi antenna and its parameters.

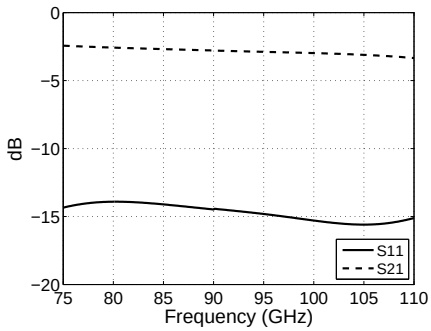

Figure 7.13 – Simulated S-parameters for the optimal microstrip-to-slotline transition.

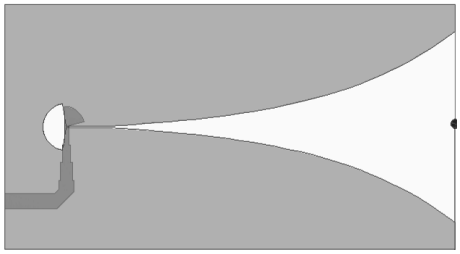

Figure 7.14 – The designed W-band Vivaldi antenna.

can be seen in Fig. 7.13. The insertion losses are around 2.7 dB along the full W-band. A small part of these losses are related to the dielectric loss tangent of the used substrate at this operating frequency. As was demonstrated in Section 4.2, the dielectric loss tangent of the 127 μm thick RO5880 substrate is approximately 0.01 at W-band. Therefore, this value has been used in the simulations. The rest of the losses corresponds to radiation.

The length of the 50 Ω microstrip line included in the transition is 1.8 mm, thereby the theoretical insertion losses produced by this line are 0.18 dB [102]. Therefore, the insertion losses in the microstrip to slotline transition are around 2.5 dB along the entire W-band.

Regarding the reflection coefficient, the transition is matched in the full W-band with S11 $\leqslant -14$ dB, see Fig. 7.13.

7.3.5 Simulation results

The resulting W-band Vivaldi antenna which consists of the optimized exponential aperture and the microstrip to slotline transition can be seen in Fig. 7.14. The darker grey area corresponds to the microstrip line and the pale grey area corresponds to the ground plane of the antenna which contains the exponential aperture and the slot radial stub.

A summary of the dimensions of the designed Vivaldi antenna at W-band can be found in Table 7.3. The parameters of the exponential aperture and of the microstrip-to-slotline transition of the antenna are defined in Fig. 7.2 and 7.12 respectively.

The most important antenna parameters are shown in the following Figures. Firstly, the reflection coefficient of the antenna is shown in Fig. 7.15 a) in which matching along the entire W-band is ensured. As can be seen the

Table 7.3 – Dimensions (mm) of the designed Vivaldi antenna at W-band.

t	L	H	R	w_s	w_m	w_1
0.127	9.72	4.86	0.3	0.05	0.4	0.11
w_2	w_3	r_m	r_s	θ_m	θ_s	l_{cheb}
0.2	0.32	0.55	0.58	75°	160°	0.6

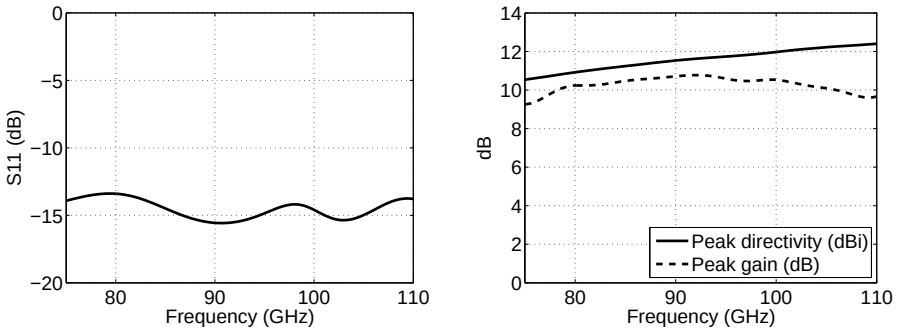

(a) S11 (dB)

(b) Peak directivity (dB)

Figure 7.15 – a) Simulated reflection coefficient and b) simulated peak directivity and gain of the designed Vivaldi antenna according to the frequency.

exponential aperture has a slight effect on the reflection coefficient of the microstrip to slotline transtion.

Fig. 7.15 b) shows the peak directivity and gain of the designed antenna depending on the frequency. Directivities above 10 dBi are ensured along the entire W-band. The lowest directivity of the antenna is 10.54 dBi at the lowest frequency of the band, i.e. 75 GHz. As expected, the directivity increases with frequency up to a value of 12.38 dBi at the highest frequency, i.e. 110 GHz. However, gains above 10 dB are obtained in a narrower bandwidth due to the losses of the used substrate, i.e. from 80 to 105 GHz.

With respect to the radiation pattern of the W-band Vivaldi antenna, the normalised E- and H-plane can be seen in Fig. 7.16. Moreover, their crosspolar components have been included in Fig. 7.17. Note that, as expected, the beamwidths of the main lobe in both planes are narrower as the frequency increases; this effect can be seen more clearly in Fig. 7.18 a) where the HPBW of both planes is depicted. Moreover, the beamwidth of the radiation pattern

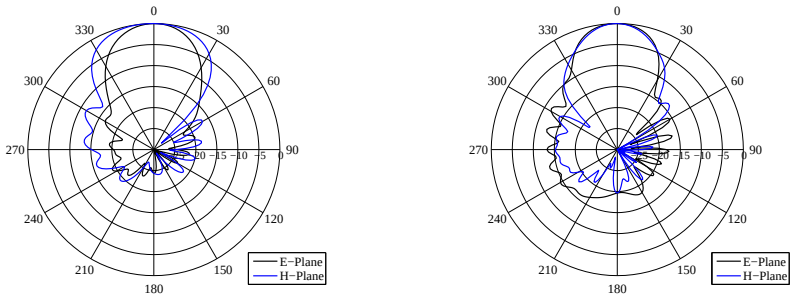

(a) 75 GHz (b) 110 GHz

Figure 7.16 – Normalised radiation pattern of the designed W-band Vivaldi antenna at a) 75 GHz and b) 110 GHz. Black and blue lines correspond to E-plane and H-plane respectively.

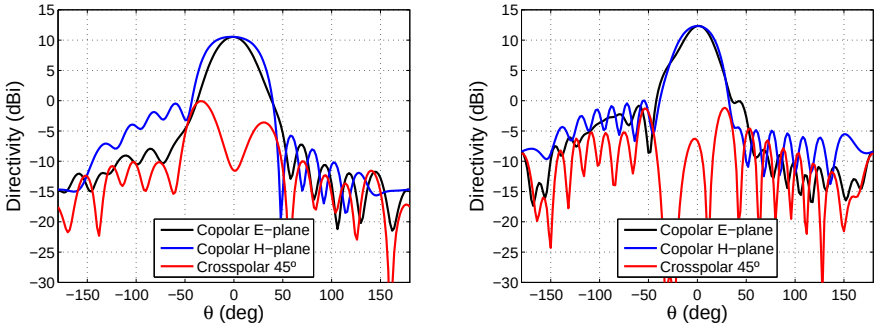

(a) 75 GHz (b) 110 GHz

Figure 7.17 – Radiation pattern of the designed W-band Vivaldi antenna at a) 75 GHz and b) 110 GHz. Copolar and crosspolar components of the E- and H-plane are included.

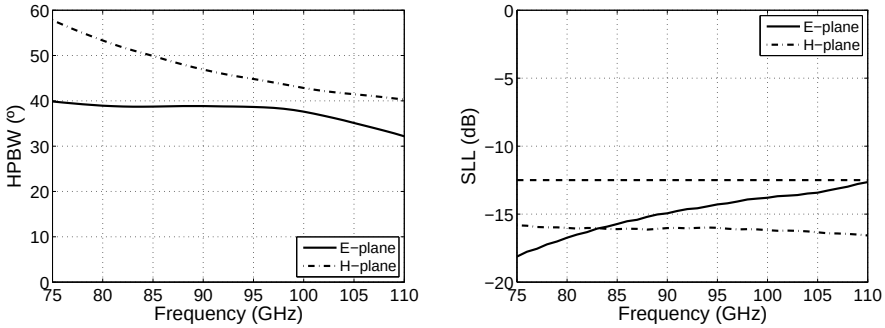

(a) HPBW (°) (b) SLL (dB)

Figure 7.18 – Frequency dependence of the a) HPBW (°) and b) SLL (dB) of the E- and H-plane of the radiation pattern of the designed W-band Vivaldi antenna. The dashed line in b) corresponds to the maximum allowed SLL.

at the H-plane is broader than the E-plane beamwidth, as it was showed in Section 7.3.1.

Finally, the SLL of the radiation pattern of the designed W-band Vivaldi antenna taking into account the E- and H-planes has been depicted in Fig. 7.18 b). As can be seen, the SLL of both planes is below the required -12.5 dB.

Therefore, the designed W-band Vivaldi antenna meets the requirements of a planar antenna suitable to be integrated with a planar W-band auto-calibrated receiver on the same substrate.

7.4 Vivaldi antenna array

After the design of a single element of a Vivaldi antenna obtaining good expected radiation performance, the coupling between two elements in a linear array has been simulated in this Section. A picture of a 1 x 2 Vivaldi antenna array is shown in Fig. 7.19.

In the design of the single element, the optimum width of the aperture was $1.5\lambda_0$. Therefore, the minimum separation between two antennas, i.e. d, should be larger or even equal to the width of the aperture, i.e. $1.5\lambda_0 = 4.86$ mm.

The results of the analysis shown that the coupling between two Vivaldi

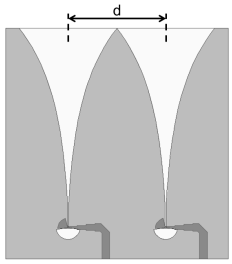

Figure 7.19 – Array of two designed Vivaldi antennas.

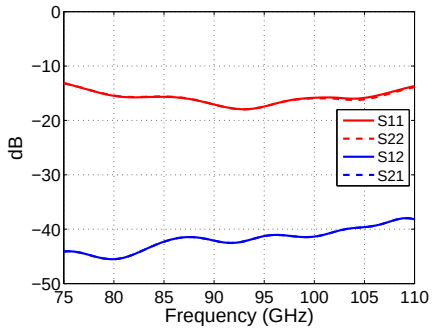

Figure 7.20 – Simulated S parameter of the array of two designed Vivaldi antennas.

antennas separated by the minimum feasible distance, i.e. $d = 4.86$ mm, is almost negligible because it is below -35 dB along the entire W-band, see the transmission coefficient in Fig. 7.20. Moreover, the matching of each single element is slightly affected by the interaction between these two elements, keeping it below -10 dB in the full W-band.

7.5 Experimental validation of the antenna

Once the design of the W-band Vivaldi antenna has been presented, a prototype has been manufactured and measured in order to validate the simulation results.

The characterization of the antenna has been accomplished by measuring reflection coefficient, radiation pattern and peak gain at W-band. These

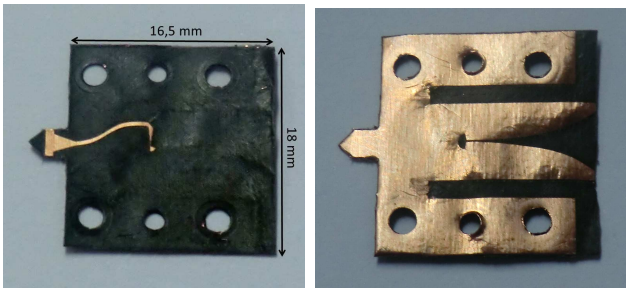

(a) (b)

Figure 7.21 – Prototype of the manufactured W-band Vivaldi antenna; a) microstrip view and b) aperture view.

measurements have been carried out with waveguide based equipment. Therefore, the designed WR10 waveguide to microstrip transition, which was presented in Section 4.3, is needed to characterize the W-band Vivaldi antenna.

The W-band Vivaldi antenna has been manufactured on 127 μm thick RO5880 substrate in the ProtoLaser 200 machine. As can be seen on Fig. 7.21 a), the microstrip part of the antenna is printed on one side of the substrate. This part includes the microstrip section required to match the WR10 waveguide to microstrip transition, a 50 Ω microstrip line, which has been bent to centre the aperture of the antenna in the same axis of the waveguide, and the microstrip to slotline transition required to feed the antenna. The exponential aperture and the slotline of the antenna are on the other side of the substrate, shown in Fig. 7.21 b). The ground plane has been extended to the sides of the substrate to ensure the ground contact between the microstrip and the metal block of the WR10 waveguide to microstrip transition.

Regarding the WR10 waveguide to microstrip transition, a new prototype has been designed and manufactured with the same method as in the previous prototype due to its good performance. Fig. 7.22 shows the prototype of the transition assembled with the W-band Vivaldi antenna. Note that the aperture of the antenna is centred in the metal block of the transition. Moreover, four metal screws and two dowel pins ensure the placement and the flatness of the antenna, which facilitates the alignment of the measurements.

The manufactured prototype, which consists of the WR10 waveguide to

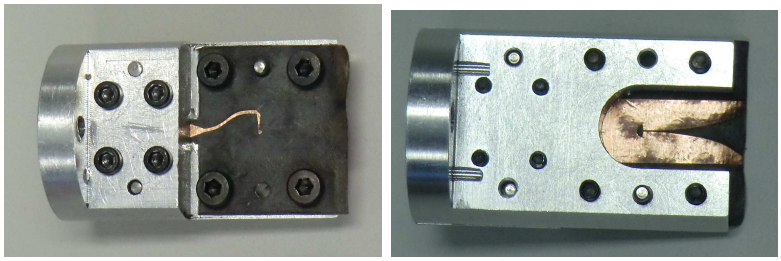

(a) (b)

Figure 7.22 – The designed WR10 waveguide to microstrip transition with the W-band Vivaldi antenna; a) Top view and b) bottom view.

microstrip transition and the W-band Vivaldi antenna, has been measured using an Agilent PNA-X Network Analyser connected to VDI VNA Extenders at W-band available at the Antenna Group of the Public University of Navarra.

The measured S11 parameter compared with the simulation is depicted in Fig. 7.23. Fig. 7.23 a) shows the comparison between measurement and simulation directly obtained by the Analyser, i.e. taking into account the WR10 waveguide to microstrip transition assembled with the antenna. The measured reflection coefficient is higher than we expected but it was below -10 dB. If a suitable time gating is applied to this measurement, the effect of the WR10 waveguide to microstrip transition can be removed and the reflection coefficient of the antenna can be obtained. The resulting S11 parameter of the antenna compared with its simulation can be seen in Fig. 7.23 b). Good agreement between measurement and simulation has been obtained. It demonstrates that the Vivaldi antenna is matched along the entire W-band.

The set-up configuration used to characterize the antenna in terms of radiation pattern is shown in Fig. 7.24. It corresponds to a near field antenna measurement set-up at W-band. On the one hand, an open-ended waveguide is placed in a XY positioner in order to be able to scan a plane. Absorbing material is placed at the back of the open-ended waveguide to remove undesired reflections. On the other hand, the manufacture prototype is fixed in the centre of the desired scan plane. The main beam of the radiation pattern of the antenna is broad, therefore, the scan plane has to be large in order to avoid truncation effects. For this reason, the distance between the prototype and

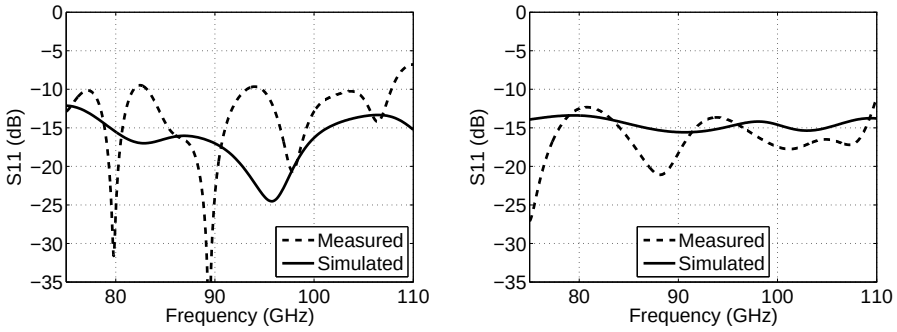

Figure 7.23 – Comparison between the simulated and measured reflection coefficient of the W-band Vivaldi antenna taking into account the WR10 waveguide to microstrip transition with the Vivaldi antenna a) without applying any gating and b) with a time gating which excludes the WR10 waveguide to microstrip transition.

the open-ended waveguide must be as small as possible but within the near field region. The selected distance has been 7.5 mm and thereby, the size of the scan plane is 720 mm x 720 mm. The data samples are taken every 1 mm verifying the Nyquist sampling criterion. Note that the open-ended waveguide must be rotated 90 degrees to align the electric fields of the antenna and the open-ended waveguide.

The measured amplitude and phase of the copolar near field of the W-band Vivaldi antenna in the measurement plane are depicted in Fig. 7.25. The shown frequencies are 75, 92.5 and 110 GHz. In these Figures, the maximum of the field distribution is easily distinguishable and it is appreciated that it is slightly deviated of the center of the scan plane. These data have been processed to obtain the radiation patterns of the antenna at W-band. In particular, the measured E- and H-plane of the W-band Vivaldi antenna at 75, 92.5 and 110 GHz have been compared with the simulations, see Fig. 7.26. Good agreement between measurements and simulations has been obtained.

Finally, the antenna gain has been characterized. The gain comparison method has been used, with a standard gain horn antenna as a reference antenna. The transmission coefficient of two standard horn antennas separated by a certain distance in the far field region has been used as reference. Then,

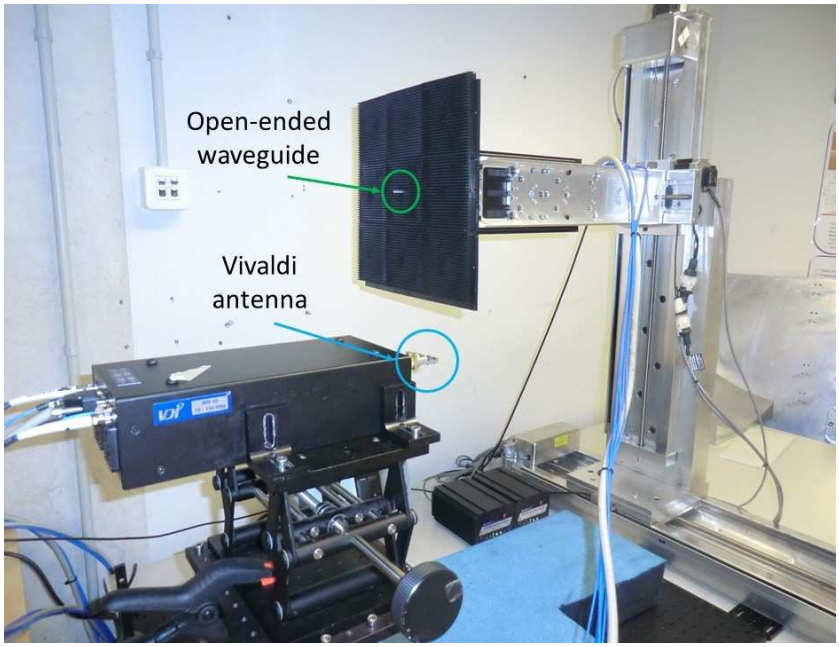

Figure 7.24 – Set-up of the radiation pattern measurement of the W-band Vivaldi antenna.

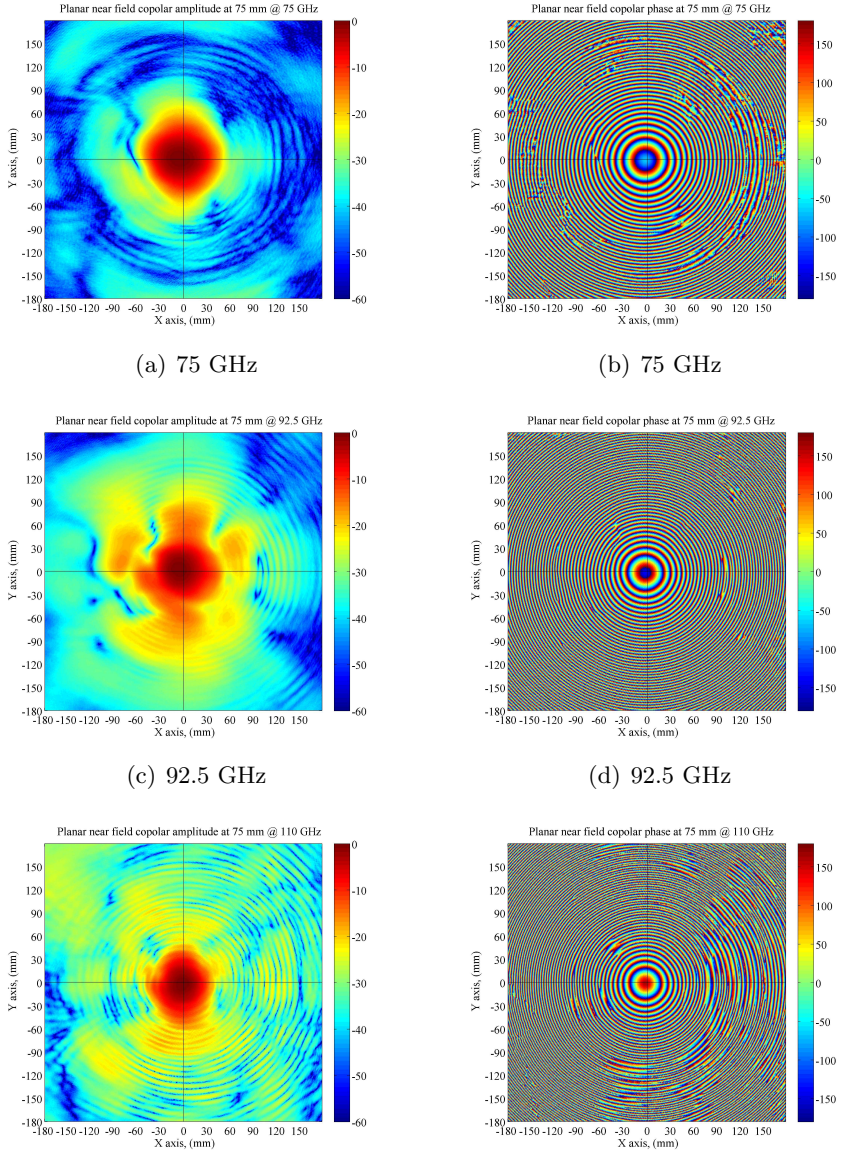

(a) 75 GHz (b) 75 GHz

(c) 92.5 GHz (d) 92.5 GHz

(e) 110 GHz (f) 110 GHz

Figure 7.25 – Normalized measured planar near field copolar amplitude at a) 75 GHz, c) 92.5 GHz and e) 110 GHz. Measured planar near field copolar phase at b) 75 GHz, d) 92.5 GHz and f) 110 GHz.

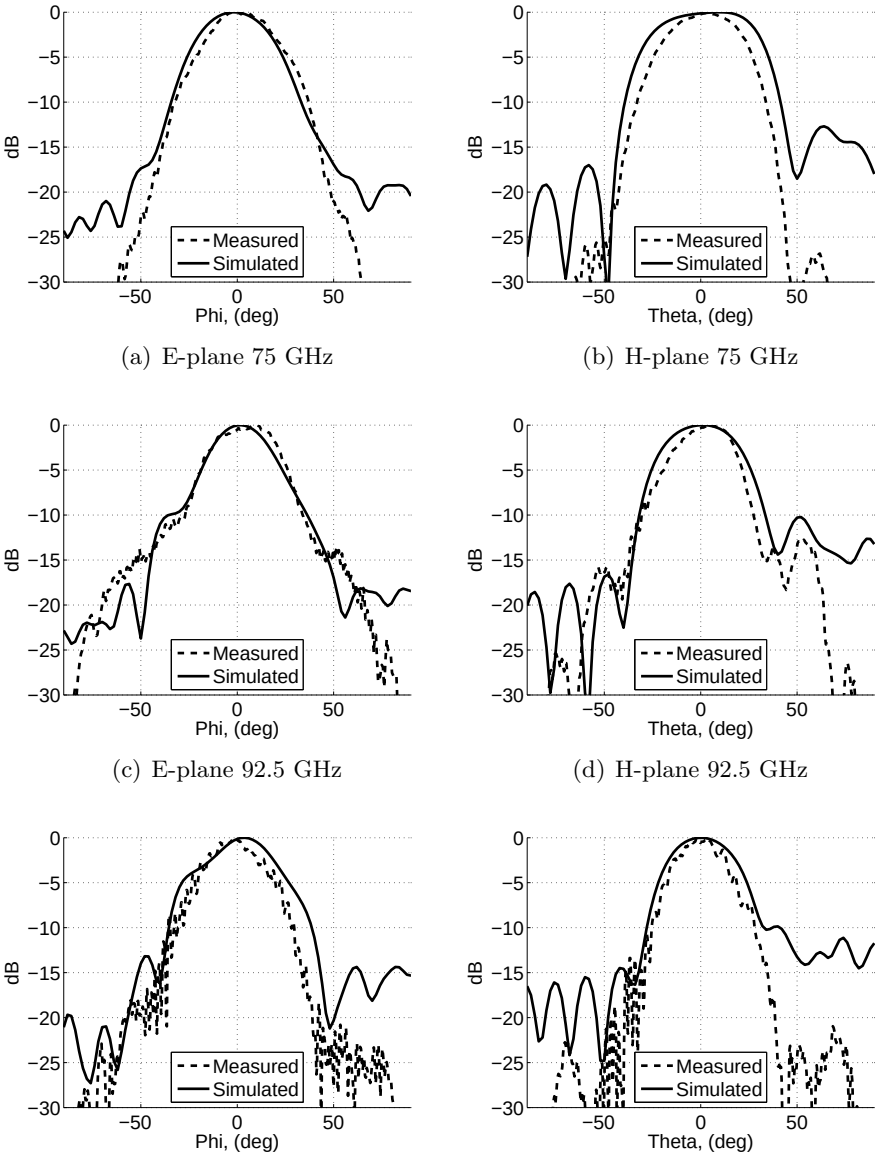

(a) E-plane 75 GHz

(b) H-plane 75 GHz

(c) E-plane 92.5 GHz

(d) H-plane 92.5 GHz

(e) E-plane 110 GHz

(f) H-plane 110 GHz

Figure 7.26 – Comparison between measurement and simulation of the E-plane and H-plane of the W-band Vivaldi antenna; a) E-plane 75 GHz, b) H-plane 75 GHz, c) E-plane 92.5 GHz, d) H-plane 92.5 GHz, e) E-plane 110 GHz and f) H-plane 110 GHz.

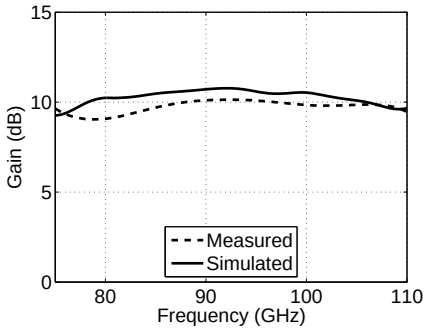

Figure 7.27 – Comparison between the simulated and measured peak gain of the W-band Vivaldi antenna.

a Vivaldi antenna is placed instead of one of these standard horn antennas and the transmission coefficient is measured. Taking into account this last measurement, the peak gain of the W-band Vivaldi antenna is the difference between this transmission coefficient and the peak gain of the standard horn antenna at W-band. This result is shown in Fig. 7.27. As can be seen, the expected peak gain is close to the measurement.

It has been demonstrated that the designed W-band Vivaldi antenna works properly along the entire W-band in terms of reflection coefficient, radiation pattern and peak gain. Therefore, the use of this planar antennas can be a good alternative to replace horn antennas in a multiple-beam imaging system. In this way, compact and light systems are provided.

7.6 Conclusions

In this Chapter, a Vivaldi antenna compatible with the proposed receiver configuration with broadband performance has been designed, manufactured and measured. This is an interesting alternative in order to reduce the size and weight of the receivers. Moreover, the integration of the W-band auto-calibrated receiver and the planar antenna on the same substrate provides a compact and easy to manufacture receiver. In addition, this facilitates the implementation of a multiple pixel imaging system. The antenna consists of an exponential aperture and a broadband slotline to microstrip transition. The broadband slotline to microstrip transition has been designed to have

return losses larger than 10 dB in the full W-band. The characterization of the W-band Vivaldi antenna shows good agreement with the predictions.

Chapter 8

Conclusions and guidelines for future research

This Chapter summarizes the main results obtained in this Thesis. Some guidelines for future research are also given.

8.1 Conclusions

In this dissertation, the design, fabrication, assembly and characterization of a W-band auto-calibrated receiver have been carried out. The main advantage of this receiver is its balanced structure which performs the internal calibration of the system. This calibration minimizes the effect of receiver instabilities which strongly penalize the sensitivity of a total power receiver. Moreover, this configuration improves the sensitivity by a factor of $\sqrt{2}$ with respect to other calibrated configurations such as Dicke receivers. Other advantages of this proposed receiver are its planar structure and that it is based on a direct detection scheme. On the one hand, its planar structure facilitates the assembly, the integration of the MMIC components and the realization of its required connections by gold wire bonging. Moreover, a planar antenna could be also built on the same substrate. Consequently, the receiver could be more compact and lighter than waveguide based receivers. On the other hand, a direct detection scheme makes it simpler extending the number of receivers for imaging applications. In addition, it uses commercially available low loss dielectric substrates and W-band MMIC devices such as Low Noise Amplifiers

(LNA) and detector diodes.

In Chapter 2, the theoretical analysis of the differential configuration of the W-band auto-calibrated receiver was carried out. With this analysis, the two main advantages of this configuration were demonstrated. Firstly, its capability to separate the input and reference signals and to perform the internal calibration of the system. And secondly, the reduction of the effect of gain and noise fluctuations since their contribution in both the amplified signals are equal. Therefore, their effects are removed by including a subtracting operation in the post-detection stage of the receiver. Afterwards, taking into account the planar structure of the W-band auto-calibrated receiver, a low loss dielectric substrate required to minimize the dielectric losses was selected in this Chapter. This was important because some receiver components such as the WR10 waveguide to microstrip transition and the two quadrature hybrid couplers were built on this substrate. Their dielectric losses increased the system noise temperature and penalized the sensitivity of the receiver. Moreover, the designs of these microstrip components and the selection of the suitable MMIC devices such as low noise amplifier, attenuator and detectors were presented.

Chapter 3 reported the analysis of the receiver performance using the SW package Advanced Design System (ADS) by Keysight Technologies. This analysis was carried out along the entire W-band. Firstly, the mentioned advantages of the receiver configuration, i.e. the reduction of the gain and noise imbalance effect of the amplifiers and the internal calibration of the system, were demonstrated by means of an AC simulation taken into account ideal components. Next, the effect of each microstrip component and MMIC device was discussed by simulation in terms of its impact on the noise figure, noise temperature, gain and reflection coefficient. As Friis equation shows, the components which mainly contribute to the noise of the receiver were its first components, i.e. the WR10 waveguide to microstrip transition and the first quadrature hybrid and its input lines. It is therefore important to minimize these losses by using a low loss tangent substrate. It was demonstrated that the most critical part on the receiver performance was the length of the gold wire bondings since standing waves were created due to reflections in the wire junctions. Specifically, lengths above 0.20 mm drastically increased the receiver noise temperature, which implied a loss of sensitivity. Furthermore, these bondwires also deteriorated the input return losses and the gain of the receiver. In conclusion, the length of the bondwires had to be carefully

considered in the assembly of the components of the W-band auto-calibrated receiver to obtain high sensitivity.

Chapter 4 presented the fabrication and characterization of the planar components of the W-band auto-calibrated receiver. The microstrip components were built on 0.127 mm thick RO5880 substrate. The dielectric constant and loss tangent of this substrate was measured by the manufacturer only at 10 GHz. Therefore, first of all, the characterization of this substrate in the W-band was indispensable in order to compare the simulation performance of these microstrip components with their experimental results. Two different set-ups were taken into account to measure the transmission coefficient through a thin sample of these materials: one based on lenses and other one based on mirrors. The experimental results confirmed that the set-up based on lenses was able to obtain better results thanks to its accurate alignment and narrower beam waist. In conclusion, the retrieved dielectric constant and loss tangent of 0.127 mm thick RO5880 substrate at W-band were found to be 2.22 and 0.01 respectively. It is worth noticing that the losses are one order of magnitude higher than the value given by the manufacturer at 10 GHz. Then, in order to characterize the microstrip components of the receiver with waveguide based measurement equipment, the design, manufacture and validation of a novel inline WR10 waveguide to microstrip transition which covers the full W-band were also shown in this Chapter. Next, the characterization of the quadrature hybrid coupler and the MMIC attenuator were carried out with this transition. The experimental results verified their expected performances.

In Chapter 5, the design of the cavity which packages the planar structure of the W-band auto-calibrated receiver was presented. This cavity used an innovative solution in order to prevent resonances which degrade the receiver performance. The propagation of parallel-plate modes was blocked within a certain frequency band (stop-band) by means of a periodic structure placed in the top ground plate of this cavity. In particular, the selected periodic structure was based on a square pin surface. For the first time, a deep understanding of the behaviour of its modes and the influence of the different parameters on its performance were shown in this Chapter. Besides, as a result of the acquired knowledge in the complete parametric study, the design guidelines of this pin surface were defined in order to create a certain stop-band. Moreover, a prototype was manufactured and assembled and the removal of the propagation of cavity modes was demonstrated experimentally.

At that point, the design of the last components of the W-band auto-calibrated receiver was carried out, i.e. the DC circuit and the packaging aluminium block which will contain all the components. The DC circuit consisted of two blocks: the circuit of the amplifiers and the DC output amplification circuit. Finally, the packaging metal block of the W-band auto-calibrated receiver was designed considering the implementation of both square and pyramidal arrays of receivers.

Chapter 6 presented the fabrication and assembly of both the packaging metal block and the microstrip part of the receiver. Once it was done, the gold wire bondings and the biasing of the amplifiers were carried out. This bias was adjusted to 35 mA drain current, as the manufacturer recommended. Finally, the complete W-band auto-calibrated receiver was characterized in terms of input reflection coefficient, dynamic range, RF-DC response and effective bandwidth. Moreover, the measurement of the dynamic range of the W-band auto-calibrated receiver in its output reference signal verified that the balanced structure of the receiver worked as expected and it was able to perform the internal calibration of the system. Although the measurement of its input reflection coefficient confirmed that the amplifiers were amplifying, the dynamic range of the receiver showed that the receiver gain was not as high as expected. Indeed, the reduction of receiver gain was between 10 and 23 dB. As explained in this Chapter, some problems contributed to this reduction of receiver gain. Firstly, the added dielectric losses in the microstrip part of the receiver increase the receiver noise and reduce its sensitivity. The use of a lower loss substrate such as COC polymer could be an improvement. Indeed, simulations show that the receiver dielectric losses would decrease in at least 7 dB if COC polymer was used and the gold wire bondings were shortened. However, the reduction of the receiver gain was found to be mainly produced by the fact that the amplifiers were not working at their optimum operating point as it was demonstrated experimentally. Certainly, better results would have been obtained if other bias point had been used. An increase of at least 16 dB in the receiver gain at 93 GHz was confirmed by analysing the differences between the dynamic range of the receiver taking into account two drain currents, i.e. the optimum experimental value (20 mA) and the value recommended by the manufacturer (35 mA). This implied that the performance of the amplifiers of the W-band auto-calibrated receiver were not optimum in the measurements. Therefore, readjusting the drain current of the amplifiers would be required in order to accomplish the expected performance

of the receiver. However, the W-band auto-calibrated receiver can not be characterized taking into account the commented improvements because no MMIC amplifiers are now available.

Finally, in Chapter 7, a Vivaldi antenna compatible with the proposed receiver configuration with broadband performance was designed, manufactured and measured. This is an interesting alternative in order to reduce the size and weight of the receivers. Moreover, the integration of the W-band auto-calibrated receiver and the planar antenna on the same substrate provides a compact and easy to manufacture receiver. In addition, this facilitates the implementation of a multiple pixel imaging system. The antenna consisted of an exponential aperture and a broadband slotline to microstrip transition. The broadband slotline to microstrip transition was designed to have return losses larger than 10 dB in the full W-band. The characterization of the W-band Vivaldi antenna shown good agreement with the predictions.

8.2 Guidelines for future research

Given the limited time available for this Thesis, there are some open issues that should be explored in order to complete the work carried out. First, the results shown in Chapter 6 proved that the dynamic range of the receiver was not enough since the amplifiers were not operating in their optimum point. For this reason, the first line of future research would be to evaluate this bias issue. In addition, the losses of the circuit could be improved if shorter bondings and a COC substrate were used. In this last case the bonding procedure should be optimized.

The following topic for future research would be checking the performance of the W-band auto-calibrated receiver working as an imaging receiver at W-band. This could be carried out obtaining different images in which the receiver should be able to detect, for instance, metals or ceramic materials. In addition, it would be interesting to give a comparison between the performance of the W-band auto-calibrated receiver and a commercial total power receiver, e.g. those commercialised by MMIC Solutions [97]. This is essential to confirm the mentioned advantages of this proposed configuration taking into account the effect of gain and noise fluctuations of the amplifiers. Moreover, a comparison between the performance of the W-band auto-calibrated receiver when it is connected to a standard horn antenna and to the designed W-band

Vivaldi antenna, which was validated in Chapter 7, would be also interesting.

The implementation of an array of W-band auto-calibrated receivers would be the next guideline for future research. Moreover, the array would have to be placed in Alfa imaging's imager. This is based on a Cassegrain configuration suitable to take outdoor images using an array of W-band auto-calibrated receivers.

Finally, in order to reduce the losses, novel implementations based e.g. on gap waveguide could be used. The integration of the MMICs on this type of waveguide is not evident and should be explored.

Appendices

Appendix A

Datasheets of the MMIC devices

The aim of this Appendix is to include the datasheets of the commercial MMIC devices selected for being part of the W-band auto-calibrated receiver. These components are the LN4-110 low noise amplifiers, the V1A detector diodes and the TGL4201-10 attenuator. The manufacturer of both amplifier and detector is HRL Laboratories [144] whereas the attenuator is commercialised by TriQuint Semiconductor [138].

HRL LABORATORIES

LN4-110

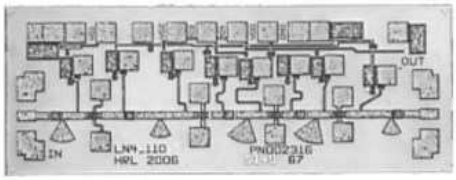

- **InP Low Noise Amplifier**
- **Full W-Band operation**
- **22 dB Gain**
- **3.5 dB Noise Figure**

The LN4-110 is a four stage MMIC amplifier that covers the entire W-Band. The amplifier is fabricated using HRL's passivated H2 InP HEMT process that is AS9100B certified. The LNA has a single drain supply and is typically used with an independent gate bias for the first stage and a common gate bias for the remaining stages.

Electrical Specifications, T_A=25°C, Vd=1.2 V, Id=35 mA, Pin = -30 dBm

Specification	Units	Min	Typ	Max
Frequency	GHz	75		110
Gain	dB	22	24	27
Input Return Loss	dB		-3	-3
Output Return Loss	dB		-5	0
Noise Figure	dB		3.5	

Typical Gain and Return Loss Performance

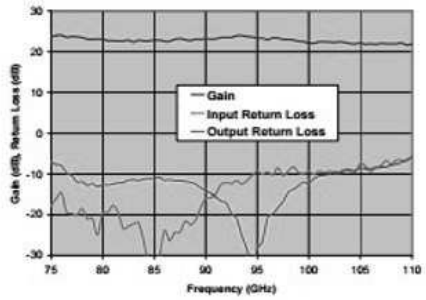

Table I Maximum Ratings

Symbol	Parameter	Value	Note
P_{IN}	Input Power	-20 dBm	1
I_G	Gate Current	1 mA	1
V_{DS}	Drain to Source Voltage	1.5 V	1
V_{GD}	Gate to Drain Voltage	-2.5 to 0.2 VDC	1
V_{GS}	Gate to Source Voltage	-1.0 to 0.2 VDC	1
T_M	Die Attach Temperature (30 seconds)	290° C	

1 T_{base} = 25 °C unless specified otherwise

Typical Noise Figure Performance

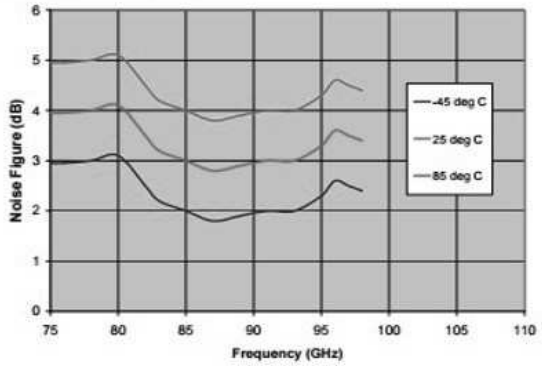

Typical Saturated Output Power Performance

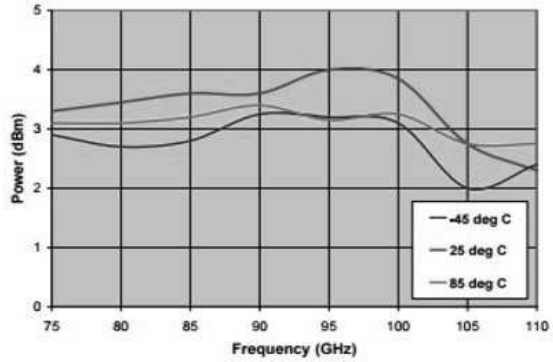

Outline Drawing

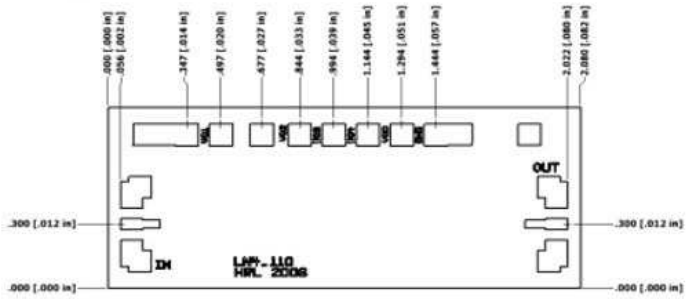

Bond pads are nominally 0.1mm square	Die thickness is nominally 50 um
Bond pad locations shown from die edge to pad center	Die should not be plasma cleaned

Typical Assembly Drawing

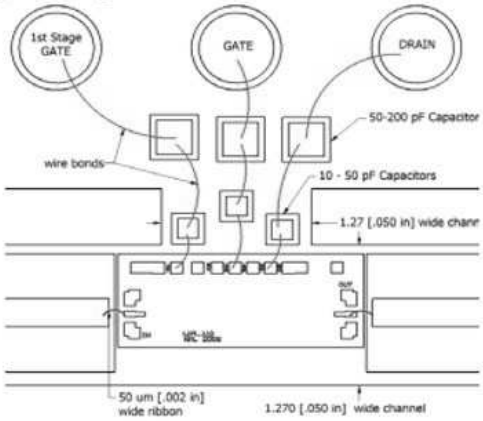

Schematic

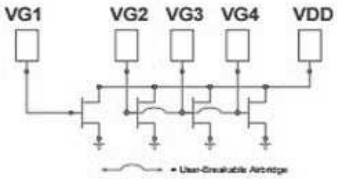

HRL LABORATORIES

V1A

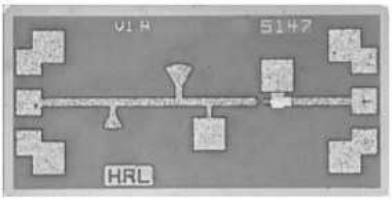

- **Detector Diode MMIC**
- **W-Band 75-110 GHz**
- **Lowest 1/f Noise**
- **Zero Bias Detector**

The V1A is a tunnel diode W-band square law detector fabricated using HRL's advanced InAs/GaAlSb growth and fabrication processes that are AS9100B certified. The zero bias diode produces a DC voltage proportional to input power with high sensitivity. Linearity is excellent up to the -30 dBm input power level. Noise equivalent power is less than 1 pW/Hz$^{1/2}$.

Electrical Specifications, T_A= 25°C

Specification	Symbol	Units	Min	Typical	Max
Diode Resistance	R_d	Ω	900	1400	3000
Curvature Coefficient	γ	mA/mW	15	32	
Mean Sensitivity	β_{avg}	V/mW	7	15	
Center Frequency	f_0	GHz	85	95	105
Bandwidth	$\Delta\nu$	GHz	25	35	
Return Loss	RL	dB	5	7	

R_d = dV/dI = slope of DC I(V) curve at zero bias, V=0.
$\gamma = (d^2I/dV^2)/(dI/dV)$ at V=0.
RL = -10 $\log_{10}(S_{11,ave})$
Other parameters are defined as:

$$f_0 = \frac{\int_0^\infty \beta(f) f df}{\int_0^\infty \beta(f) df}, S_{11,ave} = \frac{\int_0^\infty |S_{11}(f)|^2 \beta(f) df}{\int_0^\infty \beta(f) df}, \Delta\nu = \frac{\left(\int_0^\infty \beta(f) df\right)^2}{\int_0^\infty \beta^2(f) df}, \beta_{avg} = \frac{\int_0^\infty \beta^2(f) df}{\int_0^\infty \beta(f) df}$$

Table I Maximum Ratings

Symbol	Parameter	Value	Note
P_{IN}	Input Power	-10 dBm	
$\|V_{MAX}\|$	DC Voltage Magnitude	0.2 V	
T_M	Mounting Temperature (30 seconds)	290	

ESD Sensitivity

Diodes are ESD sensitive. ESD preventive measures must be employed in all aspects of storage, handling, and assembly. Common causes of ESD include attaching and detaching high capacitance cables, electronic equipment that may produce power spikes, and DC voltage offsets in post-detection amplifiers.

Typical DC Current Voltage Performance

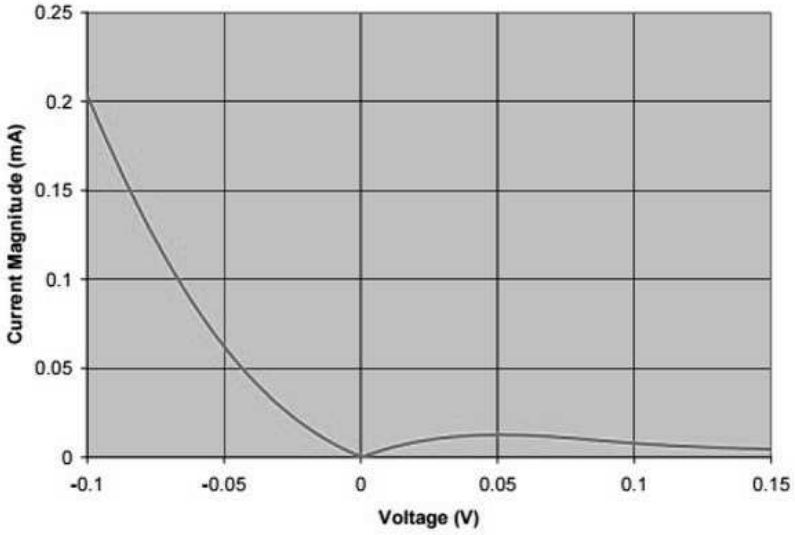

Typical Return Loss Performance

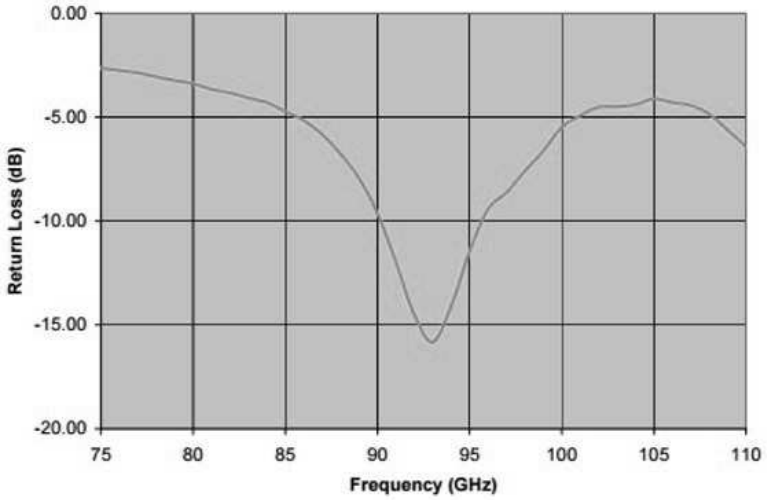

Typical Sensitivity Performance

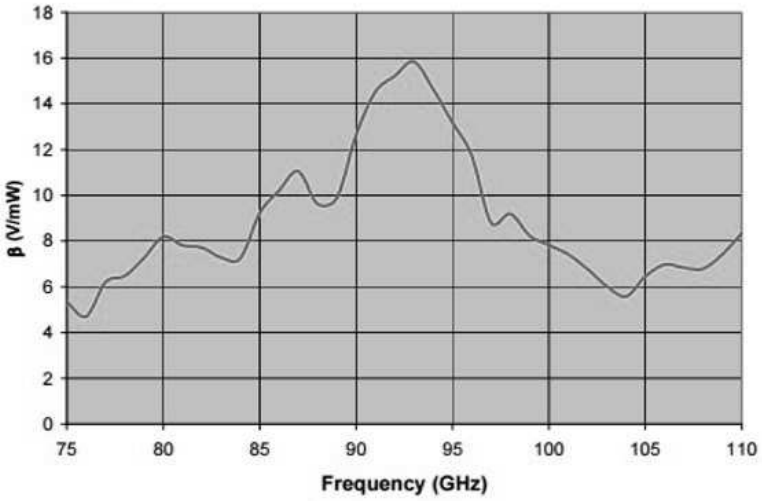

Outline Drawing

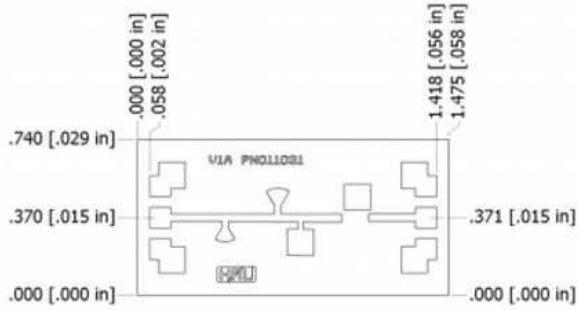

Bond pads are nominally 0.1mm square
Bond pad locations shown from die edge to pad center
Die thickness is nominally 50 um

TriQuint SEMICONDUCTOR

TGL4201

Wideband Fixed Attenuators

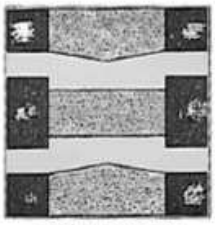

0 dB Attenuator

2 dB Attenuator

3 dB Attenuator

6 dB Attenuator

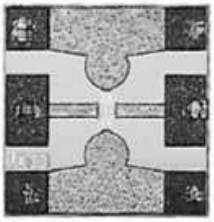

10 dB Attenuator

Key Features and Performance

- Fixed 0, 2, 3, 6 and 10dB Attenators
- Broadband Response DC to > 40 GHz
- Excellent Return Loss > 15 dB
- Power Handling = 20 dBm
- On-Chip Grounding Vias
- 3MI Passive Part
- Low Price
- Small size: 0.5 x 0.5 x 0.1 mm (0.02 X 0.02 X 0.004 in)

Primary Applications

- Point to Point Radio
- Fiber Optic
- Wideband Military & Space
- Test Equipment

Typical Electrical Characteristics

Attenuators Probed in Fixtures

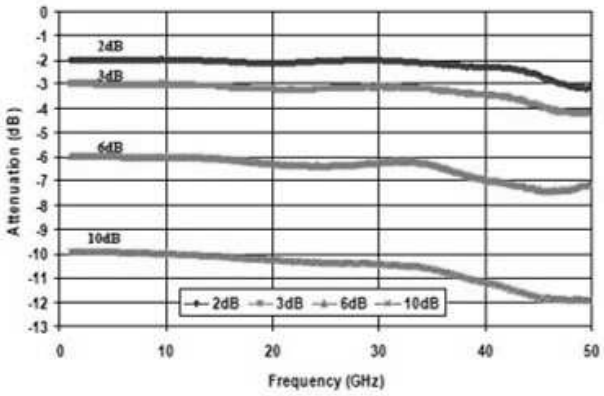

Datasheet subject to change without notice.

TriQuint Semiconductor: www. triquint.com (972)994-8465 Fax (972)994-8504 Info-mmw@tqs.com

Aug 2011 © Rev B

TriQuint SEMICONDUCTOR

TGL4201

TABLE I
ELECTRICAL CHARACTERISTICS
(Ta = 25 °C Nominal)

PARAMETER		TEST CONDITIONS	MIN	TYP	MAX	UNIT
	0dB Attenuation (-00)	DC – 30 GHz 1/	0	0.1	0.2	dB
	2dB Attenuation (-02)	DC – 30 GHz 1/	1.75	2	2.25	dB
	3dB Attenuation (-03)	DC – 30 GHz 1/	2.65	3	3.35	dB
	6dB Attenuation (-06)	DC – 30 GHz 1/	5.3	6	6.3	dB
	10dB Attenuation (-10)	DC – 30 GHz 1/	9.4	10	10.4	dB
IRL	Input Return Loss	DC – 40 GHz		15		dB
ORL	Output Return Loss	DC – 40 GHz		15		dB
	Maximum Power	2 - 18 GHz			20	dBm

1/ Measured on wafer with RF probes. Bond wires are not included in this measurement. Wafer is sample tested at ~10%. TGL4201-00 is not RF tested.

TriQuint Semiconductor: www. triquint.com (972)994-8465 Fax (972)994-8504 Info-mmw@tqs.com

Aug 2011 © Rev B

TriQuint SEMICONDUCTOR

TGL4201

Typical Measurement Attenuators
Attenuators Probed in Fixtures

2 dB Attenuator

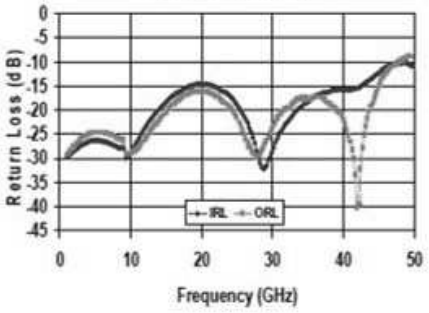

3 dB Attenuator

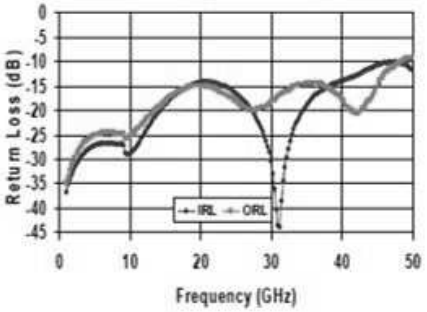

6 dB Attenuator

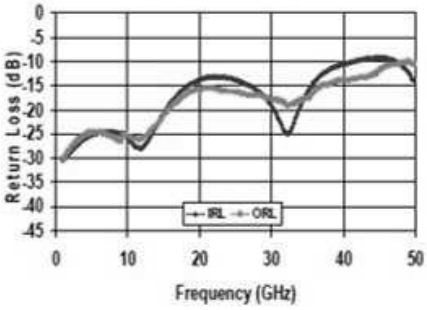

10 dB Attenuator

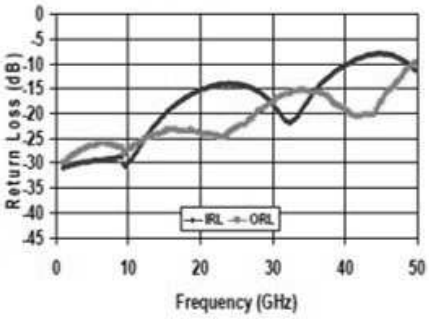

TriQuint Semiconductor: www.triquint.com (972)994-8465 Fax (972)994-8504 Info-mmw@tqs.com
Aug 2011 © Rev B

TriQuint SEMICONDUCTOR

TGL4201

Typical Measurement Attenuators
No Bond Wires, Probed from 45 MHz to 110GHz

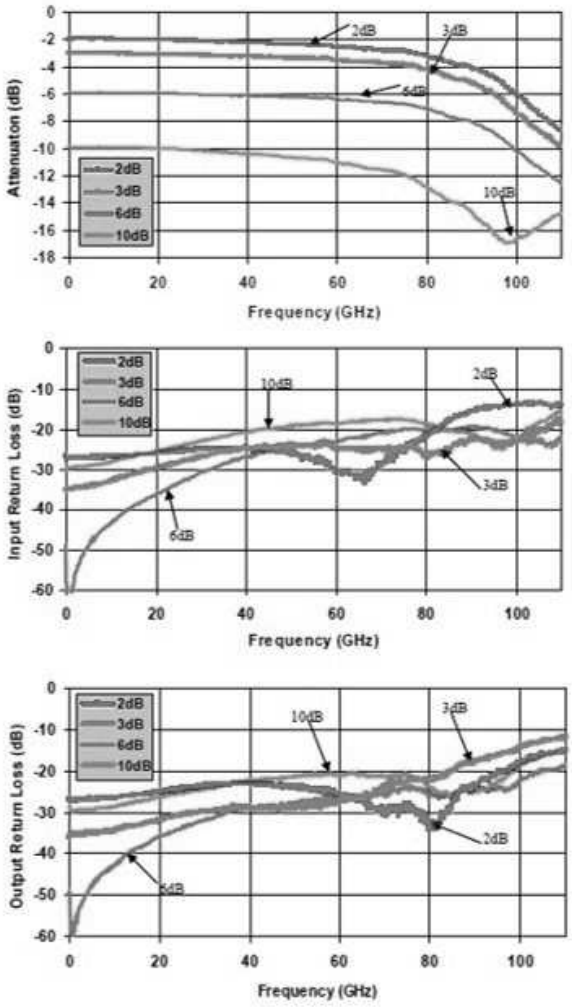

TriQuint Semiconductor: www.triquint.com (972)994-8465 Fax (972)994-8504 Info-mmw@tqs.com

TriQuint SEMICONDUCTOR

TGL4201

Mechanical Drawing

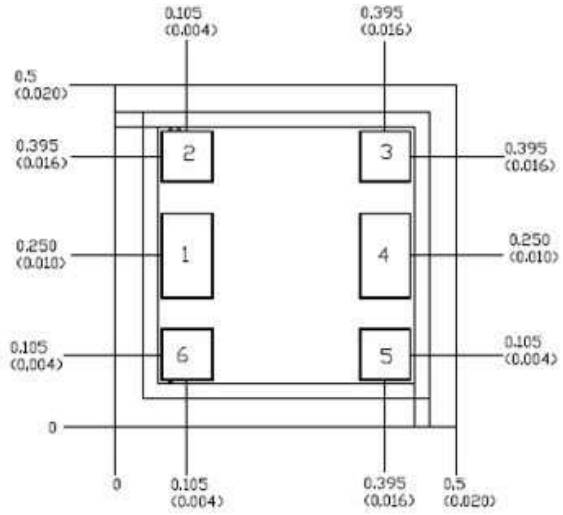

Units: millimeters (inches)
Thickness: 0.100 (0.004)
Chip edge to bond pad dimensions are shown to center of bond pad
Chip size tolerance: +/- 0.051 (0.002)

Bond Pad #1:	(RF In)	0.075 x 0.125	(0.003 x 0.005)
Bond Pad #2:	(N/C)*	0.075 x 0.075	(0.003 x 0.003)
Bond Pad #3:	(N/C)*	0.075 x 0.075	(0.003 x 0.003)
Bond Pad #4:	(RF Out)	0.075 x 0.125	(0.003 x 0.005)
Bond Pad #5:	(N/C)*	0.075 x 0.075	(0.003 x 0.003)
Bond Pad #6:	(N/C)*	0.075 x 0.075	(0.003 x 0.003)

* Note: GND is back side of MMIC

GaAs MMIC devices are susceptible to damage from Electrostatic Discharge. Proper precautions should be observed during handling, assembly and test.

TriQuint Semiconductor: www. triquint.com (972)994-8465 Fax (972)994-8504 Info-mmw@tqs.com

Aug 2011 © Rev B

TriQuint SEMICONDUCTOR

TGL4201

Chip Assembly Diagram

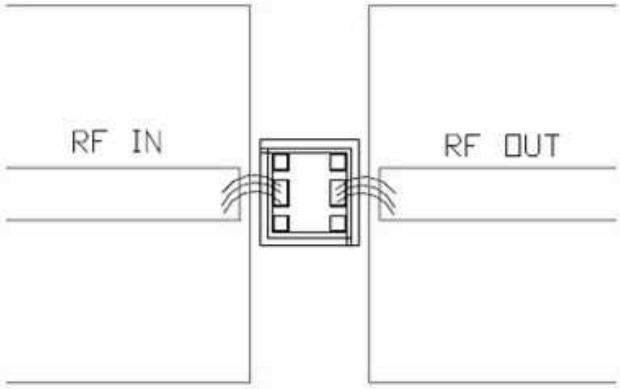

GaAs MMIC devices are susceptible to damage from Electrostatic Discharge. Proper precautions should be observed during handling, assembly and test.

TriQuint Semiconductor: www. triquint.com (972)994-8465 Fax (972)994-8504 Info-mmw@tqs.com

Aug 2011 © Rev B

TriQuint SEMICONDUCTOR

TGL4201

Assembly Process Notes

Reflow process assembly notes:

- Use AuSn (80/20) solder with limited exposure to temperatures at or above 300•C (30 seconds max)
- An alloy station or conveyor furnace with reducing atmosphere should be used.
- No fluxes should be utilized.
- Coefficient of thermal expansion matching is critical for long-term reliability.
- Devices must be stored in a dry nitrogen atmosphere.

Component placement and adhesive attachment assembly notes:

- Vacuum pencils and/or vacuum collets are the preferred method of pick up.
- The force impact is critical during auto placement.
- Organic attachment can be used in low-power applications.
- Curing should be done in a convection oven; proper exhaust is a safety concern.
- Microwave or radiant curing should not be used because of differential heating.
- Coefficient of thermal expansion matching is critical.

Interconnect process assembly notes:

- Thermosonic ball bonding is the preferred interconnect technique.
- Force, time, and ultrasonics are critical parameters.
- Aluminum wire should not be used.
- Maximum stage temperature is 200•C.

GaAs MMIC devices are susceptible to damage from Electrostatic Discharge. Proper precautions should be observed during handling, assembly and test.

Ordering Information

PART NUMBER	ATTENUATOR
TGL4201-00	0 dB Attenuator
TGL4201-02	2 dB Attenuator
TGL4201-03	3 dB Attenuator
TGL4201-06	6 dB Attenuator
TGL4201-10	10 dB Attenuator

TriQuint Semiconductor: www. triquint.com (972)994-8465 Fax (972)994-8504 Info-mmw@tqs.com

Appendix B

Dimensions of the packaging metal block of the W-band auto-calibrated receiver

This Appendix shows the dimensions of the packaging metal block of the W-band auto-calibrated receiver. This packaging aluminium block has been split along the E-plane of its input WR10 waveguide. As a result, it consists of two blocks, i.e. the top and bottom blocks, and a cover. The total dimensions of the packaging are 130.5 mm length and 19.05 mm width and height. All the dowel pins have a diameter of 1.6 mm and a length of 8 mm and the screws are M2 with different lengths, i.e. eight screws of 12 mm and four of 6 mm. The shorter ones are those placed inside the cavity of the DC circuit. With respect to the flange is a standard WR10 flange whose width is 19.05 mm. It consists of the WR10 waveguide which has four 4-40 UNC-2B screws and four dowel pins. The dimensions of the cover are 100.63 mm length, 15.98 mm width and 2 mm thick.

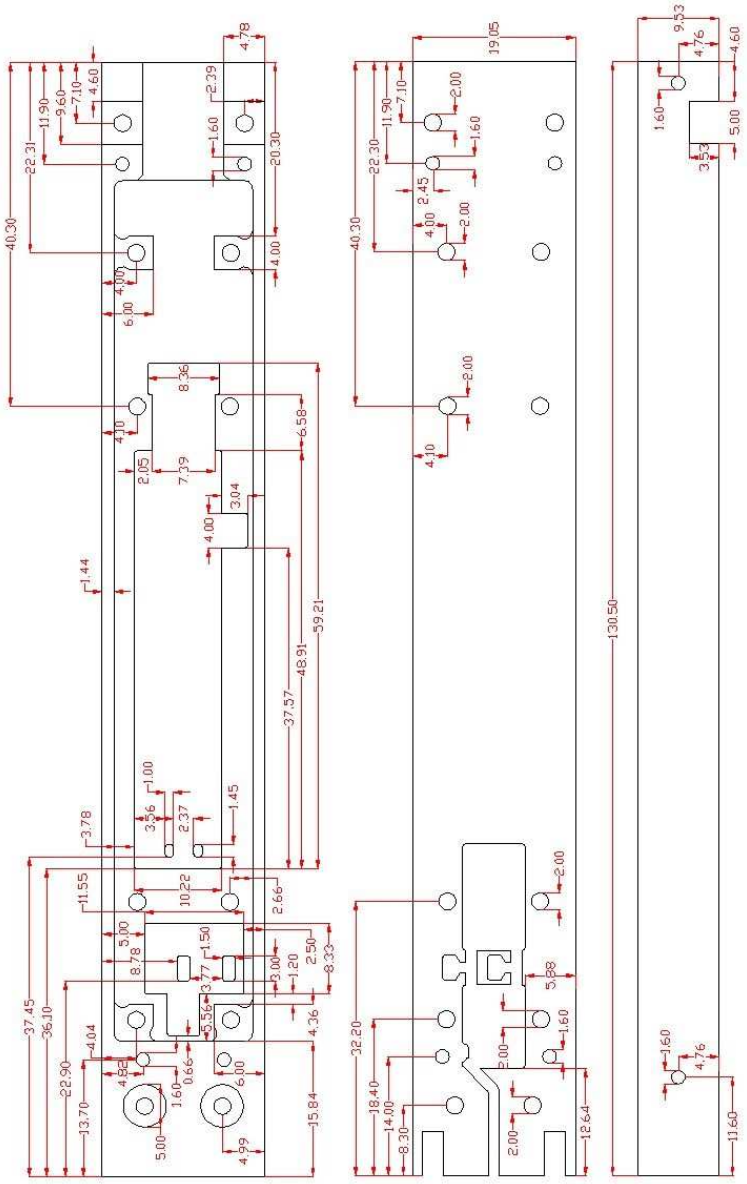

Figure B.1 – Views and dimensions (mm) of the top metal block of the packaging aluminium block.

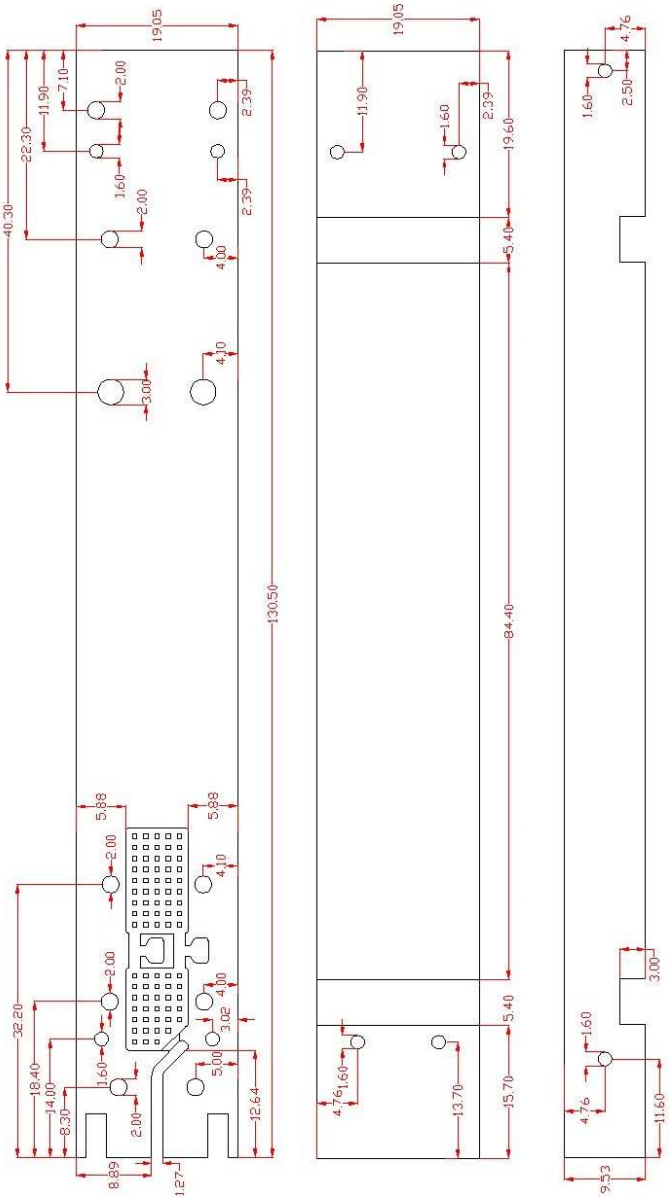

Figure B.2 – Views and dimensions (mm) of the bottom metal block of the packaging aluminium block.

Bibliography

[1] L. Yujiri, M. Shoucri and P. Moffa, *Passive Millimeter-Wave Imaging*, IEEE Microwave Magazine, vol. 4, no. 3, pp. 39-50, Sep. 2003.

[2] H.J. Liebe, *Atmospheric EHF window transparencies near 35, 90, 140 and 220 GHz*, IEEE Trans. Ant. and Propag., vol.31, no.1, pp.127,135, Jan 1983.

[3] T. Bryllert, V. Drakinskiy, K.B. Cooper and J. Stake, *Integrated 200240-GHz FMCW Radar Transceiver Module*, IEEE Trans. Microw. Theory Techn., vol. 61, no. 10, Oct. 2013.

[4] T.-J. Baek, D.-S. Ko, S.-J. Lee, Y.-H. Baek, M. Han, S.-G. Choi, J.-H. Choi, W.-J. Kim and J.-K. Rhee, *A Transceiver Module for FMCW Radar Sensors Using 94-GHz Dot-Type Schottky Diode Mixer*, IEEE Sensors Journal, vol. 11, no. 2, Feb. 2011.

[5] J. Lee, Y.-A. Li, M.-H. Hung and S.-J. Huang, *A Fully-Integrated 77-GHz FMCW Radar Transceiver in 65-nm CMOS Technology*, IEEE Journal of Solid-State Circuits, vol. 45, no. 12, Dec. 2010.

[6] J. Hasch, E. Topak, R. Schnabel, T. Zwick, R. Weigel and C. Waldschmidt, *Millimeter-Wave Technology for Automotive Radar Sensors in the 77 GHz Frequency Band*, IEEE Trans. Microw. Theory Techn., vol. 60, no. 3, Mar. 2012.

[7] T.K. Johansen and V. Krozer, *A 38 to 44 GHz Sub-Harmonic HBT Mixer with Integrated Miniature Spiral Type Marchand Balun*, Progress In Electromagnetics Research, vol. 135, pp. 317330, 2013.

[8] T. J. Chung and W.-H. Lee, *10-Gbit/s Wireless Communication System at 300 GHz*, ETRI Journal, vol. 35, no. 3, pp. 386-396, June 2013.

[9] A. Rubin and E. Socher, *Dual band 18.5Gbps transmitter at 60GHz and 80GHz in 65nm CMOS*, 2013 European Microwave Integrated Circuits Conference (EuMIC), pp. 7780, 2013.

[10] D.D. King, *Radar Handbook*, 1st ed. New York, USA: McGraw-Hill, 1970, ch. 39-Passive Detection, pp. 39-1 to 39-36.

[11] F.T. Ulaby, R.K. Moore and A.K. Fung, *Microwave Remote Sensing: Active and Passive*, Dedham, USA: Artech House, vol. 3, 1983.

[12] W.J. Wilson, R.J. Howard, A.C. Ibbot, G.S. Parks et al., *Millimeter-Wave Imaging Sensor*, IEEE Trans. Microw. Theory Techn., vol. 34, no. 10, pp. 1026-1035, Oct. 1986.

[13] D. Ewen ; R.M. Smith and B.W. Belcher, *All-weather capabilities of passive millimeter-wave sensors*, Proceedings of SPIE: Passive Millimeter-Wave Imaging Technology IV, vol. 4032, no. 103, July 2000).

[14] R.L. Howald, G. Clark, J. Hubert and D. Ammar, *Millimeter Waves: The Evolving Scene*, IEEE Conference on Technologies for Homeland Security, pp.234-239, May 2007.

[15] L. Hai-Bo H. Zhong, N. Karpowicz, Y. Chen and Z. Xi-Cheng, *Terahertz Spectroscopy and Imaging for Defense and Security Applications*, Proceedings of the IEEE , vol.95, no.8, pp.1514-1527, Aug. 2007.

[16] R. Appleby and R.N. Anderton, *Millimeter-wave and submillimeter-wave imaging for security and surveillance*, Proceedings of the IEEE, vol. 95, no 8, pp. 1683-1690, 2007.

[17] E.J. Boettcher, K. Krapels, R. Driggers, J. Garcia, C. Schuetz, J. Samluk, and R. Harris, *Modeling passive millimeter wave imaging sensor performance for discriminating small watercraft*, Applied optics, vol. 49, no 19, pp. E58-E66, 2010.

[18] N. Palka, M. Szustakowski, M. Kowalski, T. Trzcinski, R. Ryniec, M. Piszczek, W. Ciurapinski, M. Zyczkowski, P. Zagrajek and J. Wrobel, *THz*

Spectroscopy and Imaging in Security Applications, 19th International Conference on Microwave Radar and Wireless Communications (MIKON), vol.1, pp.265-270, May 2012.

[19] E. Heinz, T. May, D. Born, G. Zieger, A. Brmel, et al., *Development of passive submillimeter-wave video imaging systems for security applications*, Proc. SPIE Millimetre Wave and Terahertz Sensors and Technology V, vol. 8544, Oct. 2012

[20] A.H. Lettington, D. Dunn, N.E. Alexander, A. Wabby, B.N. Lyons, et al., *Design and development of a high-performance passive millimeter-wave imager for aeronautical applications*, Opt. Eng., vol. 44, no.9, pp. 093202-1 to 093202-6, Sept. 2005.

[21] J.E. Bjarnason, T.L.J. Chan, A.W.M. Lee, M.A. Celis and E.R. Brown, *Millimeter-wave, terahertz, and mid-infrared transmission through common clothing*, App. Phys. Lett., vol. 85, pp. 519-521, 2004.

[22] R. Appleby and H.B. Wallace, *Standoff Detection of Weapons and Contraband in the 100 GHz to 1 THz Region*, IEEE Trans. Ant. and Propag., vol. 55, no. 11, pp. 2944-2956, Nov. 2007.

[23] D.M. Sheen, D.L. McMakin and T.E. Hall, *Three-Dimensional Millimeter-Wave Imaging for Concealed Weapon Detection*, IEEE Trans. Microw. Theory Techn, vol. 49, no. 9, Sept. 2001.

[24] C. Baker, T. Lo, W.R. Tribe, B.E. Cole, M.R. Hogbin and M.C. Kemp, *Detection of Concealed Explosives at a Distance Using Terahertz Technology*, Proceedings of the IEEE, vol.95, no.8, pp.1559-1565, Aug. 2007.

[25] Outdoors PMMW image at 94 GHz extracted from www.vision4thefuture.org

[26] Indoors PMMW image at 94 GHz extracted from www.alfaimaging.com

[27] M.C. Kemp, P.F. Taday, B.E. Cole, J.A. Cluff, A.J. Fitzgerald, and W.R. Tribe, *Security applications of terahertz technology*, Proc. in SPIE, vol. 5070, pp. 4452, 2003.

[28] K. Yamamoto, M. Yamaguchi, F. Miyamaru, M. Tani, and M. Hangyo, *Non-invasive inspection of C-4 explosive in mails by terahertz timedomain spectroscopy*, Jpn. J. Appl. Phys., Part 2: Lett., vol. 43, no. 3B, pp. L414L417, Mar. 2004.

[29] D. Etayo, I. Maestrojuan, J. Teniente, I. Ederra, R. Gonzalo, *Experimental Explosive Characterization for Counterterrorist Investigation*, Journal of Infrared Millimeter and Terahertz Waves, vol. 34, no.7-8, pp. 468479, 2013.

[30] J. Chen, Y. Chen, H. Zhao, G.J., Bastiaans, and X.-C. Zhang, *Absorption coefficients of selected explosives and related compounds in the range of 0.1-2.8 THz*, Optics Express, vol. 15, pp. 12060-12067, 2007.

[31] K. Ajito, J.-. Kim, Y. Ueno, H.-J. Song, K. Ueda, W. Limwikrant, K. Yamamoto and K. Moribe, *Nondestructive Multicomponent Terahertz Chemical Imaging of Medicine in Tablets*, J. Electrochem. Soc., vol. 161, no. 9, pp. 171-175, 2014.

[32] P. Voll, S. Lorene, S. Church, J.M. Lau, M. Sieth, T. Gaier, P. Kangaslahti, M. Soria, S. Tantawi and D. Van Winkle,*A G-band cryogenic MMIC heterodyne receiver module for astronomical applications*, International Journal of Microwave and Wireless Technologies, vol.4, pp. 283-289, 2012.

[33] C. Kulesa, *Terahertz Spectroscopy for Astronomy: From Comets to Cosmology*, IEEE Transactions on Terahertz Science and Technology, vol. 1, no. 1, pp. 232-240, Sept. 2011.

[34] B.J. Drouin, K. Cooper, R. Dengler, M. Chavez, W. Chun and T. Crawford, *Submillimeter wave spectrometry for in-situ planetary science*, IEEE Aerospace Conference, pp.1-4, Mar. 2012.

[35] Planck's mission by ESA: *http* : *//sci.esa.int/planck/*

[36] Alfa Imaging: http://www.alfaimaging.com/products/alfa3-series/

[37] Digital Barriers: https://www.digitalbarriers.com/products/thruvision/

[38] Microsemi: http://www.microsemi.com/products/

[39] Millivision: http://www.millivision.com/products.html

[40] Rapidscan WaveScan 200:
http://itt-kubba.com/products/Rapiscan/RapiscanPS/wavescan/

[41] Trex Enterprises Corporation, Sago Systems:
http://www.trexenterprises.com/Pages/Subsidiaries/sago.html

[42] Qinetic PMMW cameras:
http://www.npl.co.uk/upload/pdf/20080404-appleby-1.pdf

[43] A. Tessmann, A. Leuther, H. Massler, V. Hurm, M. Kuri, M. Zink, M. Riessle, H.P. Stulz, M. Schlechtweg and O. Ambacher, *A 600 GHz low-noise amplifier module*, IEEE MTT-S International Microwave Symposium (IMS), pp.1-3, June 2014.

[44] Low noise 100-160 GHz Amplifier commercialised by OMMIC:
http://www.ommic.fr/produits/w2191-16

[45] Low noise 130-140 GHz Amplifier commercialised by Northrop Grumman:
http://www.northropgrumman.com/BusinessVentures/Microelectronics/Products/Documents/pageDocs/MLA1101rev.pdf

[46] John D. Kraus, *Radio astronomy*, Cignus-Quasar Books, second edition, 1986.

[47] M.E. Tiuri, *Radio Astronomy Receivers*, IEEE Trans. Antennas Propagation, vol. AP-12, pp. 930-938, Dec. 1964.

[48] M:S. Hersman and G.A. Poe, *Sensitivity of the Total Power Radiometer with Periodic Absolute Calibration*, IEEE Transactions on Microwaves Theory and Techniques, vol. MTT-29, no.1, pp. 32-40, Jan. 1981.

[49] R:S: Colvin, *A Study of Radio-Astronomy Receivers*, Ph.D. dissertation, Standford University, Standford, California 1961.

[50] A. Denisov, A. Gorishnyak, S. Kuzmin, V. Miklashevich, V. Obolonskv, V. Radzikhovsky, and J. Son, *Some experiments concerning resolution of 32 sensors passive 8 mm wave imaging system*, Proceeding of the 20th International Symposium on Space Terahertz Technology (ISSTT), pp. 227-229, April 2009.

[51] G.N. Sinclair, R.N. Anderton and R. Appleby, *Outdoor passive millimetre wave security screening*, IEEE 35th International Carnahan Conference on Security Technology, pp. 172-179, Oct 2001.

[52] K. Mizuno, H. Sato, T. Hirose, M. Sato and T. Ohki, *Development of Passive Millimeter-wave Imaging Sensors*, 5th SCOPE meeting, pp. 50-51, June 2009.

[53] A. Vertiy, S. Ozbek, A. Pavlyuchenko, M. Tekbas, A. Kizilhan, H. Cetinkaya and S.B. Panin, *Short-and long-range passive imaging in millimeter-wave-band*, XXXth URSI General Assembly and Scientific Symposium, pp. 1-4, Aug. 2011.

[54] V.G. Kolinko, S.H. Lin, A. Shek, W. Manning, C. Martin, M. Hall, O. Kirsten, J. Moore and D.A. Wikner, *A passive millimeter-wave imaging system for concealed weapons and explosives detection*, Proc. SPIE, vol. 5781, pp.85-92, 2005.

[55] D.W. Thomas and M.V. Nitin, *A compact, low-cost, passive MMW security scanner*, Proc. SPIE Passive Millimeter-Wave Imaging Technology VIII, vol. 5789, no. 109, May 2005.

[56] L. Yujiri, *Passive Millimeter Wave Imaging*, IEEE MTT-S Int. Microwave Symp. Digest, pp. 98-101, June 2006.

[57] M. Sato, H. Sato, T. Hirose, T. Ohki, T. Takahashi, K. Makiyama, H. Kobayashi, K. Sawaya and K. Mizuno, *Compact receiver module for a 94 GHz band passive millimetre-wave imager*, IET Microw. Antennas Propag., vol. 2, no. 9, pp. 848-853, 2009.

[58] J. J. Lynch, H. P. Moyer, J. H. Schaffner, Y. Royter, M. Sokolich, B. Hughes, Y. J. Yoon, and J. N. Schulman, *Passive millimeter-wave imaging module with preamplified zero-bias detection*, IEEE Microw. Theory Tech., vol. 56, no. 7, pp. 15921600, Jul. 2008.

[59] J. J. Lynch, P.A. Macdonald, H. P. Moyer abd R.G. Nagele, *Passive millimeter wave imaging sensors for commercial markets*, Applied Optics, vol. 49, no. 19, pp. E7E12, Jul. 2010.

[60] A. Tomkins, P. Garcia and S.P. Voinigescu,*A Passive W-Band Imaging Receiver in 65-nm Bulk CMOS*, IEEE Journal of Solid-State Circuits, vol. 45, no. 10, pp. 1981-1991, Oct. 2010.

[61] N. Alexander, P. Frijlink, J. Hendricks, E. Limiti, S. Lffler, C. Macdonald, H. Maher, L. Pettersson, D. Platt, P. Rice, M. Riester, D. Schulze and V. Vassilev, *IMAGINE project: a low cost, high performance, monolithic passive mm-wave imager front-end*, Proc. SPIE Millimetre Wave and Terahertz Sensors and Technology V, vol. 8544, pp., Oct. 2012.

[62] R.G. Humphreys, S.M. Taylor, P.A. Manning, P.D. Munday and J. Powell, *Performance of 94GHz receivers for passive imaging*, Proc. SPIE Passive Millimeter-Wave Imaging Technology X, vol. 65480H, May 2007.

[63] D.R. Vizard and R. Doyle (2006). *Advances in Millimeter Wave Imaging and Radar Systems for Civil Applications*, IEEE MTT-S Int. Microwave Symp. Digest, pp. 94-97, June 2006.

[64] 94 GHz direct detection module by Farran Technology: http://www.farran.com/shop/passive-imaging/

[65] TSW-90 (T-SENSOR-W-070100-01) by Anteral: http://www.anteral.com/sites/default/files/downloads/T-SENSOR -W-070100-01.pdf

[66] C.D. Dietlein, A. Luukanen, F. Meyer, Z. Popovic and E.N. Grossman, *Phenomenology of passive broadband terahertz images*, 4th ESA Millimeter Wave Technol. Applicat. Work-shop, Espoo, Finland 2006.

[67] R.H. Dicke, *The Measurement of Thermal Radiation at Microwave Frequencies*, Review of Scientific Instruments, vol. 17, pp. 268-275, 1946.

[68] R.L. Schmid, A.. Ulusoy, P. Song and J.D. Cressler, *A 94 GHz, 1.4 dB Insertion Loss Single-Pole Double-Throw Switch Using Reverse-Saturated SiGe HBTs*, IEEE Microw. Wireless Compon. Lett., vol. 24, no. 1, pp. 56-58, Jan. 2014.

[69] R.-B. Lai, J.-J. Kuo and H. Wang, *A 60110 GHz Transmission-Line Integrated SPDT Switch in 90 nm CMOS Technology*, IEEE Microw. Wireless Compon. Lett., vol. 20, no. 2, pp. 85-87, Feb. 2010.

[70] Z. Chen, W.C.-C. Wang, H.-C. Yao and P. Heydari, *A BiCMOS W-band 2 2 focal-plane array with on-chip antenna*, IEEE J. SolidState Circuits, vol. 47, no. 10, pp. 23552371, Oct. 2012.

[71] G. Smoot, C. Bennett, R. Weber, J. Maruschak, R. Ratliff, M. Janssen and E. Wright, *COBE Differential Microwave Radiometers-Instrument design and implementation*, The Astrophysical Journal, vol. 360, pp. 685-695, 1990.

[72] G.F. Smoot, C.L. Bennett, A. Kogut, E.L. Wright, J. Aymon, N.W. Boggess and D.T. Wilkinson, *Structure in the COBE differential microwave radiometer first-year maps*, The Astrophysical Journal, vol. 396, L1-L5, 1992.

[73] D.C.W. Lo, E.W. Lin, H. Wang, M. Biedenbender, R. Lai, G. Ng, G.S. Dow and B.R. Allen, *MMIC-based W-band Dicke switched direct-detection receiver*, 17th Annual IEEE Technical Digest Gallium Arsenide Integrated Circuit (GaAs IC) Symposium, pp. 226-229, Oct. 1995.

[74] J.J. Lynch, H.P. Moyer, J.H. Schaffner, Y. Royter, M. Sokolich, B. Hughes, Y.J. Yoon and J.N. Schulman, *Passive Millimeter-Wave Imaging Module With Preamplified Zero-Bias Detection*, IEEE Transactions on Microwave Theory and Techniques, vol. 56, no. 7, pp. 1592-1600, July 2008.

[75] L. Gilreath, V. Jain, Y. Hsin-Cheng, Z. Le and P. Heydari, *A 94-GHz passive imaging receiver using a balanced LNA with embedded Dicke switch*, IEEE Radio Frequency Integrated Circuits Symposium (RFIC), pp.79-82, May 2010.

[76] A. Tomkins, P. Garcia and S.P. Voinigescu, *A passive W-band imaging receiver in 65-nm bulk CMOS*, IEEE Journal of Solid-State Circuits, vol. 45, no. 10, pp. 1981-1991, 2010.

[77] J. W. May and G. M. Rebeiz, *Design and characterization of W-band SiGe RFICs for passive millimeter-wave imaging*, IEEE Trans. Microw. Theory Tech., vol. 58, no. 5, pp. 14201430, May 2010.

[78] Q.J. Gu, Z. Xu, H.-Y. Jian, A. Tang, M.-C.F. Chang, C.-Y. Huan and, C.-C. Nien, *100 GHZ integrated CMOS passive imager with ¿100 MV/W*

responsivity, 23fW/ HZ NEP, Electronics Letters , vol. 47, no. 9, pp. 544-545, April 2011.

[79] A. Tang, Q.J. Gu and M.-C.F. Chang, *CMOS receivers for active and passive mm-wave imaging*, IEEE Communications Magazine, vol. 49, no. 10, pp. 190-198, Oct. 2011.

[80] S. Padin, *Stable differential radiometers*, Electronic letters, vol. 30, no. 2, pp. 125-127, Jan. 1994.

[81] N. Jarosik, C.L. Bennett, M. Halpern, G. Hinshaw, A. Kogut, M. Limon, S.S. Meyer, L. Page, M. Pospieszalski, D.N. Spergel, G.S. Tucker, D.T. Wilkinson, E. Wollack, E.L. Wright and Z. Zhang, *Design, Implementation, and Testing of the Microwave Anisotropy Probe Radiometers*, The Astrophysical Journal Supplement Series, vol. 145, no. 2, pp. 413-436, April 2003.

[82] C.L. Bennett, M. Bay, M. Halpern, G. Hinshaw, C. Jackson, N. Jarosik and E.L. Wright, *The microwave anisotropy probe mission*, The Astrophysical Journal, vol. 583, no. 1, pp. 1, 2003.

[83] A. Mennella, M. Bersanelli, M. Seiffert, D. Kettle, N. Roddis, A. Wilkinson and P. Meinhold, *Offset balancing in pseudo-correlation radiometers for CMB measurements*, Astronomy Astrophysics, vol. 410, no. 3, pp. 1089-1100, 2003.

[84] B. Aja, E. Artal, L. de la Fuente, J.P. Pascual, A. Mediavilla, N. Roddis, D. Kettle, W.F. Winder, L.Pi. Cara, and P. de Paco, *Very low-noise differential radiometer at 30 GHz for the PLANCK LFI*, IEEE Transactions on Microwave Theory and Techniques, vol. 53, no. 6, pp. 2050-2062, June 2005.

[85] M. Seiffert, A. Mennella, C. Burigana, N. Mandolesi, M. Bersanelli, P. Meinhold and P. Lubin, *1/f noise and other systematic effects in the Planck-LFI radiometers*, Astronomy Astrophysics, vol. 391, no. 3, pp. 1185-1197, 2002.

[86] K. Fujimoto, *On the Correlation Radiometer Technique*, IEEE Transactions on Microwave Theory and Techniques, vol. 12, no.2, pp.203-212, Mar 1964.

[87] G.W. Swenson, Jr. and N.C. Mathur, *The interferometer in radio astronomy*, Proc. IEEE, vol. 56, no. 12, pp. 2114-2130, Dec. 1968.

[88] A.R. Thompson, J.M. Moran and G.W. Swenson, *Interferometry and Synthesis in Radio Astronomy*, New York: Wiley, 2001.

[89] D.M. Le Vine, *Synthetic aperture radiometer systems*, IEEE Trans. Microw. Theory Tech., vol. 47, no. 12, pp. 2228-2236, Dec. 1999.

[90] C.S. Ruf, C.T. Swift, A.B. Tanner and D.M. Le Vine, *Interferometric synthetic aperture microwave radiometry for the remote sensing of the earth*, IEEE Tran. Geosci. Remote Sens., vol. 26, no. 5, pp. 597-611, May 1988.

[91] C. Straub, A. Murk, N. Kampfer, D. Zardet and B. Stuber, *Development of a 22 GHz correlating radiometer for the observation of stratospheric water vapor*, Microwave Radiometry and Remote Sensing of the Environment (MICRORAD), pp.1-4, 2008.

[92] J.A. Nanzer and R.L. Rogers, *Human presence detection using millimeter-wave radiometry*, IEEE Trans. Microw. Theory Tech., vol. 55, no. 12, pp. 2727-2733, Dec. 2007.

[93] J.A. Nanzer and R.L. Rogers, *Applying millimeter-wave correlation radiometry to the detection of self-luminous objects at close range*, IEEE Trans. Microw. Theory Tech., vol. 56, no. 9, pp. 2054-2061, Sep. 2008.

[94] J.A. Nanzer, *Interferometric detection of the angular velocity of moving objects*, IEEE MTT-S Int. Microw. Symp. Dig., pp. 1628-1631, 2010.

[95] J.A. Nanzer, *Millimeter-wave interferometric angular velocity detection*, IEEE Trans. Microw. Theory Tech., vol. 58, no. 12, pp. 4128-4136, Dec. 2010.

[96] D. OsowskiNeil, J.-H Yee, J. Boldt and D. Edwards, *Development of an Instrument Performance Simulation Capability for an Infrared Correlation Radiometer for Troposheric Carbon Monoxide Measurements From Geo*, 61st International Astronautical Congress, 2010.

[97] 94 GHz direct detection module by MMIC Solutions: P.J. Rice, M. Black, J. McNicol, P.D. Munday, K. Adamson and L. Smethurst, *Development of*

a low cost 94GHz imaging receiver using multi-layer liquid crystal polymer technology, Proc. SPIE 6948 Passive Millimeter-Wave Imaging Technology XI, 694809, April 2008.

[98] TACONIC: www.taconic-add.com

[99] ARLON: www.arlon-med.com

[100] NELCO: www.parkelectro.com

[101] ROGERS: www.rogerscorp.com

[102] D.M. Pozar, *Microwave Engineering*, John Wiley & Sons, fourth edition, 2012.

[103] R.E. Collin, *Foundations for Microwave Engineering*, New York: IEEE Press, 2nd. edition, 1992.

[104] A.F. Sheta, *A novel H-shaped patch antenna*, Microw. Opt. Tech. Lett., vol. 29, no. 1, pp. 62-65, April 2001.

[105] R. Baliram Singh and T.M. Weller, *Miniaturized* 20 *GHz CPW quadrature coupler using capacitive loading*, Microw. Opt. Tech. Lett., vol. 30, no. 1, pp. 3-5, July 2001.

[106] H. Tanaka, Y. Sasaki, T. Hashimoto, Y. Yagi and Y. Ishikawa, *Miniaturized* 90 *degree hybrid coupler using high dielectric substrate for QPSK modulator*, IEEE MTT-S Int. Microwave Symp. Dig., pp. 793-796, June 1996.

[107] Z. Liu and R.W. Weikle, *A Compact Quadrature Coupler Based on Coupled Artificial Transmission Lines*, IEEE Microw. Wireless Compon. Lett., vol. 15, no. 12, pp. 889-891, Dec. 2005.

[108] A.F. Sheta, A. Mohra and S.F. Mahmoud, *A New Class of Miniature Quadrature Couplers for MIC and MMIC Applications*, Microw. Opt. Tech. Lett., vol. 34, no. 3, pp. 215-219, August 2002.

[109] I.-H. Lin, M. Devincentis, C. Caloz and T. Itoh, *Arbitrary dual-band components using composite right/left-handed transmission lines*, IEEE Trans. Microw. Theory Techn., vol. 52, no. 4, pp. 1142-1149, Dec. 2004.

[110] X.Q. Lin, R.P. Liu, X.M. Yang, J.X. Chen, X.X. Ying and Q. Cheng, *Arbitrarily dual-band components using simplified structures of conventional CRLH TLs*, IEEE Trans. Microw. Theory Techn., vol. 54, no. 7, pp. 2902-2909, Jul. 2006.

[111] M.-J. Park and B. Lee, *Dual-band, cross coupled branch line coupler*, IEEE Microw. Wireless Compon. Lett., vol. 15, no. 10, pp. 655-657, Oct. 2005.

[112] F.-L. Wong and K.-K.M. Cheng, *A novel planar branch-line coupler design for dual-band applications*, IEEE MTT-S Int. Microwave Symp. Dig., vol. 2, pp. 903-906, Jun. 2004.

[113] C. Collado, A. Grau and F. De Flaviis, *Dual-band planar quadrature hybrid with enhanced bandwidth response*, IEEE Trans. Microw. Theory Techn., vol. 54, no. 1, pp. 180-188, Jan. 2006.

[114] K.-K.M. Cheng and F.-L. Wong, *A novel approach to the design and implementation of dual-band compact planar* 90 *branch-line coupler*, IEEE Trans. Microw. Theory Techn., vol. 52, no. 11, pp. 2458-2463, Nov. 2004.

[115] H. Zhang and K.J. Chen, *A stub tapped branch-line coupler for dual-band operation*, IEEE Microw. Wireless Compon. Lett., vol. 17, no. 2, pp. 106-108, Feb. 2007.

[116] T. Kim, B. Lee and M.-J. Park, *Dual-band branch-line coupler with two center-tapped stubs*, Microw. Opt. Tech. Lett., vol. 50, no. 11, pp. 3136-3139, Dec. 2008.

[117] M.-J. Park, *Dual-band, unequal length branch-line coupler with center-tapped stubs*, IEEE Microw. Wireless Compon. Lett., vol. 19, no. 10, pp. 617-619, Oct. 2009.

[118] S.Y. Zheng, S.H. Yeung, W.S. Chan, K.F. Man, S.H. Leung and Q. Xue, *Dual-band rectangular patch hybrid coupler*, IEEE Trans. Microw. Theory Techn., vol. 56, no. 7, pp. 1721-1728, Jul. 2008.

[119] Z. Atlasbaf and K. Forooraghi, *A new dual-band branch-line coupler using coupled lines*, 7th Int. Antennas Propag. EM Theory Symp., Oct. 2006.

[120] C.-L. Hsu, J.-T. Kuo and C.-W. Chang, *Miniaturized dual-band hybrid couplers with arbitrary power division ratios*, IEEE Trans. Microw. Theory Techn., vol. 57, no. 1, pp. 149-156, Jan. 2009.

[121] C.-L. Hsu, *Dual-band branch line coupler with large power division ratios*, 2009 Proc. Asia-Pacific Microw. Conf., pp. 2088-2091, Dec. 2009.

[122] C.-L. Hsu, and J.-T. Kuo, *Design of dual-band branch line coupler with circuit miniaturization*, 2008 Proc. Asia-Pacific Microw. Conf., pp. 1-4, Dec. 2008.

[123] K.-S. Chin, K.-M. Lin, Y.-H. Wei, T.-H. Tseng and Y.-J. Yang, *Compact dual branch-line and rat-race couplers with stepped-impedance stub lines*, IEEE Trans. Microw. Theory Techn., vol. 58, no. 5, pp. 1213-1221, May 2010.

[124] M.-J. Park and B. Lee, *Wilkinson power divider with extended ports for dual-band operation*, Electron. Lett., vol. 44, no. 15, pp. 916-917, Jul. 2008.

[125] H. Kim, B. Lee and M.-J. Park, *Dual-band branch-line coupler with port extensions*, IEEE Trans. Microw. Theory Techn., vol. 58, no. 3, pp. 651-655, Mar. 2010.

[126] V. Sinchangreed, M. Uthansakul and P. Uthansakul, *Design of Tri-band Quadrature Hybrid coupler for WiMAX Applications*, 2011 Int. Symp. on Intelligent Signal Processing and Communication Systems (ISPACS), Dec. 2011.

[127] A.M. Abbosh and M.E. Bialkowski, *Design of compact directional couplers for UWB applications*, IEEE Trans. Microw. Theory Techn., vol. 55, no. 2, pp. 189-194, Feb. 2007.

[128] A.M. Abbosh and M.E. Bialkowski, *Design of ultra wideband 3 dB quadrature microstrip/slot coupler*, Microw. Opt. Tech. Lett., vol. 49, no. 9, pp. 2101-2103, Sep. 2007.

[129] H.-C. Chen and C.-Y. Chang, *Modified vertically installed planar coupling for ultrabroadband multisection quadrature hybrid*, IEEE Microw. Wireless Compon. Lett., vol. 16, no. 8, pp. 446-448, Aug. 2006.

[130] A. Moscoso-Martir, J.G. Wanguemert-Perez, I. Molina-Fernandez and E. Marquez-Segura, *Slot-coupled multisection quadrature hybrid for UWB applications*, IEEE Microw. Wireless Compon. Lett., vol. 19, no. 3, pp. 143-145, Mar. 2009.

[131] C.-H. Liang and C.-Y. Chang, *Design of microstrip ultrabroadband multisection quadrature hybrid*, Proc. of APMC, pp. 977-979, Dec. 2012.

[132] B. Mayer and R. Knöchel, *Branchline-couplers with improved design flexibility and broad bandwidth*, IEEE MTT-S Int. Microwave Symp. Dig., vol. 1, pp. 391-394, May. 1990.

[133] R. Knöchel, *Broadband flat coupling two-branch and multibranch directional couplers*, IEEE MTT-S Int. Microwave Symp. Dig., vol. 3, pp. 1327-1330, Jun. 1999.

[134] R. Levy and L. Lind, *Synthesis of symmetrical branch-guide directional couplers*, IEEE Trans. Microw. Theory Techn., vol. 16, no. 2, pp. 80-89, Feb. 1968.

[135] G.P. Riblet, *A directional coupler with very flat coupling*, IEEE Trans. Microw. Theory Techn., vol. 26, no. 2, pp. 70-74, Feb. 1978.

[136] M. Muraguchi, T. Yukitake and Y. Naito, *Optimum design of 3-dB branch-line couplers using microstrip lines*, IEEE Trans. Microw. Theory Techn., vol. 31, no. 8, pp. 674-678, Aug. 1983.

[137] J. Bonney and J. Schoebel, *Synthesis of extremely flat broadband multisection quadrature coupler*, German Microw. Conf. (GeMIC), pp. 1-4, Mar. 2008.

[138] TriQuint Semiconductor: http://www.triquint.com/products/p/TGL4201-10

[139] Hittite: http://www.hittite.com/products/view.html/view/HMC658

[140] Northrop Grumman Corporation: http://www.northropgrumman.com/BusinessVentures/... Microelectronics/Products/Pages/WBandProducts.aspx

[141] UMS: http://www.ums-gaas.com/all-products-selection-guide.php

[142] HRL Laboratories: http://www.hrl.com/capabilities/mmics/InP.html

[143] OMMIC Innovating with III-IV's: http://www.ommic.fr/produits/w2190c2-15

[144] HRL Laboratories: http://www.hrl.com/capabilities/mmics/index.html

[145] Virginia Diodes Inc. (VDI): http://vadiodes.com/index.php/en/products/diodes

[146] Y.-C. Leong and S. Weinreb, *Full Band Waveguide-to-Microstrip Probe Transitions*, IEEE MTT-S International Microwave Symposium Digest, vol. 4, pp. 1435-1438, June 1999.

[147] R. Shireen, S. Shi and D.W. Prather, *W-Band Microstrip-to-Waveguide Transition Using Via Fences*, Progress in Electromagnetics Research Letters, vol. 16, pp. 151-160, 2010.

[148] E.S. Li, G.-X. Tong and D.C. Niu, *Full W-Band Waveguide-to-Microstrip Transition With New E-Plane Probe*, IEEE Microw. Wireless Compon. Lett., vol. 23, no. 1, pp. 4-6, Jan. 2013.

[149] L. Duvillaret, F. Garet and J.-L. Coutaz, *A Reliable Method for Extraction of Material Parameters in Terahertz Time-Domain Spectroscopy*, IEEE J. Sel. Topics Quantum Electron., vol. 2, no. 3, pp. 739-746, Sept. 1996.

[150] A.M. Nicolson and G.F. Ross, *Measurement of the intrinsic properties of materials by time-domain techniques*, IEEE Trans. Instrum. Meas., vol. IM-19, no. 4, pp. 377-382, Nov. 1970.

[151] W.B. Weir, *Automatic measurement of complex dielectric constant and permeability at microwave frequencies*, Proc. IEEE, vol. 62, no. 1, pp. 33-36, Jan. 1974.

[152] T.L. Blankey and W.B. Weir, *Comments on Automatic measurement of complex dielectric constant and permeability at microwave frequencies*, Proc. IEEE, vol.63, no.1, pp. 203-205, Jan. 1975.

[153] O. Luukkonen, S.I. Maslovski and S.A. Tretyakov, *A Stepwise Nicolson-Ross-Weir-Based Material Parameter Extraction Method*, IEEE Antennas Wireless Propag. Lett., vol. 10, pp. 1295-1298, Dec. 2011.

[154] M.C. Bailey, *Design and Evaluation of an Electromagnetic Beam Waveguide for Measuring Electrical Properties of Materials*, NASA-TP-3418, 1994.

[155] D. Etayo, *New developments in the Thz field for imaging applications*, Doctoral Thesis directed by Professor R. Gonzalo, Antenna Group of the Public University of Navarra, March 2014.

[156] Topas COC Polymers: http://www.topas.com/products/topas-coc-polymers

[157] I. Maestrojuan, I. Palacios, I. Ederra and R. Gonzalo, *USE of COC substrates for millimeter-wave devices*, Microw. Opt. Tech. Lett., vol. 57, no. 2, pp. 371-377, Feb. 2015.

[158] Teraview Spectra 3000 TDS system: http://www.teraview.com/products/terahertz-pulsed-spectra-3000/

[159] N. Kaneda, Y. Qian and T. Itoh, *A Broad-band Microstrip-to-Waveguide Transition Using quasi-Yagi Antenna*, IEEE. Trans. Microw. Theory Tech., vol. 47, no. 12, pp. 2562-2567, Dec. 1999.

[160] M.H. Yang, J. Xu, Q. Zhao, G.P. Li and L. Peng, *Compact, Broadband Waveguide-to-Microstrip Transition Using Slotline Antenna*, International Conference on Microwave and Millimeter Wave Technology (ICMMT), pp. 744-747, May 2010.

[161] G. Zarba, G. Bertin and P. Besso, *An Optimised Waveguide to Microstrip Transition at K-band*, 26th European Microwave Conference, vol. 2, pp. 836-838, Sept. 1996.

[162] Z.X. Wang, P.G. Su, L. Shang and W.B. Dou, *A Waveguide-to-Microstrip Transition at W-band*, International Conference on Microwave and Millimeter Wave Technology (ICMMT), pp. 1486-1489, May 2010.

[163] Y. Lou, C.H. Chan and Q. Xue, *An In-line Waveguide to Microstrip Transition Using Radial-Shaped Probe*, IEEE Microw. Wireless Compon. Lett., vol. 18, no. 5, pp. 311-313, May 2008.

[164] Y. Zhang, J.A. Ruiz-Cruz, K.A. Zaki and A.J. Piloto, *A Waveguide to Microstrip Inline Transition With Very Simple Modular Assembly*, IEEE Microw. Wireless Compon. Lett., vol. 20, no. 9, pp. 480-482, Sept. 2010.

[165] B. Bouraki, E. Moldovan, S. Affes, K. Wu, R.G. Bosisio and S.O. Tatu, *Robust Microstrip-to-Waveguide Transitions for Millimeter-Wave Radar Sensor Applications*, IEEE Antennas Wireless Propag. Lett., vol. 8, pp. 759-762, Sept. 2009.

[166] K.Y. Han and P. Cheng-keng, *A V-band waveguide to microstrip inline transition*, IEEE MTT-S Int. Microwave Symp. Dig., pp. 1-3, June 2012.

[167] Cascade Microtech:
https://www.cmicro.com/products

[168] T.A. Midford, J.J. Wooldridge and R.L. Sturdivant, *The evolution of Packages for Monolithic Microwave and Millimeter-Wave Circuits*, IEEE Trans. Antennas Propag., vol. 43, no. 9, pp. 983-991, Sept. 1995.

[169] B.R. Hallford and C.E. Bach, *Lid interaction protected shield enclosed dielectric mounted microstrip*, U.S. Patent 3638148, Jan. 1972.

[170] P-S. Kildal and A. Kishk, *EM Modeling of surfaces with STOP or GO characteristics-artificial magnetic conductors and soft and hard surfaces*, App. Comput. Electromagn. Soc. J., vol. 18, no. 1, pp. 32-40, Mar. 2003.

[171] D. Sievenpiper, L. Zhang, R. F. Jimenez Broas, N. G. Alexopolous and E. Yablonovitch, *High-Impedance Electromagnetic Surfaces with a Forbidden Frequency Band*, IEEE Trans. Microw. Theory Techn., vol. 47, no. 11, pp. 2059-2074, Nov. 1999.

[172] E. Pucci, E. Rajo-Iglesias and P-S. Kildal, *New Microstrip Gap Waveguide ion Mushroom-Type EBG for Packaging of Microwave Components*, IEEE Microw. Wireless Compon. Lett., vol. 22, no. 3, pp. 129-131, Mar. 2012.

[173] M. Silveirinha, C. Fernandes and J. Costa, *Electromagnetic characterization of textured surfaces formed by metallic pins*, IEEE Trans. Antennas Propag., vol. 56, no. 2, pp. 405-415, Feb. 2008.

[174] E. Rajo-Iglesias, P-S. Kildal, A. Uz Zaman and A. Kishk, *Bed of Springs for Packaging of Microstrip Circuits in the Microwave Frequency Range*, IEEE Trans. Compon., Packag. and Manuf. Technol., vol. 2, no. 10, pp. 1623-1628, Oct. 2012.

[175] D. Dawn, Y. Ohashi and T. Shimura, *A novel electromagnetic bandgap metal plate for parallel plate mode suppression in shielded structures*, IEEE Microw. Wireless Compon. Lett., vol. 12, no. 5, pp. 166-168, May 2008.

[176] P-S. Kildal, E. Alfonso, A. Valero-Nogueira and Eva Rajo-Iglesias, *Local Metamaterial-Based Waveguides in Gaps Between Parallel Metal Plates*, IEEE Antennas Wireless Propag. Lett., vol. 8, pp. 84-87, 2009.

[177] P.-S. Kildal, A.U. Zaman, E. Rajo-Iglesias, E. Alfonso and A. Valero-Nogueira, *Design and experimental verification of ridge gap waveguide in bed of nails for parallel-plate mode suppression*, IET Microw. Antennas Propag., vol. 5, no. 3, pp. 262-270, Feb. 2011.

[178] E. Rajo-Iglesias andP.-S. Kildal, *Numerical studies of bandwidth of parallel-plate cut-off realised by a bed of nails, corrugations and mushroom-type electromagnetic bandgap for use in gap waveguides*, IET Microw. Antennas Propag., vol. 5, no. 3, pp. 282-289, Feb. 2011.

[179] S. Rahiminejad, A.U. Zaman, E. Pucci, H. Raza, V. Vassilev, S. Haasl, P. Lundgren, P-S. Kildal and P. Enoksson, *Micromachined ridge gap waveguide and resonator for millimeter-wave applications*, Sensors and Actuators A: Physical, vol. 186, pp. 264-269, Oct. 2012.

[180] A. Uz Zaman, J. Yang and P-S. Kildal, *Using Lid of Pins for Packaging of Microstrip Board for Descrambling the Ports of Eleven Antenna for Radio Telescope Applications*, Proc. IEEE Antennas Propag. Soc. Int. Symp. (APSURSI), pp. 1-4, July 2010.

[181] A.A. Brazalez, A.U. Zaman and P-S. Kildal, *Improved Microstrip Filters Using PMC Packaging by Lid of Nails*, IEEE Trans. Compon. Packag. Manuf. Technol., vol. 2, no. 7, pp. 1075-1084, July 2012.

[182] A.Uz Zaman, M.S. Ellis and P-S. Kildal, *Metamaterial based Packaging Method for Improved Isolation of Circuit Elements in Microwave Module*, 42nd Eur. Microwave Conf. (EuMC), Oct. 2012

[183] E. Rajo-Iglesias, A. Uz Zaman and P-S. Kildal, *Parallel Plate Cavity Mode Suppresion in Microstrip Circuit Packages Using a Lid of Nails*, IEEE Microw. Wireless Compon. Lett., vol. 20, no. 1, pp. 31-33, Jan. 2010.

[184] J. D. Joannopoulos, R. D. Meade and J. N. Finn, *Photonic Crystals: Molding the Flow of Light.* Princeton University Press, 1995.

[185] F.T. Ulaby, R.K. Moore and A.K. Fung, *Microwave Remote Sensing: Active and Passive*, vol. 1, Artech house, 1981.

[186] Eurocircuits PCB manufacturer: http://www.eurocircuits.com/

[187] Samtec Connectors: https://www.samtec.com/ftppub/pdf/sfm-sm.pdf

[188] Utilmet S.L.: http://www.utilmec.es/

[189] Agilent Technologies: "Noise Figure Measurement Accuracy: The Y-factor Method", Application Note 57-2, Feb. 2014.

[190] Rohde-Schwarz: "The Y Factor Technique for Noise Figure Measurements", Application Note, May. 2012.

[191] B. Aja, J.P. Pascual, L. de la Fuente, J. Gallegos and E. Artal, *A New Method to Obtain Total Power Receiver Equivalent Noise Temperature*, 33rd European Microwave Conference, pp. 355-358, Oct. 2003.

[192] U. Kotthaus and B. Vowinkel, *Investigation of Planar Antennas for Submillimeter Receivers*, IEEE Trans. Microw. Theory Techn., vol. 37, no. 2, pp. 375-380, Feb. 1989.

[193] K.S. Yngvesson, D.H. Schaubert, T.L. Korzeniowski, E.L. Kollberg, T. Thungren and J.F. Johansson, *Endfire Tapered Slot Antennas on Dielectric Substrates*, IEEE Trans. Antennas Propag., vol. 33, no. 12, pp. 1392-1400, Dec. 1985.

[194] N. Nikolic and A.R. Weily, *Compact E-band planar quasi-Yagi antenna with folded dipole driver*, IET Microw. Antennas Propag., vol. 4, no. 11, pp. 1728-1734, 2010.

[195] R. Janaswamy and D.H. Schaubert, *Analysis of tapered slot antenna*, IEEE Trans. Antennas Propag., vol. 33, pp. 1058-1065, Sept. 1987.

[196] B. Schoenlinner, X. Wu, J.P. Ebling, G.V. Eleftheriades and G.M. Rebeiz, *Wide-scan spherical-lens antennas for automotive radars*, IEEE Trans. Microw. Theory Techn., vol. 50, no. 9, pp. 2166-2175, Sep. 2002.

[197] A.Z. Hood, T. Karacolak and E. Topsakal, *A Small Antipodal Vivaldi Antenna for Ultrawide-Band Applications*, IEEE Antennas Wireless Propag. Lett., vol. 7, pp. 656-660, 2008.

[198] A.L. Amadjikpe, D. Choudhury, G.E. Ponchak and J. Papapolymerou, *A Compact Conformal End-Fire Antenna for 60 GHz Wireless Applications*, IEEE Antennas Propag. Soc. Int. Symposium (APSURSI), pp. 1-4, Jun. 2009.

[199] K.S. Yngvesson, T.L. Korzeniowski, Y-S. Kim, E.L. Kollberg and J.F. Johansson, *The Tapered Slot Antenna - A New Integrated Element for Millimeter-Wave Applications*, IEEE Trans. Microw. Theory Techn., vol. 37, no. 2, pp. 365-374, Feb. 1989.

[200] A. Hirata, H. Ishii and T. Nagatsuma, IEEE Trans. Microw. Theory Techn., vol. 49, no. 11, pp. 2157-2162, Nov. 2001.

[201] J.B. Rizk, and G.M. Rebeiz, *Millimeter-Wave Fermi Tapered Slot Antennas on Micromachined Silicon Substrates*, IEEE Trans. Antennas Propag., vol. 50, no. 3, pp. 379-383, Mar. 2002.

[202] N.-W. Chen, C.-T. Chuang and J.-W. Shi, *A W-Band Linear Tapered Slot Antenna on Rectangular-Grooved Silicon Substrate*, IEEE Antennas Wireless Propag. Lett., vol. 6, pp. 90-92, 2007.

[203] J.B. Muldavin and G.M. Rebeiz, *Millimeter-Wave Tapered Slot Antenna On Synthesized Low Permittivity Substrates*, IEEE Trans. Antennas Propag., vol. 47, no. 8, pp. 1276-1280, Aug. 1999.

[204] N. Ghassemi and K. Wu, *Planar High-Gain Dielectric-Loaded Antipodal Linearly Tapered Slot Antenna for E- and W-Band Gigabyte Point-to-Point Wireless Services*, IEEE Trans. Antennas Propag., vol. 61, no. 4, pp. 1747-1755, April 2013.

[205] J.D.S. Langley, P.S. Hall and P. Newham, *Novel ultrawide-band width vivaldi antenna with low cross polarisation*, Electron. Lett., vol. 29, no. 23, pp. 2004-2005, Nov. 1993.

[206] P.J. Gibson, *The Vivaldi aerial*, Proc. 9th Eur. Microw. Conf., 1979, pp. 101-105.

[207] M. Chiappe and G.L. Gragnani, *Vivaldi Antennas for Microwave Imaging: Theoretical Analysis and Design Considerations*, IEEE Trans. Instrum. Meas., vol. 55, no. 6, pp. 1885-1891, Dec. 2006.

[208] T.J. Ellis and G.M. Rebeiz, *Millimeter-Wave Tapered Slot Antennas on Micromachined Photonic Bandgap Dielectrics*, IEEE MTT Int. Microwave Symp., pp. 1157-1160, San Francisco, CA, June 1996.

[209] T.G. Lim, H.N. Ang., I.D. Robertson and B.L. Weiss, *Tapered Slot Antenna Using Photonic Bandgap Structure to Reduce Substrate Effects*, Electron. Lett., vol. 41, pp. 393-394, Mar. 2005.

[210] I.K. Kim, N. Kidera, S. Pinel, J. Papapolymerou, J. Laker, J.-G. Yook and M.M. Tentzeris, *Linear Tapered Cavity-Backed Slot Antenna for Millimeter-Wave LTCC Module*, IEEE Antennas Wireless Propag. Lett., vol. 5, pp. 175-178, Mar. 2007.

[211] R. Janaswamy and D. Schaubert, *Characteristic impedance of a wide slotline on low-permittivity substrates*, IEEE Trans. Microw. Theory Techn., vol.34, no. 8, pp. 900-902, Aug. 1986.

[212] R. Rajaraman, *Design of wideband Vivaldi antenna array for the snow radar*, B.E. Electronics & Communications Engg., Coimbatore Inst. of Tech., India, 2001.

[213] L. Pazin and Y. Leviatan, *A Compact 60-GHz Tapered Slot Antenna Printed on LCP Substrate for WPAN Applications*, IEEE Antennas Wireless Propag. Lett., vol. 9, pp. 272-275, 2010.

[214] J.B. Knorr, *Slotline Transitions*, IEEE Trans. Microw. Theory Techn., May. 1974.

[215] B. Schüppert, *Microstrip/Slotline Transitions: Modeling and Experimental Investigation*, IEEE Trans. Microw. Theory Techn., vol. 36, no. 8, pp. 1272-1282, Aug. 1988.

[216] M.M. Zinieris, R. Sloan and L.E. Davis, *A broadband Microstrip-to-Slotline Transition*, Microw. Opt. Tech. Lett., vol. 18, no. 5, pp. 339-342, Aug. 1998.

[217] J. Schorer and J. Bornemann, *Broadband Feed for Low Cross-Polarization Uniplanar Tapered Slot Antennas on Low-Permittivity Substrate*, Wireless Engineering and Technology, vol. 4, no. 1, pp. 13-18, Jan. 2013.

[218] K. U-yen, E.J. Wollack, S. Horst, T. Doiron, J. Papapolymerou and J. Laskar, *Slotline Stepped Circular Rings for Low-Loss Microstrip-to-Slotline Transitions*, IEEE Microw. Compon. Lett., vol. 17, no. 2, pp. 100-102, Feb. 2007.

[219] N.-B. Wang, Y.-C. Jiao, L. Zhang, Y. Song and F.-S. Zhang, *A Simple Low-Loss Broadband* $1-14GHz$ *Microstrip-to-Slotline Transition*, Microw. Opt. Tech. Lett., vol. 51, no. 9, pp. 2236-2239, Sept. 2009.

List of Publications

Journal Papers

1. **A. Rebollo**, R. Gonzalo, and I. Ederra, "An Inline Microstrip-to-Waveguide Transition Operating in the Full W-Band", *Journal of Infrared, Millimeter, and Terahertz Waves*, Accepted on May 2015.

2. **A. Rebollo**, R. Gonzalo, and I. Ederra, "Optimization of a Pin Surface as a Solution to Suppress Cavity Modes in a Packaged W-band Microstrip Receiver", *IEEE Transactions on Components, Packaging and Manufacturing Technology*, vol. 4, no. 6, pp. 975–982, June 2014.

International Conferences

1. **A. Rebollo**, B. Larumbe-Gonzalo, R. Gonzalo, I. Ederra, "Full W-Band Microstrip-to-Waveguide Inline Transition", *8th European Conference on Antennas and Propagation (EuCAP)*, The Hague, The Netherlands, April, 2014.

2. **A. Rebollo**, I. Maestrojuan, B. Larumbe-Gonzalo, R. Gonzalo, I. Ederra, "Parametric Study of Pin Surface Used to Suppress Undesired Modes in a Packaged W-band Microstrip Receiver", *7th European Conference on Antennas and Propagation (EuCAP)*, Goteborg, Sweden, April, 2013.

3. B. Larumbe-Gonzalo, A. Ibanez, **A. Rebollo**, R. Gonzalo, J. Teniente, "Image Acquisition at W-Band Using a Frequency Scanning Array", *7th European Conference on Antennas and Propagation (EuCAP)*, Goteborg, Sweden, April, 2013.

4. **A. Rebollo**, I. Maestrojuan, B. Larumbe-Gonzalo, R. Gonzalo, I. Ederra, "Design and Characterization of W-band Components in Planar Technology", *6th European Conference on Antennas and Propagation (EUCAP)*, Prague, Czech Republic, April, 2012.

5. B. Larumbe-Gonzalo, **A. Rebollo**, J. Teniente, "Coherently Fed Frequency Scanning Phased Array Structure for Imaging Applications", *6th European Conference on Antennas and Propagation (EUCAP)*, Prague, Czech Republic, April, 2012.

6. **A. Rebollo**, I. Maestrojuan, R. Gonzalo, I. Ederra, "A broadband Radiometer Configuration at 94GHz in Planar Technology", *IEEE MTT-S International Microwave Workshop Series on Millimeter Wave Integration Technologies (IMWS)*, Sitges, Spain, September, 2011.

7. I. Maestrojuan, I. Palacios, **A. Rebollo**, D. Etayo, J. Teniente, I. Ederra, R. Gonzalo, "Development of a Sub-Harmonic Mixer Working at 220GHz", *IEEE MTT-S International Microwave Workshop Series on Millimeter Wave Integration Technologies (IMWS)*, Sitges, Spain, September, 2011.

8. J. Teniente, R.M. Gomez, I. Maestrojuan, **A. Rebollo**, R. Gonzalo, C. del Río, "Corrugated Horn Antenna Noise Temperature Characterisation for the NRL Water Vapor Millimeter-Wave Spectrometer Project", *5th European Conference on Antennas and Propagation (EUCAP)*, Rome, Italy, April, 2011.

9. J.C. Iriarte, D. Etayo, I. Palacios, I. Maestrojuan, I. Liberal, **A. Rebollo**, J. Teniente, I. Ederra, R. Gonzalo, "Water Content Evolution in Leaves Based on Active THZ Imaging System", *5th European Conference on Antennas and Propagation (EUCAP)*, Rome, Italy, April, 2011.

10. J.C. Iriarte, J.L. Martínez de Falcón, I. Maestrojuan, I. Liberal, **A. Rebollo**, I. Ederra, R. Gonzalo, "Broadband RCS Reduction Using AMC Technology", *5th European Conference on Antennas and Propagation (EUCAP)*, Rome, Italy, April, 2011.

National Conferences

1. B. Larumbe-Gonzalo, **A. Rebollo**, J. Teniente, "Frequency Scanning Phased Array Structure for Imaging Applications", *URSI*, Elche, Spain, September, 2012.

2. **A. Rebollo**, I. Maestrojuan, R. Gonzalo, I. Ederra, "Configuración de Receptor de Banda Ancha a 94GHz en Tecnología Plana", *URSI*, Leganés, Spain, September, 2011.

3. D. Etayo, J.C. Iriarte, I. Palacios, I. Maestrojuan, I. Liberal, **A. Rebollo**, J. Teniente, I. Ederra, R. Gonzalo, "Evolución del contenido en agua de hojas basado en imágenes activas en Terahercios", *URSI*, Leganés, Spain, September, 2011.